Controlling Rydberg atoms in external electric fields

Dissertation

der Mathematisch-Naturwissenschaftlichen Fakultät
der Eberhard Karls Universität Tübingen
zur Erlangung des Grades eines
Doktors der Naturwissenschaften
(Dr. rer. nat.)

vorgelegt von
Jens Grimmel
aus Reutlingen

Tübingen
2018

Gedruckt mit Genehmigung der Mathematisch-Naturwissenschaftlichen Fakultät der Eberhard Karls Universität Tübingen.

Tag der mündlichen Qualifikation:	23.02.2018
Dekan:	Prof. Dr. Wolfgang Rosenstiel
1. Berichterstatter:	Prof. Dr. József Fortágh
2. Berichterstatter:	Prof. Dr. Nils Schopohl

Contents

Abstracts

Zusammenfassung

Im Rahmen dieser Arbeit wurden numerische Berechnungen durchgeführt, die auf der Diagonalisierung einer Matrix-Repräsentation des Stark-Hamilton-Operators auf einer Untermenge der Basis, gegeben durch den Null-Feld-Hamilton-Operator, beruhen. Es wurden Dipol-Matrix-Elemente zwischen den beteiligten Zuständen berechnet, die die Vorhersage der Übergangsstärken in Stark-verschobene Zustände ermöglichen. Die Anwendbarkeit der numerischen Methoden wurde experimentell durch Präzisionsspektroskopie in einer Rubidium-Dampfzelle mit Elektroden, unter Ausnutzung von elektromagnetisch induzierter Transparenz (EIT), bestätigt.

Die numerischen Methoden wurden erweitert, um die Ionisationsraten von Rydberg-Atomen im weit-Stark-verschobenen Regime, d. h. jenseits der klassischen Ionisationskante, vorherzusagen. Zu diesem Zweck wurde ein "complex absorbing potential" (CAP) speziell an den Stark-Hamilton-Operator angepasst. In einem Experiment wurden kalte Atome aus einer magneto-optischen Falle (engl. "magneto-optical trap", kurz MOT) in Stark-verschobene Rydberg-Zustände angeregt und die entstehenden Ionen anschließend detektiert. Die erhaltenen Ionisationsspektren stimmen mit den Ergebnissen der numerischen Berechnungen gut überein.

Daneben wurde eine Erweiterung der numerischen Methoden für gekreuzte elektrische und magnetische Felder implementiert. Dies wurde zur näherungsweisen Berechnung des "motional Stark effect" (MSE) für Atome verwendet, die sich in statischen Magnetfeldern bewegen und dadurch ein Lorentz-elektrisches Feld erfahren. In einer Präzisionsspektroskopie, wiederum unter Verwendung von EIT in einer Dampfzelle, wurde der MSE zum ersten Mal an Rubidium in niedrigen Magnetfeldern beobachtet. Die spektrale Verschiebung, die durch den MSE verursacht wird, stimmt mit der Vorhersage aus den numerischen Berechnungen überein.

In einem letzten Experiment wurde der praktische Nutzen der Kenntnis einiger Eigenschaften von Stark-verschobenen Rydberg-Zuständen illustriert. Die numerischen

Methoden inklusive des CAPs wurde verwendet, um Zustände speziell nach ihrer optischen Adressierbarkeit, ihren permanenten elektrischen Dipolmomenten und ihren Ionisationsraten auszuwählen. Im zugehörigen Experiment wurden Atome aus einer MOT in diese Zustände angeregt, um die unterschiedlichen Charakteristika des Dipol-Blockade-Effekts zu beobachten. Das Detektionsschema für dieses Experiment wurde durch eine kontrollierte Ionisation mittels kleiner Änderungen des externen elektrischen Feldes realisiert.

Abstract

In this work, numerical calculations were implemented based on the diagonalisation of a matrix representation of the Stark Hamiltonian on a subset of the basis given by the zero-field Hamiltonian. Dipole matrix elements between the involved states were calculated, which allow for the prediction of transition strengths to Stark shifted Rydberg states. The applicability of the numerical methods were confirmed experimentally by precision spectroscopy in a rubidium vapour cell with electrodes using electromagnetically induced transparency (EIT).

The numerical methods were then extended to predict ionisation rates of Rydberg states in the highly Stark shifted regime beyond the classical ionisation threshold. For this purpose, a complex absorbing potential (CAP) was specifically adjusted to the Stark Hamiltonian. An experiment was conducted, in which cold atoms from a magneto-optical trap (MOT) were excited to Stark shifted Rydberg states and the arising ions were detected. The obtained ionisation spectra agree well with the results from the numerical calculations.

Another extension of the numerical methods was implemented for crossed electric and magnetic fields. This was used for approximate calculations of the motional Stark effect (MSE), which acts on atoms moving through static magnetic fields and thereby experiencing a Lorentz electric field. In a precision spectroscopy, once more using EIT in a vapour cell, the MSE was observed in low magnetic fields for the first time in rubidium. The spectral shift, which is caused by the MSE, matches the prediction from the numerical calculations.

In a final experiment, the practical use of the knowledge of several properties of Stark shifted Rydberg states was illustrated. The numerical methods including the CAP were used to specifically select states for their optical accessibility, permanent electric dipole moments and ionisation rates. In the experiment, atoms from a MOT were excited to these states to observe different characteristics of the dipole blockade effect. The detection scheme for this experiment was realised by controlled ionisation using only small changes in the external electric field.

List of Publications

Appended Publications

This is a cumulative thesis based on the publications listed below. The complete and unaltered publications are appended at the very end of this thesis.

Publication [1]

Measurement and numerical calculation of Rubidium Rydberg Stark spectra
J. Grimmel, M. Mack, F. Karlewski, F. Jessen, M. Reinschmidt, N. Sándor, and J. Fortágh
New J. Phys. **17**, 053005 (2015).

Publication [2]

Quasiclassical quantum defect theory and the spectrum of highly excited rubidium atoms
A. Sanayei, N. Schopohl, **J. Grimmel**, M. Mack, F. Karlewski, and J. Fortágh
Phys. Rev. A **91**, 032509 (2015).

Publication [3]

State-selective all-optical detection of Rydberg atoms
F. Karlewski, M. Mack, **J. Grimmel**, N. Sándor, and J. Fortágh
Phys. Rev. A **91**, 043422 (2015).

Publication [4]

All-optical measurement of Rydberg-state lifetimes
M. Mack, **J. Grimmel**, F. Karlewski, L. Sárkány, H. Hattermann, and J. Fortágh
Phys. Rev. A **92**, 012517 (2015).

Publication [5]

Field ionization of Rydberg atoms for high-brightness electron and ion beams

A. J. McCulloch, R. W. Speirs, **J. Grimmel**, B. M. Sparkes, D. Comparat, and R. E. Scholten
Phys. Rev. A **95**, 063845 (2017).

Publication [6]

Ionization spectra of highly Stark-shifted rubidium Rydberg states
J. Grimmel, M. Stecker, M. Kaiser, F. Karlewski, L. Torralbo-Campo, A. Günther, and J. Fortágh
Phys. Rev. A **96**, 013427 (2017).

Publication [7]

Observation of the motional Stark shift in low magnetic fields
M. Kaiser, **J. Grimmel**, L. Torralbo-Campo, M. Mack, F. Karlewski, F. Jessen, N. Schopohl, and J. Fortágh
Phys. Rev. A **96**, 043401 (2017).

Publication [8]

Controlling the dipole blockade of highly Stark-shifted rubidium Rydberg states
M. Stecker, **J. Grimmel**, R. Nold, J. Fortágh and A. Günther
Ready for submission (2018).

Personal Contribution

Publication [1]

I took over the main responsibility for setting up and developing the experiment to its final state, performing the measurements, as well as the interpretation of the experimental results for this publication. I was also responsible for the continued development and extension of the numerical calculations.

Publication [2]

I was involved in the discussions for the development of the concept for this work and in editing the manuscript.

Publication [3]

I helped setting up the experiment for this work. I was involved in the discussions concerning the development of the concept and the theoretical model as well as the interpretation of the results.

Publication [4]

I helped developing the numerical calculations and setting up the experiment. I was involved in discussions about the idea for this work and in the interpretation of the results.

Publication [5]

I provided the program to perform the numerical calculations of the Stark spectrum in this publication.

Publication [6]

I had the main responsibility for the development of the numerical methods. I was involved in developing the concept for the experiment and the interpretation of the results.

Publication [7]

I helped developing the concept for this experiment as well as the interpretation of the results. The numerical calculation is based on code that was mostly written by me and partially improved from previously existing code.

Publication [8]

I was responsible for the numerical calculations for this publication. I helped in the conceptual development of the experiment and the interpretation of the experimental results.

1 Introduction

The study of Rydberg atoms, i.e. atoms in highly excited states, over the last few decades has been generally spurred by the interest in their exaggerated properties and the exploitation of such properties [9]. These range from the long lifetimes of the excited states over the large geometrical extent of their quantum mechanical wavefunctions to high sensitivity to external electric and magnetic fields, which in turn leads to additional effects, like high sensitivity to black body radiation (BBR) and strong atomic interactions. The exploitation of these effects has spawned a variety of applications, a couple of which shall be briefly reviewed in the next few paragraphs.

The conceptually most direct use of the high sensitivity of Rydberg states to environmental factors is their utilisation for the detection and quantisation of said factors. The sensing of DC electric fields, by various means and using different atomic species, has been demonstrated in free space [10–12] as well as near surfaces [13–17] and a range of different methods for the electrometry of AC fields from radio frequencies [18–20] to the microwave regime [21–23] have been successfully employed. Furthermore, a scheme for the real-time imaging of terahertz (THz) radiation via THz-to-optical conversion from Rydberg states has been implemented, thereby achieving spatial resolution below the wavelength of the THz radiation and including calibration of the THz field strength [24]. Moreover, Rydberg states of atoms and molecules can be used to record the presence of very few of these particles within a background gas with a sensitivity down to 100ppb by detecting the ions which arise from collisions of the excited atoms or molecules with the background gas [25]. Recently, there has also been a proposal for the non-destructive detection of polar molecules by using resonant energy transfer, i.e. Förster resonances, between the molecules and Rydberg atoms followed by state-selective detection of the Rydberg atoms [26].

The work presented in this thesis directly connects to many of these schemes. Our measurements and numerical calculations of Stark spectra [1] are a useful reference for electrometry of DC fields, especially near surfaces. Other schemes for the detection of electromagnetic waves benefit from these results as well, as they can be used to find

and tune pairs of states with suitable transition frequencies ranging from the radio frequency to the terahertz regime. Moreover, our obeservation of the motional Stark effect (MSE) in low magnetic fields [7] opens up new perspectives for electrometry and magnetometry in experiments using thermal gases or beams of atoms. The ionisation spectra, which we have numerically calculated and experimentally observed [6], may aid in detection schemes for atoms and molecules like the last two examples mentioned above, as they offer more deterministic ways for ionisation of Rydberg states than collisions with a background gas or field ionisation.

Another field, which has gained a lot of attention over the last few decades, is quantum information processing and quantum simulation. The general concept that spawned this field was brought forward by Richard Feynman in the early 1980s [27]. In contrast to classical computers which switch the state of bits between 0 and 1 using gate operations, quantum computation uses qubits which can be prepared in superposition states $c_0 |0\rangle + c_1 |1\rangle$ with $|c_0|^2 + |c_1|^2 = 1$ and can then be manipulated by quantum gate operations that change the probability amplitudes c_0 and c_1 to find the qubit in the state $|0\rangle$ or $|1\rangle$. The prospect of quantum computing is to find solutions to problems which can not be solved in reasonable time using conventional computers, e.g. the simulation of quantum mechanical many-particle systems or the prime factorisation of large numbers. Ever since the first theoretical proposals for quantum computing [27, 28], almost all fields of physics have started research to investigate systems which could be suitable for this purpose, including nuclear spins [29, 30], quantum dots [31, 32] and photons using linear optices [33]. Promising advances have been made in systems of trapped ions [34, 35], nitrogen-vacancy (NV) centres [36, 37], superconducting circuits [38–40] and neutral atoms, which can be excited to Rydberg states to foster interactions [41–44].

However, all of the systems that have been investigated so far for their use in quantum information processing suffer from certain drawbacks. For example, solid state systems consisting of superconducting circuits offer scalability and fast quantum gate operations, but only exhibit relatively short coherence times of the qubits on the order of 200 µs [45–47]. On the other hand, atomic qubits have coherence times on the order of seconds and optical transitions which offer the possibility to create optical connections between several of these systems, but the implementation of fast operations on a large scale remains technically challenging [44, 45]. It has therefore been proposed to create hybrid quantum systems consisting of neutral atoms in Rydberg states which can be strongly coupled to microwave cavities, which in turn can be

coupled to superconducting qubits, to overcome their individual shortcomings and combine their best features [48–51]. In this kind of system, the quantum computations would be performed on the superconducting circuit while the atoms would serve as a short-term memory of the qubit states. Unfortunately, there are still a number of obstacles to overcome in order to experimentally implement such systems, e.g. realising the coupling of Rydberg states to a stripline microwave resonator on a superconducting chip and dealing with the disruptive influence of electric fields caused by adsorbates at the surface of the chip [13–17].

Our work on Stark spectra of Rydberg atoms [1] was initiated with this last issue of adsorbate fields in mind and one of its goals was to create a reference system for electrometry near surfaces. The results from the numerical calculations in this work can also be used to search for and finetune suitable transition frequencies in the microwave regime between pairs of Stark shifted Rydberg states, which allows us to partially compensate for the limited tunability of superconducting coplanar microwave resonators [52]. Moreover, the control over the dipole blockade in the presence of an electric field, which we have demonstrated in our work [6, 8], may also be applied, for example to create a Rydberg superatom [53, 54], in the vicinity of the surface of a superconducting chip and thereby aid in the implementation of this type of hybrid quantum systems. Other experiments, which guide beams of atoms near the surface of a chip and excite them to Rydberg states [17, 55], may benefit in a similar way from our work on the motional Stark effect [7].

A further application of Rydberg atoms that has sprouted over the last decade is their use in the development of sources of cold ions and electrons as well as deterministic single ion and electron sources [56]. These sources are of particular interest for their use in ion and electron microscopy, where a low temperature source results in a beam of high brightness and high coherence, and their use for nano-fabrication methods, where ion implantation and cutting techniques benefit from their controllability [57]. Initially, this field started from a first proposal [58] and a first implementation [59] of a system in which laser-cooled atoms were directly photoionised to create cold ions and shape them into a nanoscale focused ion beam. It was then proposed that such sources could be further developed into quasideterministic single ion source by making use of the blockade effect in samples of Rydberg atoms [60]. Furthermore, the excitation to Rydberg states followed by ionisation may offer an additional degree of control over the ionisation process and therefore the properties of the resulting electron and ion beams [61–65].

In the first work included in this thesis we have investigated the energy level structure of Stark shifted Rydberg states up to the region around the classical ionisation threshold [1]. The results from this work have already been used in a collaborative work on cold ion and electron sources based on Rydberg atoms as they have enabled us to identify optically accessible states for this purpose [5]. Moreover, we have extended our numerical methods in order to predict the ionisation rates of states in this regime [6], which allows for the identification of suitable states for this type of applications. Based on and extending this work, we have observed the dipole blockade effect on various Rydberg states which were selected from the results of our numerical calculations and we have applied a controlled ionisation scheme to these states [8]. This, in turn, can serve as an additional control parameter for the creation of single ion sources from similar systems [60].

One of the key challenges for many of the aforementioned applications using Rydberg atoms is that, besides the limited number of properties one would like to exploit, there is still a countless number of other properties that make them undesirably sensitive to environmental factors. However, several different approaches to overcome this obstacle have already been implemented successfully. Probably the most obvious one is to simply remove or at least limit the presence of these environmental factors, for example by compensating external electric and magnetic fields via arrangements of electrodes and coils [66, 67] or by working in a cryogenic environment to reduce BBR [4, 68, 69]. Another approach is to dress Rydberg states using microwave fields so that the dressed states become insensitive to external fields and interactions [70–72].

The work we present in this thesis opens up new ways to specifically select Rydberg states which are insensitive to undesirable environmental factors and to simultaneously control their properties. The intricate spectra of highly Stark shifted Rydberg states that we have investigated in our works [1, 6] allow for the identification of states with decreased sensitivity to fluctuations or inhomogeneities of external electric fields, even beyond the regime of the classical ionisation threshold, as well as states which are protected from coupling to other states by searching for small dipole matrix elements between these states. Furthermore, our work regarding the MSE [7] offers the perspective to provide similar concepts for Rydberg atoms moving in magnetic fields as well as in crossed-fields configurations. Finally, the preparation of Stark shifted Rydberg states with permanent electric dipole moments, undergoing interatomic interactions followed by controlled ionisation, illustrates the practical use of choosing suitable states for the experiment in our latest work [8].

2 Stark shifted Rydberg states and their dipole matrix elements

Rydberg atoms exhibit exaggerated properties as well as extreme sensitivity to interactions with their environment due to the scaling laws of these atomic properties and interactions with powers of the principal quantum number n [73]. One of these interactions is the influence of static external electric fields on the atomic energy levels, i.e. the DC Stark effect, which is often illustrated by the scaling of the polarisability with n^7. However, one should keep in mind that the polarisability only quantifies the curvature of the parabola in the approximation of a quadratic Stark shift. This scaling law is based on an estimate given by second order perturbation theory [9, 74], which only applies to some non-degenerate states in low fields. So, while the scaling law of n^7 may result in enormous estimates of the polarisabilities of some high lying Rydberg states, the Stark effect can, in general, yield a wide range of different shifts in sign and shape. It is this variety of peculiarities of the Stark effect that require special attention in experimental situations, where inadvertent electric fields may disturb the experiment, as well as situations, where the Stark effect is used to intentionally tune atomic properties. The investigation of the DC Stark effect in a controlled experimental environment and the prediction of Stark shifts via numerical calculations were therefore the goal of the first work in this thesis [1].

For the theoretical treatment of the DC Stark effect on an atom in an external homogeneous electric field F_E we consider the Stark Hamiltonian

$$\hat{H} = \hat{H}_0 + F_\mathrm{E}\hat{z}, \tag{2.1}$$

with $\hat{H}_0$ denoting the Hamiltonian of the atom in zero-field, which we will specify for our calculations later in this chapter. We presume that the electric field is applied along the z-axis. All equations that concern the theoretical treatment in this chapter will be given in atomic units. From this simple way of writing down the Hamiltonian $\hat{H}$ we can already see one of its key features. With $\hat{H}_0$ forming a potential well which

we may presume to be approximately coulombic for this purpose and the electric field term diverging to $-\infty$ in one direction, it becomes clear that the Hamiltonian $\hat{H}$ formally has no bound states. Therefore, all states of this Hamiltonian couple to the continuum to some extent and while this is mostly negligible for the considerations in this chapter, we will revisit this topic later on (see Ch. 3).

It has already been shown in the 1970s that perturbation theory applied to this Hamiltonian only results in an asymptotic series which does not converge. This means that, for a given number of terms from the series and desired accuracy of the result, one can find a maximum useful field strength, which decreases again for higher order terms [75]. Therefore, the numerical method of representing the Hamiltonian $\hat{H}$ on a subset of the basis given by $\hat{H}_0$ and calculating the Stark shifted eigenenergies of this matrix representation is usually favoured over perturbation theory [76]. But even though this numerical method has been in use since the 1970s, its applicability was greatly extended in recent years with the development of more powerful computers since the matrix representation of the Hamiltonian $\hat{H}$ requires a bigger basis for higher principal quantum numbers and higher electric fields F_E in order to obtain accurate results.

For the representation of the Stark Hamiltonian $\hat{H}$ (see Eq. (2.1)) as a matrix we use the energy levels relative to the ionisation energy, which are given by the Rydberg formula

$$E(n,l,j) = -\frac{R_{87}}{(n-\delta(n,l,j))^2}, \tag{2.2}$$

with the Rydberg constant R_{87} for ^{87}Rb, for the entries of the diagonal zero-field Hamiltonian $\hat{H}_0$ [9]. The quantum defects $\delta(n,l,j)$ are determined experimentally [77–80]. We calculate the matrix representation of $\hat{z}$ using

$$\begin{aligned}\left\langle n,l,j,m_j \,\middle|\, \hat{z} \,\middle|\, n',l',j',m_j' \right\rangle =& \delta_{m_j,m_j'}\delta_{l,l'\pm1} \left\langle n,l,j \,\middle|\, r \,\middle|\, n',l',j' \right\rangle \\ &\times \sum_{m_l=m_j\pm\frac{1}{2}} \left\{ \left\langle l, s=\frac{1}{2}, m_l, m_s=m_j-m_l \,\middle|\, j, m_j \right\rangle \right. \\ &\times \left\langle l', s=\frac{1}{2}, m_l, m_s=m_j-m_l \,\middle|\, j', m_j' \right\rangle \\ &\left. \times \left\langle l, m_l \,\middle|\, \cos\theta \,\middle|\, l', m_l \right\rangle \right\}\end{aligned} \tag{2.3}$$

from [76], where the result of the angular overlap integral in the fourth line can be calculated analytically [81] and the second and third line are composed of Clebsch-

Gordan coefficients. We employ the same energy levels as before (see Eq. (2.2)) to numerically integrate the radial wavefunctions utilising a parametric model potential [82] in order to determine the radial overlap integrals in the first line.

Following our use of this model potential in this work [1], our theory collaborator Professor Schopohl has developed a modified effective single electron potential [2]. This development was spurred by the fact that recent variational calculations using the aforementioned parametric model potential [83] and spectroscopic measurements [77, 78] deviate significantly. The newly modified potential introduces a correction to one of the parameters, which essentially governs the effective charge distribution in the ionic core, as well as a spin-orbit term, which is cut off for the region inside the ionic core. Thereby, this modified effective single electron potential correctly describes the spectrum of Rydberg states on the fine-splitting scale.

For the calculation of the Stark spectra, we then diagonalise the complete matrix representation of the Stark Hamiltonian numerically, not only calculating the eigenvalues but also the eigenvectors β for all Stark shifted states. Thereby, we can represent each Stark shifted state as a linear combination of eigenstates of the zero-field Hamiltonian $\hat{H}_0$. We use this to calculate the dipole matrix elements between the intermediate state $5P_{3/2}$ (see Fig. 2.1) and each Stark shifted Rydberg state ξ:

$$\begin{aligned}\left\langle \xi \left| \vec{r} \right| 5P_{3/2}, F{=}3, m_F \right\rangle &= \sum_{n,l,j,m_j} \left\langle \xi \left| n,l,j,m_j \right\rangle \left\langle n,l,j,m_j \right| \vec{r} \left| 5P_{3/2}, F{=}3, m_F \right\rangle \right. \\ &= \sum_{n,l,j,m_j} \beta_{n,l,j,|m_j|} \left\langle n,l,j,m_j \right| \vec{r} \left| 5P_{3/2}, F{=}3, m_F \right\rangle . \end{aligned} \tag{2.4}$$

The x- and y-entries are calculated in a similar fashion as the z-entry (see Eq. (2.3)) using the numerically calculated radial overlap integrals and the analytical formulas for the angular overlap integrals, which are replaced by the according terms for x and y in spherical coordinates [81].

Using the same algorithms, we can then calculate dipole matrix elements between the ground state $5S_{1/2}$ and the excited state $5P_{3/2}$. We combine them for all m'_F substates of the ground state to calculate weighting factors

$$\eta_{m_F} = \sum_{m'_F} \left| \left\langle 5P_{3/2}, F{=}3, m_F \right| \vec{\varepsilon}_\mathrm{p} \vec{r} \left| 5S_{1/2}, F'{=}2, m'_F \right\rangle \right|^2 \tag{2.5}$$

for each m_F substate of the excited state, taking into account the polarisation $\vec{\varepsilon}_\mathrm{p}$ of the probe laser. We then combine all of the above, also including the polarisation $\vec{\varepsilon}_\mathrm{c}$

of the coupling laser, into a measure for the transition strength

$$D = \sum_{m_F} \eta_{m_F} \left| \left\langle \xi \left| \vec{\varepsilon}_{\mathrm{c}} \vec{r} \right| 5\mathrm{P}_{3/2}, F{=}3, m_F \right\rangle \right|^2. \tag{2.6}$$

This quantity D can now be used to predict which Stark shifted states will be optically accessible in the three-level ladder-scheme (see Fig. 2.1).

We compare the results from the numerical calculations to experimental data obtained via an electromagnetically induced transparency (EIT) measurement in a vapour cell setup [12, 84–87]. The EIT measurement is performed in a three-level ladder-configuration (see Fig. 2.1(a)) with the probe laser on resonance with the transition between the ground and excited state at low Rabi frequency Ω_{p} and the coupling laser scanning across the transition between the excited state and Rydberg states at high Rabi frequency Ω_{c}. This results in increased transmission of the probe laser when both lasers are on resonance, which is caused by Autler-Townes splitting of the intermediate state $|e\rangle$ and a Fano-like destructive interference of the excitation paths $|g\rangle \rightarrow |e\rangle$ and $|g\rangle \rightarrow |e\rangle \rightarrow |r\rangle \rightarrow |e\rangle$ (see Fig. 2.1(a)) [84].

In the experiment, two frequency stabilised diode lasers counter-propagate through a vapour cell which contains a plate capacitor (see Fig. 2.1(b)). A voltage is applied to the plate capacitor to create an electric field F_{E} that Stark shifts the Rydberg states in the sample. The transmission of the probe laser through the rubidium vapour is monitored using a photodiode and, in order to improve the signal-to-noise ratio, a frequency-modulated lock-in technique is employed [1]. For this technique, we modulate the intensity of the coupling beam using an acousto-optic modulator (AOM) with a frequency, which is modulated as well. We demodulate on the carrier frequency as well as two of the arising sidebands and average over these three signals.

The recorded EIT signal is then plotted in false colours against the coupling laser detuning Δ_{c} relative to the zero-field state and the electric field F_{E} to create a Stark map (see Fig. 2.2(a) and 2.3(a)). The results from the numerical calculations are plotted for the same region and for $|m_j| = 1/2$, $3/2$ and $5/2$ (see Fig. 2.2(b) and 2.3(b)), because these are the only accessible states in the three-level ladder-scheme starting from the $5\mathrm{S}_{1/2}$ ground state due to dipole selection rules, i.e. $\Delta m_j = 0, \pm 1$ for each transition. The opacity of the lines is determined from the measure for the transition strength D (see Eq. (2.6)). We find very good agreement of the energy levels from the measured and numerically calculated results down to the experimental accuracy of 2 MHz [1]. Furthermore, the intensity of the EIT signal from the experiment and the

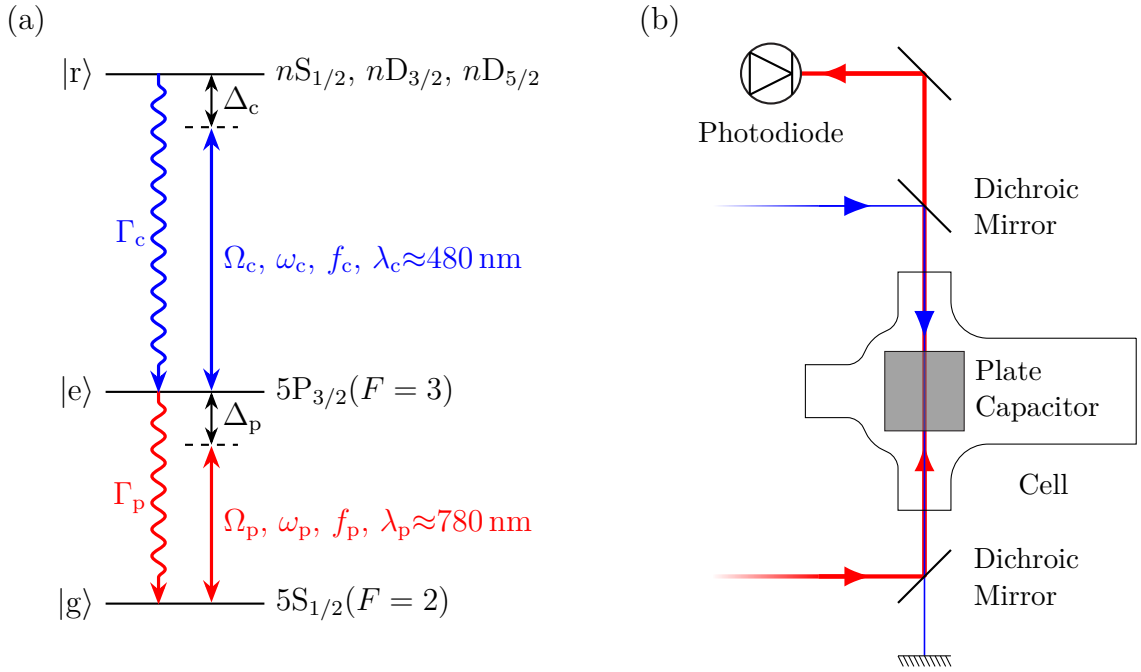

Figure 2.1: (a) Three-level ladder-scheme used for electromagnetically induced transparency (EIT) and excitation to Rydberg states of ^{87}Rb. Due to dipole selection rules, only the depicted Rydberg states may be probed or excited in this scheme. The left-hand sides of the energy levels are labelled with the notation widely used in theory for the ground, excited and Rydberg states and the right-hand sides are labelled with the matching states of ^{87}Rb which are used in the experiments in the present work. The indices p and c are used to label the according properties (decay rate Γ, Rabi frequency Ω, transition angular frequency ω, transition frequency f, detuning from the resonance Δ and wavelength λ) of the probe and coupling transitions, respectively. Please note that the detuning Δ in this thesis refers to a detuning in frequency and not angular frequency. It may therefore differ by a factor of 2π from the detunings in some of the included publications. The labels introduced in this figure will be used throughout this thesis. (b) Schematic diagram of the central part of the experimental setup for the measurement of Stark maps using EIT. The lasers are overlapped to counter-propagate along the cell and through the plate capacitor using the dichroic mirrors. The intensity and polarisation of both laser beams can be adjusted independently. The volume of the cell can be filled with rubidium vapour from a dispenser located to the right of the part depicted here. For the measurement of the Stark spectra (see Fig. 2.2 and 2.3) a voltage was applied to the plate capacitor and the transmission of the probe beam through the cell was recorded using the photodiode. Figure (b) taken from [1] and adapted for this thesis.

predictions from the measure for the transition D show good qualitative agreement, even in the 'spaghetti region' [88], where the spectrum exhibits an intricate tangle of avoided crossings.

However, the agreement of the measure for the transition strength D with the experimentally observed resonances deteriorates at higher electric fields (see Fig. 2.3), especially near and beyond the classical ionisation threshold

$$E_{\mathrm{ion}} = -2\sqrt{F_{\mathrm{E}}}, \tag{2.7}$$

which is determined from the position of the saddle point in the approximation of the atomic potential by a Coulomb potential plus an external electric field

$$V_{\mathrm{C,E}} = -\frac{1}{r} - F_{\mathrm{E}} z. \tag{2.8}$$

In the original publication we have discussed that these discrepancies could be corrected in the numerical calculations by using more accurate radial wavefunctions for states with low angular momentum numbers l and by including a mechanism to simulate ionisation effects [1]. With the benefit of hindsight, we can now revisit this topic and include the knowledge we have gained in our following work [6], where we used the same method to calculate the radial wavefunctions but included ionisation effects (see Ch. 3). It is therefore evident that ionisation effects constitute the main contribution to this kind of deviations.

In a subtle way, this work [1] has close connections to our other works on the all-optical detection of Rydberg state populations [3] and lifetimes [4]. Namely, our numerical implementation of the theoretical model for the time evolution of Rydberg state populations using a Lindblad master equation is built upon a shared code library with our numerical calculations of Stark spectra. This code library includes functions for zero-field energy levels, radial wavefunctions, radial and angular overlap integrals, and Clebsch-Gordan coefficients. Thereby, each of our implementations that make use of this code library has furthered its development with new functions and has led to optimisations and refinements of the existing functions.

This work [1] presents a confirmation of the methods from [76] on a larger scale of principle quantum numbers and electric field range as well as an extension by utilising the dipole matrix elements to calculate the measure for the transition strength D. With this, we have not only created a reference system for the measurement of electric fields in other experiments, but have also gained knowledge about the spaghetti

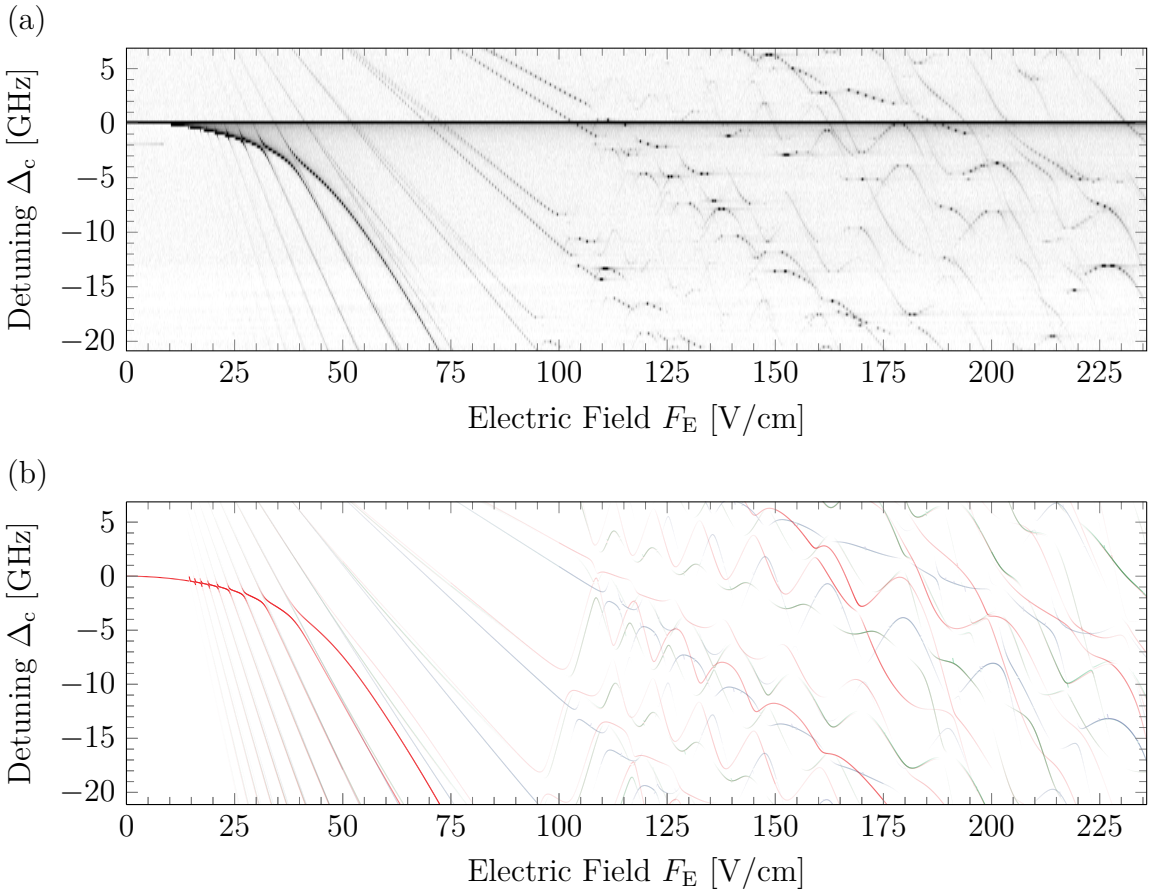

Figure 2.2: (a) Experimental results of an EIT measurement for a Stark spectrum near the unperturbed $35S_{1/2}$ state. The signal, which is plotted in gray scale, is given by the transmission of the probe beam through the sample in a lock-in measurement. Some lines appear dotted here because of the experimental frequency resolution of 125 MHz. The data shows the zero-field resonance as a horizontal line since the plate capacitor does not cover the full optical path of the lasers through the cell. (b) Numerically calculated energy levels for the same region of the spectrum. The calculation was performed for $|m_j| = 1/2$ (red), $|m_j| = 3/2$ (green) and $|m_j| = 5/2$ (blue). The opacity of the lines is determined from the calculated transition strength D (see Eq. (2.6)). The comparison between (a) and (b) shows agreement of the energy levels down to the experimental frequency resolution as well as the transition strengths. Figures (a) and (b) taken from [1] and adapted for this thesis.

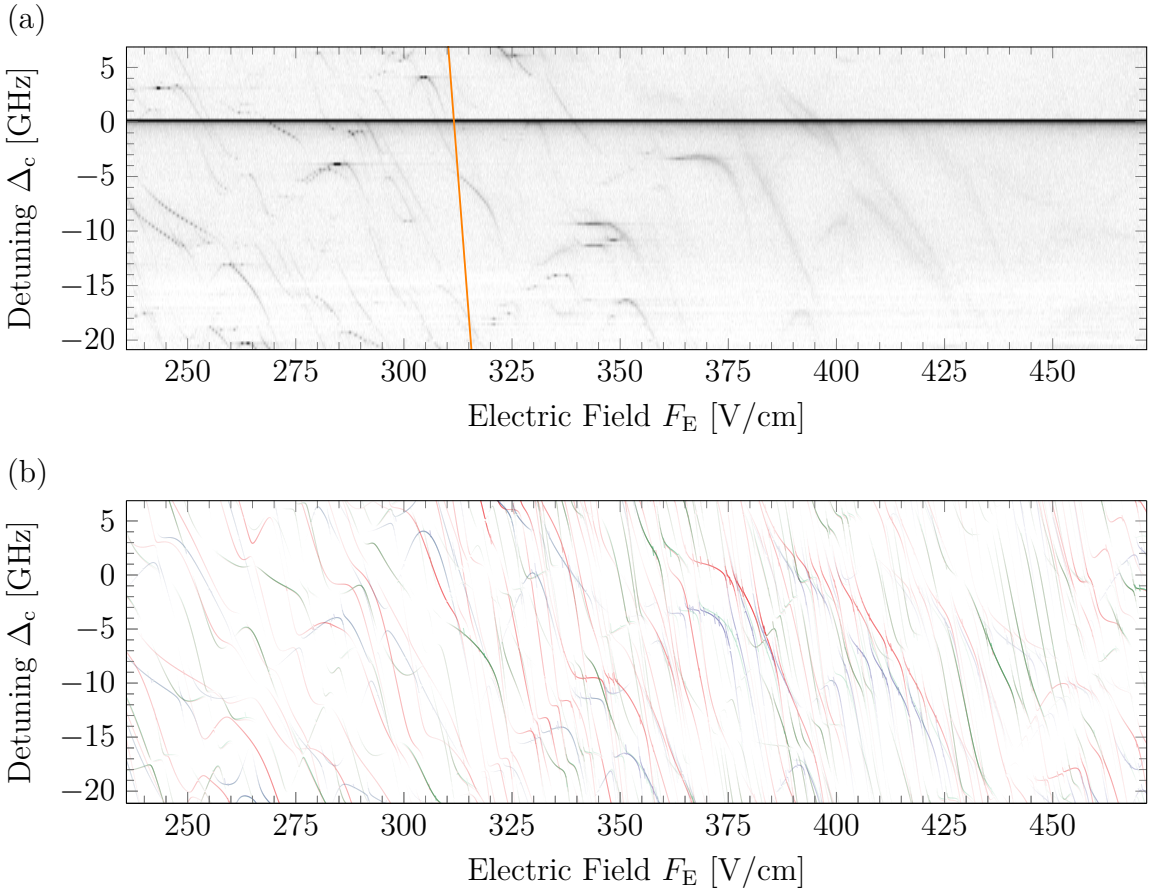

Figure 2.3: (a) and (b) are continuations of the respective subfigures of Fig. 2.2. The orange line in (a) indicates the classical ionisation threshold according to Eq. (2.7). In this high field region, the resonances in the experimental data show significant broadening beyond the classical ionisation threshold due to the ionisation rate. At the same time, we find that all resonances we observe in the experimental data are also still present in the results from the numerical calculations but not vice versa. The states we do not observe experimentally are states with such high ionisation rates that their signal disappears in the noise. Figures (a) and (b) taken from [1] and adapted for this thesis.

region of the Stark maps. The spaghetti region should therefore not be seen as an uncontrollable tangle of states any more, but rather as an opportunity to pick and tailor Stark shifted states to experimental needs. From the numerical calculations we can choose states according to their energy levels and level splittings, as well as the transition strengths to other states and their sensitivity to external electric fields and their polarisability. We have applied our numerical methods in a collaborative work with the group of Professor Scholten [5], where Stark shifted Rydberg states just below the classical ionisation threshold have been studied for their use in sources for high-brightness, highly monochromatic electron and ion beams. Furthermore, we can control the aforementioned properties using the external electric field, for example to efficiently excite to a Stark shifted state and then tune it to a state with only a small dipole matrix element and therefore vanishing decay rate to the $5P_{3/2}$ state, rendering it a state similar to a 'dark state'.

3 Ionisation spectra beyond the classical ionisation threshold

In the previous chapter we have investigated the Stark effect on rubidium Rydberg states from zero-field up to the region around the classical ionisation threshold [1]. We have seen that by calculating the dipole matrix elements between Stark shifted Rydberg states and the intermediate state $5P_{3/2}$ we can compute a measure for the transition strength D (see Eq. (2.6)) that allows us to predict, which states in the Stark map will be optically accessible. However, the high field region of the spectrum starting around the classical ionisation threshold (see Eq. (2.7)) is governed by the coupling of states to the continuum, via tunnelling through the Coulomb barrier or directly, where the barrier already opens. On the one hand, this means that the linewidth of resonances in this region is dominated by the ionisation rate and that a high ionisation rate may render resonances optically inaccessible. But on the other hand, a precise knowledge of these spectra can be used to gain improved control over the ionisation process, e.g. to trigger ionisation on purpose for detection schemes or to stabilise atoms in excited states by keeping their ionisation rate low.

A well known method which can be used for the calculation of ionisation rates of hydrogen and hydrogen-like atoms is the method of complex rotation (CR), which is also referred to as the method of complex coordinates [88–90]. The basic idea of this method is to 'rotate' the coordinates of the Hamiltonian into the complex plane by substituting $\hat{r} \rightarrow \hat{r} \cdot \exp(i\theta)$ and $\hat{p} \rightarrow \hat{p} \cdot \exp(-i\theta)$, using the rotation angle θ [89]. The opposing signs in the exponents assure that the commutator relation remain unchanged. The substitution makes the Hamiltonian non-Hermitian. Its eigenvalues may therefore be complex and can be interpreted as the energy levels and coupling rates to the continuum [89]. In order to find the correct value of θ in a numerical calculation on a limited set of states, one can vary θ for each resonance and map out 'θ-trajectories', which exhibit stationary points near resonances. The stationary point marks the value that is then chosen for θ at this resonance. This variational

process generally has to be performed separately for each resonance in the spectrum, making this method computationally very expensive because of the large number of resonances we usually observe in a Stark map (see Ch. 2).

Another method, which bears certain similarities to CR, but may be perceived as more illustrative, is the utilisation of a complex absorbing potential (CAP) [91–94]. For this method, a term of the form $-i\eta W(\vec{r})$ is added to the original Hamiltonian, which renders it non-Hermitian in a way similar to CR. The free parameter η is generally varied for each resonance in a similar fashion as θ for CR to find stationary points of the complex energy eigenvalues. This presents us with the same difficulty as with CR, namely the high computational expense due to the large number of resonances. However, in our publication [6] we have shown that we can choose a CAP, which is adapted to the Stark Hamiltonian and which allows us to work with one constant value of η for all resonances across the whole range of the external electric field F_E in an energy region, which spans principle quantum numbers of at least $\Delta n = \pm 1$ [6].

We start from the same Stark Hamiltonian $\hat{H}$ as before (see Eq. (2.1)) and add the CAP to it

$$\hat{H}_\mathrm{CAP} = \hat{H} - i\eta W(\hat{r}, F_\mathrm{E}) \tag{3.1}$$

with the free scaling parameter $\eta \in \mathbb{R}^+$. In general, the CAP can be chosen freely within certain limits [92]. However, here we chose the shape of the CAP as

$$W(\hat{r}, F_\mathrm{E}) = \Theta(\hat{r} - r_c(F_\mathrm{E})) \cdot (\hat{r} - r_c(F_\mathrm{E}))^6. \tag{3.2}$$

This potential resembles an r^6 shape that is radially shifted by r_c using the Heaviside function Θ [92, 93, 95]. We adapt the radius for the shift

$$r_c(F_\mathrm{E}) = \frac{1}{\sqrt{F_\mathrm{E}}} \tag{3.3}$$

with the external electric field F_E to represent the radius of the saddle point of the potential $V_\mathrm{C,E}$ (see Eq. (2.8)). Thereby, the r^6 scaling of the potential radially starts at the saddle point for each value of the external electric field F_E (see Fig. 3.1). The general idea of a CAP is that it froms absorbing boundaries, meaning that it absorbs the wavefunction in an 'outside' region of the original Hamiltonian (see Eq. (2.1) and (3.1)) without introducing reflections [91, 92]. Our choice for the CAP is adjusted to the external electric field F_E via the radial shift $r_c(F_\mathrm{E})$ (see Eq. (3.3)), because

we can graphically interpret this radius as the limit between the 'inside' and the 'outside' region of the atom (see Fig. 3.1). In effect, this means that we absorb the wavefunction only in this 'outside' region for each value of the external electric field F_{E}.

For the numerical calculation, we represent the CAP Hamiltonian H_{CAP}, including W, as a matrix using similar methods as for the regular Stark Hamiltonian (see Ch. 2). We calculate its entries using the same radial wavefunctions as for the matrix representation of the $\hat{z}$-operator (see Eq. (2.3)). We vary the free parameter η for exemplary values of the electric field F_{E} and then fix it to one value, which is used for all resonances calculated on the previously chosen subset of the basis given by $\hat{H}_0$. It is convenient to choose the first exemplary value of the electric field F_{E} near the classical ionisation threshold (see Eq. (2.7)) to determine a rough order of magnitude for η. Further exemplary values can then be picked at higher values of the electric field to determine η more precisely. Since the CAP Hamiltonian $\hat{H}_{\mathrm{CAP}}$ is non-Hermitian, diagonalisation may yield complex eigenvalues of the form

$$E_{\mathrm{c}} = E_r - i\frac{\Gamma_{\mathrm{ion}}}{2}. \tag{3.4}$$

We interpret the real part of these complex numbers as the Stark shifted energy levels E_r and the imaginary part as the ionisation rate Γ_{ion} [94]. We also calculate the eigenvectors and use them to obtain the measure for the transition strength D as described in Ch. 2. Combining all of this, we can then compute a Lorentzian curve

$$I(E) = \frac{D}{\pi} \cdot \frac{\Gamma_{\mathrm{ion}}}{\Gamma_{\mathrm{ion}}^2 + (E - E_r)^2} \tag{3.5}$$

against the energy E for each resonance, which are all summed up to create a diagram that resembles the ionisation spectrum (see Figs. 3.2(b), 3.3(b) and 3.4(b)).

In order to verify the results from these numerical calculations we have conducted an experiment in which we excite rubidium atoms to Rydberg states in the presence of an electric field and count the arising ions. In the experiment, we continuously load a magneto-optical trap (MOT) from a dispenser and shine in a coupling beam, which is focussed to a light sheet (see Fig. 3.1). Together, the MOT beams and the coupling beam implement the three-level ladder-scheme for the excitation to Rydberg states (see Fig. 2.1(a)). The plane of the light sheet is chosen to be perpendicular to the direction of the electric field, which is created by the extractor electrodes. The electric field serves two purposes here: on the one hand it imposes the Stark effect onto

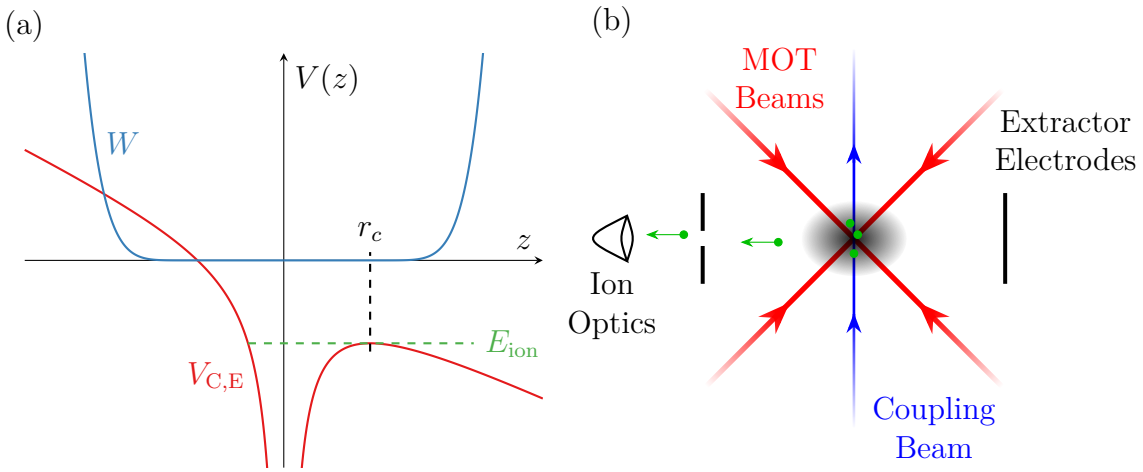

Figure 3.1: (a) Illustration of our choice of the complex absorbing potential (CAP). The red curve represents a Coulomb potential with an external electric field (see Eq. (2.8)). From this potential $V_{\text{C,E}}$ we can easily determine the radial position r_c (black dashed line) of the saddle point, which appears as a local maximum along the z-axis here. The energy of the saddle point marks the classical ionisation threshold E_{ion} (green dashed line). The potential W that we have chosen for the CAP in this work (see Eq. (3.2)) is depicted in blue. The shape of W follows an r^6 potential which starts at the radial position of r_c. Graphically speaking, we thereby create a CAP which is zero 'inside' the atomic potential and radially diverges on the 'outside'. (b) Schematic diagram of the central part of the experimental setup. In the centre of a vacuum chamber, we load rubidium atoms into a magneto-optical trap (MOT). We apply a voltage to the extractor electrodes to create an approximately homogeneous electric field at the position of the atoms. The three-level ladder-scheme for the excitation to Rydberg states (see Fig. 2.1) is realised by the MOT beams (red) for the probe transition and the coupling beam (blue), which is focused to form a light sheet, for the coupling transition. The electric field serves to Stark shift the excited Rydberg atoms as well as to guide the emerging ions to the ion optics. Figures (a) and (b) taken from [6] and adapted for this thesis.

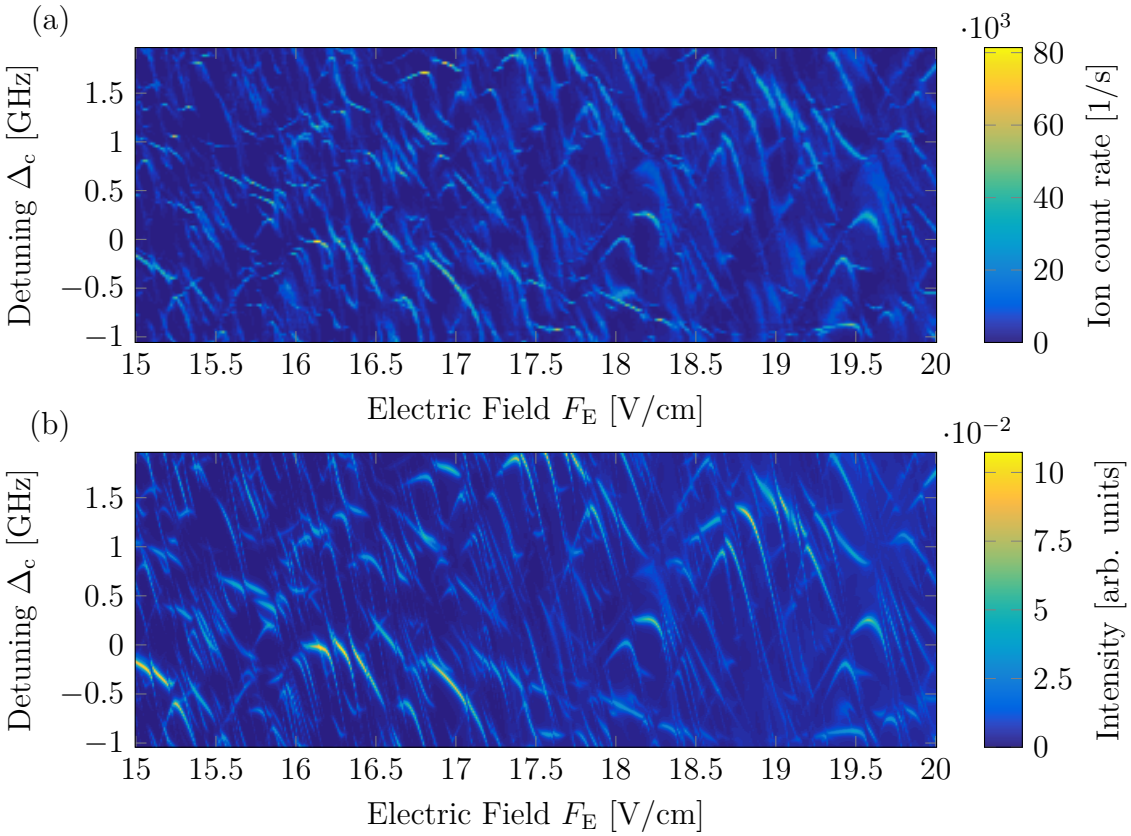

Figure 3.2: Measured and numerically calculated ionisation spectrum near $70S_{1/2}$. In this energy region, the classical ionisation threshold (see Eq. (2.7)) is at $F_{\text{ion}} \approx 16.1\,\text{V/cm}$. (a) The diagram shows the ion count rate from the experiment in false colours. The experimental data has been scaled linearly to match the electric field axis to the numerically calculated results. (b) The plot shows the matching results from the numerical calculations. The false colours are determined by summing up the Lorentzian curves according to Eq. (3.5). For the numerical calculations, we have used a basis size of ≈10 000 and have carried out a variation of the free parameter η for exemplary values of the electric field and thereby ended up with a value of $\eta = 2 \times 10^5$, which was fixed for all results shown in Figs. 3.2, 3.3 and 3.4. We find good agreement between the experimental and theoretical results in this region. In particular, the broadening of the resonances as we cross the classical ionisation threshold as well as the appearance and disappearance of resonances along the electric field are well reproduced by our numerical model. Figures (a) and (b) taken from [6] and adapted for this thesis.

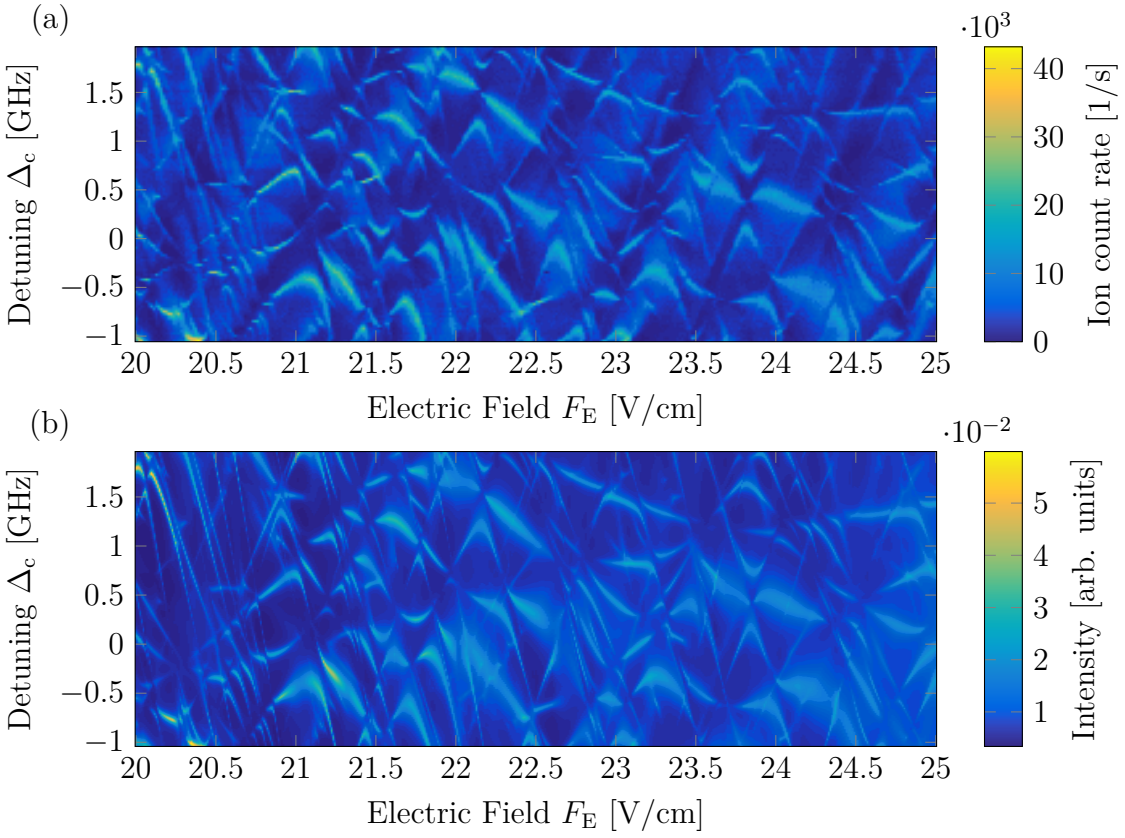

Figure 3.3: (a) and (b) are continuations of the respective subfigures of Fig. 3.2. In this region we find that the resonances get generally even broader due to the increased ionisation rates. The good general agreement we found for the data in Fig. 3.2 still holds in this region. Figures (a) and (b) taken from [6] and adapted for this thesis.

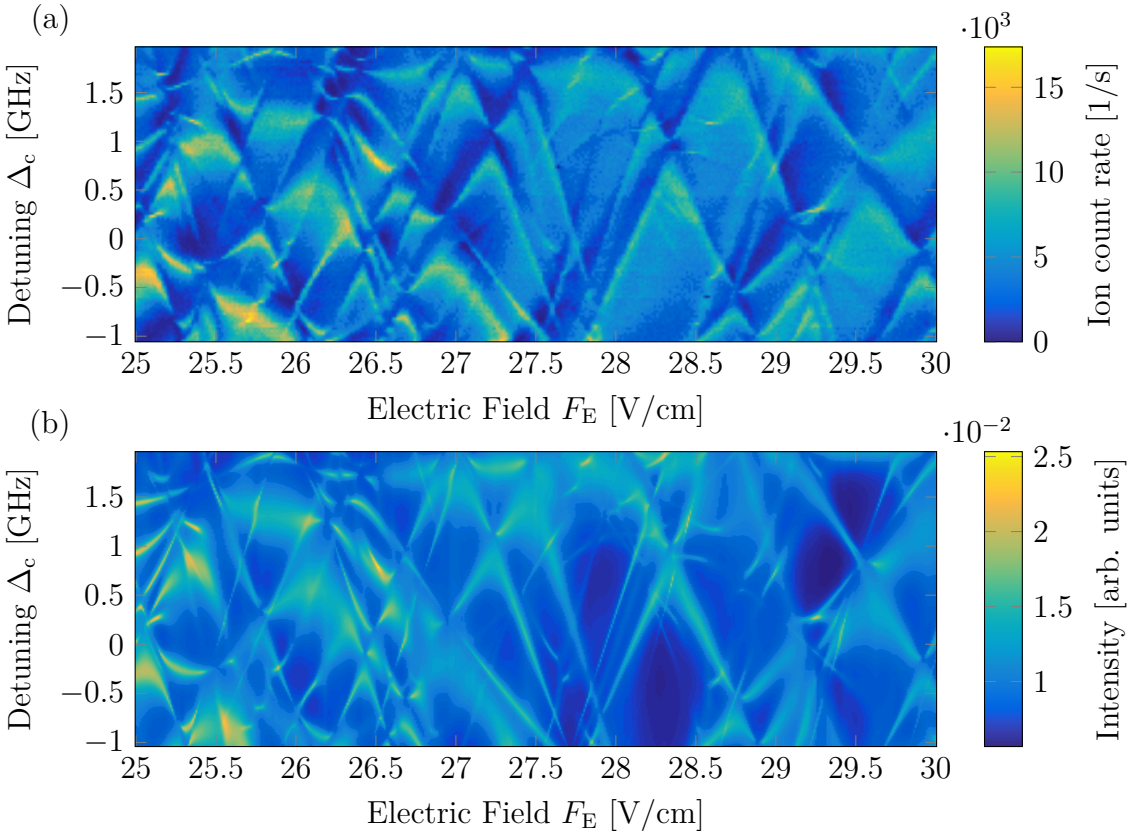

Figure 3.4: (a) and (b) are continuations of the respective subfigures of Fig. 3.3. It is remarkable that, even in this high field region, we can still identify and predict narrow resonances like the one at $F_E \approx 29.3\,\mathrm{V/cm}$ and $\Delta_c \approx 0.3\,\mathrm{GHz}$. However, the general agreement slightly deteriorates in this region. One likely cause for these discrepancies is that the Lorentzian curves we use to create the false colour plot of the numerically calculated data do not approximate the actual lineshapes well enough. We observe 'anti-resonances' in (a) where our numerically calculated spectrum in (b) shows narrow resonances, like the group of three that cross from $-1\,\mathrm{GHz}$ to $2\,\mathrm{GHz}$ in the electric field range from $27.5\,\mathrm{V/cm}$ to $28.5\,\mathrm{V/cm}$. This kind of feature could indicate Fano resonances. Figures (a) and (b) taken from [6] and adapted for this thesis.

the atoms and on the other it extracts the ions, which emerge due to autoionisation as well as direct photoionisation, from the MOT region and guides them to the ion optics. In general, this ion microscope offers spatially resolved detection [96], but here we only use it to count the ions which arrive at the detector for a given detuning of the coupling laser Δ_c relative to the zero-field state and electric field F_E.

From the comparison of the experimental data to the numerically calculated results we find good general agreement across the whole range depicted in Figs. 3.2 to 3.4, and beyond [6]. As the electric field crosses the classical ionisation threshold at $F_{ion} \approx 16.1\,\mathrm{V/cm}$ for $70S_{1/2}$ (see Eq. (2.7) and Fig. 3.2) there is a general broadening of states due to increased ionisation rates. The broadening of states continues, as one would expect due to the opening of the Coulomb barrier, as the electric field increases in Figs. 3.3 and 3.4. However, there are still remarkably narrow resonances, down to and below the experimental frequency steps of 25 MHz, in the high field range of Fig. 3.4. This means that, even in this regime, we can identify states which are optically accessible with lifetimes up to the order of microseconds.

In the high field region we find an interesting set of deviations between our experimental results and the calculated spectra of Fig. 3.4. Namely, some resonances from the numerical calculations appear to be present in the measured data but with a negative sign, i.e. like a suppression of ionisation within the background of ions from photoionisation (see for example the three resonances in the field range from 27.5 V/cm to 28.5 V/cm crossing the whole spectrum in Fig. 3.4). Some of these resonances also exhibit an asymmetric lineshape, for example the lowest one in frequency of the aforementioned set of three. These different kinds of lineshapes indicate that what we are observing could be Fano resonances. Indeed, our system closely resembles the original description of Fano [97] and other groups have already reported on Fano resonances in similar systems [98–100]. We start from a low lying state that is coupled to a narrow state, i.e. a Stark shifted Rydberg state in our case, via the laser light and this excited state can couple to a continuum. At the same time, there is a direct coupling from the lower state to the same continuum. In our system, we can interpret this as interference between two ionisation paths, which are excitation to the Stark shifted Rydberg state followed by autoionisation on the one hand and direct photoionisation from the low lying state on the other. However, a full theoretical Fano-treatment of the present system would require taking into account the overlap of all broad and narrow states in the high field region, since the ionisation paths through all overlapping states could, in principle, interfere, and such an extension of

our numerical methods is therefore beyond the scope of this work.

Altogether, the ionisation spectra which we have calculated using the CAP and observed experimentally mark an important step on the way to complete control over the autoionisation process of highly Stark shifted Rydberg states. We can now use the calculated spectra, which naturally span a larger energy range than shown here for the comparison to the experimental data, in order to look for states that exhibit desirable properties for further experiments. For example, we can choose a narrow resonance with small sensitivity to the electric field F_E, which can therefore be easily addressed optically. After we excite to this state, we can then increase the ionisation rate in a controlled way by switching the electric field F_E by a properly chosen small value (see Ch. 5). The calculated ionisation spectra can also be used for the selection of slowly ionising states for experiments near a superconducting chip surface, where electric fields are always present due to adsorbates [13–16], as well as to create sources of cold electrons and ions for microscopy purposes [61, 62, 64, 65]. Especially in the latter example, the existing schemes for controlled ionisation may benefit greatly from the ionisation spectra we can now calculate using the CAP method presented in this publication [6].

Furthermore, the possible Fano resonances we have found in the experimentally observed spectra could present even more advanced possibilities for the aforementioned applications, as a specifically chosen Fano resonance could enable switching between constructive and destructive interference between the two paths of direct photoionisation and excitation followed by autoionisation. Therefore, this could be seen as an 'on/off'-switch for ionisation in contrast to the changes in the ionisation rate we have shown (see also Ch. 5). Also, to the best of our knowledge, our method of adjusting the CAP to the external electric field is the first instance of a CAP that is adapted to the physical situation well enough to enable the calculation of numerous resonances using only one fixed value of the free parameter η. In comparison to the conventional application of a CAP, this means that our field-adjusted CAP does not require a variation of η for every resonance and therefore saves a lot of computational power. Therefore, our method enables the study of spectra on the scale we have shown here for the first time.

As a step of taking the results from our calculations to the next level, one could use the energy levels and ionisation rates to calculate the time evolution of the population of Rydberg states in the presence of an electric field ramp, i.e. simulate selective field ionisation (SFI). Other groups have already performed similar calculations [101, 102]

using a semiempirical formula for the ionisation rates [103]. A major drawback of this method is that the calculation of each timestep requires transformations of the Stark shifted states between the fine-structure basis and the parabolic basis, i.e. the basis in which the wavefunction is represented in parabolic coordinates [101]. In contrast, our numerical method using the field-adjusted CAP directly yields ionisation rates for each Stark shifted state and could therefore be used to greatly reduce the computational expense of simulations of SFI. However, as the CAP method works with a non-Hermitian Hamiltonian, its application to time evolution calculations is still challenging and may require a more fundamental theoretical treatment.

4 Motional Stark effect of Rydberg states in small magnetic fields

A particle moving at a velocity $\vec{v}$ in a magnetic field $\vec{B}$ is subject to a Lorentz electric field

$$\vec{F}_{\mathrm{L}} = \vec{v} \times \vec{B} \tag{4.1}$$

in its frame of reference (see Fig. 4.1). For a negatively charged electron and a positively charged ionic core forming an atom, this results in forces of opposing signs and therefore has an impact on the atomic spectrum. It is evident that, even though the Lorentz electric field may be small, we can use the high sensitivity of Rydberg states to observe its effect on the atomic energy levels, i.e. the motional Stark effect (MSE). As the Lorentz electric field is still accompanied by the magnetic field in the reference frame of the moving atom, we can expect to see spectra with similarity to crossed electric and magnetic fields at zero velocity.

A thorough theoretical explication of the system has been given by our theory collaborator Professor Schopohl in our joint publication [7]. It is based on a two-particle Hamiltonian for the ionic core and the electron. One of the predictions which arise from this theory is, that the atom velocity $\vec{v}_{\mathrm{A}}$ is not only given by the center-of-mass momentum $\vec{P}$ but also includes a correction term:

$$\vec{v}_{\mathrm{A}} = \frac{1}{M}\left(\vec{P} + \frac{e}{2}\vec{B} \times \vec{r}\right) = \frac{\vec{P}}{M} + \vec{v}_{\mathrm{corr}}. \tag{4.2}$$

Consequently, this means that the collective motion of the atom is coupled to its internal degrees of freedom. This correction to the velocity was too small to play a role in the region of study in our publication [7], but we have given an estimate that it should become crucial for the same magnetic field at higher principle quantum numbers n. We are now convinced that this is not the case and that the correction to the atomic velocity may be much more difficult to observe in rubidium after all. By rewriting the correction term $\vec{v}_{\mathrm{corr}}$ we can give an estimate for the separation that

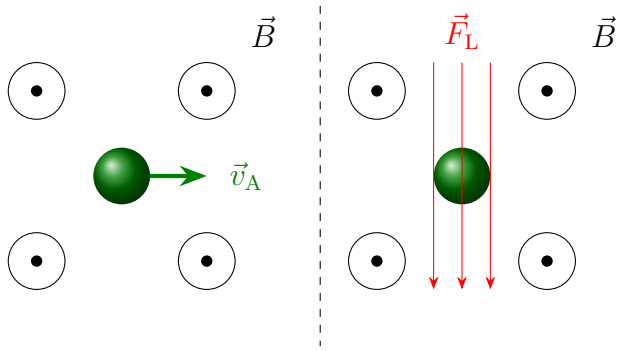

Figure 4.1: Illustration of a Lorentz electric field $\vec{F}_\mathrm{L}$. We consider an atom, which is moving with a velocity $\vec{v}_\mathrm{A}$ in a magnetic field $\vec{B}$ in the laboratory frame (left hand side). In the frame of reference of the moving atom (right hand side), the Lorentz transformation results in an electric field $\vec{F}_\mathrm{L}$ perpendicular to the direction of both, the velocity $\vec{v}_\mathrm{A}$ and the magnetic induction field $\vec{B}$. Figure taken from [7] and adapted for this thesis.

would be required between the ionic core and the electron

$$|\vec{r}| = \frac{2M}{e|\vec{B}|}|\vec{v}_\mathrm{corr}| \approx 1.8\,\mathrm{cm}, \tag{4.3}$$

using the atomic mass of ^{87}Rb, i.e. $M = 87\,\mathrm{u}$, the elementary charge e, the magnetic field $|\vec{B}| = 100\,\mathrm{G}$, and a desired correction to the velocity of $|\vec{v}_\mathrm{corr}| = 100\,\mathrm{m/s}$. This means that the electron would have to be separated from the ionic core by $\approx$1.8 cm on average, which is unrealistic to achieve, even for very high lying and strongly Stark shifted Rydberg states of rubidium. However, for lighter elements like lithium with $M = 7\,\mathrm{u}$ the detection of the correction may come into reach on the order of $|\vec{v}_\mathrm{corr}| = 10\,\mathrm{m/s}$ at high magnetic fields $|\vec{B}| = 1\,\mathrm{T}$ as we find $|\vec{r}| \approx 1.5\,\mu\mathrm{m}$, which may be achievable.

Since the correction term $|\vec{v}_\mathrm{corr}|$ is well below 10 mm/s for Rydberg states of ^{87}Rb with principal quantum number $n = 100$ in magnetic fields of $|\vec{B}| = 100\,\mathrm{G}$, we can neglect it in the following numerical calculations. We use the same routines as before (see Ch. 2), but for the crossed-fields Hamiltonian [9]

$$\hat{H}_\mathrm{MSE} = \hat{H}_0 + |e|\hat{\vec{r}}\cdot\vec{F}_\mathrm{E} + \frac{\mu_\mathrm{B}}{\hbar}\left(g_L\hat{\vec{L}} + g_S\hat{\vec{S}} + g_I\hat{\vec{I}}\right)\cdot\vec{B} + \frac{|e^2|}{8m}\left(\vec{B}\times\hat{\vec{r}}\right)^2 \tag{4.4}$$

with the Bohr magneton μ_B, the operators for angular momentum $\hat{\vec{L}}$, spin $\hat{\vec{S}}$ and nuclear spin $\hat{\vec{I}}$, and the respective g-factors g_L, g_S and g_I. We choose the magnetic

field in z-direction and the electric field along the x-axis, i.e. the electric field $\vec{F}_{\mathrm{E}}$ is given by the Lorentz electric field $\vec{F}_{\mathrm{L}} = |\vec{v}_{\mathrm{A}}||\vec{B}|\hat{e}_z$ with the atomic velocity $\vec{v}_{\mathrm{A}}$ in y-direction. The numerical calculation then works similar to the one we used for the Stark effect (see Ch. 2) with some additional terms containing the $\hat{x}$ and $\hat{y}$ operators [81]. However, due to these differences as compared to the Stark effect, the matrix representations cannot be separated for different values of $|m_j|$ any more (see Ch. 2) but only for the parity ± 1 of the states with respect to the x-y-plane [104, 105]. Therefore, the matrix representation of the Hamiltonian can only be separated into two sub-matrices for the parity, which include states with all values of m_j. Because of this, the computational effort for the calculation of the MSE is considerably higher than for the Stark effect.

For the experiment, we have used a similar setup as in Ch. 2, but with an oven enclosing the cell, which allows us to heat the cell to $T \approx 50\,^{\circ}\mathrm{C}$ to increase the density of the atoms and to broaden the Maxwell-Boltzman distribution of the atom velocities. We also use a pair of coils in Helmholtz configuration to create a homogeneous magnetic field. The probe and coupling beam are counter-propagating through the cell and the transmission of the probe beam is detected on a photodiode using a frequency-modulated lock-in technique like in the previous experiment (see Fig. 2.1(b)). We deliberately make use of the Doppler shift in this experiment by detuning both lasers according to the condition

$$\Delta_{\mathrm{p}} + \Delta_{\mathrm{c}} = v_{\mathrm{A}} \left(\frac{f_{\mathrm{p}} - f_{\mathrm{c}}}{c} \right). \tag{4.5}$$

This combined detuning of both lasers relative to a given resonance of the zero-velocity class effectively allows us to select from a wide range of velocities up to $v_{\mathrm{A}} \approx 600\,\mathrm{m/s}$.

In a first experiment, we have recorded EIT spectra near the state $100\mathrm{D}_{5/2}$ in the presence of a magnetic field of $B = 98\,\mathrm{G}$, which was calibrated using a Hall probe, for the velocity classes $v_{\mathrm{A}} = 0\,\mathrm{m/s}$ and $v_{\mathrm{A}} = 390\,\mathrm{m/s}$ (see Fig. 4.2(a)). From the relative shift of the spectra for these two velocity classes we can evaluate a motional Stark shift of 10 MHz, corresponding to a Lorentz electric field $F_{\mathrm{L}} \approx 0.038\,\mathrm{V/cm}$. A comparison of this measured shift as well as the absolute positions of the resonances on a detailed part of the spectra to the results from our numerical calculations show very good agreement within the experimental frequency accuracy of $\approx$2 MHz (see Fig. 4.2(b)). As a reversal test to show that the shifts we are observing really are caused by the MSE, we have conducted the same experiment as before but with the

magnetic field in parallel to the selected velocity, i.e. in parallel to the optical axis. Since this situation always results in a Lorentz electric field of $F_\mathrm{L} = 0\,\mathrm{V/cm}$ (see Eq. (4.1)), we expect to see no motional Stark shift. And, indeed, this is what we observe in the experiment (see Fig. 4.2(c)). However, we do find an asymmetry of the resonances in this case, which could be caused by velocity components perpendicular to the selected velocity component, i.e. perpendicular to the optical axis, or by an inhomogeneity of the magnetic field in this measurement.

We have then investigated the dependence of the motional Stark shift on the velocity v_A by evaluating the positions of two resonances for a set of different velocity classes (see Fig. 4.3(a)). For this, it is important to bear in mind that, due to the MSE, not only a shift of the energy levels but also a change of the dipole matrix elements between the intermediate state $5\mathrm{P}_{3/2}$ and the Rydberg states occurs, just like for the conventional Stark effect (see Ch. 2). As this causes the intensity of one of the two resonances to diminish and the intensity of the other to increase for higher velocities v_A, we can only evaluate one of the two for each velocity class. Given this slight limitation, the evaluated positions of the resonances still agree very well with the motional Stark shifted resonances we obtain from our numerical calculations. Furthermore, we have conducted another experiment using the velocity classes $v_\mathrm{A} = 0\,\mathrm{m/s}$ and $v_\mathrm{A} = 390\,\mathrm{m/s}$ to observe the magnetic field dependence of the motional Stark effect (see Fig. 4.3(b)). Again, we find that the energy levels of the resonances that we have been able to evaluate from the experimental data agree very well with the results from the numerical calculations.

Altogether, the excellent agreement between the measured spectra and the numerically calculated energy levels across all of these measurements shows the practical use of our numerical approach using the crossed-fields Hamiltonian in the regime of this work [7]. To the best of our knowledge, it also marks the first observation of the MSE in low magnetic fields using Rydberg states. Future work may extend these studies to systems of Rydberg atoms moving in crossed electric and magnetic fields, for example to compensate the Lorentz electric field by an additional external electric field or vice versa. Furthermore, the present work implies even greater effects, including the correction term for the atom velocities (see Eq. (4.2)) and thereby coupling of the atomic motion to the internal degrees of freedom, for Rydberg states of light atoms like helium [55] or positronium [106].

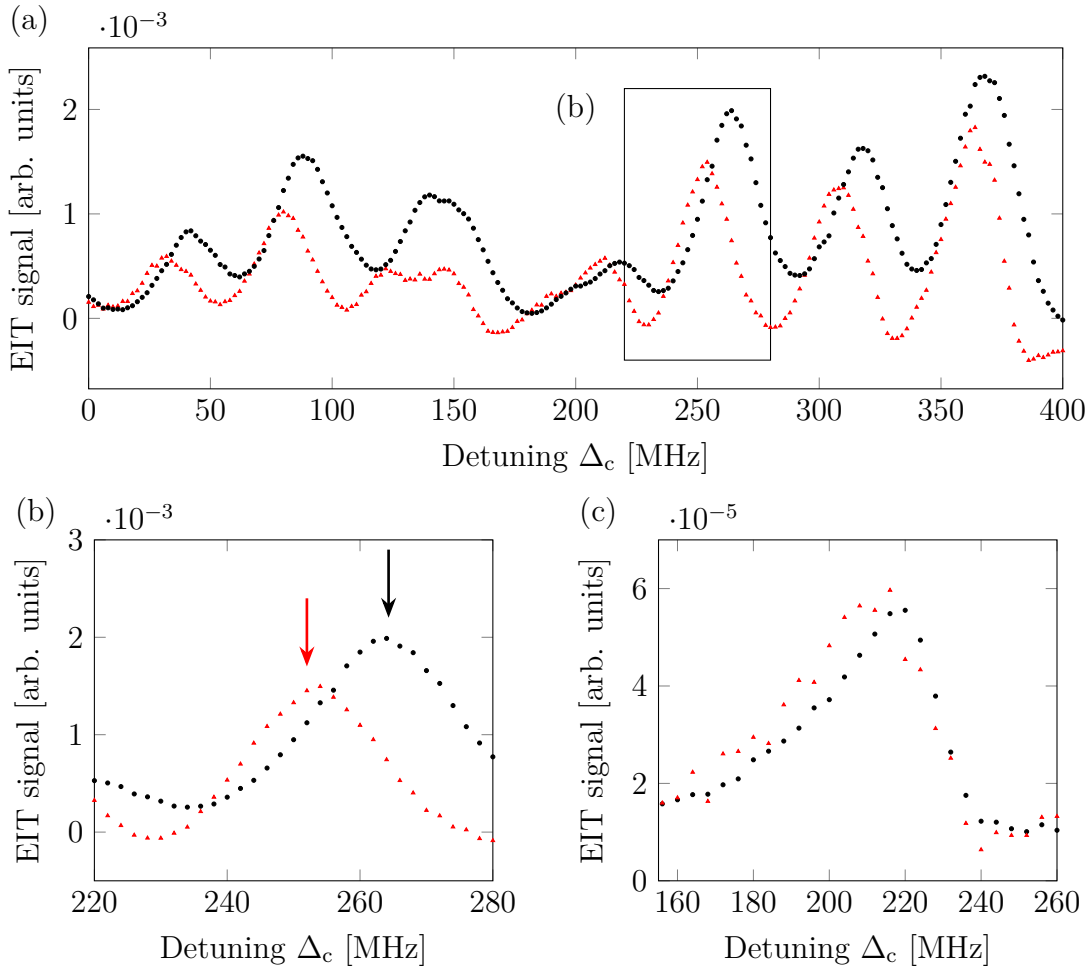

Figure 4.2: (a) Experimental results of EIT spectra near the unperturbed $100D_{5/2}$ state for different velocity classes. Both spectra have been recorded for a magnetic field of $B = 98\,\mathrm{G}$. The black dots correspond to atoms at rest, i.e. $v_A = 0\,\mathrm{m/s}$, and the red triangles to atoms at $v_A = 390\,\mathrm{m/s}$. By comparing the two spectra, we find a motional Stark shift of $\approx$10 MHz, which is caused by a Lorentz electric field of $F_L \approx 0.038\,\mathrm{V/cm}$. (b) Detailed part of the spectra from (a). The arrows mark the resonances we obtain from our numerical calculations, which agree with the experimental results to within the frequency accuracy of $\approx$2 MHz. (c) EIT spectra for atoms moving in parallel to the magnetic field for the same velocity classes as in (a). We observes no significant motional Stark shift, only a slight asymmetry to the left hand side of the peaks, which is probably caused by velocity components perpendicular to the optical axis. Figures (a), (b) and (c) taken from [7] and adapted for this thesis.

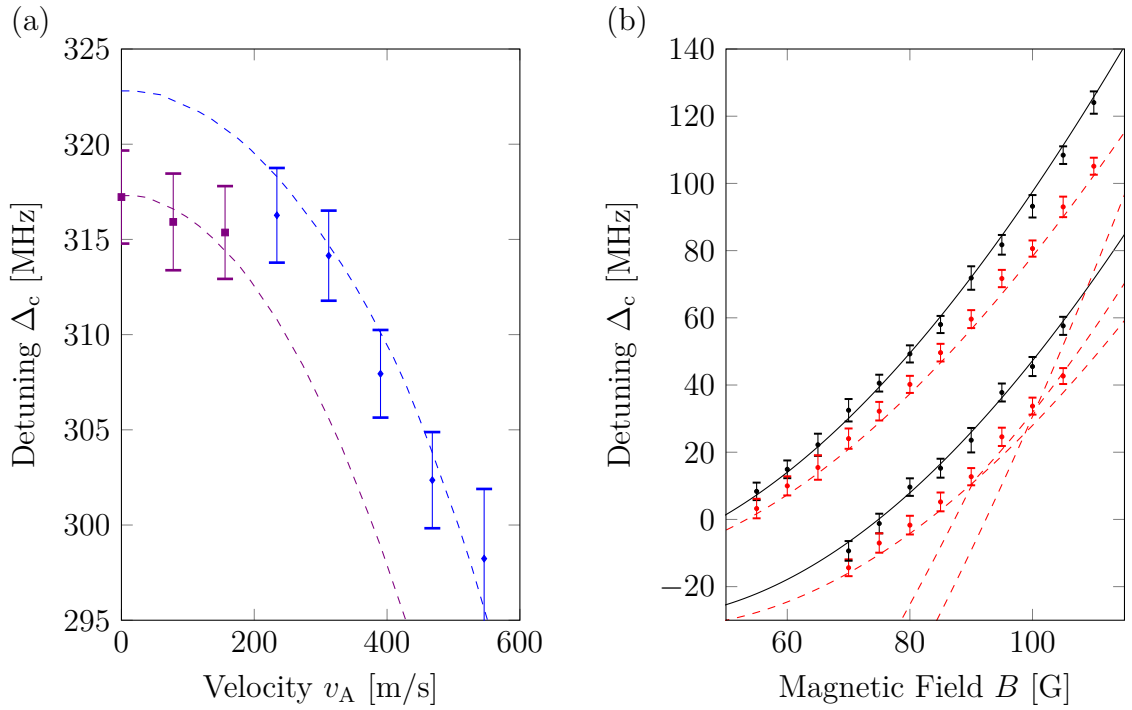

Figure 4.3: (a) Velocity dependence of the motional Stark shift for two resonances near the unperturbed $100D_{5/2}$ state. The purple and blue dashed lines depict the results from our numerical calculations and the purple square and blue diamond marks show the experimentally observed shift. We evaluate two neighbouring resonances here, because as the motional Stark shift increases a change in the dipole matrix elements also changes the intensity of the EIT signals. (b) Magnetic field dependence of the motional Stark shift for resonances near the unperturbed $100D_{5/2}$ state. The colours black and red correspond to the velocity classes $v_A = 0\,\mathrm{m/s}$ and $v_A = 390\,\mathrm{m/s}$, respectively. The solid and dashed lines show the results from our numerical calculations. The marks with error bars depict the resonances that we were able to evaluate from the experimental spectra. Figures (a) and (b) taken from [7] and adapted for this thesis.

5 Dipole blockade of highly Stark shifted Rydberg states

Probably the most striking effect that is caused by electrostatic interactions between Rydberg states is the Rydberg blockade [41]. This effect arises when the atomic interactions between a first Rydberg atom and a Rydberg state of a neighbouring atom become strong enough to shift the Rydberg state of the second atom out of resonance with the excitation laser. In simple terms, the presence of a first excited atom in a sample prohibits the excitation of other atoms in its vicinity. In general, the Rydberg blockade can be induced by van der Waals as well as dipole-dipole interactions [107–110]. In this work, we have focussed on the latter type of interactions and have investigated how we can control them by an external electric field in highly Stark shifted Rydberg states [8].

Here we use the results from our previously developed numerical methods (see Ch. 3) to choose suitable states for our experiments. These states should have low ionisation rates, i.e. lifetimes on the order of at least microseconds, various permanent electric dipole moments, in order to exhibit dipole-dipole interactions of different strengths, and it should be possible to ionise them in a controlled way. Our choices of such states in the spectral region near the unperturbed $43S_{1/2}$ state are illustrated in Fig. 5.1. These states have in common that we can transfer them to states with high ionisation rates on the order of $\Gamma_{\mathrm{ion}} \geq 10\,\mathrm{MHz}$ by ramping up the external electric field F_{E} by just $\approx 1\,\mathrm{V/cm}$ within $\approx 1\,\mu\mathrm{s}$.

For the following experiments we have used the same setup as in Ch. 3. In a first experiment, we have verified the calculated ionisation rates of one of the chosen states experimentally (see state number 1 in Fig. 5.1). We excite the atoms to the Stark shifted Rydberg states by using the MOT lasers for the lower transition and pulsing the coupling laser, which is again focussed to a light sheet, for the upper transition in the three-level ladder-scheme (see Fig. 2.1(a)). For each excitation pulse we record the time evolution of the ion signal and can thereby obtain the ionisation

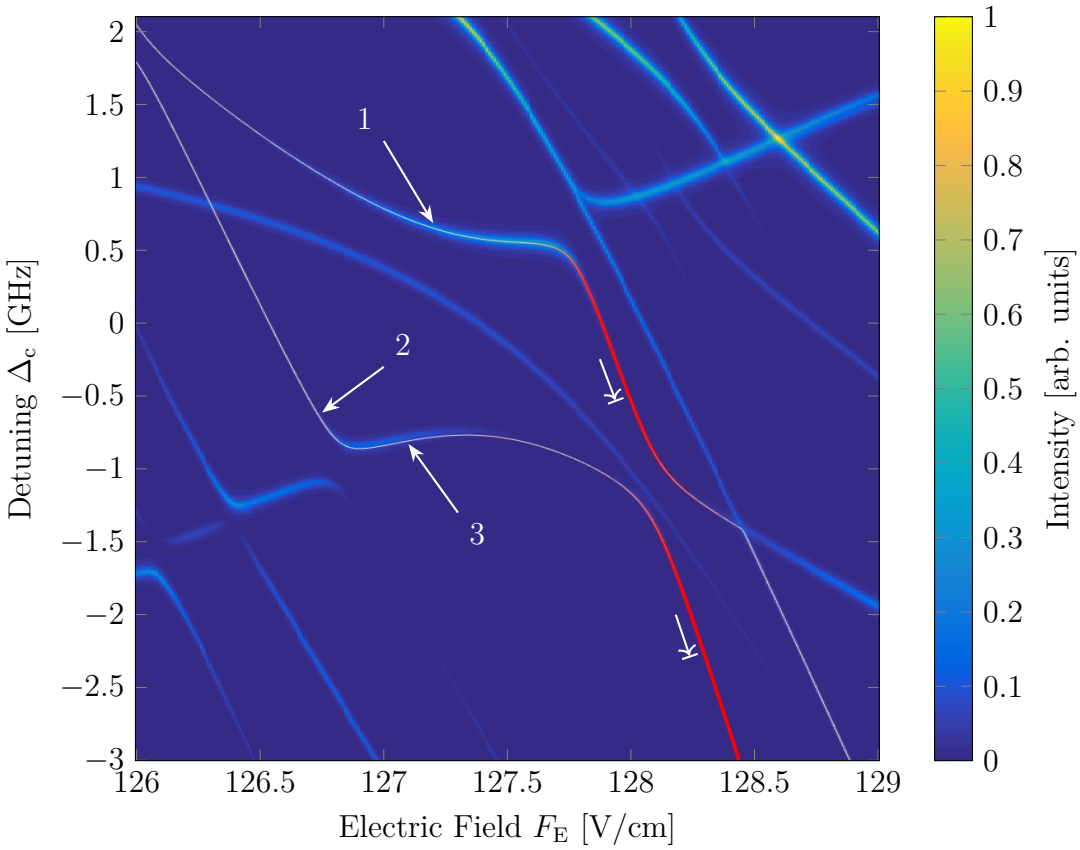

Figure 5.1: Numerically calculated ionisation spectrum near $43S_{1/2}$. The false colours are determined using our CAP method (see Ch. 3) and the colour of the solid lines show the ionisation rates of the underlying states from low (white) to high (red). The numbers 1, 2 and 3 indicate the states that we later excite the atoms to in the experiment (see Fig. 5.3). We can then, by changing the external electric field F_E, transfer the atoms to ionising states which are marked by the arrows with delimiters. Figure taken from [8] and adapted for this thesis.

rate from its decay. A comparison of the results from this measurement to our numerically calculated ionisation rates (see Ch. 3) shows good general agreement (see Fig. 5.2(a)). However, we find that the highest ionisation rates we measure in this region are slightly higher than the predictions from our numerical calculations. One reason for this deviation could be that our model does not take into account any other environmental factors that can alter the ionisation rates like black body radiation. Another possible reason is, that the shape of our CAP and the value we have determined for η are not fully optimised for this particular resonance.

In the main part of the experiment, we now made use of the spatial resolution of our ion microscope [96] in order to characterise the Rydberg blockade of the excited states. For this we excite atoms from the MOT by pulsing the coupling laser, which is tuned together with the electric field F_{E} to one of the three numbered states from Fig. 5.1. The electric field is then switched to the matching values indicated by the arrows with delimiters within $\approx$1 µs to rapidly increase the ionisation rate. The ions are then spatially detected by the ion microscope with a magnification of 1129. The acquired image from each pulse is then evaluated using the spatial correlation function

$$g^{(2)}(u,v) = \frac{\langle\langle f(x+u,y+v)f(x,y)\rangle\rangle_{x,y}}{\langle\langle f(x+u,y+v)\rangle\rangle_{x,y}\langle\langle f(x,y)\rangle\rangle_{x,y}}, \tag{5.1}$$

with the detector function $f(u,v)$ and the displacement coordinates u and v. We can write the detector function as

$$f(x,y) = \sum_{i=1}^{N} \delta(x-x_i)\delta(y-y_i), \tag{5.2}$$

with the coordinates x_i and y_i of each of the N ions that are detected after one pulse of the coupling laser. The resulting spatial correlation function $g^{(2)}(u,v)$ for resonance 1 from Fig. 5.1 is shown in Fig. 5.2. From this evaluation we can already observe the blockade effect as a circular region around $g^{(2)}(0,0)$ with $g^{(2)}(u,v) < 1$. In theory, the spatial correlation function should go down to zero for a fully blockaded sample, but due to the finite beam waist of the light sheet ($\approx$9 µm) the excitation region is not perfectly two dimensional.

We now calculate the radial mean of the spatial correlation function $g^{(2)}(u,v)$ for a quantitative analysis of the blockade radii. The result of this is depicted in Fig. 5.3(a) for resonance 1 from Fig. 5.1 and in Fig. 5.3(b) for resonances 2 and 3. In all three cases, we observe the blockade effect in the radial average. From this experimental

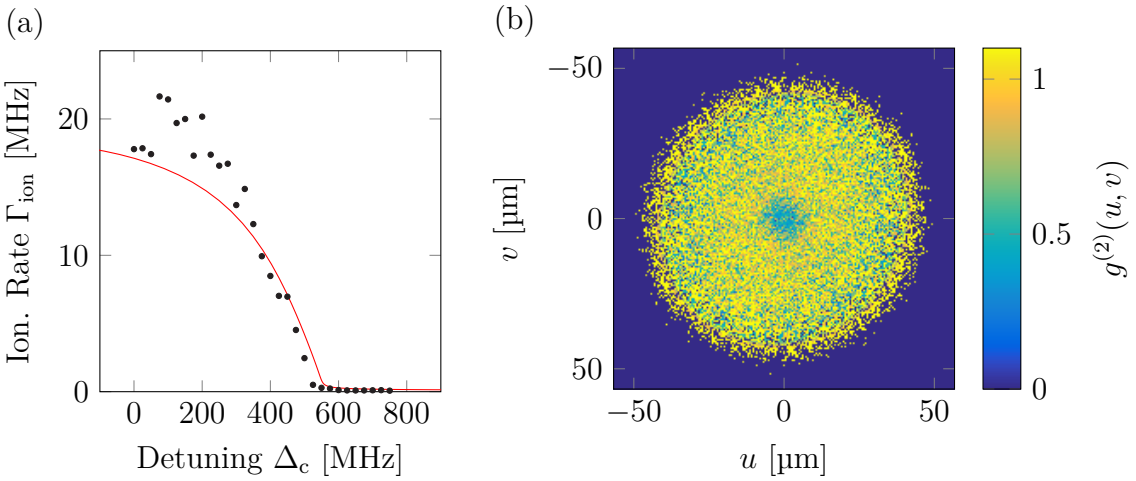

Figure 5.2: (a) Comparison of measured (black dots) and numerically calculated (red line) ionisation rates following the resonance from number 1 to the arrow with delimiter in Fig. 5.1. While we find good general agreement at lower ionisation rates, our theory seems to slightly underestimate the higher ionisation rates. (b) Spatial correlation function $g^{(2)}(u, v)$ of the detected ions in false colours (see Eq. (5.1)). For this measurement, the atoms were excited to the state marked by the number 1 in Fig. 5.1 and then transferred to the strongly ionising state marked by the arrow with delimiter by switching the electric field F_{E}. In the centre we observe a drop of the spatial correlation function to values below 1, which indicates the Rydberg blockade. Figures (a) and (b) taken from [8] and adapted for this thesis.

data we estimate blockade radii of 9 µm for resonance 1, 12 µm for resonance 2 and 2 µm for resonance 3. The strong change of the blockade radius between resonance 2 and 3 illustrates how we can control the blockade effect and therefore dipole-dipole interactions between these highly Stark shifted Rydberg states simply by means of a small change of the external electric field F_{E}.

We can compare the blockade radii, which we have estimated from the experimental data, to calculated values from a simple theoretical estimate. We consider the blockade radius r_{b} as the radius, where the energy shift ΔW caused by the dipole-dipole interaction exceeds the linewidth $\delta\nu_{\mathrm{L}}$, resulting in the condition

$$\hbar 2\pi\delta\nu_{\mathrm{L}} = \Delta W(r_{\mathrm{b}}). \tag{5.3}$$

Here, the linewidth $\delta\nu_{\mathrm{L}}$ can be either the laser linewidth or the linewidth of the resonance, whichever is broader. The dipole-dipole interactions cause an energy shift given by [107]

$$\Delta W = \frac{1}{4\pi\epsilon_0}\frac{p_z^2}{R^3}(1 - 3\cos^2\Theta) \tag{5.4}$$

with the interatomic distance R, the polar angle Θ and the permanent electric dipole moment p_z, which we can obtain from our numerical calculations from the derivative of the Stark shifted energy levels as a function of the electric field F_{E}. Using an estimated linewidth of $\delta\nu_{\mathrm{L}} = 5\,\mathrm{MHz}$ for the MOT transition, we obtain theoretical blockade radii of 4.5 µm for resonance 1, 12.5 µm for resonance 2 and 2.6 µm for resonance 3, which are marked as dashed vertical lines in Figs. 5.3(a) and (b). While these values agree well with the measured blockade radii for resonances 2 and 3, we observe a deviation for the blockade radius of resonance 1. This deviation could be caused by effects besides dipole-dipole interaction, which we have not taken into account here, for example second-order van der Waals interaction or an enhancement of the interaction by resonant energy transfer [107].

In summary, the novelty of this work [8] is twofold. Firstly, we have demonstrated a controlled ionisation scheme, which was enabled by our numerical method using a CAP (see Ch. 3). We have shown here that this scheme offers timed control over the ionisation rate via the external electric field F_{E}. It may therefore complement the method of selective field ionisation (SFI), which is usually implemented for Rydberg states starting from zero-field or the low field region by rapidly ramping up the electric field to values well beyond the classical ionisation threshold with simultaneous time-resolved ion detection. In contrast to SFI, our present method can be applied

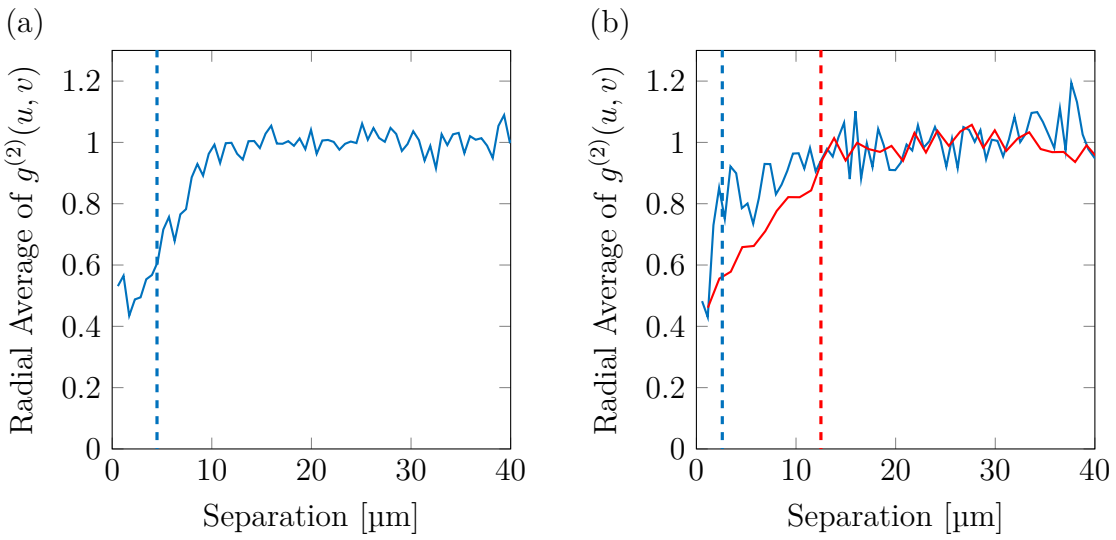

Figure 5.3: (a) Radial average of the spatial correlation function $g^{(2)}(u, v)$ from Fig. 5.2(b), i.e. for resonance 1 in Fig. 5.1. The dashed vertical line marks the blockade radius that was calculated using Eq. (5.3). (b) The red and blue solid lines show the radial average of the spatial correlation function $g^{(2)}(u, v)$ for resonances 2 and 3 from Fig. 5.1, respectively. The dashed vertical lines in matching colours again mark the calculated blockade radii. Figures (a) and (b) taken from [8] and adapted for this thesis.

in experiments using Rydberg states near or beyond the classical ionisation threshold and allows for a similar degree of state selectivity while at the same time allowing to go back and forth adiabatically between different ionisation rates. Secondly, by evaluating the spatial correlation function $g^{(2)}(u, v)$, we have shown that we have control over the permanent electric dipole moments and therefore dipole-dipole interactions of these highly Stark shifted Rydberg states. This effectively gives us control over the Rydberg blockade radius by the external electric field F_{E}.

6 Conclusion and Outlook

In the first part of this thesis we have used a vapour cell setup with a plate capacitor to perform precision spectroscopy of Stark shifted rubidium Rydberg states up to the classical ionisation threshold by means of EIT [1]. At the same time we have numerically calculated the energy levels of these states and have extended these calculations to obtain the dipole matrix elements of the states involved in the measurement scheme. The results we have thereby obtained provide a reference system for Stark shifted Rydberg states ranging from the low-field region, that is usually found near a surface due to adsorbates [15], all the way up to and beyond the classical ionisation threshold, where these states are of interest e.g. for the creation of sources of cold electrons and ions [5]. We can even extend the measurement of adsorbate fields to not only detect the absolute value of the electric field, but also its orientation, by exploiting the polarisation dependence of the measure for the transition strength.

Furthermore, our calculations of the dipole matrix elements between Stark shifted Rydberg states and other states allow for the calculation of decay rates, which may in principle include all other states in the Rydberg cascade from the highest excited state down to the ground state. Our numerical model could therefore be used to search for Stark shifted states with decreased decay rates, possibly to the extreme of states similar to a 'dark state'. Applying this idea to Stark shifted circular Rydberg states could hypothetically prolong their lifetimes indefinitely, if the dipole matrix element between a circular state and its neighbouring circular state could be tuned to zero. Lastly, our numerical calculations can be used to search for transitions between Rydberg states, which can be tuned using the external electric field, for example in the microwave regime to couple these states to a superconducting stripline cavity to create a hybrid quantum system [48, 52] or in the terahertz regime for imaging and detection of this kind of radiation [24].

We have extended our numerical model further by incorporating a field-adjusted CAP in the Stark Hamiltonian in order to determine the autoionisation rates of states near and above the classical ionisation threshold [6]. For the confirmation of

this model we have also conducted an experiment in which we have excited atoms from a MOT to Rydberg states in this regime with detection of the arising ions. Our novel approach of adjusting the CAP to the external electric field in the numerical calculations has proven to be particularly useful, as it effectively reduces the number of free parameters in this kind of calculation from 'one per resonance' to 'one per spectral region', making the calculation of ionisation spectra composed of hundreds of resonances feasible. In turn, the extent of these spectra enables the search for states with suitable ionisation rates and other properties matching experimental requirements [8].

A new approach to extend these numerical calculations to even more atomic properties and effects could be to combine them with our time evolution calculations for Rydberg state populations using a Lindblad master equation [3, 4]. This would allow for a prediction of the competition between decay through the cascade of Rydberg states back to the ground state and autoionisation affecting the lifetimes [4], possibly in the presence of BBR and taking into account effects like superradiance. A theoretical model like this could also be used to determine if a coherent superposition between the ground state and a given Stark shifted Rydberg state could be achieved [3] and if highly Stark shifted states could also be used in quantum computing protocols [41–44, 49]. At the same time, a combination of our experimental methods of all-optical detection [3, 4] and controlled ionisation for detection [6, 8] could be implemented to put such a theoretical model to the test. Furthermore, the possible Fano-resonances we have observed in the experimental ion spectra [6] point to another promising extension of our numerical methods. An implementation of the Fano model [97] for highly Stark shifted Rydberg states can be expected to yield an even broader range of ionisation effects stemming from the constructive and destructive interference of excitation and ionisation paths [98–100]. This type of resonances could therefore cover a range from fully suppressed ionisation to enhanced ionisation rates, allowing for even greater control in ion detection schemes.

We have investigated systems of moving atoms in external magnetic fields [7], which experience a Lorentz electric field in their frame of reference, i.e. become subject to the MSE. For this purpose, we have conducted an experiment using EIT spectroscopy in a vapour cell with selection of different velocity classes via the Doppler effect. In this experiment, we have observed the MSE for Rydberg atoms of rubidium in low magnetic fields for the first time. Simultaneously, we have expanded our numerical calculations to incorporate a Hamiltonian with crossed electric and magnetic fields to

obtain approximate spectra for atoms under the effect of the Lorentz electric field and the magnetic field in their frame of reference. While this approach is sufficient for the observed spectra, an in-depth theoretical treatment using a two-particle Hamiltonian for the ionic core and the electron is needed for similar work on lighter atoms and in higher magnetic fields. A detailed description of this treatment has been given by our theory collaborator Professor Schopohl in our joint publication [7].

The numerical calculations we have performed as part of this work [7] can be directly applied to systems of moving atoms in crossed electric and magnetic fields in the laboratory frame. This type of configuration can also be found in experiments in which beams of Rydberg atoms are guided along a chip surface, for example to implement a strong coupling between the Rydberg atoms and a superconducting chip [17] or to realise Rydberg atom interferometry [55]. For these types of experiments, a combination of crossed external fields and the MSE with suitable adjustments of both fields and the atomic velocity, may allow for compensation of either detrimental electromagnetic fields or of the MSE, or for the determination of an optimal working point in the presence of crossed fields. Furthermore, an extension of this type of application to even lighter systems like positronium [106] is expected to also reveal the coupling of internal degrees of freedom to the center-of-mass motion of the system, which is also predicted by the theoretical treatment using a two-particle Hamiltonian [7]. Lastly, a combination of the crossed-fields single-particle Hamiltonian from our numerical calculations with a CAP, similar to the one we have used in our other work [6], could reveal interesting regimes of ionisation, as a magnetic field can stabilise the state of an electron while an electric field opens the potential to the continuum. Therefore, the ionisation rate of such a system should strongly depend on the angle between the electric and magnetic field with vanishing ionisation rates for perfectly perpendicular fields, as preliminary calculations by our theory collaborator Professor Schopohl show.

In the last part of this thesis we have employed the results that we had obtained using the field-adjusted CAP method to specifically select states with suitable permanent electric dipole moments and ionisation rates [8]. In this experiment we have excited atoms from a MOT to these selected states and have observed the dipole blockade effect resulting from various permanent electric dipole moments. Here we have made use of our knowledge of the ionisation rates and have implemented a controlled ionisation scheme as part of the experimental cycle. This scheme can be extended to even more elaborate ionisation schemes, for example by adiabatically go-

ing back and forth between high and low ionisation rates to achieve controlled partial ionisation of a cloud of atoms. Ultimately, the control over the dipole blockade could be applied to create Rydberg superatoms [53, 54] with tunable permanent electric dipole moments and adjustable ionisation rates in the highly Stark shifted regime. This could offer unprecedented control for suggested applications of Rydberg superatoms, e.g. for high-fidelity single photon absorbers [111], for deterministic single ion sources [60] or for quantum information processing and quantum networks [53, 54].

Over the course of the works included in this thesis we have investigated properties of Rydberg atoms in external electric fields experimentally and by means of numerical calculations. The experimental results we have obtained and the numerical methods we have developed in these works give promising prospects for the search for suitable Rydberg states and the control over their properties via external electric fields. These properties include their electric dipole moments, energy level differences between pairs of states, dipole matrix elements between Stark shifted states, sensitivity to external electric and magnetic fields, and ionisation rates. Thereby, these results offer a rich toolbox for experiments in many subfields of Rydberg physics, including metrology and detection schemes, quantum information processing and the development of new types of ion and electron sources.

Bibliography

[1] J. Grimmel, M. Mack, F. Karlewski, F. Jessen, M. Reinschmidt, N. Sándor, and J. Fortágh, "Measurement and numerical calculation of Rubidium Rydberg Stark spectra", New J. Phys. **17**, 053005 (2015).

[2] A. Sanayei, N. Schopohl, J. Grimmel, M. Mack, F. Karlewski, and J. Fortágh, "Quasiclassical quantum defect theory and the spectrum of highly excited rubidium atoms", Phys. Rev. A **91**, 032509 (2015).

[3] F. Karlewski, M. Mack, J. Grimmel, N. Sándor, and J. Fortágh, "State-selective all-optical detection of Rydberg atoms", Phys. Rev. A **91**, 043422 (2015).

[4] M. Mack, J. Grimmel, F. Karlewski, L. Sárkány, H. Hattermann, and J. Fortágh, "All-optical measurement of Rydberg-state lifetimes", Phys. Rev. A **92**, 012517 (2015).

[5] A. J. McCulloch, R. W. Speirs, J. Grimmel, B. M. Sparkes, D. Comparat, and R. E. Scholten, "Field ionization of Rydberg atoms for high-brightness electron and ion beams", Phys. Rev. A **95**, 063845 (2017).

[6] J. Grimmel, M. Stecker, M. Kaiser, F. Karlewski, L. Torralbo-Campo, A. Günther, and J. Fortágh, "Ionization spectra of highly Stark-shifted rubidium Rydberg states", Phys. Rev. A **96**, 013427 (2017).

[7] M. Kaiser, J. Grimmel, L. Torralbo-Campo, M. Mack, F. Karlewski, F. Jessen, N. Schopohl, and J. Fortágh, "Observation of the motional Stark shift in low magnetic fields", Phys. Rev. A **96**, 043401 (2017).

[8] M. Stecker, J. Grimmel, R. Nold, J. Fortágh, and A. Günther, "Controlling the dipole blockade of highly Stark-shifted rubidium Rydberg states", Ready for submission (2018).

[9] T. F. Gallagher, *Rydberg Atoms*, 1. Ausgabe (Cambridge Univ. Press, Cambridge, 1994).

[10] P. P. Herrmann, J. Hoffnagle, N. Schlumpf, V. L. Telegdi, and A. Weis, "Stark spectroscopy of forbidden two-photon transitions: a sensitive probe for the quantitative measurement of small electric fields", J. Phys. B **19**, 1271 (1986).

[11] A. Osterwalder and F. Merkt, "Using High Rydberg States as Electric Field Sensors", Phys. Rev. Lett. **82**, 1831 (1999).

[12] M. G. Bason, M. Tanasittikosol, A. Sargsyan, A. K. Mohapatra, D. Sarkisyan, R. M. Potvliege, and C. S. Adams, "Enhanced electric field sensitivity of rf-dressed Rydberg dark states", New J. Phys. **12**, 065015 (2010).

[13] A. Tauschinsky, R. M. T. Thijssen, S. Whitlock, H. B. van Linden Heuvell, and R. J. C. Spreeuw, "Spatially resolved excitation of Rydberg atoms and surface effects on an atom chip", Phys. Rev. A **81**, 063411 (2010).

[14] R. P. Abel, C. Carr, U. Krohn, and C. S. Adams, "Electrometry near a dielectric surface using Rydberg electromagnetically induced transparency", Phys. Rev. A **84**, 023408 (2011).

[15] H. Hattermann, M. Mack, F. Karlewski, F. Jessen, D. Cano, and J. Fortágh, "Detrimental adsorbate fields in experiments with cold Rydberg gases near surfaces", Phys. Rev. A **86**, 022511 (2012).

[16] K. S. Chan, M. Siercke, C. Hufnagel, and R. Dumke, "Adsorbate Electric Fields on a Cryogenic Atom Chip", Phys. Rev. Lett. **112**, 026101 (2014).

[17] T. Thiele, J. Deiglmayr, M. Stammeier, J.-A. Agner, H. Schmutz, F. Merkt, and A. Wallraff, "Imaging electric fields in the vicinity of cryogenic surfaces using Rydberg atoms", Phys. Rev. A **92**, 063425 (2015).

[18] S. Kumar, H. Fan, H. Kübler, A. J. Jahangiri, and J. P. Shaffer, "Rydberg-atom based radio-frequency electrometry using frequency modulation spectroscopy in room temperature vapor cells", Opt. Express **25**, 8625 (2017).

[19] S. A. Miller, D. A. Anderson, and G. Raithel, "Radio-frequency-modulated Rydberg states in a vapor cell", New J. Phys. **18**, 053017 (2016).

[20] M. T. Simons, J. A. Gordon, and C. L. Holloway, "Simultaneous use of Cs and Rb Rydberg atoms for dipole moment assessment and RF electric field measurements via electromagnetically induced transparency", J. Appl. Phys. **120**, 123103 (2016).

[21] H. Figger, G. Leuchs, R. Straubinger, and H. Walther, "A photon detector for submillimetre wavelengths using Rydberg atoms", Opt. Commun. **33**, 37 (1980).

[22] P. Goy, L. Moi, M. Gross, J. M. Raimond, C. Fabre, and S. Haroche, "Rydberg-atom masers. II. Triggering by external radiation and application to millimeter-wave detectors", Phys. Rev. A **27**, 2065 (1983).

[23] J. A. Sedlacek, A. Schwettmann, H. Kübler, and J. P. Shaffer, "Atom-Based Vector Microwave Electrometry Using Rubidium Rydberg Atoms in a Vapor Cell", Phys. Rev. Lett. **111**, 063001 (2013).

[24] C. G. Wade, N. Šibalić, N. R. de Melo, J. M. Kondo, C. S. Adams, and K. J. Weatherill, "Real-time near-field terahertz imaging with atomic optical fluorescence", Nat. Photonics **11**, 40 (2016).

[25] J. Schmidt, P. Schalberger, H. Baur, R. Löw, T. Pfau, H. Kübler, and N. Frühauf, "A transimpedance amplifier based on a LTPS process operated in alkali vapor", in 24th International Workshop on Active-Matrix Flatpanel Displays and Devices (AM-FPD) (July 2017), pp. 296–298.

[26] M. Zeppenfeld, "Nondestructive detection of polar molecules via Rydberg atoms", EPL (Europhysics Letters) **118**, 13002 (2017).

[27] R. P. Feynman, "Simulating physics with computers", Int. J. Theor. Phys. **21**, 467 (1982).

[28] D. Deutsch, "Quantum theory, the Church–Turing principle and the universal quantum computer", Proc. R. Soc. A **400**, 97 (1985).

[29] N. A. Gershenfeld and I. L. Chuang, "Bulk Spin-Resonance Quantum Computation", Science **275**, 350 (1997).

[30] I. L. Chuang, L. M. K. Vandersypen, X. Zhou, D. W. Leung, and S. Lloyd, "Experimental realization of a quantum algorithm", Nature **393**, 143 (1998).

[31] E. Biolatti, R. C. Iotti, P. Zanardi, and F. Rossi, "Quantum Information Processing with Semiconductor Macroatoms", Phys. Rev. Lett. **85**, 5647 (2000).

[32] X. Li, Y. Wu, D. Steel, D. Gammon, T. H. Stievater, D. S. Katzer, D. Park, C. Piermarocchi, and L. J. Sham, "An All-Optical Quantum Gate in a Semiconductor Quantum Dot", Science **301**, 809 (2003).

[33] E. Knill, R. Laflamme, and G. J. Milburn, "A scheme for efficient quantum computation with linear optics", Nature **409**, 46 (2001).

[34] R. Blatt and D. Wineland, "Entangled states of trapped atomic ions", Nature **453**, 1008 (2008).

[35] A. Bermudez, X. Xu, R. Nigmatullin, J. O'Gorman, V. Negnevitsky, P. Schindler, T. Monz, U. G. Poschinger, C. Hempel, J. Home, F. Schmidt-Kaler, M. Biercuk, R. Blatt, S. Benjamin, and M. Müller, "Assessing the Progress of Trapped-Ion Processors Towards Fault-Tolerant Quantum Computation", Phys. Rev. X **7**, 041061 (2017).

[36] D. I. Schuster, A. P. Sears, E. Ginossar, L. DiCarlo, L. Frunzio, J. J. L. Morton, H. Wu, G. A. D. Briggs, B. B. Buckley, D. D. Awschalom, and R. J. Schoelkopf, "High-Cooperativity Coupling of Electron-Spin Ensembles to Superconducting Cavities", Phys. Rev. Lett. **105**, 140501 (2010).

[37] Y. Kubo, F. R. Ong, P. Bertet, D. Vion, V. Jacques, D. Zheng, A. Dréau, J.-F. Roch, A. Auffeves, F. Jelezko, J. Wrachtrup, M. F. Barthe, P. Bergonzo, and D. Esteve, "Strong Coupling of a Spin Ensemble to a Superconducting Resonator", Phys. Rev. Lett. **105**, 140502 (2010).

[38] Y. Makhlin, G. Schön, and A. Shnirman, "Quantum-state engineering with Josephson-junction devices", Rev. Mod. Phys. **73**, 357 (2001).

[39] J. Clarke and F. K. Wilhelm, "Superconducting quantum bits", Nature **453**, 1031 (2008).

[40] L. DiCarlo, J. M. Chow, J. M. Gambetta, L. S. Bishop, B. R. Johnson, D. I. Schuster, J. Majer, A. Blais, L. Frunzio, S. M. Girvin, and R. J. Schoelkopf, "Demonstration of two-qubit algorithms with a superconducting quantum processor", Nature **460**, 240 (2009).

[41] D. Jaksch, J. I. Cirac, P. Zoller, S. L. Rolston, R. Côté, and M. D. Lukin, "Fast Quantum Gates for Neutral Atoms", Phys. Rev. Lett. **85**, 2208 (2000).

[42] M. Saffman, T. G. Walker, and K. Mølmer, "Quantum information with Rydberg atoms", Rev. Mod. Phys. **82**, 2313 (2010).

[43] D. Paredes-Barato and C. S. Adams, "All-Optical Quantum Information Processing Using Rydberg Gates", Phys. Rev. Lett. **112**, 040501 (2014).

[44] M. Saffman, "Quantum computing with atomic qubits and Rydberg interactions: progress and challenges", J. Phys. B **49**, 202001 (2016).

[45] T. D. Ladd, F. Jelezko, R. Laflamme, Y. Nakamura, C. Monroe, and J. L. O'Brien, "Quantum computers", Nature **464**, 45 (2010).

[46] Z. Kim, B. Suri, V. Zaretskey, S. Novikov, K. D. Osborn, A. Mizel, F. C. Wellstood, and B. S. Palmer, "Decoupling a Cooper-Pair Box to Enhance the Lifetime to 0.2 ms", Phys. Rev. Lett. **106**, 120501 (2011).

[47] H. Paik, D. I. Schuster, L. S. Bishop, G. Kirchmair, G. Catelani, A. P. Sears, B. R. Johnson, M. J. Reagor, L. Frunzio, L. I. Glazman, S. M. Girvin, M. H. Devoret, and R. J. Schoelkopf, "Observation of High Coherence in Josephson Junction Qubits Measured in a Three-Dimensional Circuit QED Architecture", Phys. Rev. Lett. **107**, 240501 (2011).

[48] D. Petrosyan and M. Fleischhauer, "Quantum Information Processing with Single Photons and Atomic Ensembles in Microwave Coplanar Waveguide Resonators", Phys. Rev. Lett. **100**, 170501 (2008).

[49] D. Petrosyan, G. Bensky, G. Kurizki, I. Mazets, J. Majer, and J. Schmiedmayer, "Reversible state transfer between superconducting qubits and atomic ensembles", Phys. Rev. A **79**, 040304 (2009).

[50] M. Wallquist, K. Hammerer, P. Rabl, M. Lukin, and P. Zoller, "Hybrid quantum devices and quantum engineering", Phys. Scripta **2009**, 014001 (2009).

[51] J. D. Pritchard, J. A. Isaacs, M. A. Beck, R. McDermott, and M. Saffman, "Hybrid atom-photon quantum gate in a superconducting microwave resonator", Phys. Rev. A **89**, 010301 (2014).

[52] H. Hattermann, D. Bothner, L. Y. Ley, B. Ferdinand, D. Wiedmaier, L. Sárkány, R. Kleiner, D. Koelle, and J. Fortágh, "Coupling ultracold atoms to a superconducting coplanar waveguide resonator", Nat. Commun. **8**, 2254 (2017).

[53] V. Vuletic, "When superatoms talk photons", Nat. Phys. **2**, 801 (2006).

[54] T. M. Weber, M. Höning, T. Niederprüm, T. Manthey, O. Thomas, V. Guarrera, M. Fleischhauer, G. Barontini, and H. Ott, "Mesoscopic Rydberg-blockaded ensembles in the superatom regime and beyond", Nat. Phys. **11**, 157 (2015).

[55] J. Palmer and S. D. Hogan, "Experimental demonstration of a Rydberg-atom beam splitter", Phys. Rev. A **95**, 053413 (2017).

[56] J. J. McClelland, A. V. Steele, B. Knuffman, K. A. Twedt, A. Schwarzkopf, and T. M. Wilson, "Bright focused ion beam sources based on laser-cooled atoms", Appl. Phys. Rev. **3**, 011302 (2016).

[57] N. Bassim, K. Scott, and L. A. Giannuzzi, "Recent advances in focused ion beam technology and applications", MRS Bulletin **39**, 317 (2014).

[58] B. G. Freinkman, A. V. Eletskii, and S. I. Zaitsev, "Laser ion beam formation for nanotechnologies", JETP Lett. **78**, 255 (2003).

[59] B. Knuffman, A. V. Steele, J. Orloff, and J. J. McClelland, "Nanoscale focused ion beam from laser-cooled lithium atoms", New J. Phys. **13**, 103035 (2011).

[60] C. Ates, I. Lesanovsky, C. S. Adams, and K. J. Weatherill, "Fast and Quasideterministic Single Ion Source from a Dipole-Blockaded Atomic Ensemble", Phys. Rev. Lett. **110**, 213003 (2013).

[61] L. Kime, A. Fioretti, Y. Bruneau, N. Porfido, F. Fuso, M. Viteau, G. Khalili, N. Santic, A. Gloter, B. Rasser, P. Sudraud, P. Pillet, and D. Comparat, "High-flux monochromatic ion and electron beams based on laser-cooled atoms", Phys. Rev. A **88**, 033424 (2013).

[62] D. Murphy, R. E. Scholten, and B. M. Sparkes, "Increasing the Brightness of Cold Ion Beams by Suppressing Disorder-Induced Heating with Rydberg Blockade", Phys. Rev. Lett. **115**, 214802 (2015).

[63] B. M. Sparkes, D. Murphy, R. J. Taylor, R. W. Speirs, A. J. McCulloch, and R. E. Scholten, "Stimulated Raman adiabatic passage for improved performance of a cold-atom electron and ion source", Phys. Rev. A **94**, 023404 (2016).

[64] D. J. Thompson, D. Murphy, R. W. Speirs, R. M. W. van Bijnen, A. J. McCulloch, R. E. Scholten, and B. M. Sparkes, "Suppression of Emittance Growth Using a Shaped Cold Atom Electron and Ion Source", Phys. Rev. Lett. **117**, 193202 (2016).

[65] E. Moufarej, M. Vielle-Grosjean, G. Khalili, A. J. McCulloch, F. Robicheaux, Y. J. Picard, and D. Comparat, "Forced field ionization of Rydberg states for the production of monochromatic beams", Phys. Rev. A **95**, 043409 (2017).

[66] R. Löw, H. Weimer, J. Nipper, J. B. Balewski, B. Butscher, H. P. Büchler, and T. Pfau, "An experimental and theoretical guide to strongly interacting Rydberg gases", J. Phys. B **45**, 113001 (2012).

[67] H. Busche, S. W. Ball, and P. Huillery, "A high repetition rate experimental setup for quantum non-linear optics with cold Rydberg atoms", Eur. Phys. J. Spec. Top. **225**, 2839 (2016).

[68] W. P. Spencer, A. G. Vaidyanathan, D. Kleppner, and T. W. Ducas, "Temperature dependence of blackbody-radiation-induced transfer among highly excited states of sodium", Phys. Rev. A **25**, 380 (1982).

[69] I. I. Beterov, I. I. Ryabtsev, D. B. Tretyakov, and V. M. Entin, "Quasiclassical calculations of blackbody-radiation-induced depopulation rates and effective lifetimes of Rydberg nS, nP, and nD alkali-metal atoms with $n \leq 80$", Phys. Rev. A **79**, 052504 (2009).

[70] P. Bohlouli-Zanjani, J. A. Petrus, and J. D. D. Martin, "Enhancement of Rydberg Atom Interactions Using ac Stark Shifts", Phys. Rev. Lett. **98**, 203005 (2007).

[71] L. A. Jones, J. D. Carter, and J. D. D. Martin, "Rydberg atoms with a reduced sensitivity to dc and low-frequency electric fields", Phys. Rev. A **87**, 023423 (2013).

[72] S. Sevinçli and T. Pohl, "Microwave control of Rydberg atom interactions", New J. Phys. **16**, 123036 (2014).

[73] T. F. Gallagher, "Rydberg atoms", Rep. Prog. Phys. **51**, 143 (1988).

[74] M. S. O'Sullivan and B. P. Stoicheff, "Scalar and tensor polarizabilities of ^{2}D Rydberg states in Rb", Phys. Rev. A **33**, 1640 (1986).

[75] H. J. Silverstone, "Perturbation theory of the Stark effect in hydrogen to arbitrarily high order", Phys. Rev. A **18**, 1853 (1978).

[76] M. L. Zimmerman, M. G. Littman, M. M. Kash, and D. Kleppner, "Stark structure of the Rydberg states of alkali-metal atoms", Phys. Rev. A **20**, 2251 (1979).

[77] W. Li, I. Mourachko, M. W. Noel, and T. F. Gallagher, "Millimeter-wave spectroscopy of cold Rb Rydberg atoms in a magneto-optical trap: Quantum defects of the ns, np, and nd series", Phys. Rev. A **67**, 052502 (2003).

[78] M. Mack, F. Karlewski, H. Hattermann, S. Höckh, F. Jessen, D. Cano, and J. Fortágh, "Measurement of absolute transition frequencies of ^{87}Rb to nS and nD Rydberg states by means of electromagnetically induced transparency", Phys. Rev. A **83**, 052515 (2011).

[79] J. Han, Y. Jamil, D. V. L. Norum, P. J. Tanner, and T. F. Gallagher, "Rb nf quantum defects from millimeter-wave spectroscopy of cold ^{85}Rb Rydberg atoms", Phys. Rev. A **74**, 054502 (2006).

[80] K. Afrousheh, P. Bohlouli-Zanjani, J. A. Petrus, and J. D. D. Martin, "Determination of the ^{85}Rb ng-series quantum defect by electric-field-induced resonant energy transfer between cold Rydberg atoms", Phys. Rev. A **74**, 062712 (2006).

[81] H. A. Bethe and E. E. Salpeter, *Quantum mechanics of one- and two-electron atoms* (Springer, Berlin [u.a.], 1957).

[82] M. Marinescu, H. R. Sadeghpour, and A. Dalgarno, "Dispersion coefficients for alkali-metal dimers", Phys. Rev. A **49**, 982 (1994).

[83] M. Pawlak, N. Moiseyev, and H. R. Sadeghpour, "Highly excited Rydberg states of a rubidium atom: Theory versus experiments", Phys. Rev. A **89**, 042506 (2014).

[84] M. Fleischhauer, A. Imamoglu, and J. P. Marangos, "Electromagnetically induced transparency: Optics in coherent media", Rev. Mod. Phys. **77**, 633 (2005).

[85] A. K. Mohapatra, T. R. Jackson, and C. S. Adams, "Coherent Optical Detection of Highly Excited Rydberg States Using Electromagnetically Induced Transparency", Phys. Rev. Lett. **98**, 113003 (2007).

[86] D. P. Fahey and M. W. Noel, "Excitation of Rydberg states in rubidium with near infrared diode lasers", Opt. Express **19**, 17002 (2011).

[87] A. Tauschinsky, R. Newell, H. B. van Linden Heuvell, and R. J. C. Spreeuw, "Measurement of ^{87}Rb Rydberg-state hyperfine splitting in a room-temperature vapor cell", Phys. Rev. A **87**, 042522 (2013).

[88] G. D. Stevens, C.-H. Iu, T. Bergeman, H. J. Metcalf, I. Seipp, K. T. Taylor, and D. Delande, "Precision measurements on lithium atoms in an electric field compared with R-matrix and other Stark theories", Phys. Rev. A **53**, 1349 (1996).

[89] W. P. Reinhardt, "Method of complex coordinates: Application to the stark effect in hydrogen", Int. J. Quantum Chem. **10**, 359 (1976).

[90] W. P. Reinhardt, "Complex Coordinates in the Theory of Atomic and Molecular Structure and Dynamics", Ann. Rev. Phys. Chem. **33**, 223 (1982).

[91] R. Kosloff and D. Kosloff, "Absorbing boundaries for wave propagation problems", J. Comput. Phys. **63**, 363 (1986).

[92] U. V. Riss and H.-D. Meyer, "Calculation of resonance energies and widths using the complex absorbing potential method", J. Phys. B **26**, 4503 (1993).

[93] S. Sahoo and Y. K. Ho, "The complex absorbing potential method (CAP) to study the Stark effect in hydrogen and lithium", J. Phys. B **33**, 2195 (2000).

[94] Y. K. Ho, "Recent Advances in the Theoretical Methods and Computational Schemes for Investigations of Resonances in Few-Body Atomic Systems", Few-Body Syst. **54**, 31 (2013).

[95] R. Santra and L. S. Cederbaum, "An efficient combination of computational techniques for investigating electronic resonance states in molecules", J. Chem. Phys. **115**, 6853 (2001).

[96] M. Stecker, H. Schefzyk, J. Fortágh, and A. Günther, "A high resolution ion microscope for cold atoms", New J. Phys. **19**, 043020 (2017).

[97] U. Fano, "Effects of Configuration Interaction on Intensities and Phase Shifts", Phys. Rev. **124**, 1866 (1961).

[98] S. Feneuille, S. Liberman, J. Pinard, and A. Taleb, "Observation of Fano Profiles in Photoionization of Rubidium in the Presence of a dc Field", Phys. Rev. Lett. **42**, 1404 (1979).

[99] T. S. Luk, L. DiMauro, T. Bergeman, and H. Metcalf, "Continuum Stark Spectroscopy", Phys. Rev. Lett. **47**, 83 (1981).

[100] D. A. Harmin, "Theory of the Stark effect", Phys. Rev. A **26**, 2656 (1982).

[101] R. Feynman, J. Hollingsworth, M. Vennettilli, T. Budner, R. Zmiewski, D. P. Fahey, T. J. Carroll, and M. W. Noel, "Quantum interference in the field ionization of Rydberg atoms", Phys. Rev. A **92**, 043412 (2015).

[102] V. C. Gregoric, X. Kang, Z. C. Liu, Z. A. Rowley, T. J. Carroll, and M. W. Noel, "Quantum control via a genetic algorithm of the field ionization pathway of a Rydberg electron", Phys. Rev. A **96**, 023403 (2017).

[103] R. J. Damburg and V. V. Kolosov, "A hydrogen atom in a uniform electric field. III", J. Phys. B **12**, 2637 (1979).

[104] F. Penent, D. Delande, and J. C. Gay, "Rydberg states of rubidium in crossed electric and magnetic fields", Phys. Rev. A **37**, 4707 (1988).

[105] J. Main, M. Schwacke, and G. Wunner, "Hydrogen atom in combined electric and magnetic fields with arbitrary mutual orientations", Phys. Rev. A **57**, 1149 (1998).

[106] A. M. Alonso, B. S. Cooper, A. Deller, L. Gurung, S. D. Hogan, and D. B. Cassidy, "Velocity selection of Rydberg positronium using a curved electrostatic guide", Phys. Rev. A **95**, 053409 (2017).

[107] A. Reinhard, T. C. Liebisch, B. Knuffman, and G. Raithel, "Level shifts of rubidium Rydberg states due to binary interactions", Phys. Rev. A **75**, 032712 (2007).

[108] T. Vogt, M. Viteau, A. Chotia, J. Zhao, D. Comparat, and P. Pillet, "Electric-Field Induced Dipole Blockade with Rydberg Atoms", Phys. Rev. Lett. **99**, 073002 (2007).

[109] A. Gaëtan, Y. Miroshnychenko, T. Wilk, A. Chotia, M. Viteau, D. Comparat, P. Pillet, A. Browaeys, and P. Grangier, "Observation of collective excitation of two individual atoms in the Rydberg blockade regime", Nat. Phys. **5**, 115 (2008).

[110] S. Ravets, H. Labuhn, D. Barredo, L. Béguin, T. Lahaye, and A. Browaeys, "Coherent dipole–dipole coupling between two single Rydberg atoms at an electrically-tuned Förster resonance", Nat. Phys. **10**, 914 (2014).

[111] J. Honer, R. Löw, H. Weimer, T. Pfau, and H. P. Büchler, "Artificial Atoms Can Do More Than Atoms: Deterministic Single Photon Subtraction from Arbitrary Light Fields", Phys. Rev. Lett. **107**, 093601 (2011).

Appended Publications

Publication [1]

Measurement and numerical calculation of Rubidium Rydberg Stark spectra
J. Grimmel, M. Mack, F. Karlewski, F. Jessen, M. Reinschmidt, N. Sándor, and J. Fortágh
New J. Phys. **17**, 053005 (2015).

Publication [2]

Quasiclassical quantum defect theory and the spectrum of highly excited rubidium atoms
A. Sanayei, N. Schopohl, **J. Grimmel**, M. Mack, F. Karlewski, and J. Fortágh
Phys. Rev. A **91**, 032509 (2015).

Publication [3]

State-selective all-optical detection of Rydberg atoms
F. Karlewski, M. Mack, **J. Grimmel**, N. Sándor, and J. Fortágh
Phys. Rev. A **91**, 043422 (2015).

Publication [4]

All-optical measurement of Rydberg-state lifetimes
M. Mack, **J. Grimmel**, F. Karlewski, L. Sárkány, H. Hattermann, and J. Fortágh
Phys. Rev. A **92**, 012517 (2015).

Publication [5]

Field ionization of Rydberg atoms for high-brightness electron and ion beams
A. J. McCulloch, R. W. Speirs, **J. Grimmel**, B. M. Sparkes, D. Comparat, and R. E. Scholten
Phys. Rev. A **95**, 063845 (2017).

Publication [6]

Ionization spectra of highly Stark-shifted rubidium Rydberg states

J. Grimmel, M. Stecker, M. Kaiser, F. Karlewski, L. Torralbo-Campo, A. Günther, and J. Fortágh
Phys. Rev. A **96**, 013427 (2017).

Publication [7]

Observation of the motional Stark shift in low magnetic fields
M. Kaiser, **J. Grimmel**, L. Torralbo-Campo, M. Mack, F. Karlewski, F. Jessen, N. Schopohl, and J. Fortágh
Phys. Rev. A **96**, 043401 (2017).

Publication [8]

Controlling the dipole blockade of highly Stark-shifted rubidium Rydberg states
M. Stecker, **J. Grimmel**, R. Nold, J. Fortágh and A. Günther
Ready for submission (2018).

The permissions for reprinting the publications on the following pages have been kindly granted by *IOP Publishing Ltd and Deutsche Physikalische Gesellschaft* ([1]) and the *American Physical Society* ([2–7]).

New Journal of Physics
The open access journal at the forefront of physics

Deutsche Physikalische Gesellschaft DPG
IOP Institute of Physics

Published in partnership with: Deutsche Physikalische Gesellschaft and the Institute of Physics

OPEN ACCESS

RECEIVED
29 January 2015

REVISED
11 March 2015

ACCEPTED FOR PUBLICATION
31 March 2015

PUBLISHED
6 May 2015

PAPER

Measurement and numerical calculation of Rubidium Rydberg Stark spectra

Jens Grimmel[1], **Markus Mack**[1], **Florian Karlewski**[1], **Florian Jessen**[1], **Malte Reinschmidt**[1], **Nóra Sándor**[1,2] and **József Fortágh**[1]

[1] CQ Center for Collective Quantum Phenomena and their Applications, Physikalisches Institut, Eberhard-Karls-Universität Tübingen, Auf der Morgenstelle 14, D-72076 Tübingen, Germany
[2] Wigner Research Center for Physics, Hungarian Academy of Sciences, Konkoly-Thege Miklós út 29-33, H-1121 Budapest, Hungary

E-mail: jens.grimmel@uni-tuebingen.de **and** fortagh@uni-tuebingen.de

Keywords: Rydberg states, Stark effect, electromagnetically induced transparency, precision spectroscopy

Supplementary material for this article is available online

Abstract

We report on the measurement of Stark shifted energy levels of ^{87}Rb Rydberg atoms in static electric fields by means of electromagnetically induced transparency (EIT). Electric field strengths of up to 500 V cm^{-1}, ranging beyond the classical ionization threshold, were applied using electrodes inside a glass cell with rubidium vapour. Stark maps for principal quantum numbers $n = 35$ and $n = 70$ have been obtained with high signal-to-noise ratio for comparison with results from *ab initio* calculations following the method described in (Zimmerman *et al* 1979 *Phys. Rev.* A **20** 2251), which was originally only verified for states around $n = 15$. We also calculate the dipole matrix elements between low-lying states and Stark shifted Rydberg states to give a theoretical estimate of the relative strength of the EIT signal. The present work significantly extends the experimental verification of this numerical method in the range of both high principal quantum numbers and high electric fields with an accuracy of up to 2 MHz.

1. Introduction

The response of atoms to static electric fields (dc Stark effect) results in line shifts, state mixing and, for sufficiently large fields, ionization. The line shifts are conventionally summarized in Stark maps, displaying the energy levels as a function of the applied field. Stark maps of alkali atoms are routinely calculated by diagonalising the perturbed Hamiltonian [1], taking into account quantum defects and corresponding electronic wavefunctions [2]. A precise knowledge and control of Stark shifted Rydberg states is required for the application of Rydberg atoms as quantum probes [3], for controlling the interactions between Rydberg atoms [4], the production of circular Rydberg atoms [5], the structure and dynamics of Rydberg gases [6, 7], and possible applications in quantum information processing [8]. In the context of hybrid quantum systems based on atoms and solid state quantum circuits [9, 10], Stark shifts of Rydberg states [11–13] and their control [14] are of particular interest.

Stark maps of Rydberg excited alkali atoms were studied in the 1970s using pulsed laser excitations and subsequent pulsed-field ionization [1, 15]. For low-lying Rydberg states of sodium, lithium and caesium with principal quantum numbers $n < 20$, Stark maps have been recorded up to and beyond the classical ionization limit [1, 15]. Stark maps of ^{85}Rb for n up to 55 were studied in the 1980s for low electric fields using two-photon laser excitation and detecting ionization from thermal collisions [16]. In this regime of low electric fields the Stark maps do not show level crossings but quadratic dependence on the applied field with slight deviation from this for highly excited states ($n = 55$).

Many recent experiments on Stark shifts use electromagnetically induced transparency (EIT) [17–19]. This spectroscopic method provides a high resolution of the energy levels [18] and is suitable for the detection of states of high principal quantum numbers. However, the measurements so far only covered the range of low

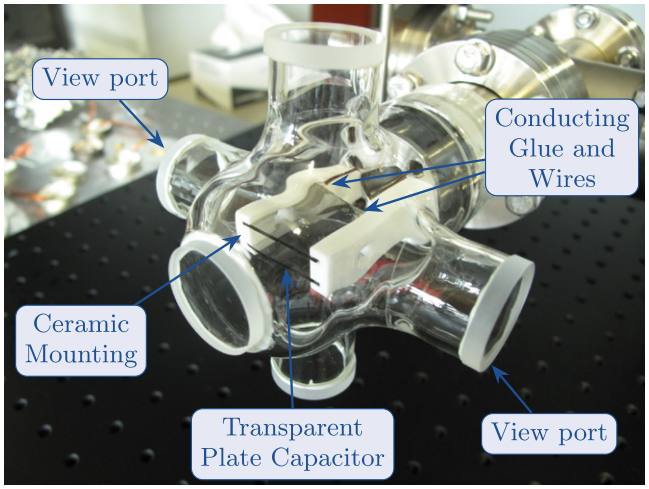

Figure 1. Vapour cell with electrodes. The capacitor plates are formed by two glass plates with 5 nm of nickel facing each other at a separation of 5 mm. Two wires are glued to each capacitor plate to contact them. For the measurements the laser beams counterpropagate through the view ports indicated in the image.

electric fields, in which just the first avoided crossings appear. Similarly, the detection of ions by micro-channel plates [20] and the technique of measuring the ionization currents from Stark-shifted Rydberg states [21] have only been used at low electric fields.

In this article, we report on the optical spectroscopy of Stark shifted Rydberg states with principal quantum numbers of $n = 35$ and $n = 70$ for electrostatic fields between 0 and 500 V cm^{-1}, ranging beyond the classical ionization limit. Our measurements go to higher principal quantum numbers and cover a three to four times larger range of electric fields relative to the classical ionization threshold than any of the aforementioned works using EIT. The observed Stark maps are compared with results from numerical calculations following the lines of the numerical method by [1], including the recently improved accuracy of the quantum defects [22]. In the original work this method was optimized for Rydberg states around $n = 15$ due to computational limitations as well as the accessible experimental data. The high accuracy of this method at low electric fields is always given by the accuracy of the unperturbed energy levels, which are used in the calculation. However, for strong electric fields and high principal quantum numbers, where a high accuracy of the calculated energy levels is desirable, this method becomes more susceptible to numerical errors [1]. In this article we show by direct comparison, that it is still applicable even in these regions of study. Furthermore, we calculate dipole matrix elements between $5P_{3/2}$ and the observed Stark shifted states, which are then used to give an estimate for the relative strength of the measured signals.

2. Measurement of Stark maps

For the measurement of Stark shifts of ^{87}Rb Rydberg atoms we use a vapour cell with a pair of plate electrodes for applying homogeneous electric fields. The electrodes are inside the cell (figure 1), trying to avoid the effect observed in previous works where static electric fields applied to a vapour cell with outside electrodes are compensated by ionized rubidium and electrons [23]. The rubidium vapour in the cell is at room temperature with an estimated pressure of $\approx 1 \cdot 10^{-7}$ mbar. The electrodes in the center of the glass cell (figure 1) are formed by two square glass plates coated with 5 nm of nickel. This gives the plates ≈60% transparency, which allows for optical access on the axis perpendicular to them. However, this optical access was not used in the experiments presented in this work. The plates are mounted with 5 mm separation on insulating ceramics (Macor) and connected to a voltage source through metallic wires. Laser beams for the optical spectroscopy are introduced through view ports and pass through the cell between the plates.

We measure the transition frequency from the rubidium ground state to Rydberg states by EIT. The EIT three level ladder scheme [23] consists of the ground state $5S_{1/2}(F = 2)$, the intermediate state $5P_{3/2}(F = 3)$ and a Rydberg state nS or nD (figure 2). However, it is important to keep in mind that l is not a good quantum number any more in the presence of an external electric field and that the Stark shifted states can be considered as a mix of all possible unperturbed l states. For the spectroscopy we use a *probe* laser that is locked to the $5S_{1/2}(F = 2) \rightarrow 5P_{3/2}(F = 3)$ transition (780 nm) and a *coupling* laser with a variable frequency close to the

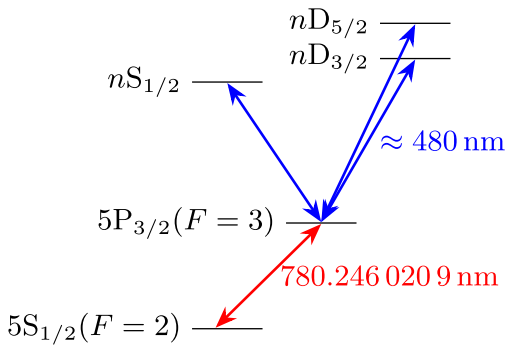

Figure 2. Ladder scheme for electromagnetically induced transparency (EIT). For our measurements the probe laser is held on resonance with the $5S_{1/2}(F = 2) \rightarrow 5P_{3/2}(F = 3)$ transition of ^{87}Rb and the coupling laser is scanned around the upper transition. Dipole selection rules only allow for the measurement of nS and nD states in this scheme.

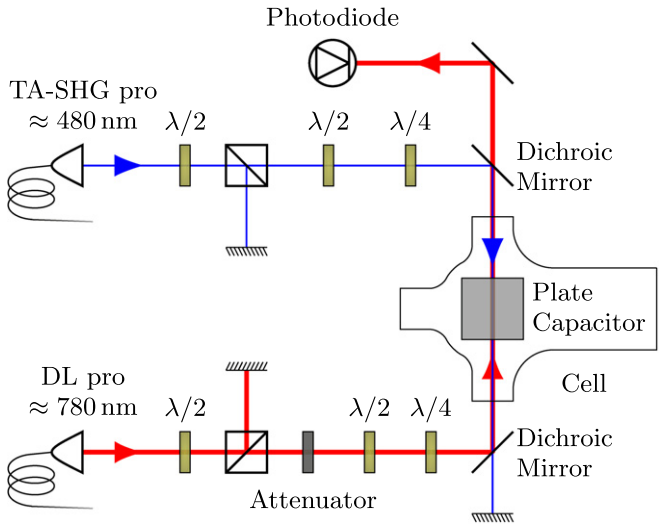

Figure 3. Optical setup (schematic) for the measurement of Stark maps using EIT. Both lasers are guided to the experiment through optical fibers and overlapped within the volume of the plate capacitor using two dichroic mirrors. Intensity and polarization of both lasers are adjusted independently. The transmission of the probe beam through the vapour cell is measured with a photodiode.

transition between $5P_{3/2}(F = 3)$ and a Rydberg state (480 nm). When the coupling laser is resonant with this transition we detect a maximum in the transmission of the probe laser through the vapour.

We use a grating-stabilized diode laser (Toptica, DL pro) of ≈100 kHz linewidth as the probe laser and a frequency-doubled, grating-stabilized diode laser of ≈200 kHz linewidth (Toptica, TA-SHG pro) as the coupling laser. Both lasers are phase-locked to a frequency comb (Menlo Systems, FC 1500). For conveniently selecting the right modes of the frequency comb for both lasers we use a calibrated wavelength meter (HighFinesse, WS Ultimate 2) [22]. The power of the probe laser is 1 μW and the power of the coupling laser is 25 mW with $1/e^2$ diameters of 450 and 150 μm in the cell, respectively. The small diameter of the coupling beam results in a high intensity and therefore high Rabi frequency on the corresponding transition while the bigger diameter of the probe beam is chosen in order to ensure maximal overlap of the two beams within the cell. The laser powers and polarizations were adjusted to maximize the EIT signal in zero field (figure 3). A measurement of the polarizations after this adjustment revealed that this resulted in circular polarizations for both lasers. The frequency of the probe laser is kept on resonance with the $5S_{1/2}(F = 2) \rightarrow 5P_{3/2}(F = 3)$ transition (figure 2) and its transmission through the cell is measured using an avalanche photodiode.

In order to reach a high signal-to-noise ratio in the spectroscopy, we use the following lock-in measurement technique. We modulate the power of the coupling laser using an acousto-optic modulator and demodulate the signal from the photodiode on the carrier frequency. In addition we modulate the frequency of the intensity modulation and demodulate the photodiode signal on two of the sidebands that arise from this. We then average the demodulated signal from the carrier and both sidebands. The additional frequency modulation decreases the signal strength on the carrier frequency and creates an even lower signal strength on the sidebands, but averaging

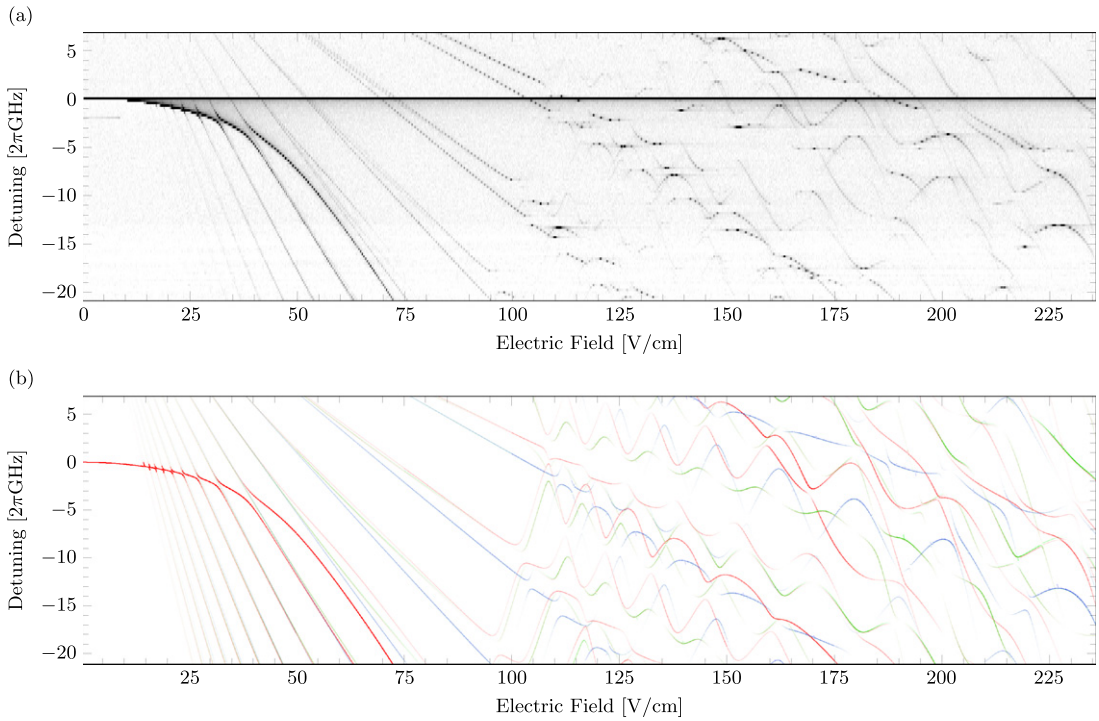

Figure 4. (a) Stark map for $35S_{1/2}$ for an electric field range of 0–235 V cm^{-1}. The gray scale is determined from the measured EIT signal, which represents the demodulated transmission signal from the photodiode. Due to the frequency resolution of 125 MHz some of the lines with a small slope appear dotted here. (b) The red, green and blue lines show the numerically calculated Stark map for $|m_j| = 1/2$, $|m_j| = 3/2$ and $|m_j| = 5/2$, respectively. The opacity gradients indicate the calculated transition strength D to the corresponding Stark shifted Rydberg states. In this region we find a very good agreement between experimental and numerically calculated results in the Stark shifts as well as the transition strengths.

the signal from three frequencies lowers the noise level at the same time. In total, the resulting signal-to-noise ratio is improved by a factor of ≈2 as compared to a simple lock-in measurement without frequency modulation. For every set frequency of the coupling laser we ramp up the voltage on the plate capacitor using an auxiliary output of the lock-in amplifier (Zurich Instruments, HF2LI). This is sufficient for electric fields up to ≈20 V cm^{-1}. For even higher fields up to ≈500 V cm^{-1} we use an additional voltage amplifier.

Measured data near the unperturbed $35S_{1/2}$ state is shown in figures 4 and 5. Near the unperturbed $70S_{1/2}$ state we conducted a preliminary measurement, which is not shown in this work, and then selected a smaller region for a more detailed measurement in order to test the frequency precision of the numerical calculations (figure 6). Each pixel in the gray scale images represents an average of the demodulated signal over 200 ms. Between every two pixels we add a waiting time of 50 ms to allow for the low-pass filter of the lock-in amplifier to settle. The gray scale was adjusted with a cutoff for better visibility of weaker signals. Our data shows states ranging up to and even beyond the classical ionization threshold that have not been measured by means of EIT before. The classical ionization threshold E_{ion}, i.e. the saddle point which is formed by a Coulomb potential with an external electric field F, is given by

$$E_{\mathrm{ion}} = -2\sqrt{F} \tag{1}$$

in atomic units ([2]). This results in an electric field strength for the ionization threshold of ≈312 V cm^{-1} for $35S_{1/2}$ and ≈16 V cm^{-1} for $70S_{1/2}$. For a quantitative analysis we give a brief review of the numerical calculation of Stark maps in section 3.

We observe two background effects (figures 4 and 6) which are caused by the region of the cell that is not covered by the plate capacitor (figure 1). The first is the line of the unperturbed state, which remains visible for all applied voltages because we probe those outer regions of the cell as well. The second is a smearing of the lines to the right at low fields as visible in figure 4 at the avoided crossings up to ≈50 V cm^{-1} and in figure 6. For a certain electric field strength inside the plate capacitor one always finds lower electric field strengths in the inhomogeneous outside region, causing the asymmetry of the smearing to the right.

Inside the capacitor undesirable electric fields could also arise from the dipole which is formed between adsorbed rubidium and the nickel surface of the capacitor plates. In previous experiments the repeated deposition of cold atom clouds of rubidium onto a copper surface led to electric fields close to the surface which saturated as the number of deposited clouds increased [11]. Since the work functions of nickel and copper are

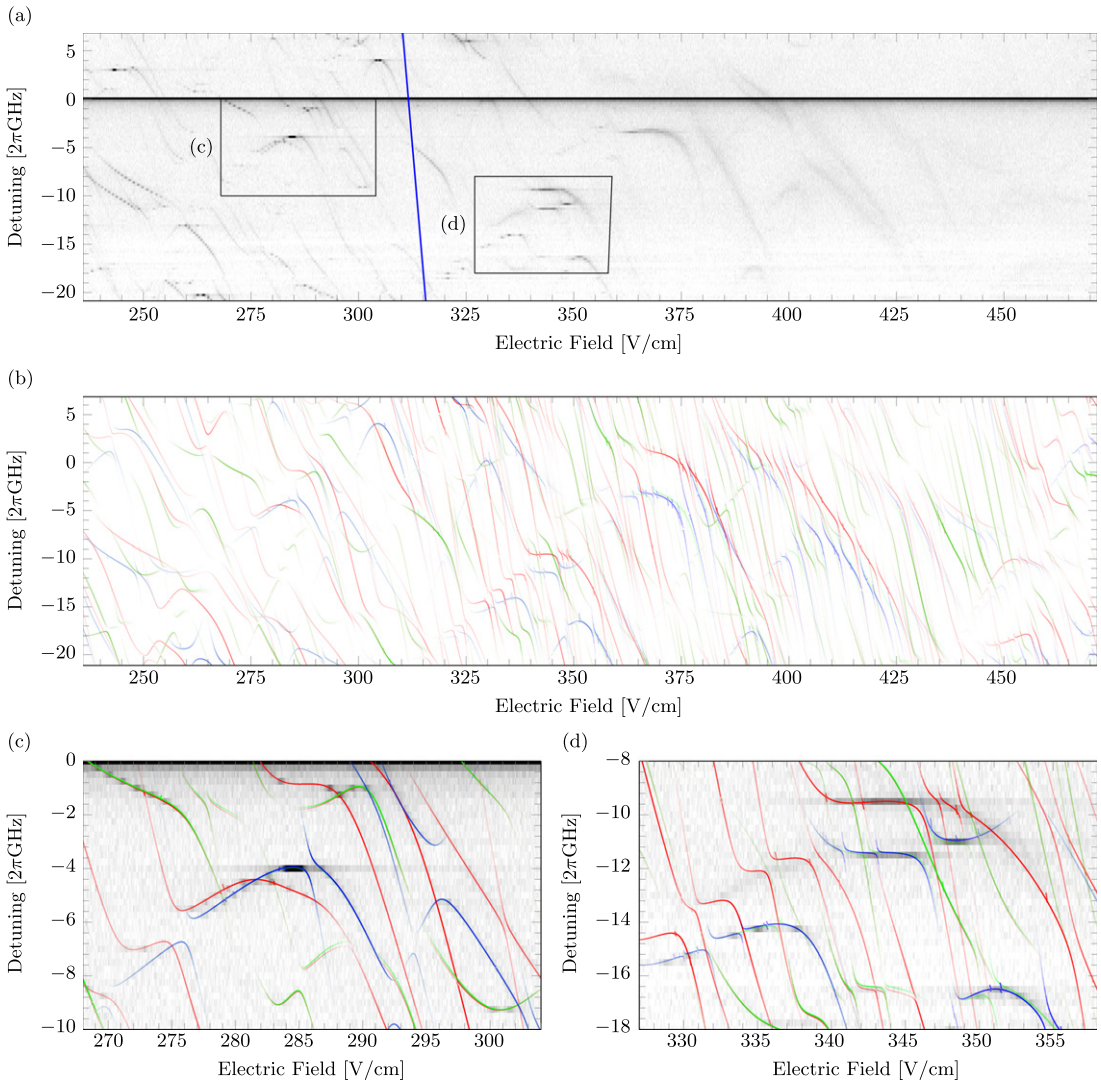

Figure 5. (a) Stark map for $35S_{1/2}$ for an electric field range of 235–470 V cm^{-1}. The gray scale represents the measured EIT signal. Due to the frequency resolution of 125 MHz some of the lines with a small slope appear dotted here. The blue solid line indicates the classical ionization limit. Beyond this limit fewer states are present in the measurement. The states also appear broader and weaker as the external electric field lowers and extends the opening of the potential barrier it forms with the atomic potential. (b) Results from our numerical calculations for the same region. The red lines represent $|m_j| = 1/2$, the green lines $|m_j| = 3/2$ and the blue lines $|m_j| = 5/2$ with the opacity gradients indicating the calculated transition strengths D to each state. (c) and (d) show details of the measurement with the numerically calculated Stark map on top. The opacity of the colors has been increased with a linear scaling in comparison to (b) for better visibility of the calculated lines on top of the experimental data. The agreement in the energy levels remains even beyond the classical ionization threshold, but we find some discrepancies in the transition strengths as the electric field strength increases.

similar and the cell is filled with rubidium vapour at all times we may find a similar effect for the capacitor plates. This effect may play a role for Rydberg states higher than $n = 70$ at low electric fields, but is negligible for the measured data presented in this article, where the distance between the laser beams and the capacitor plates is ≈2 mm. Other stray fields could originate from outside of the cell, but should be compensated by electrons and ionized rubidium [23].

3. Calculation of Stark maps and dipole matrix elements

The Hamiltonian for the valence electron in an alkali atom with an external electric field in z-direction can be written as

$$\hat{H} = \hat{H}_0 + E\hat{z} \tag{2}$$

in atomic units with $\hat{H}_0$ the Hamiltonian for the valence electron in absence of any perturbation, E the electric field strength and $\hat{z}$ the position operator in z-direction. For the following calculations we include the fine structure splitting in $\hat{H}_0$ and neglect the hyperfine structure splitting as it is smaller than our frequency

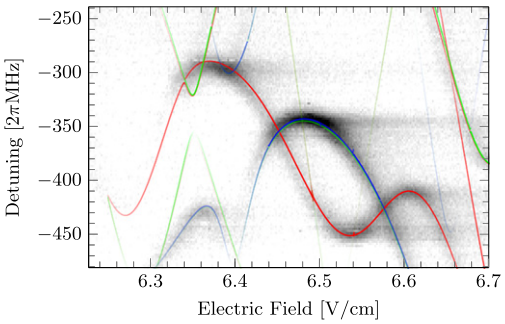

Figure 6. Detailed part of a Stark map for $70S_{1/2}$ for an electric field range of 6.23–6.70 V cm^{-1}. The gray scale represents the measured EIT signal. The red, green and blue lines plotted on top of the measured signal show the numerically calculated Stark map for $|m_j| = 1/2$, $|m_j| = 3/2$ and $|m_j| = 5/2$, respectively, with the opacity gradient scaled to the calculated transition strength D. The frequency resolution of this measurement is 2 MHz and, again, we find a very good agreement between the experimental and numerically calculated results.

resolution in the experiment [1]. The Stark shifts of the $5S_{1/2}(F = 2)$ and $5P_{3/2}(F = 3)$ states from the EIT scheme are negligible as well, as they amount to less than 100 kHz for the region of the field strength up to 500 V cm^{-1}. We then create a matrix representation of $\hat{H}$ in a subset of the basis given by $\hat{H}_0$. This way $\hat{H}_0$ is represented by a diagonal matrix with the energy levels from [22] on its diagonal.

The matrix representation of $\hat{z}$ is symmetric with only off-diagonal entries and in spherical coordinates we obtain from [1]

$$\left\langle n,\, l,\, j,\, m_j \,|\hat{z}|\, n',\, l',\, j',\, m_j' \right\rangle = \delta_{m_j,m_j'}\delta_{l,l'\pm1}\langle n,\, l,\, j \,|r|\, n',\, l',\, j'\rangle \sum_{m_l=m_j\pm\frac{1}{2}} \left\{ \left\langle l,\, \frac{1}{2},\, m_l,\, m_j - m_l \middle| j,\, m_j \right\rangle \times \left\langle l',\, \frac{1}{2},\, m_l,\, m_j - m_l | j',\, m_j \right\rangle \langle l,\, m_l \,|\cos\theta|\, l',\, m_l\rangle \right\} \tag{3}$$

with the radial overlap integral $\langle n,\, l,\, j \,|r|\, n',\, l',\, j'\rangle$ in the first line of the right hand side. From the Kronecker delta $\delta_{m_j,m_j'}$ we can see that the matrix representations of H for different values of m_j can be calculated separately. It is also evident that the Stark shifts for $\pm|m_j|$ are always equal. Therefore we only calculate matrix representations for positive values of m_j in this step. This reduces the computing time for diagonalizing the matrices, but we need to consider states with both signs for the calculation of transition strengths later on again.

For the calculation of the overlap integrals we tried two different methods to calculate the radial wavefunctions for all states in the chosen subset of the basis and also for $5S_{1/2}(F = 2)$ and $5P_{3/2}(F = 3)$, which will be used later on in the calculation of the measure for the transition strengths. One method was to further follow [1] using their atomic potential for ^{87}Rb and Numerov's method to solve the radial Schrödinger equation. We also tried using the parametric model potential from [24] with another solving algorithm[3], which allowed us to obtain parts of the wavefunctions that are located further inside the ionic core. While the two methods lead to slightly different amplitudes of the wavefunctions due to normalization, the differences in the Stark shifts and transition strengths calculated from the two methods for the observed states lie below our experimental accuracy. All calculations presented in this work utilized the latter method.

We can then calculate the matrix representations of the perturbed Hamiltonians H using equation (3) and diagonalize them efficiently in parallel for different values of the electric field strength to obtain the energy eigenvalues. In this step we also calculate the eigenvector β corresponding to every eigenvalue. With this we can further follow the method from [1] to represent every Stark shifted Rydberg state ξ as a linear combination of unperturbed states, given by the eigenvectors, and calculate the dipole matrix elements

$$\langle \xi \,|\vec{r}|\, 5P_{3/2},\, F = 3,\, m_F\rangle \quad = \sum_{n,l,j,m_j} \beta_{n,l,j,|m_j|} \left\langle n,\, l,\, j,\, m_j \,|\vec{r}|\, 5P_{3/2},\, F = 3,\, m_F \right\rangle \tag{4}$$

with $\beta_{n,l,j,|m_j|}$ the entry of β that corresponds to the states $|n,\, l,\, j,\, \pm|m_j|\rangle$. Here we sum over all states in the selected subset of the basis given by the unperturbed states and both signs for each value of m_j. For the calculation of the dipole matrix elements between the unperturbed Rydberg states and $|5P_{3/2},\, F = 3,\, m_F\rangle$ we separate the radial and the angular parts of the wavefunctions. We use the radial overlap integrals from equation (3) and calculate the three components of the angular overlap integrals following [25].

[3] MATLAB 2014a; Solver function: ode45.

We take into account the effect of the probe laser, which couples the different m_F substates of $|5S_{1/2},\ F = 2\rangle$ and $|5P_{3/2},\ F = 3\rangle$ by calculating the weighting factors

$$\eta_{m_F} = \sum_{m_F'} \left| \left\langle 5P_{3/2},\ F = 3,\ m_F \left| \vec{\varepsilon}_p \vec{r} \right| 5S_{1/2},\ F' = 2,\ m_F' \right\rangle \right|^2 \tag{5}$$

with $\vec{\varepsilon}_p$ the polarization of the probe laser. In this step we assume that all m_F substates of $|5S_{1/2},\ F = 2\rangle$ are evenly occupied. The weighting factors are then used to calculate the measure for the transition strength

$$D = \sum_{m_F} \eta_{m_F} \left| \langle \xi \left| \vec{\varepsilon}_c \vec{r} \right| 5P_{3/2},\ F = 3,\ m_F \rangle \right|^2 \tag{6}$$

with $\vec{\varepsilon}_c$ the polarization of the coupling laser. In the experiment the two lasers are counterpropagating and perpendicular to the external electric field with circular polarizations. Therefore we use $\vec{\varepsilon}_p = \vec{\varepsilon}_c = (0,\ i,\ 1)$ here. The measure for the transition strength D is used to determine the opacity gradients for the lines in figures 4–6.

The Stark map for $35S_{1/2}$, which is shown in figures 4 and 5, was calculated from a subset of the basis of approximately 1600 states and for 2000 values of the electric field strength using MATLAB. For $70S_{1/2}$, shown in figure 6, the calculations run similarly with 4000 states and 500 values of the electric field strength. The number of states that was used for these calculations was adjusted so that a further increase only yields changes which lie below the accuracy of the experimental data. Calculated Stark maps for $|m_j| = 1/2$, $|m_j| = 3/2$ and $|m_j| = 5/2$ are included in the figures. The measurements were performed in frequency regions around S states, but since l is not a good quantum number any more in the presence of an electric field [1], we find that other states with $|m_j| = 3/2$ and $|m_j| = 5/2$ are shifted far enough by the Stark effect to appear within the measured frequency range.

4. Comparison of measurements and calculations

Figures 4 and 5 show comparisons of the measured and numerically calculated Stark maps for $35S_{1/2}$. The frequency axis shows the detuning of the coupling laser relative to the absolute value of the transition frequency from [22]. A linear scaling with an offset has been applied to the electric field axis of the measured data. Using only this scaling we achieve a match between calculated and measured energy levels for Stark states in the whole range of our measurement.

The lines in the calculated Stark maps are drawn with an opacity gradient, resulting in a color range between white and the respective color associated with the different values for $|m_j|$. The opacity gradient is scaled to D from equation (6) with an upper cutoff at 70% of its maximum for better visibility. We find a good agreement between this calculated measure for the transition strength and the experimental data in the range of electric fields shown in figure 4. The quality of the agreement deteriorates slightly approaching the classical ionization threshold, but there is still good agreement beyond this point, as can be seen in figure 5. The very weak signals we still find in the experimental data at electric fields around 400 V cm^{-1} all correspond to calculated states with a strong calculated transition strength. Considering this, we think that the method described here can be applied for these high electric field strengths, where only few states are still visible in the experimental data, as a way to select potentially interesting areas before a measurement.

One important cause for discrepancies between the experimental and numerically calculated data we present here is that no ionization effects were taken into account for the calculations. However, it is interesting to note that even though the calculated measure for the transition strength shows some differences at high electric fields, we still find a remarkable agreement of calculated and measured energy levels in this region of study. These differences could be related to the calculation of the radial wavefunctions. We calculate the radial wavefunctions for $|5S_{1/2}\rangle$ and $|5P_{3/2}\rangle$ using the same method as for Rydberg states. Evidently this works quite well here, but more accurate radial wavefunctions, especially for $|5P_{3/2}\rangle$ but also for Rydberg states with low l, could further improve the quality of the calculated transition strengths. This is further emphasized as the biggest discrepancies of the transition strengths at high electric fields can be found for states $|m_j| = 1/2$ while states with $|m_j| = 5/2$ show hardly any discrepancies on the whole range of electric fields. On the other hand, these discrepancies could also be explained by a stronger coupling of Rydberg states with low l to the continuum. Some disagreements on the whole range of our measurements can also be caused by the scaling of the EIT signal with the dipole matrix elements, which is only approximated by the squared scaling in D. Furthermore, lines with small slopes and especially local extrema may appear over-pronounced in the experimental data. Since these parts of the lines are broad in the electric field domain and the inhomogeneous electric field outside of the plate capacitor still lies within the volume of the cell, this results in an effective contribution of more atoms to the signal.

We find a match similar to the one presented for $35S_{1/2}$ in the energy levels and transition strengths for $70S_{1/2}$, which is shown in detail in figure 6. Discrepancies lie within the frequency resolution of 2 MHz for figure 6, which is the highest accuracy we present here. The opacity gradients were assigned the same way as for

$35S_{1/2}$. The calculated transition strengths match the experimental data equally well as for $35S_{1/2}$. The experimental data presented in figures 4–6 is provided as supplementary data to this article[4]. All results presented in this work were measured and calculated in the energy range near nS states. However, they intrinsically include contributions from all possible l states due to the mixing of states caused by the external electric field.

For a possible extension of our measurements to a wider range of principal quantum numbers n than the region between $n = 35$ and $n = 70$, the most important limiting factor is that the coupling of Rydberg states to the intermediate $5P_{3/2}(F = 3)$ grows weaker as n increases, which leads to a lower signal-to-noise ratio. Another factor influencing the signal-to-noise ratio is the density of the vapour, which on the other hand gives rise to collective effects which in turn cause undesired changes of the EIT signal [26].

5. Conclusion

In summary, we have demonstrated agreement between measured and calculated Stark maps of ^{87}Rb up to an accuracy of 2 MHz. This agreement holds for the range from zero field to beyond the classical ionization threshold and for principal quantum numbers $n = 35$ and $n = 70$. Such data and calculations may aid the accurate mapping of electric fields at surfaces [11]. Furthermore, we presented numerical calculations to estimate the transition strength from low-lying states to Stark shifted Rydberg states. The results from these calculations show a very good agreement with our experimental data on a high range of electric fields and even beyond the classical ionization threshold.

Altogether, the methods presented in this paper can be used to find experimentally accessible Stark shifted Rydberg states with an appropriate sensitivity to external electric fields for a wide range of applications. For example, the dependence of the transition strength to different Stark shifted Rydberg levels could be used to determine not only the strength of an external electric field in an experimental system but also the electric field axis.

Acknowledgments

This work was financially supported by the FET-Open Xtrack Project HAIRS and the Carl Zeiss Stiftung. Nóra Sándor acknowledges financial support from the framework of TÁMOP-4.2.4.A/2-11/1-2012-0001 'National Excellence Program'. We thank Nils Schopohl and Ali Sanayei for helpful discussions. We acknowledge support by Deutsche Forschungsgemeinschaft and Open Access Publishing Fund of University of Tübingen.

References

[1] Zimmerman M L, Littman M G, Kash M M and Kleppner D 1979 *Phys. Rev.* A **20** 2251
[2] Gallagher T F (ed) 1994 *Rydberg Atoms* 1st edn (Cambridge: Cambridge University Press)
[3] Guerlin C, Bernu J, Deleglise S, Sayrin C, Gleyzes S, Kuhr S, Brune M, Raimond J-M and Haroche S 2007 *Nature* **448** 889
[4] Daschner R, Ritter R, Kübler H, Frühauf N, Kurz E, Löw R and Pfau T 2012 *Opt. Lett.* **37** 2271
[5] Anderson D A, Schwarzkopf A, Sapiro R E and Raithel G 2013 *Phys. Rev.* A **88** 031401
[6] Comparat D and Pillet P 2010 *J. Opt. Soc. Am.* B **27** A208
[7] Beterov I I, Ryabtsev I I, Tretyakov D B and Entin V M 2009 *Phys. Rev.* A **79** 052504
[8] Paredes-Barato D and Adams C S 2014 *Phys. Rev. Lett.* **112** 040501
[9] Petrosyan D and Fleischhauer M 2008 *Phys. Rev. Lett.* **100** 170501
[10] Tauschinsky A, Thijssen R M T, Whitlock S, van Linden van den Heuvell H B and Spreeuw R J C 2010 *Phys. Rev.* A **81** 063411
[11] Hattermann H, Mack M, Karlewski F, Jessen F, Cano D and Fortágh J 2012 *Phys. Rev.* A **86** 022511
[12] Abel R P, Carr C, Krohn U and Adams C S 2011 *Phys. Rev.* A **84** 023408
[13] Chan K S, Siercke M, Hufnagel C and Dumke R 2014 *Phys. Rev. Lett.* **112** 026101
[14] Jones L A, Carter J D and Martin J D D 2013 *Phys. Rev.* A **87** 023423
[15] Littman M G, Zimmerman M L, Ducas T W, Freeman R R and Kleppner D 1976 *Phys. Rev. Lett.* **36** 788
[16] O'Sullivan M S and Stoicheff B P 1986 *Phys. Rev.* A **33** 1640
[17] Fahey D P and Noel M W 2011 *Opt. Express* **19** 17002
[18] Tauschinsky A, Newell R, Van Linden van den Heuvell H B and Spreeuw R J C 2013 *Phys. Rev.* A **87** 042522
[19] Bason M G, Tanasittikosol M, Sargsyan A, Mohapatra A K, Sarkisyan D, Potvliege R M and Adams C S 2010 *New J. Phys.* **12** 065015
[20] Grabowski A, Heidemann R, Lw R, Stuhler J and Pfau T 2006 *Fortschr. Phys.* **54** 765
[21] Barredo D, Kübler H, Daschner R, Löw,and R and Pfau T 2013 *Phys. Rev. Lett.* **110** 123002
[22] Mack M, Karlewski F, Hattermann H, Höckh S, Jessen F, Cano D and Fortágh J 2011 *Phys. Rev.* A **83** 052515
[23] Mohapatra A K, Jackson T R and Adams C S 2007 *Phys. Rev. Lett.* **98** 113003
[24] Marinescu M, Sadeghpour H R and Dalgarno A 1994 *Phys. Rev.* A **49** 982
[25] Bethe H A and Salpeter E E 1957 *Quantum Mechanics of One- and Two-Electron Atoms* (Berlin: Springer) p 8, 368 S
[26] Ates C, Sevinçli S and Pohl T 2011 *Phys. Rev.* A **83** 041802

[4] See supplementary data available at stacks.iop.org/njp/17/053005/mmedia for the experimental data.

Quasiclassical quantum defect theory and the spectrum of highly excited rubidium atoms

Ali Sanayei and Nils Schopohl*
Institut für Theoretische Physik and CQ Center for Collective Quantum Phenomena and their Applications in LISA⁺, Eberhard-Karls-Universität Tübingen, Auf der Morgenstelle 14, D-72076 Tübingen, Germany

Jens Grimmel, Markus Mack, Florian Karlewski, and József Fortágh†
Physikalisches Institut and CQ Center for Collective Quantum Phenomena and their Applications in LISA⁺, Eberhard-Karls-Universität Tübingen, Auf der Morgenstelle 14, D-72076 Tübingen, Germany
(Received 28 January 2015; published 23 March 2015)

We report on a significant discrepancy between recently published, highly accurate variational calculations and precise measurements of the spectrum of Rydberg states in ^{87}Rb on the energy scale of fine splitting. Introducing a modified effective single-electron potential, we determine the spectrum of the outermost bound electron from a standard WKB approach. Overall very good agreement with precise spectroscopic data is obtained.

DOI: 10.1103/PhysRevA.91.032509 PACS number(s): 31.10.+z, 32.80.Ee

I. INTRODUCTION

The spectrum of the outermost bound electron of an alkali atom such as ^{87}Rb is hydrogenlike but lacks the n^2 degeneracy of the eigenstates labeled by the principal quantum number n of the pure Coulomb potential [1,2]:

$$E_{n,l} = -\frac{1}{(n-\delta_l)^2}. \tag{1}$$

This effect is the well-known quantum defect δ_l, resulting from the interaction of the outermost electron with the ionic core of the atom and the nucleus. In a refined version of the statistical Thomas-Fermi theory [3], an effective potential determining the interaction between the outermost electron and the nucleus can be modeled accurately by a spherically symmetric potential $V_{\rm eff}(r;l)$ depending on the distance r from the center and depending on the orbital angular momentum $l \in \{0,1,2,\ldots,n-1\}$ [2,4,5]:

$$V_{\rm eff}(r;l) = -2\left[\frac{Z_{\rm eff}(r;l)}{r} + V_{\rm pol}(r;l)\right]. \tag{2}$$

Here the function $Z_{\rm eff}(r;l)$ represents a position-dependent weight function that interpolates the value of the charge between unity for large r and charge number Z near to the nucleus for $r \to 0$, and $V_{\rm pol}(r;l)$ represents a short-range interaction taking into account the static electric polarizability of the ionic core [1,6].

Overall good agreement with spectroscopic data of alkali atoms (but discarding the fine splitting) has been reported in [5], choosing

$$Z_{\rm eff}(r;l) = 1 + (Z-1)e^{-ra_1(l)} - re^{-ra_2(l)}\left[a_3(l) + ra_4(l)\right] \tag{3}$$

and

$$V_{\rm pol}(r;l) = \frac{\alpha_c}{2}\frac{1-\exp\left[-\left(\frac{r}{r_c(l)}\right)^6\right]}{r^4}. \tag{4}$$

A table of the parameters $a_1(l)$, $a_2(l)$, $a_3(l)$, $a_4(l)$, α_c, and $r_c(l)$ can be found in [5].

In an attempt to also describe the fine splitting of the excitation spectrum of the outermost electron of ^{87}Rb, it has been suggested [4] to superimpose *a posteriori* a spin-orbit term

$$\widetilde{V}_{\rm SO}(r;j,l) = \frac{V_{\rm SO}(r;j,l)}{[1-\alpha^2 V_{\rm eff}(r;l)]^2} \tag{5}$$

on the potential $V_{\rm eff}(r;l)$, which then influences the spectrum $E_{n,j,l}$ on the scale of fine splitting and the orbitals $\psi_{n,j,l}(r)$ accessible to the outermost electron. Here

$$V_{\rm SO}(r;j,l) = \alpha^2\frac{1}{r}\frac{\partial V_{\rm eff}(r;l)}{\partial r}g(j,l), \tag{6}$$

and $\alpha = \frac{\lambda_C}{a_B} \simeq \frac{1}{137.036}$ denotes the fine-structure constant, and

$$g(j,l) = \begin{cases} 0 & \text{if } l = 0, \\ \frac{j(j+1)-l(l+1)-\frac{3}{4}}{2} & \text{if } l \geqslant 1, \end{cases} \tag{7}$$

where $j \in \{l-\frac{1}{2}, l+\frac{1}{2}\}$. To determine those orbitals (with principal quantum number $n = n_r + l + 1$ and radial quantum number $n_r \in \mathbb{N}_0$), a normalizable solution to the Schrödinger eigenvalue problem for the radial wave function $U_{n,j,l}(r) = rR_{n,j,l}(r)$ and associated eigenvalues $E_{n,j,l} < 0$ is required:

$$\left[-\frac{d^2}{dr^2} + \frac{l(l+1)}{r^2} + \widetilde{V}(r;j,l) - E_{n,j,l}\right]U_{n,j,l}(r) = 0, \tag{8}$$

where

$$\widetilde{V}(r;j,l) = V_{\rm eff}(r;l) + \widetilde{V}_{\rm SO}(r;j,l) \tag{9}$$

denotes the effective single-electron potential.

A highly accurate variational calculation of the excitation spectrum of the outermost electron of ^{87}Rb has been carried out recently [7], in which the authors expand the radial wave function of the Schrödinger eigenvalue problem (8) in a basis spanned by 500 Slater-type orbitals (STOs). On the other hand, modern high-precision spectroscopy of Rydberg levels of ^{87}Rb has been conducted recently. Millimeter-wave spectroscopy employing selective field ionization allows for precise measurements of the energy differences between Rydberg

*nils.schopohl@uni-tuebingen.de
†fortagh@uni-tuebingen.de

TABLE I. Fine splitting $\Delta E_{n,l=1}$ for P states in megahertz.

State $\|n,l=1\rangle$	Expt. [11]	Expt. [8]	Theory [7]	Theory (this work)
8P	$565.1(4)\times 10^3$	NA	602.04×10^3	567.75×10^3
10P	$219.1(4)\times 10^3$	NA	231.87×10^3	218.77×10^3
30P	NA	4246.30(5)	4500.50	4246.46
35P	NA	2566.41(32)	2717.41	2566.28
45P	NA	1144.09(13)	1217.24	1143.95
55P	NA	605.77(7)	644.81	605.68
60P	NA	460.76(5)	480.32	460.68

levels [8]. An independent approach is to perform purely optical measurements on absolute Rydberg level energies by observing electromagnetically induced transparency (EIT) [9,10]. However, there is a systematic discrepancy between variational calculations and the spectroscopic measurements of the fine splitting,

$$\Delta E_{n,l} = E_{n,l+\frac{1}{2},l} - E_{n,l-\frac{1}{2},l}\,, \tag{10}$$

as shown in Tables I and II. Given the fact that the error bars of the independent experiments [8,10] are below 1.1 MHz down to 20 kHz, and on the other hand considering the high accuracy of the numerical calculations presented in [7], such a discrepancy between experiment and theory is indeed significant.

So, what could be the reason for the reported discrepancies? First, it should be pointed out that in the variational calculations [7] a slightly different potential was used, that is,

$$V\,(r;j,l) = V_{\rm eff}(r;l) + V_{\rm SO}\,(r;j,l)\,. \tag{11}$$

Certainly, within the first-order perturbation theory there exists no noticeable discrepancy in the spectrum of the outermost electron on the fine-splitting scale, when taking into account the spin-orbit forces with $V_{\rm SO}\,(r;j,l)$ instead of working with $\widetilde{V}_{\rm SO}\,(r;j,l)$. This is due to the differences being negligible for $r > Z\alpha^2$. However, since $V_{\rm SO}\,(r;j,l)$ eventually dominates even the contribution of the centrifugal barrier term $\frac{l(l+1)}{r^2}$ within the tiny region $0 < r \lesssim \alpha^2 Z$, a subtle problem with a non-normalizable radial wave function $U_{n,j,l}(r)$ emerges when attempting to solve the Schrödinger eigenvalue problem for any $l > 0$ with the potential $V_{\rm SO}\,(r;j,l)$. Such a problem is absent when one works with $\widetilde{V}_{\rm SO}\,(r;j,l)$ [4].

A variational calculation with the potential (11) employing $N = 500$ normalizable STOs as basis functions thus engenders a systematic (small) error of the matrix elements calculated in [7] on the fine-splitting scale. When employing substantially more STOs this error would certainly become larger. With $N = 500$ STOs the discrepancy of these theoretical results with the high-precision spectroscopic data, as shown in Tables I and II, is far too large to be corrected by simply replacing $V_{\rm SO}\,(r;j,l)$ with $\widetilde{V}_{\rm SO}\,(r;j,l)$. Hence another explanation is required.

II. QUASICLASSICAL APPROACH AND FINE SPLITTING OF THE HIGHLY EXCITED ^{87}Rb

In 1941 alkali atoms had already been studied in the context of modern quantum mechanics in the seminal work by Mayer [3], who emphasized the exceptional role of the $l = 1$ and $l = 2$ orbitals. According to Mayer, the outermost electron of an alkali atom is governed by an effective r-dependent charge term

$$Z_{\rm eff}\,(r) = 1 + (Z-1)F(r), \tag{12}$$

where the function $F(r)$ has been determined by employing the semiclassical statistical Thomas-Fermi approach to the many-electron-atom problem, posing the boundary conditions as $\lim_{r\to 0} F(r) = 1$ and $\lim_{r\to\infty} F\,(r) = 0$. As discussed by Schwinger [12], this approach ceases to be valid in the inner-shell region $Z^{-1} < r < Z^{-\frac{1}{3}}$ of the atom. Therefore, taking into account the fine splitting in the spectrum of the outermost electron of alkali atoms *a posteriori* by simply adding the phenomenological spin-orbit term (5) to (2), resulting in the effective single-electron potential (9), seems to be questionable on general grounds in that inner-shell region.

On a more fundamental level, the treatment of relativistic effects in multi-electron-atom spectra requires an *a priori* microscopic description based on the well-known Breit-Pauli Hamiltonian [13,14]:

$$\mathcal{H} = \mathcal{H}_{\rm nr} + \mathcal{H}_{\rm rs} + \mathcal{H}_{\rm fs}. \tag{13}$$

Here $\mathcal{H}_{\rm nr}$ is the ordinary *nonrelativistic* many-electron Hamiltonian, while the *relativistic corrections* are represented by the perturbation operators $\mathcal{H}_{\rm rs}$ and $\mathcal{H}_{\rm fs}$. The perturbation term $\mathcal{H}_{\rm rs}$

TABLE II. Fine splitting $\Delta E_{n,l=2}$ for D states in megahertz.

State $\|n,l=2\rangle$	Expt. [11]	Expt. [8]	Expt. [10]	Theory [7]	Theory (this work)
8D	$30.4(4)\times 10^3$	NA	NA	113.17×10^3	36.42×10^3
10D	$14.9(2)\times 10^3$	NA	NA	52.05×10^3	16.56×10^3
30D	NA	452.42(18)	452.5(11)	1447.53	456.13
35D	NA	279.65(10)	280.4(11)	894.84	281.52
45D	NA	128.33(4)	127.8(11)	407.64	128.98
55D	NA	69.17(2)	69.4(11)	223.71	69.47
57D	NA	61.98(2)	62.2(11)	197.39	62.24

contains all the relativistic perturbations like *mass correction*, one- and two-body *Darwin terms*, and further the *spin-spin contact* and *orbit-orbit* terms, which all commute with the total angular momentum $\mathbf{L}$ and total spin $\mathbf{S}$, thus effectuating only small *shifts* of the spectrum of the nonrelativistic Hamiltonian $\mathcal{H}_{\rm nr}$. The perturbation operator $\mathcal{H}_{\rm fs}$, on the other hand, breaks the rotational symmetry. It consists of the standard *nuclear spin-orbit*, the *spin-other-orbit*, and the *spin-spin dipole* interaction terms, which all commute with $\mathbf{J} = \mathbf{L} + \mathbf{S}$, but not with $\mathbf{L}$ or with $\mathbf{S}$ separately, thus inducing the fine splitting of the nonrelativistic spectrum.

Although the proposed functional form of the potential (11) is highly plausible on physical grounds outside the inner-core region $r > Z^{-\frac{1}{3}}$, *prima facie* it appears to be inconsistent to lump the aforementioned relativistic many-body forces, spin-other-orbit and spin-spin dipole interaction, into an effective single-electron potential of the functional form (11), so that it provides an accurate description also for small distances $Z^{-1} < r < Z^{-\frac{1}{3}}$.

In the absence of a better microscopic theory for an effective single-electron potential $V_{\rm eff}\,(r;j,l)$ describing the fine splitting of the spectrum of the outermost electron in the alkali atoms, we introduce a *cutoff* at a distance $r_{\rm so}(l)$ with $Z^{-1} < r_{\rm so}(l) < Z^{-\frac{1}{3}}$ so that the effective single-electron potential is now described by the following modified potential:

$$\widetilde{V}_{\rm mod}\,(r;j,l) = \begin{cases} V_{\rm eff}(r;l) & \text{if } 0 \leqslant r \leqslant r_{\rm so}(l), \\ V_{\rm eff}(r;l) + V_{\rm SO}\,(r;j,l) & \text{if } r > r_{\rm so}(l). \end{cases} \tag{14}$$

The choice [2]

$$\begin{aligned} r_{\rm so}\,(l=1) &= 0.029\,483 \times r_c\,(l=1) = 0.044\,282\,5, \\ r_{\rm so}\,(l=2) &= 0.051\,262 \times r_c\,(l=2) = 0.249\,572\,0, \end{aligned} \tag{15}$$

gives a surprisingly accurate description of the fine splitting in the spectroscopic data for *all* principal quantum numbers n (see Fig. 1, Tables I and II). By choosing larger values for $r_{\rm so}(l)$ than stated in (15), the calculated fine splitting is too small compared to experiment, and vice versa, by choosing smaller values for $r_{\rm so}(l)$ we find the calculated fine splitting is too large compared to experiment.

The calculation of the spectrum of the outermost bound electron is then reduced to solving the radial Schrödinger equation (8) with the modified potential $\widetilde{V}_{\rm mod}\,(r;j,l)$. The resulting spectrum is actually hydrogenlike, that is,

$$E_{n,j,l} = -\frac{1}{(n-\Delta_{j,l})^2}, \tag{16}$$

where $\Delta_{j,l}$ denotes a quantum defect also comprising the fine splitting. In actual fact the quantum defect describes a reduction of the number of nodes n_r of the radial wave function for $l = 0,1,2$ as a result of the short-range interaction of the outermost electron with the ionic core of the atom. Because the higher the orbital angular momentum quantum number l, the lower the probability of the electron being located near to the center, it is clear that the quantum defect decreases rapidly with increasing orbital angular momentum l. Therefore $\Delta_{j,l}$ is only notably different from zero for $l = 0,1,2$.

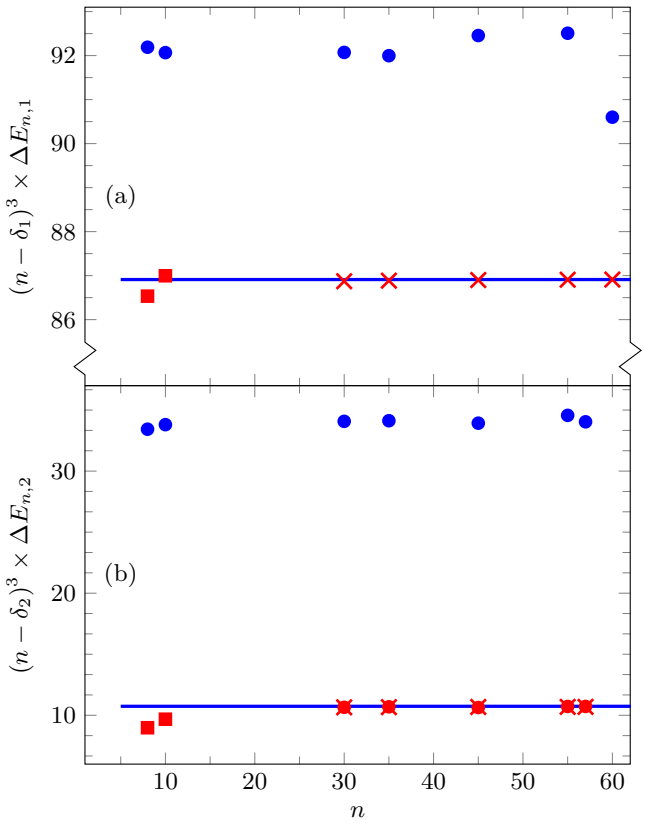

FIG. 1. (Color online) Reduced fine splitting in THz (a) for P states (cf. Table I) and (b) for D states (cf. Table II). The blue line corresponds to the theory from this work [see Eq. (17)]. The blue circles show the recent numerically calculated results from [7]. The red symbols denote experimental data from Refs. [11] (squares), [8] (crosses), and [10] (circles). The error bars for the experimental data are given in Tables I and II.

Writing $\Delta_{j,l} = \delta_l + \eta_{j,l}$ with $\eta_{j,l} \ll \delta_l$, the fine splitting to leading order in α^2 is

$$\Delta E_{n,l} = 2\frac{\eta_{l-\frac{1}{2},l} - \eta_{l+\frac{1}{2},l}}{(n-\delta_l)^3}. \tag{17}$$

The quasiclassical momentum $p \equiv \sqrt{-Q}$ of the bound electron depending on energy $E < 0$ with orbital angular momentum $l > 0$, total angular momentum $j = l \pm \frac{1}{2}$, and taking into account the Langer shift $l(l+1) \to (l+\frac{1}{2})^2$ in the centrifugal barrier [15,16] is then given by

$$Q\,(r;j,l,E) = \frac{\left(l+\frac{1}{2}\right)^2}{r^2} + \widetilde{V}_{\rm mod}\,(r;j,l) - E. \tag{18}$$

For $l = 0$ the centrifugal barrier term and the spin-orbit potential are absent.

Considering high excitation energies $E < 0$ of the bound outermost electron, i.e., a principal quantum number $n \gg 1$, the respective positions of the turning points $r^{(\pm)}$ are given

approximately by

$$r^{(-)} = \frac{\left(l+\frac{1}{2}\right)^2}{1+\sqrt{1+\left(l+\frac{1}{2}\right)^2 E}} \quad \text{if } l \geqslant 3,$$
$$r^{(+)} \simeq \frac{1}{-E}\left[1+\sqrt{1+\left(l+\frac{1}{2}\right)^2 E}\right] \quad \text{if } l \geqslant 1, \tag{19}$$

where $0 < l \ll \frac{1}{\sqrt{-E}}$. Of course, for $l = 0$ only a single (large) turning point $r^{(+)} = \frac{2}{-E}$ exists due to the absence of the centrifugal barrier. However, the lower turning points $r^{(-)}$ are strongly modified for $l = 1,2$ compared to the pure Coulomb potential case, taking into account the core polarization. For $l = 1,2$ the relation $r^{(-)}(l) \simeq 0.02 \times r_c(l)$ holds; that is, $r^{(-)}(l=1) \simeq 0.034\,72$ and $r^{(-)}(l=2) \simeq 0.128\,27$ [2]. While the analytic formula for the lower turning points $r^{(-)}(l)$ in (19), being valid for $3 \leqslant l \ll n$, depends only weakly on the principal quantum number n, we find from numerical calculations with the potential (14) that this also applies for $l = 1,2$ and $n \geqslant 8$. Since the cutoff $r_{so}(l)$ in (15) is substantially above those values of the lower turning points $r^{(-)}(l)$, a quasiclassical calculation of the fine-split spectrum of the bound outermost electron is reliable.

For a chosen radial quantum number n_r, the associated eigenvalues $E = E_{n,j,l} < 0$ of the outermost electron moving in the potential (14) now follow from the WKB patching condition [17–19]:

$$\nu(j,l,E) \stackrel{!}{=} \begin{cases} n_r + 1 & \text{if } l = 0, \\ n_r + \frac{1}{2} & \text{if } l > 0, \end{cases} \tag{20}$$

where $\nu(j,l,E)$ denotes the action integral

$$\nu(j,l,E) = \frac{1}{\pi}\int_{r^{(-)}}^{r^{(+)}} \mathrm{d}r\sqrt{-Q(r;j,l,E)} = \frac{1}{2\pi}\oint \mathrm{d}r\, p(r;j,l,E). \tag{21}$$

Plotting the function $\nu(j,l,E)$ versus $\frac{1}{\sqrt{-E}}$ for $l = 0,1,2$ clearly reveals a linear dependence of the form $\nu(j,l,E) = \frac{1}{\sqrt{-E}} + c(j,l)$ (see Fig. 2).

According to [6], for $A,B,C,D \in \mathbb{R}$, with $A > 0$, $B > 0$, $C > 0$, and $|D| \ll C$, the following equality holds:

$$\frac{1}{2\pi}\oint \mathrm{d}r\sqrt{-A+\frac{2B}{r}-\frac{C}{r^2}+\frac{D}{r^3}} = \frac{B}{\sqrt{A}} - \sqrt{C} + \frac{BD}{2C\sqrt{C}}. \tag{22}$$

For a pure Coulomb potential $A \equiv -E$, $B \equiv 1$, $C \equiv (l+\frac{1}{2})^2$, and $D \equiv \alpha^2 g(j,l)$. The corresponding action integral then reads

$$\nu^{(\mathrm{C})}(j,l,E) = \begin{cases} \frac{1}{\sqrt{-E}} & \text{if } l = 0, \\ \frac{1}{\sqrt{-E}} - \left(l+\frac{1}{2}\right) + \frac{\alpha^2 g(j,l)}{2\left(l+\frac{1}{2}\right)^3} & \text{if } l > 0. \end{cases} \tag{23}$$

It is thus found from WKB theory that the quantum defect associated with the single-electron potential $\widetilde{V}_{\mathrm{mod}}(r;j,l)$ is

$$\Delta_{j,l} = \lim_{E\to 0^-}[\nu(j,l,E) - \nu^{(\mathrm{C})}(j,l,E)]. \tag{24}$$

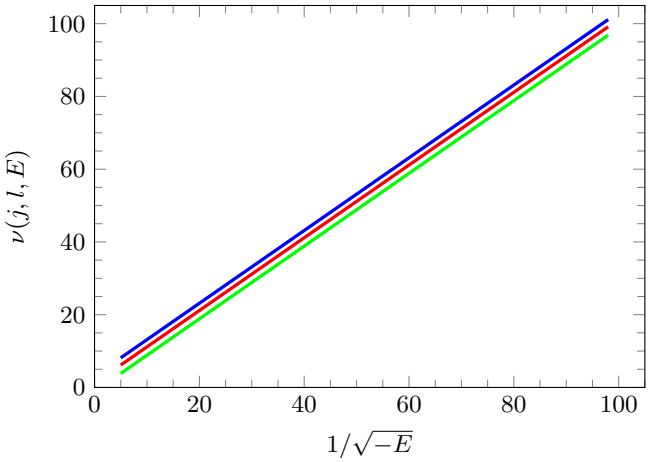

FIG. 2. (Color online) The action integral $\nu(j,l,E)$ associated with the effective single-electron potential $\widetilde{V}_{\mathrm{mod}}(r;j,l)$ vs scaled energy $\frac{1}{\sqrt{-E}}$ for $l = 0$ (blue line), $l = 1$ (red line), $l = 2$ (green line), all for $j = l + \frac{1}{2}$. The curves for $j = l - \frac{1}{2}$ differ only by a tiny shift proportional to α^2.

Ignoring spin-orbit coupling, i.e., for $\alpha = 0$, one has $\Delta_{j,l} \equiv \delta_l$, the standard quantum defect. For $l = 0$ the centrifugal barrier and the spin-orbit coupling term (6) are zero, so $\Delta_{j,l} \to \Delta_{\frac{1}{2},0} \equiv \delta_0$.

The dependence of the quasiclassical momentum $\sqrt{-Q(r;j,l,E)}$ on the scaled distance $\frac{r}{r_c(l)}$ is shown for $l = 0,1,2$ in Fig. 3. Clearly, it is the inner-core region $r^{(-)}(l) < r < r_c(l)$ that provides the main contribution to the quantum defect values. We find, for $l = 0,2$, that changing the fitting parameter $a_3(l)$ in (3) from its tabulated value in [5] according to the scaling prescription $a_3(l=0) \to 0.814 \times a_3(l=0)$ and $a_3(l=2) \to 0.914 \times a_3(l=2)$ leads to a slight downward

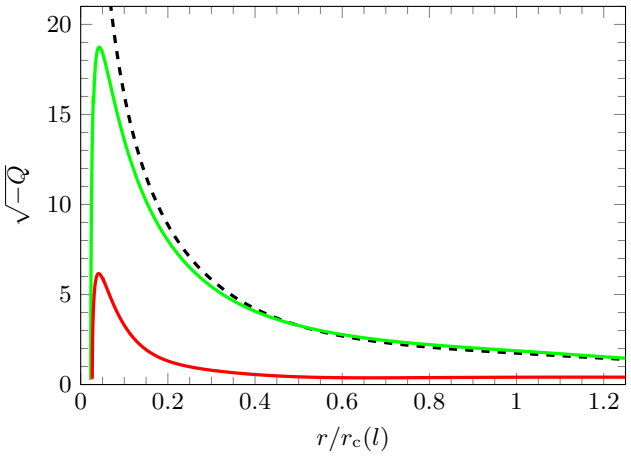

FIG. 3. (Color online) The quasiclassical momentum $\sqrt{-Q(r;j,l,E)}$ vs scaled distance $\frac{r}{r_c(l)}$ for $l = 0$ (dashed black), $l = 1$ (green), and $l = 2$ (red) for $E = E_{n,j,l}$, corresponding to principal quantum number $n = 57$ and $j = l + \frac{1}{2}$. The lower turning points $r^{(-)}(l)$ for the case of a pure Coulomb potential, for $l > 0$ all being greater than $0.6 \times r_c(l)$, are located well outside the core region. The main contribution to the quantum defect values in (24) thus originates from the inner-core region $r < r_c(l)$.

TABLE III. The values of quantum defect $\Delta_{j,l}$ associated with the Rydberg level $n = 57$ for $l = 0,1,2$.

Quantum defect $\Delta_{j,l}$	Expt. [8]	Expt. [10]	Theory [7]	Theory (this work)
$\Delta_{\frac{1}{2},0}$	3.1312419(10)	3.13125(2)	3.12791	3.13095
$\Delta_{\frac{1}{2},1}$	2.6549831(10)	NA	2.65795	2.65197
$\Delta_{\frac{3}{2},1}$	2.6417735(10)	NA	2.64399	2.63876
$\Delta_{\frac{1}{2},1} - \Delta_{\frac{3}{2},1}$	0.0132096(14)	NA	0.01396	0.01321
$\Delta_{\frac{3}{2},2}$	1.3478971(4)	1.34789(2)	1.35145	1.34851
$\Delta_{\frac{5}{2},2}$	1.3462733(3)	1.34626(2)	1.34628	1.34688
$\Delta_{\frac{3}{2},2} - \Delta_{\frac{5}{2},2}$	0.0016238(5)	0.00163(3)	0.00517	0.00163

constant shift of the WKB-quantum defect. As a result of this change, the calculated WKB-quantum defect $\Delta_{l\pm\frac{1}{2},l}$ then agrees well with the spectroscopic data (see Table III). Such a change of $a_3(l)$ does *not* affect the fine-splitting values $\Delta E_{n,l}$ though. We also find that the dependence of the fine splitting $\Delta E_{n,l}$ on the principal quantum number n is well described by (17) for all $n \geqslant 8$ (see Tables I and II).

In actual fact, for $r^{(+)} \gg r^{(-)}$, which is a criterion that is always met for high excitation energies $\sqrt{-E} \simeq 0$ of the outermost electron, the uniform Langer-WKB wave function $U^{(\mathrm{WKB})}_{n,j,l}(r)$ [19,20], with $r^{(+)}$ considered as the only turning point, describes the numerical solution $U_{n,j,l}(r)$ to the radial differential equation (8) under the influence of the effective modified single-electron potential (14) rather accurately [21]. Only very near to the second turning point $r^{(-)}$, at a distance smaller than $r_{\mathrm{so}}(l)$, does the Langer-WKB wave function $U^{(\mathrm{WKB})}_{n,j,l}(r)$ cease to be a good approximation to the numerical solution $U_{n,j,l}(r)$ of the radial Schrödinger equation (8) [21].

III. CONCLUSIONS

In this work we reported a significant discrepancy between experiment [8,10] and highly accurate variational calculations [7] of the spectrum of Rydberg states of ^{87}Rb on the energy scale of the fine splitting. We discussed that the usual *a posteriori* adding of the relativistic spin-orbit potential to the effective single-electron potential governing the outermost electron of alkali atoms is indeed inconsistent inside the inner atomic core region. In the absence of a full microscopic theory that lumps all many-body interactions together with the relativistic corrections into an effective single-electron potential in a consistent manner, we suggested a modified effective single-electron potential, cf. (14), that enables a correct description of the spectrum of Rydberg states on the fine-splitting scale in terms of a simple WKB-action integral for all principal quantum numbers $n \geqslant 8$. Modern precision spectroscopy of highly excited Rydberg states thus enables the probing of the multielectron correlation problem of the ionic core of alkali atoms. This is certainly a fascinating perspective for further experiments and theoretical studies.

ACKNOWLEDGMENTS

This work was financially supported by the EU FET-Open Xtrack Project HAIRS and the Carl Zeiss Stiftung Foundation.

[1] T. F. Gallagher, *Rydberg Atoms*, 1st ed. (Cambridge University Press, Cambridge, UK, 1994).
[2] We use scaled variables so that length is measured in units of the Bohr radius $a_B = \frac{\hbar^2}{m_e}\frac{4\pi\varepsilon_0}{|e|^2} \simeq 5.2918 \times 10^{-11}$ m and energy is measured in units of Rydberg, $\mathrm{Ry} = \frac{m_e|e|^4}{8\varepsilon_0^2 h^2} \simeq 13.605$ eV.
[3] M. Goeppert Mayer, Phys. Rev. **60**, 184 (1941).
[4] C. H. Greene and M. Aymar, Phys. Rev. A **44**, 1773 (1991).
[5] M. Marinescu, H. R. Sadeghpour, and A. Dalgarno, Phys. Rev. A **49**, 982 (1994).
[6] M. Born, *Vorlesungen über Atommechanik* (Springer, Berlin, 1925), §27, §28, and II. Anhang.
[7] M. Pawlak, N. Moiseyev, and H. R. Sadeghpour, Phys. Rev. A **89**, 042506 (2014).
[8] W. Li, I. Mourachko, M. W. Noel, and T. F. Gallagher, Phys. Rev. A **67**, 052502 (2003).
[9] A. K. Mohapatra, T. R. Jackson, and C. S. Adams, Phys. Rev. Lett. **98**, 113003 (2007).
[10] M. Mack, F. Karlewski, H. Hattermann, S. Höckh, F. Jessen, D. Cano, and J. Fortágh, Phys. Rev. A **83**, 052515 (2011).
[11] J. E. Sansonetti, J. Phys. Chem. Ref. Data **35**, 301 (2006).
[12] J. Schwinger, *Quantum Mechanics: Symbolism of Atomic Measurements*, 1st ed. (Springer, Berlin, 2001).
[13] H. A. Bethe and E. E. Salpeter, *Quantum Mechanics of One- and Two-Electron Atoms* (Springer, Berlin, 1957).
[14] C. Froese-Fischer, T. Brage, and P. Jönsson, *Computational Atomic Structure: An MCHF Approach* (IOP Physics, Bristol, 1997).
[15] R. E. Langer, Phys. Rev. **51**, 669 (1937).
[16] M. V. Berry and K. E. Mount, Rep. Prog. Phys. **35**, 315 (1972).
[17] A. B. Migdal, *Qualitative Methods in Quantum Theory* (Addison-Wesley, Reading, MA, 1977).
[18] B. M. Karnakov and V. P. Krainov, *WKB Approximation in Atomic Physics* (Springer, Berlin, 2013).
[19] C. M. Bender and S. A. Orszag, *Advanced Mathematical Methods for Scientists and Engineers* (McGraw-Hill, Singapore, 1978).
[20] R. E. Langer, Bull. Am. Math. Soc. **40**, 545 (1934).
[21] A. Sanayei and N. Schopohl (unpublished).

State-selective all-optical detection of Rydberg atoms

Florian Karlewski,[1,*] Markus Mack,[1] Jens Grimmel,[1] Nóra Sándor,[1,2,†] and József Fortágh[1,‡]

[1]*CQ Center for Collective Quantum Phenomena and their Applications, Physikalisches Institut, Eberhard-Karls-Universität Tübingen, Auf der Morgenstelle 14, D-72076 Tübingen, Germany*

[2]*Institute for Solid State Physics and Optics, Wigner Research Centre for Physics, Hungarian Academy of Sciences, H-1525 Budapest P.O. Box 49, Hungary*

(Received 13 February 2015; published 29 April 2015)

We present an all-optical protocol for detecting population in a selected Rydberg state of alkali-metal atoms. The detection scheme is based on the interaction of an ensemble of ultracold atoms with two laser pulses: one weak probe pulse which is resonant with the transition between the ground state and the first excited state, and a pulse with high intensity which couples the first excited state to the selected Rydberg state. We show that by monitoring the absorption signal of the probe laser over time, one can deduce the initial population of the Rydberg state. Furthermore, it is shown that—for suitable experimental conditions—the dynamical absorption curve contains information on the initial coherence between the ground state and the selected Rydberg state. We present the results of a proof-of-principle measurement performed on a cold gas of ^{87}Rb atoms. The method is expected to find application in quantum computing protocols based on Rydberg atoms.

DOI: 10.1103/PhysRevA.91.043422 PACS number(s): 32.80.Ee, 32.80.Qk, 32.80.Rm

I. INTRODUCTION

Rydberg atoms coupled to electromagnetic fields form a promising system for the physical realization of quantum information protocols [1] and quantum simulations [2]. In these protocols qubits are realized by a set of atomic states, which includes one or potentially more Rydberg levels. One requirement of these schemes is the ability to measure the Rydberg states' population in order to read out the results of the quantum operations. For accomplishing this task, most experiments with ultracold Rydberg gases use methods including field ionization and subsequent detection of electrons or ions on multichannel plates or channeltrons [3]. These techniques offer high sensitivity and —for carefully chosen experimental conditions [4,5]—selectivity among the Rydberg levels [6–8].

Selective field ionization (SFI) techniques are based on the fact that the ionization threshold is different for each atomic state, increasing from higher to lower lying levels. Hence, by slowly ramping up the electric field and monitoring the electrons or ions over time it is possible to deduce the initial populations in each level. However, the population of a lower lying Rydberg level cannot be probed without destroying the population of any higher lying Rydberg state. Therefore this method is not applicable in protocols which require independent probing of multiple Rydberg states [9]. Another inherent property of methods based on ionization is that the detected atoms are removed from the system and cannot be reused. Although this atomic loss is negligible in most cases [3], it might be a serious limitation in experiments working with only one or a few atoms [10].

One alternative to ionization detection methods is all-optical probing based on electromagnetically induced transparency (EIT) [11]. This approach has been successfully applied in order to nondestructively probe the Rydberg level structure in noninteracting [12,13] and weakly interacting [14] Rydberg gases, as well as in the presence of electric fields [15–19]. These experiments, however, did not access the population of the Rydberg state. On the other hand, an EIT-based scheme for the optical detection of the Rydberg population [20,21] has been proposed and demonstrated in dense atomic clouds where the Rydberg blockade allows the spatially resolved detection of Rydberg atoms.

Here we propose an all-optical scheme for detecting the population in a selected Rydberg state in dilute gases. By using a series of laser pulses in EIT configuration this technique also allows for distinction between coherent superpositions and statistical mixtures of the ground and Rydberg states of the atoms. Since this scheme is based on time-resolved observation of the optical response of individual atoms it may, in principle, be used down to the single atom level. Our method is state selective and applicable for testing the population not only in the highest Rydberg level of interest (cf. SFI) but any lower lying or intermediate Rydberg state.

We present our theoretical model along with numerical simulations and demonstrate the scheme in a proof-of-principle experiment with a dilute gas of ^{87}Rb atoms showing the detection of the population in an initially prepared Rydberg state. Our analysis includes characteristic effects of Rydberg experiments such as blackbody-induced depopulation [22,23], superradiance [24], and dipole-dipole interaction [25].

II. THEORETICAL MODEL

Let us consider a cold atomic gas interacting with two laser pulses in an EIT-like configuration [11]. One of the pulses, resonant with the atomic transition between the ground state $|1\rangle$ and the first excited state $|2\rangle$, is a weak probe pulse well below the saturation intensity, while the other one is a relatively strong coupling pulse which is resonant with the atomic transition between the first excited state $|2\rangle$ and a selected (arbitrary) Rydberg $nS_{1/2}$ state $|3\rangle$ (see Fig. 1). A

*florian.karlewski@uni-tuebingen.de

†Present address: IPCMS (UMR 7504) and ISIS (UMR 7006), Université de Strasbourg and CNRS, Strasbourg, France.

‡fortagh@uni-tuebingen.de

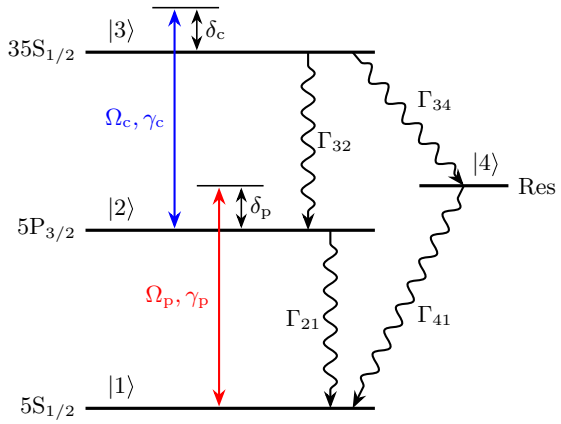

FIG. 1. (Color online) Illustration of the atom-laser interaction as used for the model of time-resolved EIT. States $|1\rangle$, $|2\rangle$, and $|3\rangle$ denote the ground state, the first excited state, and a Rydberg state of the atom, respectively. In our experimental setup, these states correspond to the $5S_{1/2}(F=2)$, $5P_{3/2}(F=3)$, and $35S_{1/2}(F=2)$ states of ^{87}Rb. The atomic transition $|1\rangle \leftrightarrow |2\rangle$ is driven by a weak probe laser with the Rabi frequency Ω_p (red), while the transition $|2\rangle \leftrightarrow |3\rangle$ is driven by a stronger coupling laser with the Rabi frequency Ω_c (blue). γ_p and γ_c denote coherence decay terms. δ_p and δ_c are the detunings of each laser to the corresponding atomic resonance. The radiative decay from the selected Rydberg state $|3\rangle$ to the neighboring states is accounted for by including a reservoir state $|4\rangle$. Γ_{ij} denote the respective incoherent decays, consisting of spontaneous emission as well as transitions induced by blackbody radiation.

single "reservoir" state $|4\rangle$ is used to model the neighboring Rydberg states [14].

We use a semiclassical approach for describing the dynamics of the system and the laser pulses are taken into account through their classical electric field. The atomic gas is modeled by a motionless ensemble of atoms. The state of the atoms is described by the density matrix $\rho = \sum_{i,j=1}^{4} \rho_{i,j} |i\rangle \langle j|$, where the states $|2\rangle$ and $|3\rangle$ rotate with the atomic transition frequencies ω_{21} and ω_{23}, respectively.

The time evolution of $\rho(t)$ is described by the master equation

$$i\hbar\dot{\rho} = [\mathcal{H}, \rho] + \mathcal{U}[\rho]. \tag{1}$$

Here the Hamiltonian $\mathcal{H}$ accounts for the interactions between the atoms and the laser pulses. The effects due to interatomic interactions are considered through dynamic effective rates in $\mathcal{U}[\rho]$ along with radiative losses occurring in the system. The Hamiltonian $\mathcal{H}$ is written as

$$\begin{aligned}\mathcal{H} = &-\frac{\hbar}{2}(\Omega_p |2\rangle \langle 1| + \Omega_c |3\rangle \langle 2| + \text{H.c.}) \\ &- \hbar(\delta_p |2\rangle \langle 2| + \delta_c |3\rangle \langle 3|),\end{aligned} \tag{2}$$

where $\Omega_p = (E_p d_{12})/\hbar$ and $\Omega_c = (E_c d_{23})/\hbar$ are the Rabi frequencies of the probe and coupling lasers, with E_p and E_c being the electric fields, and d_{12} and d_{23} the dipole matrix elements of the corresponding transitions, whereas δ_p and δ_c are the detunings of the probe and coupling laser from the corresponding transitions, respectively (see Fig. 1). Although we consider a situation where both the coupling and the probe laser are resonant with the atomic transitions they drive (i.e., $\delta_p = \delta_c = 0$), by including these detunings one can account for potentially uncompensated electric and/or magnetic fields in a specific experimental realization. The operator $\mathcal{U}$ which governs the non-Hamiltonian part of the dynamics reads as

$$\begin{aligned}\mathcal{U}[\rho] = &\frac{\Gamma_{32}}{2}(2\sigma_{13}\rho\sigma_{31} - \sigma_{33}\rho - \rho\sigma_{33}) \\ &+ \frac{\Gamma_{21}}{2}(2\sigma_{12}\rho\sigma_{21} - \sigma_{22}\rho - \rho\sigma_{22}) \\ &+ \frac{\Gamma_{34}}{2}(2\sigma_{43}\rho\sigma_{34} - \sigma_{33}\rho - \rho\sigma_{33}) \\ &+ \frac{\Gamma_{41}}{2}(2\sigma_{14}\rho\sigma_{41} - \sigma_{44}\rho - \rho\sigma_{44}) \\ &+ \frac{\gamma_p}{2}(2\sigma_{11}\rho\sigma_{11} - \rho_{11}\sigma - \rho\sigma_{11}) \\ &+ \frac{\gamma_c}{2}(2\sigma_{33}\rho\sigma_{33} - \rho_{33}\sigma - \rho\sigma_{33}),\end{aligned} \tag{3}$$

where $\sigma_{kj} = |k\rangle \langle j|$ are the atomic projection operators ($k, j \in \{1,2,3,4\}$).

There are multiple sources of nonunitary dynamics in the system. One of them is the spontaneous emission from the first excited state $|2\rangle$ and the Rydberg state $|3\rangle$ which we take into account by introducing radiative decay rates Γ_{21} and Γ_{32}. Another source, if present, is a depopulation of the Rydberg state $|3\rangle$ towards the neighboring Rydberg states. The depopulation may occur due to several phenomena depending on the actual realization of the system, such as amplified spontaneous emission and/or superradiance [24,26] as well as induced emission and absorption due to the blackbody radiation of the environment [22,23]. Following [26], we take these effects into account by modifying the third term in Eq. (3) to the dynamic effective decay rate

$$\tilde{\Gamma}_{34}(t) = \Gamma_{34,\text{sp}}[\rho_{44}(t) p_{\text{sup}} + 1] + \Gamma_{34,\text{bb}}, \tag{4}$$

with p_{sup} a superradiance parameter, and $\Gamma_{34,\text{sp}}$ and $\Gamma_{34,\text{bb}}$ the effective decay rates caused by spontaneous emission and blackbody radiation, respectively. In our model we assume that the entire population eventually ends up in the ground state $|1\rangle$. This assumption is valid provided the ionization from all involved states is negligible.

The above-mentioned phenomena cause population transfer between the atomic states. In contrast, there is a group of processes which do not result in a significant energy decay in the system but leads to a relevant coherence loss. One such process is the phase noise of the driving lasers, which is included into the model through the coherence decay rates γ_p and γ_c. Due to the redistribution of population from $|3\rangle$ to $|4\rangle$, atoms in Rydberg nP_j states are present in the cloud at various distances. As observed by [25], the dipole-dipole interaction with these nP_j state atoms results in an inhomogeneous broadening of the Rydberg $nS_{1/2}$ state. We take this into account by adding an effective dephasing term in Eq. (3) to γ_c,

$$\tilde{\gamma}_c(t) = \gamma_c + \gamma_{3,\text{dd}}\rho_{44}(t). \tag{5}$$

The optical response of the cloud under the effect of the two laser pulses is given by the macroscopic polarization $\vec{P} = \mathcal{N}\,\text{Tr}[\rho\vec{d}]$ where $\vec{d} = \sum_{i\neq j}(d_{ij} |i\rangle \langle j| + \text{H.c.})$ is the atomic dipole operator. The absorption α of the probe laser is then

given by the imaginary part of the electric susceptibility χ,

$$\alpha(t) = \mathrm{Im}[\chi(t)] = \frac{\mathcal{N} d_{12}^2}{\epsilon_0 \hbar \Omega_\mathrm{p}} \mathrm{Im}[\rho_{21}(t)], \tag{6}$$

where $\mathcal{N}$ is the atom density of the cloud. Note that here we make the approximation that the cloud is homogeneously irradiated and the propagation effects of the laser pulses can be neglected. The time-dependent absorption signal is thus given by the master equation, which, using the operators given in Eqs. (2) and (3), reads as

$$\dot{\rho}_{11} = \frac{i}{2}(\Omega_\mathrm{p}^* \rho_{21} - \Omega_\mathrm{p} \rho_{12}) + \Gamma_{21} \rho_{22} + \Gamma_{41} \rho_{44}, \tag{7a}$$

$$\dot{\rho}_{22} = \frac{i}{2}(\Omega_\mathrm{p} \rho_{12} - \Omega_\mathrm{p}^* \rho_{21} - \Omega_\mathrm{c} \rho_{23} + \Omega_\mathrm{c}^* \rho_{32}) - \Gamma_{21} \rho_{22} + \Gamma_{32} \rho_{33}, \tag{7b}$$

$$\dot{\rho}_{33} = \frac{i}{2}(\Omega_\mathrm{c} \rho_{23} - \Omega_\mathrm{c}^* \rho_{32}) - (\Gamma_{32} + \tilde{\Gamma}_{34}) \rho_{33}, \tag{7c}$$

$$\dot{\rho}_{21} = \frac{i}{2}[\Omega_\mathrm{c}^* \rho_{31} - \Omega_\mathrm{p} (\rho_{22} - \rho_{11}) + 2\delta_\mathrm{p} \rho_{21}] - \frac{1}{2}(\Gamma_{21} + \gamma_\mathrm{p}) \rho_{21}, \tag{7d}$$

$$\dot{\rho}_{31} = \frac{i}{2}[\Omega_\mathrm{c} \rho_{21} - \Omega_\mathrm{p} \rho_{32} + 2(\delta_\mathrm{p} + \delta_\mathrm{c}) \rho_{31}] - \frac{1}{2}(\gamma_\mathrm{p} + \tilde{\gamma}_\mathrm{c} + \Gamma_{32} + \tilde{\Gamma}_{34}) \rho_{31}, \tag{7e}$$

$$\dot{\rho}_{32} = \frac{i}{2}[-\Omega_\mathrm{p}^* \rho_{31} - \Omega_\mathrm{c} (\rho_{33} - \rho_{22}) - 2\delta_\mathrm{c} \rho_{32}] - \frac{1}{2}(\tilde{\gamma}_\mathrm{c} + \Gamma_{21} + \Gamma_{32}) \rho_{32}, \tag{7f}$$

$$\dot{\rho}_{44} = \tilde{\Gamma}_{34} \rho_{33} - \Gamma_{41} \rho_{44}, \tag{7g}$$

$$\dot{\rho}_{41} = \frac{i}{2}(-\Omega_\mathrm{p} \rho_{42} + 2\delta_\mathrm{p} \rho_{41}) - \frac{1}{2}(\Gamma_{41} + \gamma_\mathrm{p}) \rho_{41}, \tag{7h}$$

$$\dot{\rho}_{42} = -\frac{i}{2}(\Omega_\mathrm{p}^* \rho_{41} + \Omega_\mathrm{c} \rho_{43}) - \frac{1}{2}(\Gamma_{21} + \Gamma_{41}) \rho_{42}, \tag{7i}$$

$$\dot{\rho}_{43} = \frac{i}{2}(\Omega_\mathrm{c}^* \rho_{42} + 2\delta_\mathrm{c} \rho_{43}) - \frac{1}{2}(\Gamma_{32} + \tilde{\Gamma}_{34} + \Gamma_{41} + \tilde{\gamma}_\mathrm{c}). \tag{7j}$$

When there is no coupling to the Rydberg state ($\Omega_\mathrm{c} = 0$), an analytical steady state solution for α can be obtained, which will be used for normalization:

$$\alpha_0 = \frac{\mathcal{N} d_{12}^2}{\epsilon_0 \hbar} \Gamma_{21} (\gamma_\mathrm{p} + \Gamma_{21}) \times \left[\gamma_\mathrm{p}^2 \Gamma_{21} + 2\gamma_\mathrm{p} \left(\Omega_\mathrm{p}^2 + \Gamma_{21}^2\right) + \Gamma_{21} \left(4\delta_\mathrm{p}^2 + 2\Omega_\mathrm{p}^2 + \Gamma_{21}^2\right)\right]^{-1}. \tag{8}$$

III. DETECTION OF THE RYDBERG POPULATION: RESULTS OF THE NUMERICAL SIMULATION

We numerically solve the equation system (7) with the pulse sequence of the lasers given by $\Omega_\mathrm{p}(t)$ and $\Omega_\mathrm{c}(t)$ (see the sequence A, B, C in Fig. 2). The solution provides a description of the population dynamics while the atom is being probed by the weak laser on the $|1\rangle \leftrightarrow |2\rangle$ transition along with a time-dependent coupling between states $|2\rangle$ and $|3\rangle$. Furthermore, through Eq. (6) it describes the absorption of the probe laser, which we give relative to α_0 [see Eq. (8)]:

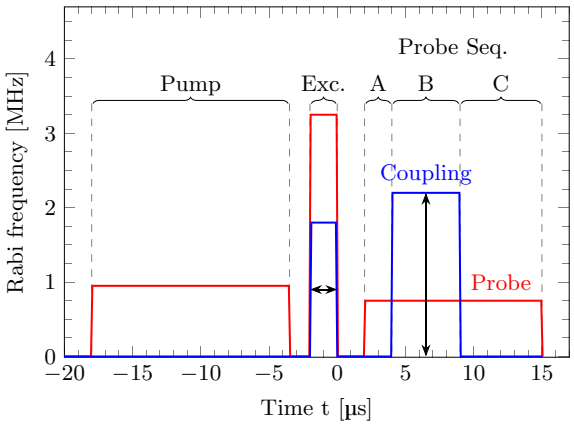

FIG. 2. (Color online) Pulse sequence for the coupling (blue) and probe (red) lasers. At $t = 0$ a fraction of the atomic population is prepared in the Rydberg state. In the simulations this fraction is an input value, while in the experiment it is determined by the length of the excitation pulse (Exc.). Before this, an optical pumping pulse (Pump) is used to pump the atoms to the correct polarization. The time evolution of the optical density is monitored after the excitation pulse with the probe laser (A, B, C). The coupling laser is added in time interval B (EIT pulse). The Rabi frequencies are taken from the experimental values in Sec. IV.

$$\alpha_\mathrm{rel}(t) = \frac{\alpha(t)}{\alpha_0}. \tag{9}$$

In Fig. 3 we show results for the cases where the entire population is initially (a) in the ground state [$\rho_0 \equiv \rho(t = 0) = |1\rangle\langle 1|$] or (b) in the selected Rydberg state ($\rho_0 = |3\rangle\langle 3|$). In (c) the population is split between the Rydberg state and the reservoir state ($\rho_0 = 0.7\,|3\rangle\langle 3| + 0.3\,|4\rangle\langle 4|$).

Following the pulse sequence, the time evolution of the system can be separated into three major parts. When the atoms are initially prepared in the ground state, only small changes in the populations are visible [see Fig. 3(a)]. However, the reasons for these changes are not the same in the different parts of the time evolution. In part A, when the atoms are only irradiated by the relatively weak probe laser ($\Omega_\mathrm{p} \ll \Gamma_{21}$), a small fraction of the population is transferred to the first excited state $|2\rangle$ by the absorbed light. In part B, the population transfer to state $|2\rangle$ is prevented by the strong coupling laser applied on the transition between states $|2\rangle$ and $|3\rangle$ and the absorption is reduced, which is the well-known effect of EIT. The time scale for the transparency to build up is defined by the Rabi frequency Ω_c of the coupling laser. If the requirement $\Omega_\mathrm{p} \ll \Omega_\mathrm{c}$ is not fulfilled, the transparency is only partial. In this case, the two laser fields cause two-photon transitions to state $|3\rangle$, and the absorption of the probe pulse is nonzero. This absorption level (in the case of $\delta_\mathrm{p} = \delta_\mathrm{c} = 0$) depends on $\Omega_\mathrm{p}/\Omega_\mathrm{c}$ and the decoherences γ_p and γ_c. A consequence of this effect is that different initial populations of Rydberg states cause a different absorption level in the equilibrium of part B

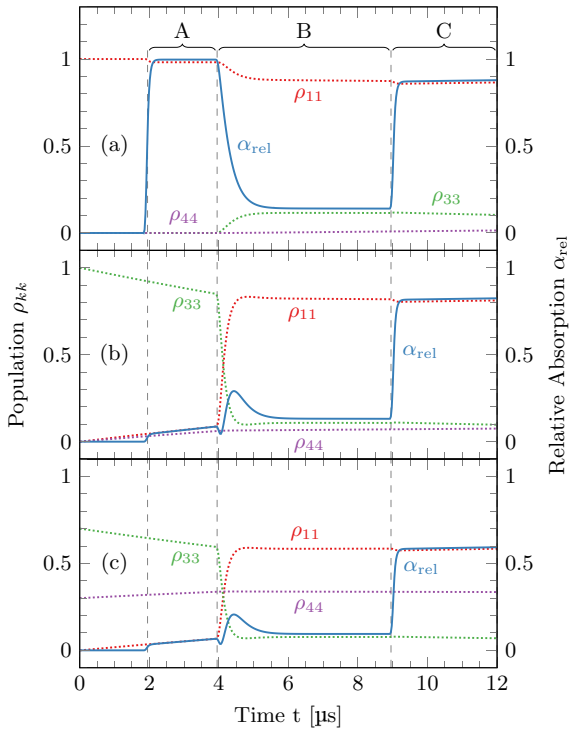

FIG. 3. (Color online) Dynamics of the populations $\rho_{kk}(t)$ of the atomic states (dotted lines) and the relative absorption $\alpha_{\rm rel}(t)$ (solid lines) of the probe laser induced by the pulse sequence A, B, C (see Fig. 2) for atoms initially prepared in the ground state (a), the selected Rydberg state (b), and the reservoir state (c). Since the population ρ_{22} is almost zero at all times, except for a transient population in the first 100 ns of B, it is not shown here.

due to the dependence of $\gamma_{\rm c}$ on ρ_{44}. In part C, where the atom cloud is again only irradiated by the weak probe laser, the process is very similar to what happens in part A with the exception that there is a small fraction of population in state $|3\rangle$. Consequently, the absorption level of the probe laser is smaller, because atoms are missing from the ground state.

In the case of initial population in the selected Rydberg state $|3\rangle$, the dynamics of the system only differ in parts A and B, provided B is long enough to reach steady state EIT. In part A, the absorption of the probe laser is close to zero, and slowly increases while a small fraction of the population decays from the Rydberg state $|3\rangle$. Since the lifetime of the Rydberg states is much longer than 10 μs, the amount of population transferred by spontaneous decay is small although not negligible on the microsecond time scale of the pulse sequence. At the beginning of part B the population in the selected Rydberg state is transferred to the ground state $|1\rangle$ through a resonant transfer from state $|3\rangle$ to $|2\rangle$ induced by the coupling laser with Rabi frequency $\Omega_{\rm c}$ and the consecutive spontaneous emission from $|2\rangle$ to $|1\rangle$. For $\Omega_{\rm c} < \Gamma_{21}$, this process results in only a small increase in ρ_{22}, because a half Rabi cycle induced by $\Omega_{\rm c}$ between states $|2\rangle$ and $|3\rangle$ would take longer than the lifetime of state $|2\rangle$ [see Fig. 3(b)]. Hence, assuming the initial population is either in the ground state $|1\rangle$ or the selected Rydberg state $|3\rangle$, we can determine the fractions by monitoring the absorption of the probe laser in part A of the time evolution. If there is a way to ensure that all the population missing from the ground state $|1\rangle$ is in the selected Rydberg state $|3\rangle$, then this is indeed sufficient. However, if the probability that a fraction of the population is in another state (for example, the interaction scheme to be realized contains more than one Rydberg state), the absorption level in part A of the time evolution is not enough in itself to give information about the population of the selected Rydberg state $|3\rangle$.

As illustrated in Figs. 3(b) and 3(c), the absorption of the probe laser in part A is the same for different initial states of the atoms as long as the population in the ground state is the same. In contrast, the dynamics and the equilibrium become significantly different in part B. Since only the population in the selected Rydberg state is transferred back to the ground state by the coupling field, the absorption level in part C also changes with the initial population in $|3\rangle$.

Another result of the simulations is the possibility to obtain information on the initial coherence of the system. The time evolution of the relative absorption in the beginning of part B for three different initial preparations of the atoms is shown in Fig. 4. These initial preparations consist of the same fraction of population in the ground state $|1\rangle$ and the selected Rydberg state $|3\rangle$, but the coherence between these two states is different. One of the initial preparations is the mixed state $\rho_{\rm m}(t=0) = \frac{1}{2}(|1\rangle\langle 1| + |3\rangle\langle 3|)$, while the other two preparations are $\rho_{\pm}(t=0) = \frac{1}{4}(|1\rangle \pm |3\rangle)(\langle 1| \pm \langle 3|)$. Comparing numerical calculations for these three cases, we find significant changes in the beginning of part B, where the EIT did not yet reach equilibrium. The absorption level during the rest of the pulse sequence is not sensitive to the initial coherence. If the Rabi frequency $\Omega_{\rm c}$ of the coupling laser is on the order of Γ_{23} or higher, oscillations of the absorption signal can be observed.

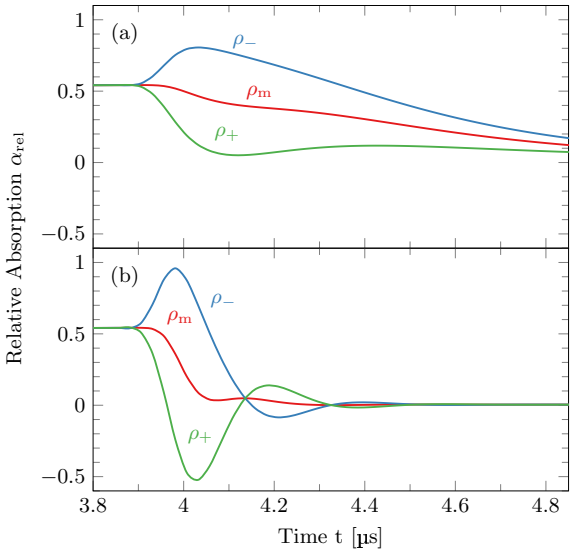

FIG. 4. (Color online) Numerically calculated relative absorption $\alpha_{\rm rel}$ of the probe laser in the beginning of part B for atoms prepared in states $\rho_{\rm m}(t=0) = \frac{1}{2}(|1\rangle\langle 1| + |3\rangle\langle 3|)$ and $\rho_{\pm}(t=0) = \frac{1}{4}(|1\rangle \pm |3\rangle)(\langle 1| \pm \langle 3|)$. The parameters used for the calculation are the same as for Fig. 3 with $\Omega_{\rm c} < \Gamma_{21}$ in (a) and $\Omega_{\rm c} \approx \Gamma_{21}$ in (b). This distinct signature of coherent states is expected to be experimentally observable and even more pronounced if $\Omega_{\rm c}$ is larger.

IV. EXPERIMENTAL SETUP

For demonstrating the detection of Rydberg population with time-resolved EIT, we have conducted an experiment on a cloud of $\approx 2 \times 10^7$ ^{87}Rb atoms at a temperature of ≈ 150 μK. In this experiment the atoms are trapped in a magneto-optical trap, loaded to a magnetic quadrupole trap and then released. The time-resolved measurements are started after 3 ms of time of flight, in order to ensure that all magnetic fields have fully decayed while the effects of atomic motion are still negligible. The measurements are performed within 30 μs (excitation pulse and probe sequence, cf. Fig. 2). The density and optical density at the center of the cloud, measured by absorption imaging, are 5×10^9 cm^{-3} and 1.7, respectively.

The transitions from the ground state $|5S_{1/2}, F = 2\rangle$ to the first excited state $|5P_{3/2}, F = 3\rangle$ and from there to the selected Rydberg state $|35S_{1/2}\rangle$ are driven by two lasers with wavelengths of $\approx$780 nm (red, probe) and $\approx$480 nm (blue, coupling), respectively (see Fig. 1). Additionally, we use a repumper to pump atoms from $|5S_{1/2}, F = 1\rangle$ back to $|5S_{1/2}, F = 2\rangle$ via $|5P_{3/2}, F = 2\rangle$ during the whole pulse sequence. The frequencies of both lasers used in the experiment are referenced to a frequency comb and controlled with slow servo loops (<100 Hz bandwidth). The linewidths of both lasers are narrowed to less than $2\pi \times 20$ kHz with fast locks (>1 MHz bandwidth) to scanning Fabry-Pérot interferometers. As the Fabry-Pérot cavities are sensitive to acoustic noise, the effective linewidth for the experiment can be larger. The red and the blue lasers are aligned in a counterpropagating configuration (see Fig. 5). We use an acousto-optic modulator (AOM) in each beam to create the intensity envelopes of the pulses. The switching time of the AOMs is 50 ns (20%–80% light intensity). The time-dependent intensity of the red laser (probe signal) is measured with an avalanche photodetector (Thorlabs APD120A/M) and recorded with a digital oscilloscope. The time resolution of the setup is 20 ns.

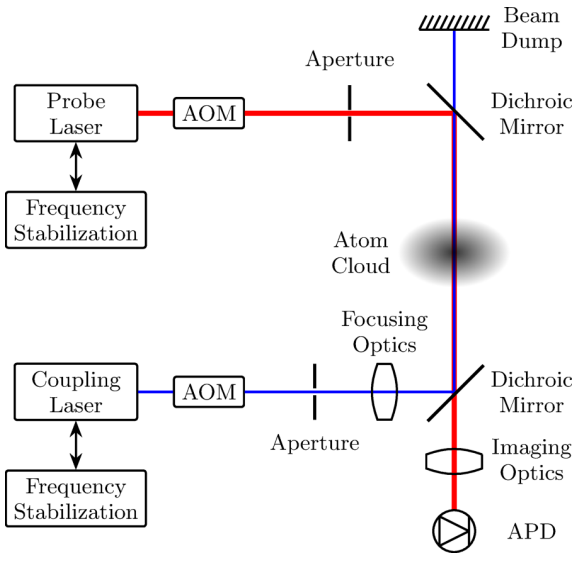

FIG. 5. (Color online) Experimental setup for time-resolved EIT measurements. The counterpropagating coupling (blue) and probe (red) beams are superimposed on the atom cloud and separated with dichroic mirrors. The transmission of the probe laser is detected by an avalanche photo diode (APD). The intensities of the lasers are controlled with acousto-optic modulators (AOM). Both laser frequencies are stabilized using a frequency comb.

As shown in Fig. 2, our measurement consists of three main parts. First we put all the atomic population into the Zeeman-sublevel of the ground state matching the polarization of the red laser by optically pumping for 14.5 μs. This pulse is also long enough that any transient effects due to the switching of the AOM wear off before the next pulse. Next, we prepare the initial state of the atomic cloud with an excitation pulse. We always apply the red laser for 2 μs with a Rabi frequency of $2\pi \times 3.3$ MHz. If we want no population to be transferred to the Rydberg state, the blue laser remains switched off and due to the very short lifetime of the first excited state, practically the entire population remains in the ground state. Applying the blue laser with a Rabi frequency of $2\pi \times 1.8$ MHz for up to 2 μs causes a fraction of the population to be transferred to the Rydberg state, with the most atoms being excited in the case of the full 2 μs pulse. Due to the high Rabi frequency of the red laser there is no coherent excitation of Rydberg atoms. In the third part (probe sequence in Fig. 2), we use the red laser at a low intensity as the probe laser during time intervals A, B, and C together with the blue laser as the coupling laser during time interval B (EIT pulse).

As a reference, we always add one experimental cycle without atoms in order to measure the intensity $I_{\mathrm{ref}}(t)$ of the red laser with the photodetector and another one with atoms but no excitation pulse and no coupling pulse to normalize the data later on. The parameters are then varied from cycle to cycle and the transmitted intensity $I_{\mathrm{T}}(t)$ of the probe light after passing through the cloud is measured. The experiment is repeated several times for each set of parameters to reduce photodiode noise. The optical density (OD) is calculated as follows:

$$\mathrm{OD}(t) = -\ln\left(\frac{I_{\mathrm{T}}(t)}{I_{\mathrm{ref}}(t)}\right). \tag{10}$$

The resulting OD datasets are then normalized by dividing them by the OD dataset that had no excitation pulse and no EIT pulse [$\mathrm{OD}_0(t)$]:

$$\mathrm{OD}_{\mathrm{rel}}(t) = \frac{\mathrm{OD}(t)}{\mathrm{OD}_0(t)} \hat{=} \frac{\alpha(t)}{\alpha_0}. \tag{11}$$

This relative optical density $\mathrm{OD}_{\mathrm{rel}}$ is comparable to the relative absorption $\alpha(t)/\alpha_0$ that is calculated in the numerical simulation. To reduce the effect of the acoustic noise on our Fabry-Pérot cavities, we selected the 30 datasets where the mean transparency in the EIT pulse between 7 and 9 μs was maximal. We observe that in all measurements the relative optical density eventually returns to the level before the excitation pulse, ensuring that ionization effects are negligible.

In general this scheme is applicable in situations where the optical density can be precisely measured. The resolution is limited by technical noise from the photodiode and the digital resolution of the subsequent data acquisition system. For low optical densities it is necessary to detect not only the absorption of the atoms, but to resolve the EIT signal as well. At high optical densities the constant resolution of the intensity measurement additionally leads to a lower

resolution of the optical density due to the logarithmic scaling in Eq. (10). For sufficient averaging, we estimate the presented scheme to be applicable in the range of optical densities between ≈0.1 and ≈4. In principal, the optical density can be lowered by detuning the probe laser while maintaining the two-photon resonance for the EIT condition, which on the other hand decreases the contrast for the EIT signal and therefore only allows for a limited extension of the range.

V. DETECTION OF THE INITIAL POPULATION: EXPERIMENTAL RESULTS

We demonstrate the optical detection of population for three different initial Rydberg excitation pulses. The experimental results for the optical density are shown in Fig. 6. In order to compare these results to the model we calculate values for the decay rates matching the chosen combination of states in our experiment (see Fig. 1). We calculate the spontaneous emission rates using the wave functions calculated in [19]. Γ_{32} is approximated by summing the spontaneous decay rates from $|35S_{1/2}\rangle$ to all nP_j states, which results in

$$\Gamma_{32} = \sum_{n>5} \Gamma_{\mathrm{sp},35S\to n\mathrm{P}} = 2\pi \times 3.9\ \mathrm{kHz}. \tag{12}$$

The main contribution comes from $|5P_{3/2}\rangle$ ($\Gamma_{\mathrm{sp},35S\to 5P} = 2\pi \times 1.2$ kHz) and other low-lying, fast-decaying states. The spontaneous decay rate $\Gamma_{34,\mathrm{sp}}$ is given by the rate $\Gamma_{\mathrm{sp},35S\to 34P} = 2\pi \times 16.8$ Hz. Here we take only the strongest superradiant transition into account. The transition rate $\Gamma_{34,\mathrm{bb}}$ is approximated by a sum over all transition rates induced by blackbody radiation from $|35S_{1/2}\rangle$ to all nP_j states

$$\Gamma_{34,\mathrm{bb}} = \sum_{n>5} \Gamma_{\mathrm{bb},35S\to nP} = 2\pi \times 2.7\ \mathrm{kHz}, \tag{13}$$

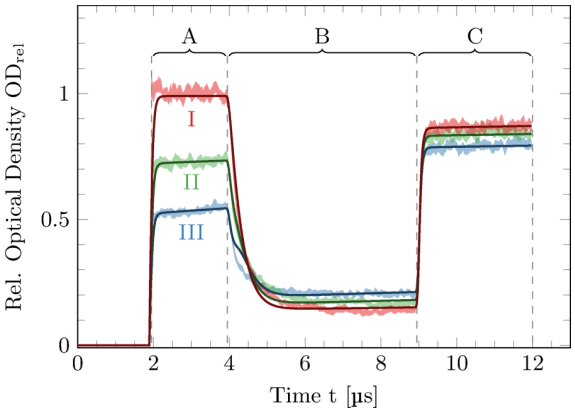

FIG. 6. (Color online) Measured optical density for the dynamics during the probe sequence. The shaded areas are 95% confidence intervals for the relative optical densities $\mathrm{OD}_{\mathrm{rel}}(t)$ obtained from the measurements by applying Eqs. (10) and (11) for three durations of the excitation pulse (0 μs for I, 0.5 μs for II, and 2 μs for III). Solid lines represent fit results for the simulated relative absorption $\alpha(t)/\alpha_0$. The reversed order of the absorption signals in part B can be explained by dipole-dipole interactions.

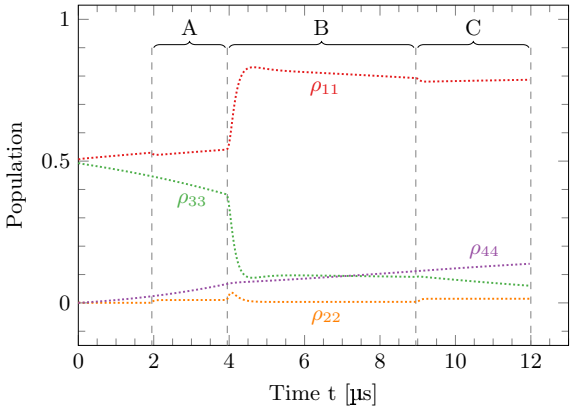

FIG. 7. (Color online) Dynamics of the population of the four states ($\rho_{11} \mathrel{\hat{=}} 5S_{1/2}$, $\rho_{22} \mathrel{\hat{=}} 5P_{3/2}$, $\rho_{33} \mathrel{\hat{=}} 35S_{1/2}$, $\rho_{44} \mathrel{\hat{=}}$ Reservoir) retrieved from the fit to the dataset with high excitation (see Fig. 6). The colors match those of the states in Fig. 3. The population of the Rydberg state ($35S_{1/2}$) starts to decay immediately after excitation at $t = 0$.

in which the rates $\Gamma_{\mathrm{bb},35S\to nP}$ are calculated as in [22,23]. The main contribution to $\Gamma_{34,\mathrm{bb}}$ comes from neighboring Rydberg states. For the transitions induced by blackbody radiation a temperature of 300 K is assumed. The preceding approximations for the decay rates ensure that the total decay out of the state $|35S_{1/2}\rangle$ is modeled correctly. Similar to the calculation of Γ_{32} we obtain

$$\Gamma_{41} = \sum_{n>5} \Gamma_{\mathrm{sp},34P\to nS} = 2\pi \times 0.8\ \mathrm{kHz}. \tag{14}$$

The Rabi frequencies of the two lasers $\Omega_{\mathrm{p}} = 2\pi \times 0.83$ MHz and $\Omega_{\mathrm{c}} = 2\pi \times 2.10$ MHz and the coherence decay $\gamma_{\mathrm{c}} = 2\pi \times 112$ kHz are fitted to the dataset without Rydberg excitation (see curve "I" in Fig. 6). The Rabi frequencies are consistent with estimates based on beam power and geometry. The noise γ_{c} is mainly caused by the acoustic noise on the Fabry-Pérot cavities. As the fit is only sensitive to $\gamma_{\mathrm{p}} + \gamma_{\mathrm{c}}$ and not to the single values, we choose $\gamma_{\mathrm{p}} = 2\pi \times 20$ kHz.

An analysis of the datasets with the same conditions, but with Rydberg excitation, allows us to fit the fraction of atoms excited to a Rydberg state [0.494(8) and 0.284(10)] within interval A, where only the red laser is on. The superradiance parameter $p_{\mathrm{sup}} = 7.9(8) \times 10^3$ is fitted to parts B and C and the dipole-dipole interaction parameter $\gamma_{3,\mathrm{dd}}$ is adjusted in part B. The former scales with the absolute atom number, while the latter scales with the atomic density. From the model one can now derive the time-resolved populations of the participating states as can be seen in Fig. 7. The accuracy of these populations is within ±0.01 compared with values calculated using a variation method.

VI. CONCLUSION

We have demonstrated the all-optical detection of Rydberg population in a dilute gas, which is an alternative to the methods based on field ionization. Our results show that Rydberg population fractions can be measured with an accuracy of 0.01. By comparing the dynamics of the measured optical densities to our numerical simulations we have quantified the

decoherence effects occurring in the system, namely, blackbody radiation induced transitions, superradiant decay, and inhomogeneous broadening due to dipole-dipole interactions.

From our simulations we conclude that the detection scheme can also be used to obtain information on the coherence between the ground state and the Rydberg state. The numerical results predict that future studies using a coherent excitation method and experimental parameters similar to our experiment will be able to detect the initial and time-dependent coherence.

ACKNOWLEDGMENTS

The authors thank Daniel Cano and Florian Jessen for the design and setup of the experimental chamber and Claus Zimmermann for valuable discussions. This work was financially supported by the FET-Open Xtrack Project HAIRS and the Carl Zeiss Stiftung. N.S. acknowledges financial support from the framework of TÁMOP-4.2.4.A/2-11/1-2012-0001 "National Excellence Program."

[1] M. Saffman, T. G. Walker, and K. Mølmer, Quantum information with Rydberg atoms, Rev. Mod. Phys. **82**, 2313 (2010).

[2] H. Weimer, M. Muller, I. Lesanovsky, P. Zoller, and H. P. Büchler, A Rydberg quantum simulator, Nat. Phys. **6**, 382 (2010).

[3] R. Löw, H. Weimer, J. Nipper, J. B. Balewski, B. Butscher, H. P. Büchler, and T. Pfau, An experimental and theoretical guide to strongly interacting Rydberg gases, J. Phys. B **45**, 113001 (2012).

[4] D. A. Tate, Comment on "measurement of the lifetimes of s and d states below $n = 31$ using cold Rydberg gas", Phys. Rev. A **75**, 066502 (2007).

[5] L. L. Caliri and L. G. Marcassa, Reply to "comment on 'measurement of the lifetimes of s and d states below $n = 31$ using cold Rydberg gas"', Phys. Rev. A **75**, 066503 (2007).

[6] A. L. de Oliveira, M. W. Mancini, V. S. Bagnato, and L. G. Marcassa, Measurement of Rydberg-state lifetimes using cold trapped atoms, Phys. Rev. A **65**, 031401 (2002).

[7] V. A. Nascimento, L. L. Caliri, A. L. de Oliveira, V. S. Bagnato, and L. G. Marcassa, Measurement of the lifetimes of s and d states below $n = 31$ using cold Rydberg gas, Phys. Rev. A **74**, 054501 (2006).

[8] D. B. Branden, T. Juhasz, T. Mahlokozera, C. Vesa, R. O. Wilson, M. Zheng, A. Kortyna, and D. A. Tate, Radiative lifetime measurements of rubidium Rydberg states, J. Phys. B **43**, 015002 (2010).

[9] D. Cano and J. Fortágh, Multiatom entanglement in cold Rydberg mixtures, Phys. Rev. A **89**, 043413 (2014).

[10] H. Labuhn, S. Ravets, D. Barredo, L. Béguin, F. Nogrette, T. Lahaye, and A. Browaeys, Single-atom addressing in microtraps for quantum-state engineering using Rydberg atoms, Phys. Rev. A **90**, 023415 (2014).

[11] M. Fleischhauer, A. Imamoglu, and J. P. Marangos, Electromagnetically induced transparency: Optics in coherent media, Rev. Mod. Phys. **77**, 633 (2005).

[12] A. K. Mohapatra, T. R. Jackson, and C. S. Adams, Coherent optical detection of highly excited Rydberg states using electromagnetically induced transparency, Phys. Rev. Lett. **98**, 113003 (2007).

[13] M. Mack, F. Karlewski, H. Hattermann, S. Höckh, F. Jessen, D. Cano, and J. Fortágh, Measurement of absolute transition frequencies of ^{87}Rb to nS and nD Rydberg states by means of electromagnetically induced transparency, Phys. Rev. A **83**, 052515 (2011).

[14] K. J. Weatherill, J. D. Pritchard, R. P. Abel, M. G. Bason, A. K. Mohapatra, and C. S. Adams, Electromagnetically induced transparency of an interacting cold Rydberg ensemble, J. Phys. B **41**, 201002 (2008).

[15] A. Tauschinsky, R. M. T. Thijssen, S. Whitlock, H. B. van Linden van den Heuvell, and R. J. C. Spreeuw, Spatially resolved excitation of Rydberg atoms and surface effects on an atom chip, Phys. Rev. A **81**, 063411 (2010).

[16] M. G. Bason, M. Tanasittikosol, A. Sargsyan, A. K. Mohapatra, D. Sarkisyan, R. M. Potvliege, and C. S. Adams, Enhanced electric field sensitivity of rf-dressed Rydberg dark states, New J. Phys. **12**, 065015 (2010).

[17] H. Hattermann, M. Mack, F. Karlewski, F. Jessen, D. Cano, and J. Fortágh, Detrimental adsorbate fields in experiments with cold Rydberg gases near surfaces, Phys. Rev. A **86**, 022511 (2012).

[18] A. Tauschinsky, R. Newell, H. B. van Linden van den Heuvell, and R. J. C. Spreeuw, Measurement of ^{87}Rb Rydberg-state hyperfine splitting in a room-temperature vapor cell, Phys. Rev. A **87**, 042522 (2013).

[19] J. Grimmel, M. Mack, F. Karlewski, F. Jessen, M. Reinschmidt, N. Sándor, and J. Fortágh, Measurement and numerical calculation of rubidium Rydberg stark spectra [New J. Phys. (to be published)], arXiv:1503.08953.

[20] G. Günter, M. Robert-de-Saint-Vincent, H. Schempp, C. S. Hofmann, S. Whitlock, and M. Weidemüller, Interaction enhanced imaging of individual Rydberg atoms in dense gases, Phys. Rev. Lett. **108**, 013002 (2012).

[21] G. Günter, H. Schempp, M. Robert-de-Saint-Vincent, V. Gavryusev, S. Helmrich, C. S. Hofmann, S. Whitlock, and M. Weidemüller, Observing the dynamics of dipole-mediated energy transport by interactionenhanced imaging, Science **342**, 954 (2013).

[22] I. I. Beterov, I. I. Ryabtsev, D. B. Tretyakov, and V. M. Entin, Quasiclassical calculations of blackbodyradiation-induced depopulation rates and effective lifetimes of Rydberg ns, np, and nd alkali-metal atoms with $n \leqslant 80$, Phys. Rev. A **79**, 052504 (2009).

[23] I. I. Beterov, I. I. Ryabtsev, D. B. Tretyakov, and V. M. Entin, Erratum: Quasiclassical calculations of blackbody-radiation-induced depopulation rates and effective lifetimes of Rydberg ns, np, and nd alkali-metal atoms with $n \leqslant 80$ [Phys. Rev. A **79**, 052504 (2009)], Phys. Rev. A **80**, 059902(E) (2009).

[24] T. Wang, S. F. Yelin, R. Côté, E. E. Eyler, S. M. Farooqi, P. L. Gould, M. Koštrun, D. Tong, and D. Vrinceanu, Superradiance in ultracold Rydberg gases, Phys. Rev. A **75**, 033802 (2007).

[25] W. R. Anderson, M. P. Robinson, J. D. D. Martin, and T. F. Gallagher, Dephasing of resonant energy transfer in a cold Rydberg gas, Phys. Rev. A **65**, 063404 (2002).

[26] J. O. Day, E. Brekke, and T. G. Walker, Dynamics of low-density ultracold Rydberg gases, Phys. Rev. A **77**, 052712 (2008).

All-optical measurement of Rydberg-state lifetimes

Markus Mack,* Jens Grimmel, Florian Karlewski, Lőrinc Sárkány, Helge Hattermann, and József Fortágh†
CQ Center for Collective Quantum Phenomena and Their Applications, Physikalisches Institut, Eberhard-Karls-Universität Tübingen, Auf der Morgenstelle 14, D-72076 Tübingen, Germany
(Received 26 May 2015; published 24 July 2015)

We have developed an all-optical method for measuring the lifetimes of nS and nD Rydberg states and demonstrate its capabilities with measurements on a dilute cloud of ultracold ^{87}Rb atoms in a cryogenic environment. The method is based on the time-resolved observation of resonant light absorption by ground-state atoms and selective transfer of Rydberg atoms into the ground state at varying delay times in order to reconstruct Rydberg decay curves. Our measurements of the ^{87}Rb $30S_{1/2}$ state indicate an increase of the lifetime at lowered environment temperatures, as expected due to decreased blackbody radiation. For the $38D_{5/2}$ state with an attractive dipole-dipole interaction, ionization and lifetime reduction due to collisional effects are observed.

DOI: 10.1103/PhysRevA.92.012517 PACS number(s): 32.10.−f, 32.80.Ee, 32.80.Rm

I. LIFETIMES OF RYDBERG ATOMS

Rydberg atoms are promising for quantum information processing due to their strong and highly tunable interaction properties [1]. High-fidelity quantum gates and coherent-state transfer between Rydberg and long-living ground states have been proposed [2,3]. The fidelity of these operations is, however, fundamentally limited by the finite lifetime of Rydberg states [1]. Besides the natural decay of the Rydberg excitation, blackbody-radiation-induced transitions [4,5], collisions [6], and superradiance [7] may also limit the lifetime. The characterization of the Rydberg-state decay is thus of significant interest.

For individual Rydberg atoms at an environment temperature $T = 0$ the lifetime of an excited state is given by the inverse sum over all spontaneous decay rates into lower-lying states [8]. Due to the highest energy difference, the lowest-lying states contribute most to the decay. This is a limiting factor for calculations because the potentials for low-lying states cannot be described as accurately as those of higher states, which become more and more hydrogenlike with increasing n and l quantum numbers. In a finite-temperature environment, transitions induced by blackbody radiation (BBR) occur. The strongest transitions are those to nearby dipole-allowed Rydberg states both above and below in energy. For a perfect Planck photon distribution and well-known temperature the corresponding rates can be calculated with high accuracy [4,5]. The experimental verification of BBR-induced transition rates is possible not only through Rydberg lifetime measurements [9] but also indirectly by, e.g., measurements of Stark maps [10], which depend on the same dipole matrix elements. Any incoherent repopulation of the originally excited Rydberg state by multiple BBR transitions can be easily included in theoretical models but is usually negligible in magnitude. Also, blackbody-induced ionization by transitions to continuum states can be taken into account [11].

Direct lifetime measurements at lowered environment temperatures, as well as measurements of temperature-dependent BBR transfer rates, have been conducted for Na atoms [9,12]. The most accurate values for Rb Rydberg lifetimes to date have been measured in a room-temperature environment, relying on the knowledge of BBR transition rates in order to extract zero-temperature natural lifetimes. Measurements of nS and nD states in the range of $n = 27$ to 44 were conducted by exciting Rydberg atoms from a cloud of ultracold atoms prepared in a magneto-optical trap (MOT), waiting some varying delay time, and then applying an electric-field pulse while monitoring the time-dependent ionization signals (selective field ionization, SFI) [13,14]. Due to the difficulty of accurately distinguishing between close-lying Rydberg states which are populated because of BBR (see discussion in [15,16]), the technique was improved in [17]. By adding a microwave transfer of the "target" Rydberg atoms to a higher-lying state which can be accurately discriminated, this potential source of systematic error was eliminated. The results of [17] generally agree with previous work and cover Rb nS, nP, and nD states in the range $28 \leqslant n \leqslant 45$. To our knowledge, neither lifetimes of Rb at lowered environment temperatures nor any BBR transition rates have yet been measured. Consequently, an experimental verification of the BBR rate calculations [4] for Rb is still required.

In general, the lifetime of Rydberg atoms in ultracold gases is altered by several effects. Any electric fields lead to state mixing and ionization [8]. Collisions between atoms, as well as dipole-dipole and higher-order interaction between Rydberg atoms, which may also lead to collisions [18], cause changes of the atomic states and ionization [6,19]. Furthermore, depending on atomic density and cloud geometry, microwave superradiance is likely to occur, which can be triggered by blackbody radiation [7,20]. Due to such effects, the lifetimes of Rydberg atoms can differ greatly from the undisturbed values, as well as from one experiment to another. Therefore, measuring Rydberg lifetimes under the given conditions is necessary.

While the SFI methods mentioned above can be used when an electron or ion detector is present, an increasing number of recent cold-atom experiments have relied solely on optical detection, mostly employing electromagnetically induced transparency (EIT) instead [21–24]. In order to enable the determination of Rydberg lifetimes in such systems, as well as in cases where a reduced complexity of the setup

*markus.mack@uni-tuebingen.de
†fortagh@uni-tuebingen.de

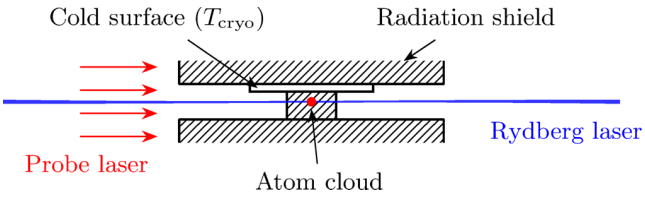

FIG. 1. (Color online) Cloud of ultracold ^{87}Rb atoms (center) inside the radiation shield of a cryostat (hatched). The radiation shield is cylindrical in shape with a 4.5-mm gap and 35-mm diameter. While the cold surface is at T_{cryo}, the temperature of the radiation shield is slightly higher. The outside temperature is assumed to be close to 300 K.

compared to that of the SFI approach with the additional microwave is desired, we developed a similarly powerful, all-optical method for measuring state-specific lifetimes. The approach is technologically simplified as the same lasers that are used for Rydberg excitation are employed for detection, requiring only an additional photodiode for the measurement of resonant absorption.

We describe the optical lifetime measurement of Rydberg states in Sec. II and demonstrate its application in a setup with cold ^{87}Rb atoms (see Fig. 1) at cryogenic environmental temperatures in Sec. III. Factors influencing the accuracy of the method are discussed in Sec. IV.

II. OPTICAL LIFETIME MEASUREMENT METHOD

The optical measurements presented in this article rely on time-resolved resonant absorption detection in an effective three-level ladder-type system, as shown in the inset of Fig. 2, similar to the scheme in [25]. The transmission of a *probe laser* pulse resonant to a closed cycling transition between a ground state $|g\rangle$ and a quickly decaying intermediate excited state $|e\rangle$ is monitored with a photodiode. The duration of this pulse should be several times the expected Rydberg lifetime. The lifetime of $|e\rangle$ must be shorter than the expected time resolution of the final Rydberg decay curves. For Rydberg excitation a *Rydberg laser* resonant to the transition between $|e\rangle$ and the target Rydberg state $|r_1\rangle$ is used simultaneously with the probe laser. In principle, this configuration allows excitation by means of a stimulated Raman adiabatic passage pulse [26]. The experimental sequence, aimed at measuring changes in the optical density due to the laser pulses, consists of several steps. In each step, a cloud of ultracold atoms is prepared and released from the trap, and after a given time of flight a series of laser pulses depending on the current step is applied, as shown in Fig. 2.

As a baseline calibration, the probe laser-light-intensity signals without any atoms [step I, signal $I_0(t)$] and with ground-state atoms [step II, $I_{\mathrm{g}}(t)$] are recorded, giving the time-dependent optical density (Lambert-Beer law):

$$D^{\mathrm{opt}}_{\mathrm{noexc.}}(t) = -\ln[I_{\mathrm{g}}(t)/I_0(t)], \tag{1}$$

In general, during the relevant time scales, the optical density is proportional to the number of atoms in the volume of the cloud "seen" by the probe laser beam.

In step III, the Rydberg excitation at $t = 0$ just before the start of the probe pulse is added. Due to excited atoms that

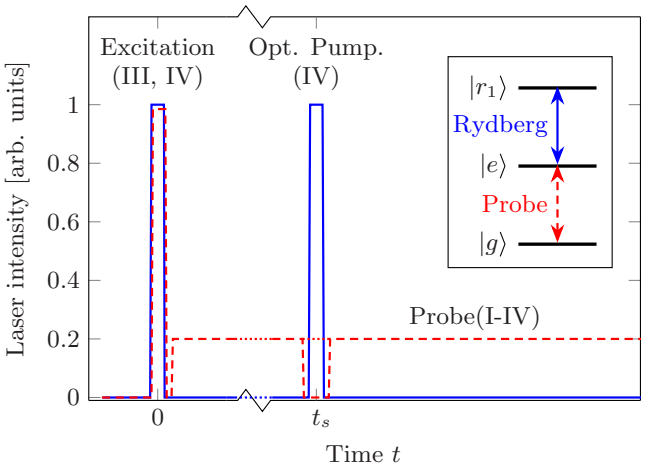

FIG. 2. (Color online) Illustration of the pulse sequence for steps I to IV used for the optical lifetime measurement for the probe (dashed red lines) and Rydberg (solid blue lines) lasers, resonant to the $|g\rangle \leftrightarrow |e\rangle$ and $|e\rangle \leftrightarrow |r_1\rangle$ transitions. For the calibration (step I without atoms and step II with atoms), only the probe laser is turned on after $t = 0$ for a duration of several hundred microseconds (much greater than the Rydberg lifetime; only the initial part is shown in the plot). Starting at step III, at $t = 0$ atoms are excited to the Rydberg state $|r_1\rangle$ (Excitation). For step IV, which is repeated several times, the long probe pulse is interrupted at time t_s for a short duration, during which an optical pumping pulse of the Rydberg laser is applied (Opt. Pump.). t_s is varied with each repetition of step IV.

are missing from the ground state, there will be increased transmission compared to that in step II. Again, the optical density of ground-state atoms $D^{\mathrm{opt}}_{\mathrm{w/exc.}}(t)$ can be calculated as in (1). In combination with the result from step II, an additional quantity

$$p_{\neq \mathrm{g}}(t) = 1 - D^{\mathrm{opt}}_{\mathrm{w/exc.}}(t)/D^{\mathrm{opt}}_{\mathrm{noexc.}}(t) \tag{2}$$

can be determined, which gives the number of atoms *not* in the ground state due to the excitation pulse, normalized to the total number of atoms in the detection volume. The value of $p_{\neq \mathrm{g}}$ in the beginning is the fraction of atoms that have been excited to the Rydberg state, except for transitions to other states that have already happened due to BBR and possible superradiance, as was noted in [25]. The whole $p_{\neq \mathrm{g}}$ curve represents an effective decay of all directly and indirectly excited states, which is nearly, but generally not perfectly, exponential in shape because of the differing lifetimes of the constituent Rydberg states that become populated. Also, if ionizing effects played a role, the curve will not return to zero for long times but converge towards a finite value. The resulting $p_{\mathrm{ion}} = p_{\neq \mathrm{g}}(t \to \infty)$ is a measure for the strength of any ionizing effects if other mechanisms can be excluded that specifically remove Rydberg atoms, but not ground-state atoms, from the detection volume or, alternatively, transfer them into other stable states outside the probe transition. In general, the decay curve must consist of the (as yet unknown) parts

$$p_{\neq \mathrm{g}}(t) = p_{\mathrm{r_1}}(t) + p_{\mathrm{r}_{\neq 1}}(t) + p_{\mathrm{ion}}(t), \tag{3}$$

i.e., the population of the originally excited Rydberg state, other Rydberg states, and the number of ionized atoms.

In order to separate the decay of the originally excited Rydberg state $|r_1\rangle$ from others that become populated, a state transfer similar to the microwave transfer in [17] is employed in step IV. However, instead of the additional microwave, the same Rydberg laser which was used for the excitation is used for a short optical pumping pulse at various times t_s during the expected decay of $|r_1\rangle$. This pumps a fraction of atoms still in the $|r_1\rangle$ state down to the intermediate $|e\rangle$ state. During this pulse, the probe laser needs to be turned off to prevent any reexcitation of the Rydberg state. Because the lifetime of the intermediate state is short, the atoms pumped back in this fashion will reappear as ground-state atoms as soon as the probe laser is turned on again after the optical pumping pulse. Following the same evaluation procedure as for step III, using (1) and (2), decay curves $p_{\neq g,s}(t)$ can be obtained. These must consist of the same parts with equal values as (3), except for a change in $p_{r_1}(t)$ at $t \geqslant t_s$, which has been reduced by some fraction α by the optical pumping pulse due to the Rydberg population in $|r_1\rangle$ at time $t = t_s$, leaving

$$p_{r_1,s}(t_s) = (1-\alpha)p_{r_1}(t_s). \tag{4}$$

Thus, by subtracting the decay curves $p_{\neq g,s}(t)$ from the curve without optical pumping $p_{\neq g}(t)$ of step III, information about the original $|r_1\rangle$ population at time $t = t_s$ can be obtained:

$$\alpha p_{r_1}(t_s) = p_{\neq g}(t_s) - p_{\neq g,s}(t_s). \tag{5}$$

As long as the optical density of the Rydberg atoms for the Rydberg laser is small or the optical pumping is fast enough to transfer all of the $|r_1\rangle$ atoms ($\alpha = 1$), α will be a constant fraction for each t_s. Repetition of step IV for different t_s and evaluation of $\alpha p_{r_1}(t_s)$ yields the decay of the population p_{r_1}, giving the lifetime of the Rydberg state $|r_1\rangle$. In the case only spontaneous decay and BBR contribute to the lifetime, this will be an exponential decay with a decay parameter τ independent of α.

III. CONDUCTED MEASUREMENTS AND RESULTS

We employed the method in a series of experiments in a setup where a cloud of 4×10^5 to 8×10^5 ^{87}Rb atoms with a temperature of 1.5 μK is transferred into a gap of the radiation shield of a tunable temperature cryostat by means of optical tweezers (detailed in [27]). Details of the geometry are shown in Fig. 1. For excitation and detection we used the ^{87}Rb $5S_{1/2}(F = 2) \leftrightarrow 5P_{3/2}(F = 3)$ transition and a circular polarization, which is commonly used for imaging purposes. A repumping laser resonant to $5S_{1/2}(F = 1) \leftrightarrow 5P_{3/2}(F = 2)$, which was needed for the MOT operation as well, was used to effectively keep the $F = 1$ ground state unpopulated at all times. The Rydberg excitation to $|r_1\rangle$ is done by a pulse of the probe laser, with a higher intensity (approximately five times) than in actual probing, and, simultaneously, the Rydberg laser pulse resonant to the $5P_{3/2}(F = 3) \leftrightarrow 30S_{1/2}$ or $38D_{5/2}$ state. The probe and Rydberg lasers are frequency stabilized to a frequency comb and arranged as described in [25]. The Rydberg laser was focused down to a size of $\approx$100 μm with a total power of $\approx$20 mW. The measurement sequence as described in Sec. II was conducted at times of flight (TOFs) of 12.0 and 20.5 ms in order to reduce the atom density to $7(3) \times 10^9/\mathrm{cm}^{-3}$ and $1.5(5) \times 10^9/\mathrm{cm}^{-3}$, respectively. The setup did not allow for controlled compensation of stray electric fields (which have been investigated in detail elsewhere [28]), leaving residual fields of 6.6 V cm^{-1} for the $30S$ state measurements and, after optimizing the cloud position, 0.5V/cm for those in the $38D$ state. Due to limited Rydberg laser power, pulse durations of 1μs were chosen for both the excitation and optical pumping pulses. In order to reduce the statistical errors, mainly a result of photodiode and other technical noise, $\geqslant$30 shots per step were averaged. The time resolution of the photodiode signal of each shot was digitally reduced to 0.5μs by temporal averaging. Furthermore, because of atom-number fluctuations, (1) and (2) were individually calculated for each single-shot measurement and corrected for atom-number drifts. In order to decrease statistical noise, the results of shots belonging to the same step (and repetition number s for step IV) were averaged.

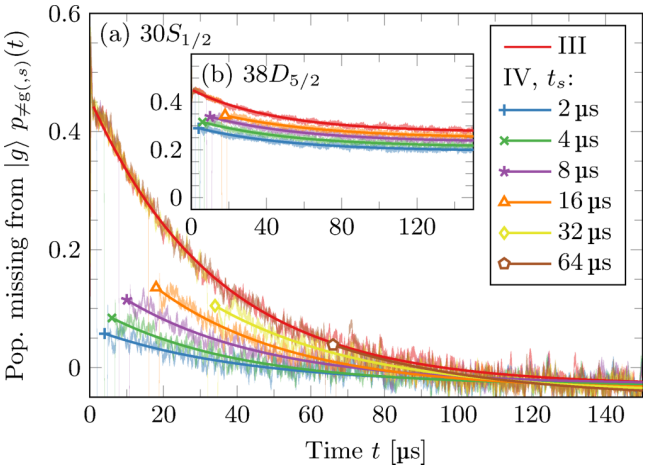

FIG. 3. (Color online) (a) Time-dependent populations of states not contributing to the probe transition, $p_{\neq g}$ (step III) and $p_{\neq g,s}(t)$ (step IV with repetition number s and corresponding optical pumping time t_s), representing an intermediate result of the evaluation of the measurement of the $30S_{1/2}$ state at $T_{\mathrm{cryo}} = 300$ K and a TOF of 20.5 ms. Shaded areas show statistical errors of the signal at each instant of time. Solid lines show exponential fits corresponding to each measurement step. Markers show the values $p_{\neq g,s}(t_s)$ obtained from the fit. (b) $38D_{5/2}$ state at $T_{\mathrm{cryo}} = 160$ K, showing only a fraction of atoms returning to the ground state depending on the optical pumping time t_s, converging towards values up to $p_{\mathrm{ion}} \approx 0.3$.

Figure 3 shows exemplary results for the number of atoms missing from the ground state, $p_{\neq g}(t)$ and $p_{\neq g,s}(t)$, where up to six values of t_s have been used at increasing intervals. For both states, an approximation of the curves by exponential functions, which were used for fitting in order to determine the points $p_{\neq g,s}(t_s)$, was sufficient. While for $30S_{1/2}$ all atoms eventually return to the ground state, for the $38D_{5/2}$ state this is clearly not the case. This is most probably caused by ionizing collisions due to the known attractive dipole-dipole interaction for this state [29]. While more than half of the Rydberg atoms are apparently already lost at $t < 2\mu$s, a small fraction was prevented from being ionized by the optical pumping pulses.

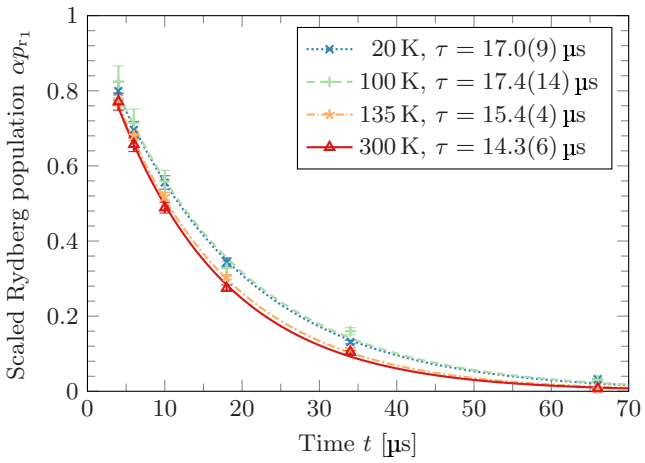

FIG. 4. (Color online) Measured populations $\alpha p_{r_1}(t_s)$ of the $30S_{1/2}$ state, proportional to the decays of $|r_1\rangle$, at several cryostat temperatures in the range 20 to 300 K. The lines are exponential fits to the data, giving the decay parameters τ and their estimated error based on the fit (add $\pm 1.0\mu$s systematic error common to all measurements for absolute uncertainty).

The final evaluation step yielding $\alpha p_{r_1}(t_s)$ is shown in Fig. 4 for the state $|r_1\rangle = 30S_{1/2}$, measured at cryostat temperatures in the range of 20 to 300 K, at a TOF of 20.5 ms, resulting in values $\tau = 14.3(6)\mu$s ($T_{\text{cryo}} = 300$ K) up to $\tau = 17.0(8)\mu$s ($T_{\text{cryo}} = 20$ K) with an additional common systematic error of $\pm 1.0\mu$s. Compared with the established measured value $\tau = 14.5(12)\mu$s ($30S_{1/2}, T = 300$ K, Fig. 2 in [14]), our result is very compatible.

However, while in our measurements there is a clear tendency for increased lifetimes at lowered temperatures, the effect is not as pronounced as expected from the calculated values from [4], giving $\tau = 26.6$ μs at $T = 0$ K. In order to check for any systematic dependencies on geometrical effects arising due to the falling and expanding cloud, as well as the presence of any density-dependent lifetime-reducing effects, the measurements for $30S_{1/2}$ were repeated with a time of flight of 12 ms. This resulted in an increase of the atom density and the optical density by roughly a factor of 2. The resulting lifetimes for $30S_{1/2}$ were $\tau = 14.1(14)\mu$s ($T_{\text{cryo}} = 300$ K) up to $\tau = 16.0(7)\mu$s ($T_{\text{cryo}} = 20$ K), i.e., no discernible difference compared to the measurements with TOF of 20.5 ms. Therefore, we suspect insufficient shielding from outside thermal radiation in our setup as the main cause for the discrepancy in comparison to theory at low temperatures. The geometry as shown in Fig. 1 leads to a solid angle of $4\pi \times 0.87$ covered by cold surfaces. Also, the lower part of the radiation shield is not ideally thermally coupled to the cryostat and is estimated to be at least 20 K warmer than the upper surface at temperatures near $T_{\text{cryo}} = 4.2$ K, causing the effective temperature relevant for BBR to be significantly higher than the cryostat temperature.

The lifetime of the $38D_{5/2}$ state, with a TOF of 20.5 ms, was measured to be 13(4) μs ($T_{\text{cryo}} = 160$ K) and 19(3) μs ($T_{\text{cryo}} = 20$ K), much lower than the reference value of $\tau = 30(2)\mu$s ($T = 300$ K; Fig. 2 in [14]). This lifetime reduction comes as no surprise due to the interaction-induced ionizing collisions already observed in Fig. 3.

IV. ACCURACY CONSIDERATIONS

The time resolution of the method presented in Sec. II is limited by the length and timing accuracy of the excitation and optical pumping pulses, effectively adding uncertainty to times $t = 0$ and t_s. For our 1-μs pulses with a timing accuracy of <10 ns, this results in a systematic uncertainty of $\pm 1.0\mu$s common to all measurements taken under the same excitation conditions, limiting their absolute, but not differential, accuracy. Higher laser intensities, particularly of the Rydberg laser, would allow for shorter pulses. When choosing the sizes for both laser beams, geometry effects need to be considered: If there is any significant atomic motion due to time of flight or atomic temperature, the excitation volume should be smaller than the detection volume in order to avoid any Rydberg atoms leaving the detection volume during the measurement time. However, the measured Rydberg signal will be lower for increased detection volumes, affecting the signal-to-noise ratio. Furthermore, prolonged acceleration of the atoms due to radiation pressure will lead to Doppler shifts which can lead to systematical errors, especially with regard to the narrow Rydberg transitions. This is particularly relevant for the probe laser, which must be well below the saturation intensity of the probe transition ($I_0 \lesssim 0.2 I_{\text{sat}}$ in our experiments).

If, like in our experiments, the pulses are created using an acousto-optical modulator (AOM) in the laser-beam path, the probe pulse will have a certain switching time of $\approx$100 ns and will show intensity drifts resulting from polarization drifts during some device-dependent warm-up time. As long as the signal remains proportional to the light level seen by the atoms and the pulse shapes are well reproducible, these drifts cancel out when calculating the $D^{\text{opt}}(t)$ terms. The optical density itself will not be constant over the duration of the laser pulse since the atomic cloud is expanding, as well as being accelerated downwards by gravity; however, these effects cancel out as well in $p_{\neq g}(t)$.

The measured optical densities depend on the probe light polarization and Zeeman substates of the atoms. For low Rabi frequencies, optical pumping effects can become visible in the dynamic parts of the measured signals, particularly when turning the probe laser back on after the Rydberg laser pulses at times t_s, which in turn limits the accuracy of the determination of $p_{r_1,s}(t_s)$. These effects become especially pronounced when any stray magnetic fields split up the Zeeman sublevels, which would need to be compensated well below the magnitude of the earth's magnetic field for high accuracy. Stray electric fields, if sufficiently strong, would additionally lead to state mixing affecting the underlying physical lifetime of the measured state. According to our calculations (detailed in [10]), this would become relevant on a 1% (probability) level at 30 V/cm for the $30S_{1/2(|m_j|=1/2)}$ state and 2.2 V/cm for $38D_{5/2(|m_j|=1/2)}$, i.e., not leading to significant state mixing in our setup.

Regarding the measurements taken at a lowered environment temperature, mainly two sources of systematic error need to be taken into account: First, as mentioned before and discussed in [8], the effective temperature as seen by the atoms

will not be the temperature of the cryostat unless the full 4π solid angle is covered. Second, the geometry of conducting parts of the experimental setup, like the radiation shield of the cryostat, can form an effective microwave resonator altering the BBR spectrum. This becomes especially relevant if their dimensions are close to the strongest transition wavelengths (like the $30S \leftrightarrow 30P$ transition with a wavelength of 1.9 mm or $30S \leftrightarrow 29P$ with a wavelength of 1.7 mm).

V. CONCLUSION AND OUTLOOK

We have presented an optical method for the measurement of Rydberg atom lifetimes, providing information about how they are influenced by effects like blackbody radiation and interactions between Rydberg atoms. Because no detector parts or high voltages are needed inside the vacuum chamber of the experimental setup, this method might prove particularly useful in otherwise complex systems, including atom-chip setups such as the one used here [27], or millikelvin systems [30], which might eventually lead to the realization of proposed quantum gate schemes such as those in [31,32].

While the use of an additional microwave population transfer such as the one in [17] is not necessary for state selectivity, it might be employed to measure the populations of neighboring Rydberg nP and nF states by generalizing the scheme to measure signal differences due to the microwave transfer. This way, both the populations of, e.g., a Rydberg nS and close-lying nP states could be monitored. This would, for example, allow for the distinction between superradiance, which highly depends on the population of such strongly coupled states, and other lifetime-reducing effects.

ACKNOWLEDGMENTS

This work was financially supported by the FET-Open Xtrack Project HAIRS and the Carl Zeiss Stiftung.

[1] M. Saffman, T. G. Walker, and K. Mølmer, Rev. Mod. Phys. **82**, 2313 (2010).
[2] D. Jaksch, J. I. Cirac, P. Zoller, S. L. Rolston, R. Côté, and M. D. Lukin, Phys. Rev. Lett. **85**, 2208 (2000).
[3] M. M. Müller, M. Murphy, S. Montangero, T. Calarco, P. Grangier, and A. Browaeys, Phys. Rev. A **89**, 032334 (2014).
[4] I. I. Beterov, I. I. Ryabtsev, D. B. Tretyakov, and V. M. Entin, Phys. Rev. A **79**, 052504 (2009).
[5] I. I. Beterov, I. I. Ryabtsev, D. B. Tretyakov, and V. M. Entin, Phys. Rev. A **80**, 059902(E) (2009).
[6] A. Walz-Flannigan, J. R. Guest, J.-H. Choi, and G. Raithel, Phys. Rev. A **69**, 063405 (2004).
[7] T. Wang, S. F. Yelin, R. Côté, E. E. Eyler, S. M. Farooqi, P. L. Gould, M. Koštrun, D. Tong, and D. Vrinceanu, Phys. Rev. A **75**, 033802 (2007).
[8] T. F. Gallagher, *Rydberg Atoms* (Cambridge University Press, Cambridge, 1994).
[9] W. P. Spencer, A. G. Vaidyanathan, D. Kleppner, and T. W. Ducas, Phys. Rev. A **25**, 380 (1982).
[10] J. Grimmel, M. Mack, F. Karlewski, F. Jessen, M. Reinschmidt, N. Sándor, and J. Fortágh, New J. Phys. **17**, 053005 (2015).
[11] I. I. Beterov, D. B. Tretyakov, I. I. Ryabtsev, V. M. Entin, A. Ekers, and N. N. Bezuglov, New J. Phys. **11**, 013052 (2009).
[12] W. P. Spencer, A. G. Vaidyanathan, D. Kleppner, and T. W. Ducas, Phys. Rev. A **24**, 2513 (1981).
[13] A. L. de Oliveira, M. W. Mancini, V. S. Bagnato, and L. G. Marcassa, Phys. Rev. A **65**, 031401 (2002).
[14] V. A. Nascimento, L. L. Caliri, A. L. de Oliveira, V. S. Bagnato, and L. G. Marcassa, Phys. Rev. A **74**, 054501 (2006).
[15] D. A. Tate, Phys. Rev. A **75**, 066502 (2007).
[16] L. L. Caliri and L. G. Marcassa, Phys. Rev. A **75**, 066503 (2007).
[17] D. B. Branden, T. Juhasz, T. Mahlokozera, C. Vesa, R. O. Wilson, M. Zheng, A. Kortyna, and D. A. Tate, J. Phys. B **43**, 015002 (2010).
[18] W. Li, P. J. Tanner, and T. F. Gallagher, Phys. Rev. Lett. **94**, 173001 (2005).
[19] R. A. D. S. Zanon, K. M. F. Magalhães, A. L. de Oliveira, and L. G. Marcassa, Phys. Rev. A **65**, 023405 (2002).
[20] J. O. Day, E. Brekke, and T. G. Walker, Phys. Rev. A **77**, 052712 (2008).
[21] A. Tauschinsky, R. M. T. Thijssen, S. Whitlock, H. B. van Linden van den Heuvell, and R. J. C. Spreeuw, Phys. Rev. A **81**, 063411 (2010).
[22] G. Günter, H. Schempp, M. Robert-de Saint-Vincent, V. Gavryusev, S. Helmrich, C. S. Hofmann, S. Whitlock, and M. Weidemüller, Science **342**, 954 (2013).
[23] D. Maxwell, D. J. Szwer, D. Paredes-Barato, H. Busche, J. D. Pritchard, A. Gauguet, M. P. A. Jones, and C. S. Adams, Phys. Rev. A **89**, 043827 (2014).
[24] H. Gorniaczyk, C. Tresp, J. Schmidt, H. Fedder, and S. Hofferberth, Phys. Rev. Lett. **113**, 053601 (2014).
[25] F. Karlewski, M. Mack, J. Grimmel, N. Sándor, and J. Fortágh, Phys. Rev. A **91**, 043422 (2015).
[26] T. Cubel, B. K. Teo, V. S. Malinovsky, J. R. Guest, A. Reinhard, B. Knuffman, P. R. Berman, and G. Raithel, Phys. Rev. A **72**, 023405 (2005).
[27] D. Cano, H. Hattermann, B. Kasch, C. Zimmermann, R. Kleiner, D. Koelle, and J. Fortágh, Eur. Phys. J. D **63**, 17 (2011).
[28] H. Hattermann, M. Mack, F. Karlewski, F. Jessen, D. Cano, and J. Fortágh, Phys. Rev. A **86**, 022511 (2012).
[29] A. Reinhard, T. C. Liebisch, B. Knuffman, and G. Raithel, Phys. Rev. A **75**, 032712 (2007).
[30] F. Jessen, M. Knufinke, S. Bell, P. Vergien, H. Hattermann, P. Weiss, M. Rudolph, M. Reinschmidt, K. Meyer, T. Gaber, D. Cano, A. Günther, S. Bernon, D. Koelle, R. Kleiner, and J. Fortágh, Appl. Phys. B **116**, 665 (2014).
[31] D. Petrosyan and M. Fleischhauer, Phys. Rev. Lett. **100**, 170501 (2008).
[32] J. D. Pritchard, J. A. Isaacs, M. A. Beck, R. McDermott, and M. Saffman, Phys. Rev. A **89**, 010301 (2014).

Field ionization of Rydberg atoms for high-brightness electron and ion beams

A. J. McCulloch,[1] R. W. Speirs,[1] J. Grimmel,[2] B. M. Sparkes,[1] D. Comparat,[3] and R. E. Scholten[1,*]

[1]*School of Physics, The University of Melbourne, Victoria, 3010, Australia*

[2]*CQ Center for Collective Quantum Phenomena and their Applications, Physikalisches Institut, Eberhard-Karls-Universität Tübingen, Auf der Morgenstelle 14, D-72076 Tübingen, Germany*

[3]*Laboratoire Aimé Cotton, CNRS, Université Paris-Sud, ENS Cachan, Bât. 505, 91405 Orsay, France*

(Received 2 November 2016; published 28 June 2017)

We present an ionization mechanism for use in a cold atom electron source with the goal of producing highly monochromatic electron beams. We experimentally produce a map of the Stark states of ^{85}Rb below the ionization threshold and identify states that undergo selective field ionization. The properties of an electron beam produced by field-assisted ionization of such states are quantified. A theoretical framework is established to predict the improvement to beam quality when ionization is conducted above the ionization threshold, where ionization conditions are typically more favorable than below the threshold. Calculations suggest that selective ionization of Rydberg states may offer a pathway to the production of high-brightness, highly monochromatic ion and electron beams.

DOI: 10.1103/PhysRevA.95.063845

I. INTRODUCTION

Monochromatic electron beams are critically important for structuring and analysis of materials, from nanofabrication via electron-beam milling to compositional and structural analysis using electron energy loss spectroscopy (EELS). The advent of aberration-corrected optical systems has reduced limitations previously placed on electron-beam probe sizes by polychromatic beams at high energies (>100 keV), but at low energies, chromatic aberration is usually the limiting parameter [1]. High-resolution electron energy loss spectroscopy (HREELS), which combines EELS with highly monochromatic beams, can produce elemental maps with atomic resolution and probe the nature of atomic bonds in a variety of materials. The current standard for a highly monochromatic beam is an energy spread of less than 0.2 eV, which allows for observation of surface plasmons of gold nanoparticles [2] and the spectroscopic detection of single atoms [3]. More recently, monochromatic electrons have allowed atomic resolution to be realized in a transmission electron microscope operating with a beam energy of 15 keV [4].

Electron energy resolution of less than 0.1 eV is required to control and orient chemicals in the condensed phase [5,6]. State-of-the-art cold field emitting sources produce 100 keV electrons with an energy spread $\Delta U = 0.3$ eV [7] and hence still require energy filtering. Monochromators are well developed but nevertheless complicated and, critically, rely upon removing a significant fraction of the electrons from the beam, thus limiting the beam current.

Recently, a new source of electrons based on the ionization of laser-cooled atoms has emerged. Careful ionization of an atomic ensemble, either directly or via a field-assisted process, produces inherently cold electron bunches, giving an impressively small transverse energy spread [8,9]. Electron beams with energies of $U = 1$–10 keV [10,11] have been produced by ionizing atoms in a static electric field, with the finite size of the ionization volume giving rise to a longitudinal energy spread on the order of 0.01% of the beam energy ($\Delta U = 0.1$–1 eV). One possible mechanism to achieve reduced energy spread is field ionization of highly excited Rydberg atoms [12]. Under certain conditions, Rydberg atoms will ionize only at a specific value of the electric field. By using high field gradients, the length scale over which a beam of atoms will ionize can be very small, greatly reducing the energy spread of the beam.

Here we investigate the suitability of field-assisted ionization of rubidium Rydberg atoms for creating highly monochromatic electron and ion beams. We produce a high-resolution map of the Stark states below the ionization threshold and observe states which selectively ionize. For a particular selectively ionizing state, we predict the expected reduction in energy spread for an electron beam produced via selective field ionization. Finally, we model the effects of selective-state ionization for above-threshold Stark states, which are known to have higher ionization rates, to investigate the possibilities for further reducing the energy spread.

II. BACKGROUND

In HREELS, the energy resolution of the electron beam is not only critical to determining the structure that can be resolved, but also for improving the spatial resolution of bright field images [13], which is often limited by chromatic aberration. For a focused electron beam, the combination of beam emittance and aberrations arising from the source and the optical system determine the minimum achievable spot size. The dominant aberrations in the context of focused beams are spherical and chromatic. Spherical aberrations are a consequence of the optical system used, whereas chromatic aberrations and beam emittance are properties of the source. A common measure for the minimum achievable spot size is the beam diameter d_{50}, which is the diameter within which 50% of the beam current is encapsulated. With Gaussian distributions of both the beam energy U and the convergence angle α,

$$d_{50} = \sqrt{\left(d_{50,\mathrm{s}}^{1.3} + d_{50,\epsilon}^{1.3}\right)^{2/1.3} + d_{50,\mathrm{c}}^{2}}, \quad (1)$$

*scholten@unimelb.edu.au

where $d_{50,s}$, $d_{50,\epsilon}$, and $d_{50,c}$ are the beam diameters arising from the spherical aberration, emittance, and chromatic aberration, respectively [14]. Spherical aberration arises due to a differing focal length as a function of position from the optic axis. Emittance is a measure of the transverse phase-space volume occupied by the beam, which characterizes both the lateral size and angular divergence of the beam, and thus its inherent focusability. Chromatic aberration is the variation in focal length for particles of different energy. The chromatic aberration spot size $d_{50,c}$ is proportional to the energy spread of the beam ΔU and is given by [15]

$$d_{50,c} = \zeta C_c \Delta\alpha \frac{\Delta U}{U_0}, \tag{2}$$

where ζ is a numerical constant for a given system [16], C_c is the aberration coefficient of the lensing system, and U_0 is the mean beam energy. It is clear that increasing the beam energy will reduce $d_{50,c}$ but for many applications higher beam energies are not desirable. Consequently, the only method to minimize $d_{50,c}$ is to reduce ΔU.

The Cold Atom Electron Source (CAES) produces inherently cold electron bunches. The transverse beam properties have been investigated in detail, and the beam emittance measured to be a few nmrad for millimeter-sized beams [17,18], orders of magnitude lower than other sources. Consequently, the CAES will have a much smaller value of $d_{50,\epsilon}$ and given comparable values of $d_{50,s}$ and $d_{50,c}$, the CAES promises values of d_{50} below the current state-of-the art [19]. In contrast to the transverse beam properties, the longitudinal beam properties have hitherto remained largely unstudied, despite the relative simplicity with which the CAES can produce highly monochromatic electron beams.

In a CAES, ionization typically occurs in a region with width Δ_z determined by the spot size of the ionizing laser beam and can be as small as 10 μm. Given an extraction field of strength F which is created by electrodes separated by distance d the energy spread can be expressed as

$$\frac{\Delta U}{U_0} = \frac{\Delta_z}{d}. \tag{3}$$

Reduction of this value could in principle be achieved by reducing the photoionization laser beam size through the use of high-numerical-aperture optical systems, but these are not always feasible and the ionization width Δ_z will still be constrained by the diffraction-limited spot size. Using Rydberg atoms and the combination of a high-gradient electric field with a rapidly ionizing state may allow ionization widths of hundreds of nanometers or below, reducing the fractional energy spread by one to two orders of magnitude. If achieved, a system would effectively be "super-resolution," with electron emission spot sizes below the optical diffraction-limited spot sizes of the photoexcitation lasers.

Use of Rydberg atoms for the creation of monochromatic beams was first proposed in Ref. [20], but its application in the context of CAESs was first proposed in Ref. [12]. The scheme proposed there involves the creation of a beam of Rydberg atoms that enters into a high-gradient electric field. The atoms are ionized once the field value is large enough to permit field-assisted ionization. In principle, the Δ_z would then be limited by the gradient of the electric field. In practice, the evolution of Rydberg states through the electric field results in state mixing, leading to a range of threshold electric-field values and ionization rates. The degree to which Rydberg states mix is highly variable. Selective field ionization occurs when a state displays minimal mixing, and also rapidly ionizes near a specific value of the electric field [21]. By addressing states that undergo selective field ionization, it may be possible to reduce Δ_z well below optical diffraction-limited spot sizes.

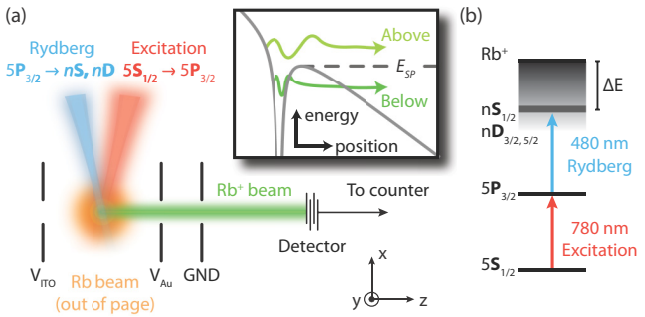

FIG. 1. A schematic of the experiment to produce Stark maps of ^{85}Rb. (a) A neutral beam of rubidium propagates along y, before entering a region of electric field produced between plates separated by 50 mm. Coupling to the Stark states is achieved with excitation and Rydberg laser beams, which are directed perpendicular to the field with polarizations parallel to the field. Ions are detected 680 mm downstream. Inset shows a plot of the electron potential versus position, showing the saddle-point energy E_{sp}. (b) The energy-level diagram for ^{85}Rb.

A key parameter in the study of the ionization of Rydberg atoms is the saddle-point energy $E_{sp} = -2\sqrt{F}$ (see Fig. 1), below which an electron cannot classically escape the ionic potential. Quantum mechanically, this corresponds to the energy below which only tunneling ionization can occur. Ionization occurs when the quasidiscrete hydrogenic basis states (Stark states) couple to the continuum. This coupling arises from the nonhydrogenic component of the Hamiltonian which, in turn, gives rise to anticrossings in the Stark spectrum. Near anticrossings, the behavior of state lifetimes can be dramatically altered, especially in the case of interference narrowing, where a stable state may have an avoided crossing with an unstable state, resulting in a reduction in the ionization rate of the unstable state by many orders of magnitude [22–29]. Interference narrowing has previously been used for selective field ionization of helium [20] and precision mapping of electric fields [30]. By applying selective field-ionization techniques to the CAES, it should be possible to produce a highly monochromatic electron beam, provided the appropriate state and selective ionization channel can be found. Here we map the Stark states of rubidium in the region around commonly used field strength values to identify states that selectively ionize and investigate their suitability for the production of highly monochromatic electron beams.

III. MAPPING STARK STATES

We performed a search for states which experience selective field ionization in the region below the saddle-point energy for $F = 600$ V/cm. A schematic of the experiment is shown

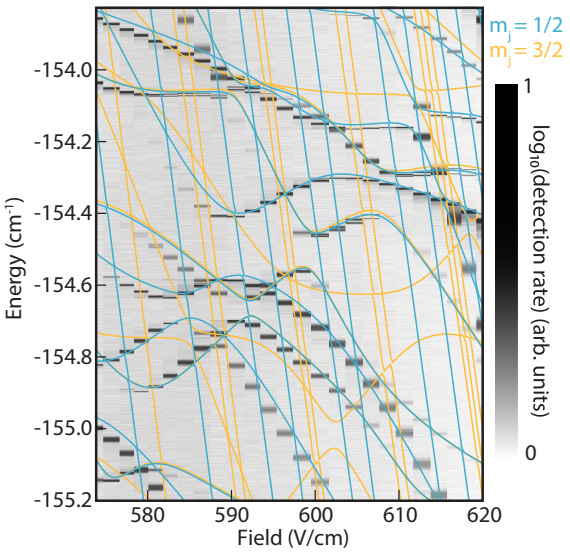

FIG. 2. A map of the Stark states, presented as a waterfall diagram, produced near the ionization threshold at $F = 600\,\mathrm{V/cm}$. The grayscale image shows the logarithm (base 10) of the rate of detected ionization events and the lines depict the calculated Stark states for both $m_j = 1/2$ [blue (dark gray)] and $m_j = 3/2$ [yellow (light gray)].

in Fig. 1. A neutral beam of rubidium effuses from an oven before passing through an aperture of $\phi 2\,\mathrm{mm}$ (where ϕ denotes diameter) and subsequently a 70 mm differential pumping tube of $\phi 7.5\,\mathrm{mm}$, and free-space propagates for 940 mm before entering the ionization region. An electric field is produced between two electrodes separated by 50 mm with $\phi 20\,\mathrm{mm}$ holes to allow ion extraction. Excitation to Stark states was performed by using a two-color process, with a continuous-wave (CW) excitation laser beam resonantly coupling the $5S_{1/2}F = 3$ and $5P_{3/2}F = 4$ states, and a CW probe laser beam coupling the exited $5P$ state to a high-lying Rydberg state. The laser beams are directed perpendicular to the electric field, with the polarization parallel to the field. The beams are focused as to intersect with the neutral atom beam as shown in Fig. 1 with spot sizes for the excitation and probe laser beams of 30 and 10 μm, respectively. Ions are accelerated towards a charge amplifying detector located 680 mm from the ionization region, where the current is amplified and filtered, with the discrimination of single-ionization events.

To map Stark states, an adjustable potential difference between the plates fixes the electric field, before the probe laser wavelength was scanned and the number of ionization events at a given wavelength recorded. The probe laser (linewidth $<500\,\mathrm{kHz}$) was scanned at 5000 discrete frequencies over 40 GHz and the number of ionization events were recorded for 750 ms at each point. For each change in the value of the electric field, the laser wavelength was reset and allowed 10 ms to respond and stabilize to avoid counting spurious ionization events. Upon completion of the laser scan, the electric field was adjusted and the wavelength scan repeated. Each scan took approximately one hour to complete and an entire Stark map took approximately one day to generate.

Figure 2 shows the map of Stark states for ^{85}Rb, both measured and calculated. The density plot displays the log (base 10) of the detected rate of ionization events, which has been normalized so the most rapidly ionizing state (measured at a rate of 17 kHz) appears black, with white indicating that no counts were detected. Background counts are expected from photoionization of Rydberg states and blackbody ionization while Penning ionization is not expected to contribute due to the low density. The measured rates of ionization are overlaid with the calculations of Stark states, with $m_j = 1/2$ states shown in blue (dark gray) and $m_j = 3/2$ states in yellow (light gray). Because the value of the electric field at the position of the atoms is not known precisely, a single value offset was applied to the measured field values to obtain agreement between the data to the calculations. It should be noted that the electric-field values used to produce the density plot in Fig. 2 are the mean of the measured field values recorded over the duration of each given scan. The variation in the measured field values relative to the mean-field value was approximately 0.1%. There is good agreement between predictions and observations, with mismatch attributable to field jitter, field inhomogeneity, and drift in the wavelength calibration.

The theoretical locations of Stark states were computed following the method detailed in Ref. [31]. The method numerically calculates the energy eigenvalues for a Hamiltonian of the form

$$\hat{H} = \hat{H}_0 + F\hat{z}, \tag{4}$$

where $\hat{H}_0$ is the Hamiltonian for the valence electron in the presence of the ionic core and $F\hat{z}$ is a perturbation due to the electric field of strength F directed along z. For excitation from the $5P_{3/2}$ states, we expect coupling to the $nS_{1/2}$, $nD_{3/2}$, and $nD_{5/2}$ states. With the probe laser polarization parallel to the electric field, we expect minimal coupling to $m_j = 5/2$ states, which are not observed in Fig. 2. The states were computed for 400 field values between $F = 550\,\mathrm{V/cm}$ and $F = 650\,\mathrm{V/cm}$ with 2000 states included in the calculation.

IV. SELECTIVE FIELD IONIZATION

Critical to the production of a monochromatic beam is the identification of states that experience a rapid growth in the ionization rate or, equivalently, a dramatic broadening of the resonance peak. One such process that can result in localized growth in the ionization rate is interference narrowing, which occurs when two Stark states that are coupled to the continuum with the same autoionization rates experience an anticrossing [32]. The coupling to the continuum for one of the eigenstates will vanish and the coupling for the other eigenstate will be enhanced due to the interference between the coupling amplitudes that govern their ionization. Such observations have been made previously in sodium [24,29], rubidium [33,34], and in cesium [35,36].

Another process that can result in localized growth in the ionization rate is when a stable "blue" state ($\Gamma \approx 0$) couples to a degenerate "red" state(s) ($\Gamma \gg 0$) which is (are) unbound, resulting in rapid ionization around the crossing [24]. An example of this latter behavior can be seen in Fig. 3, which shows a section of the Stark diagram in the region around

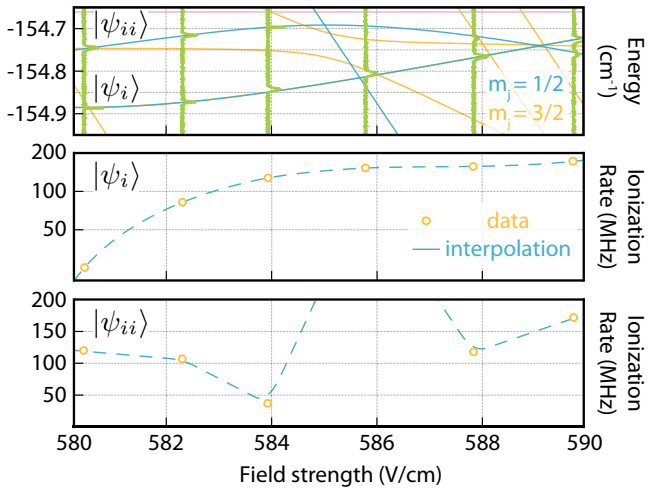

FIG. 3. Experimental Stark map in the region of 585 V/cm. The measured ion counts are shown in green (thick), and the calculated Stark states for $m_j = 1/2$ are shown in blue (dark gray) and for $m_j = 3/2$ are shown in yellow (light gray). State $|\psi_i\rangle$ undergoes monotonic growth in the ionization rate with respect to the electric field whereas, in contrast, state $|\psi_{ii}\rangle$ experiences a dramatic growth near a predicted anticrossing at $F = 585$ V/cm. The measured ionization rates for $|\psi_i\rangle$ and $|\psi_{ii}\rangle$ are shown in yellow (light gray) with the blue line (dark gray, dashed) showing the interpolation of the linewidth as a function of field strength. As no peak is present near the anticrossing, the linewidth of $|\psi_{ii}\rangle$ near $F = 586$ V/cm is not well known; a value of $\eta = 10$ (see text) was used to estimate the linewidth.

$F = 585$ V/cm. State $|\psi_{ii}\rangle$ shows a stable state evolving into a rapidly ionizing state near the crossing with a highly unstable state, which returns to a relatively stable state over a small change in field strength. This is in contrast to state $|\psi_i\rangle$, an initially stable state which becomes unstable with increasing field strength.

The state $|\psi_{ii}\rangle$ in Fig. 3, and other states in Fig. 2, show qualitatively the desired traits for producing a monochromatic beam; namely, a stable state which transitions to rapidly ionizing state over a small change in field. In the following section we model the ionization probability given to predict the effectiveness of selective field ionization for the minimization of energy broadening and therefore determine how monochromatic the electron beam can be.

V. BEAM MONOCHROMATICITY

To model the energy spread of the beam, the range of field values over which the beam is ionized must be calculated. We consider an apparatus optimized for field ionization by using high-gradient fields, such as the apparatus outlined in Ref. [12] or the apparatus currently under construction in our research group. These systems are similar to Fig. 1, but the electrode system is oriented along the same axis as the neutral atom beam propagation direction. They are optimized for the production of monochromatic electron beams with electrodes that can create a very uniform electric field in one region and high-gradient electric fields in adjacent regions, required for precise excitation and ionization, respectively. The combination of an optimized neutral atomic beam and adjacent regions of highly uniform electric fields with regions of high field gradient should allow creation of a high-quality beam of Rydberg atoms that can be efficiently ionized with a small ionization region (small Δ_z).

We assume an atom within the atomic beam traveling at speed v is excited to a Rydberg state $|\mathscr{R}\rangle$ in a uniform field of strength F_0 and propagates through a region with a high field gradient. Assuming the field is aligned along the z axis with a gradient of ζ, the field is then given by $F(z) = F_0 + \zeta z$. We define the effective ionization width $\Delta_{\text{eff}} \equiv 1/2(z_{\sigma^+} - z_{\sigma^-})$ as the region over which 68.2% of the atoms are ionized:

$$\Delta_{\text{eff}} = \tfrac{1}{2}[(z|\mathscr{P}(F) = 0.841) - (z|\mathscr{P}(F) = 0.159)], \quad (5)$$

allowing for direct comparison with Δ_z, typically defined as the standard deviation of the ionization laser spatial profile. $\mathscr{P}(F)$ denotes the cumulative probability that the atom will be ionized at a field between F_0 and F after having been excited in a field of strength F_0:

$$\mathscr{P}(F) = 1 - \exp\left[\frac{1}{\zeta \bar{v}_z}\int_{F_0}^{F} \Gamma(F')dF'\right], \quad (6)$$

where $\bar{v}_z$ is the mean atomic velocity within the beam and $\Gamma(F)$ is the ionization rate of the Rydberg state $|\mathscr{R}\rangle$. In expressing the cumulative probability as a function of the field strength F, we assume the field is linear in z and also that $t = (z - z_0)/\bar{v}_z$. Provided the form of $\Gamma(F)$ is known, Eqs. (3) and (5) allow the energy spread of the beam to be calculated. We insist that, for an ionization scheme to be useful, that the cumulative ionization probability be near unity after the anticrossing. If this were not the case, any Rydberg atoms not ionized would continue to propagate into a high-field region where they would be ionized via an alternate mechanism, resulting in a complicated longitudinal energy distribution and a reduction in beam monochromaticity.

By using the above formulation, we can calculate Δ_{eff} for the state shown in Fig. 3, which shows the measured ionization rate as a function of the electric-field strength that was interpolated to produce an approximation of $\Gamma(F)$. The ionization rate is determined by the width σ of the observed ionization peaks. In our apparatus, the maximum field gradient we can produce is on the order of $\zeta = 1 \times 10^9$ V/m^2. This value was calculated by using detailed modeling of the electrode system in SIMION [37] and shows the length scale over which the field has an appreciable gradient is 5 mm. Given a neutral rubidium beam produced from an oven at 373 K and an excitation field of 580 V/cm, with excitation to state $|\psi_i\rangle$ (Fig. 3), we calculate the ionization probability as a function of F by using equation (6). A rapid growth in the ionization probability occurs over approximately 250 nm and as expected and continues to increase with increasing F. While a localized growth in ionization probability is observed over some hundreds of nanometers, the total number of ionization events in this region is extremely small, owing to the small ionization rates. Consequently, the majority of the ionization takes places at higher values of the electric field and hence results in a ionization over a range of positions (large Δ_{eff}).

In contrast, the scale over which state $|\psi_{ii}\rangle$ destabilizes is much shorter due to the highly localized growth of the

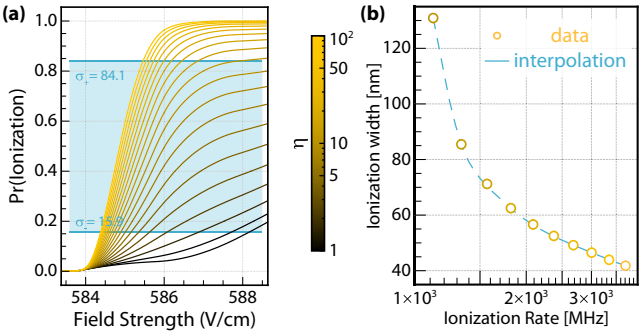

FIG. 4. Ionization properties of a selectively ionizing Rydberg state in rubidium. (a) Predicted cumulative ionization probability of $|\psi_{ii}\rangle$ as a function of electric-field strength around $F = 585\,\mathrm{V/cm}$. The blue shaded region from $\sigma_- = 15.9\%$ to $\sigma_+ = 84.1\%$ defines the region over which the beam ionizes. The color scale indicates the growth of ionization rate at the crossing, with $\eta = 1$ corresponding to 37 MHz. (b) Predicted ionization width as a function of the maximum ionization rate of $|\psi_{ii}\rangle$ at the crossing. The parameters for excitation and ionization are given in the text.

ionization rate. The exact growth in the ionization rate cannot be well predicted because no additional data were recorded in the region around the destabilization. Because there is no peak in the Stark map, we therefore include an enhancement of the ionization rate by a factor of η at the anticrossing. Previously, the ionization rate in the region of the crossing was measured by Ref. [24] to increase under similar conditions by two orders of magnitude relative to the stable state ($\eta = 10^2$), with a greater growth predicted but not measured. Assuming the value of Γ grows by a factor of η to a maximum rate Γ_M over the crossing, it is possible to calculate the expected value of Δ_{eff} given excitation to $|\psi_{ii}\rangle$, with all other parameters the same as were used to calculate the ionization width of $|\psi_i\rangle$.

Figure 4(a) shows the cumulative ionization probability for a rubidium atom excited to $|\psi_{ii}\rangle$ in the region around $F = 584\,\mathrm{V/cm}$. The different curves display how the cumulative ionization probability varies with the maximum ionization rate of $|\psi_{ii}\rangle$ at the anticrossing. It is clear that the ionization probability experiences highly localized growth and, as expected, with increased ionization rate the range of field values over which the ionization occurs decreases. In addition, a greater ionization rate also ensures near-unity ionization probability. For values of $\Gamma_M > 2.5 \times 10^9\,\mathrm{Hz}$, we calculate Δ_{eff} to be on the order of 50 nm, far below the tens of microns typically achieved by using photoionization and in the super-resolution regime (Δ_{eff} of order 100 nm). Figure 4(b) shows the ionization width Δ_{eff} as a function of the maximum ionization rate Γ_M. With greater values of Γ_M, the ionization width decreases, but it is clear that large growth in the ionization rate, at least $\eta > 30$, is required to produce super-resolution values of Δ_{eff}. For values of $\eta < 30$, values of Δ_{eff} near or below the diffraction limit are achievable; however, we are primarily interested in the super-resolution regime. A growth factor of $\eta = 30$, which corresponds to $\Gamma_M \approx 1 \times 10^9\,\mathrm{Hz}$ is not entirely unreasonable; in other work, a growth value of $\eta = 10^2$ has been measured [24], and separately a value of $\Gamma_M = 1 \times 10^9\,\mathrm{Hz}$ has been measured over a anticrossing [34]. A growth factor of $\eta = 30$ would yield a $\Delta_{\mathrm{eff}} = 130\,\mathrm{nm}$ and a higher growth rate, $\eta > 70$ (corresponding to $\Gamma_M > 2.5 \times 10^9\,\mathrm{Hz}$), is required to achieve $\Delta_{\mathrm{eff}} < 50\,\mathrm{nm}$. However, for growth rates less than $\eta \approx 80$, the cumulative ionization probability is below unity, meaning that any atoms not ionized will undergo ionization in the high-field region downstream, subsequently reducing the monochromaticity and increasing Δ_{eff}. This means that, for a monochromatic beam, we require a growth rate of at least $\eta = 80$, which would require an exceptional state with an ionization rate greater than that previously observed in Ref. [34]. Thus, in all likelihood, a sufficient value of Γ_M would not be reached to simultaneously ensure both efficient ionization and a small ionization width.

Further measurements of Γ_M are required to determine the suitability of state $|\psi_{ii}\rangle$ for monochromatic beam electron-beam production. The above results demonstrate that selective field ionization can result in ionization widths much smaller than conventional photoionization sources, but may come at the cost of ionization efficiency. One possible solution is to work in the region above the ionization threshold, where the transverse beam properties will be slightly degraded, but the ionization rates are typically many orders of magnitude higher. Provided an appropriate state with a localized growth in the ionization rate is used, a small ionization width could be combined with high-efficiency ionization. In the following section, we seek to validate this idea theoretically.

VI. MODELING ABOVE-THRESHOLD IONIZATION

The purpose of this section is to theoretically model the ionization rate for a state that experiences selective field ionization above the ionization threshold. We then seek to determine whether field ionization of Rydberg states is a viable method for highly monochromatic electron-beam production.

Calculation of the ionization width Δ_{eff} requires that one have precise knowledge of $\Gamma(F)$, and accurate prediction of the form of $\Gamma(F)$ is often difficult. In the case of hydrogen, the value of $\Gamma(F)$ can be calculated in a relatively straightforward manner [38], but for other atoms it is more complicated due to the coupling of states at the core and the associated avoided crossings of Stark states, though calculation of the lineshapes is possible [39]. For high-lying Rydberg states in alkali metals, the states of hydrogen provide a good approximation provided the quantum defect is small [40]. Since we are interested in the ionization rate of states near avoided crossings, we need only model the two-state system, provided the states are isolated.

More explicitly, to ensure the states are isolated, we require that the scale of the coupling between the states (V_c) is less than the difference in energy to neighboring states. Given the principal quantum number n, the separation of states to first order can be approximated by $(3/2)nF$, within an n manifold, before the first crossings with other n manifolds. The first crossings occur at a field strength of $1/(3n^5)$, hence the minimum energy separation for different values of n will vary as $1/(2n^4)$. The core coupling V_c can be approximated by using quantum-defect theory, where $V_c \approx \delta_m/n^4$ [21,41,42]. This suggests that, provided the quantum defect is small (less than 0.5), a two-level model should well approximate the system. In the case of rubidium, the δ_2 defect value for the

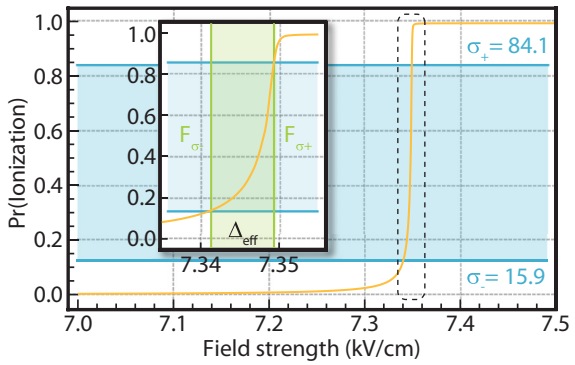

FIG. 5. Cumulative ionization probability of the $|17,0,13,3\rangle$ state for a rubidium beam (as detailed in Sec. V) as a function of electric-field strength. The blue shaded region from $\sigma_- = 15.9\%$ to $\sigma_+ = 84.1\%$ defines the region over which the beam ionizes. The inset shows a close up of the transition region, with the green area marking the range of the electric field over which the ionization occurs.

$nS_{1/2}$ states is approximately 0.18 and the values for $nP_{1/2,3/2}$ are approximately 0.29 [43], with the defect values for states of higher l being significantly smaller. Consequently, we use the two-level model to demonstrate the qualitative behavior, but do not expect quantitative agreement unless states of large l are considered.

Selective field-ionization processes above the ionization threshold usually occur when a stable "blue" state ($\Gamma \approx 0$) couples to degenerate "red" state(s) ($\Gamma \gg 0$) which are unbound, resulting in rapid ionization around the crossing; the field at which this occurs defines F_χ. We use a two-level model based on states of hydrogen A that allows for the calculation of $\Gamma(F)$ around F_χ. A similar model has been previously used to obtain excellent quantitative agreement for the ionization rate of sodium near the anticrossing of the $|12,6,3,2\rangle$ and $|14,0,11,2\rangle$ states [24] (labeled $|n,n_1,n_2,m\rangle$). By choosing states with a large value of $|m|$, we can ensure a small value of δ_2 and hence expect our model to be valid. The primary criterion for state selection is that a stable blue state crosses an unstable red state, which for even moderate electric fields is very common. We choose the states $|17,0,13,3\rangle$ and $|14,10,0,3\rangle$, but it should be emphasized that these are not unique. There are a multitude of states that display similar properties; we choose these simply because they are experimentally compatible with our system. In reality, the exact states to be used would, in great part, be determined by the core coupling V_c between the two states. The value of V_c is critical to determining the lineshape of state-selective ionization and hence the ionization width Δ_z but is not readily tunable, meaning that the crossing to be used must be selected for the appropriate value of V_c.

Using Eq. (6), it is again possible to calculate the cumulative ionization probability for a Rydberg atom propagating into an electric-field gradient as described above. We calculate the probability of ionization as a function of the electric field near the crossing of the $|17,0,13,3\rangle$ and $|14,10,0,3\rangle$ states (Fig. 5), by using $\bar{\Gamma}_-(F)$ [Eq. (A2)] [42] and an excitation field of 6 kV/cm, with the other parameters as in Sec. V. With a coupling strength of $V_c = \bar{\Gamma}_-(F_\chi)/4$ the rapid growth of the ionization rate near $F = F_\chi$ results in the rapid increase of the ionization probability, as was previously observed with below-threshold states. Due to the greatly increased ionization rate, on the order of 10^{10} Hz, a much higher ionization efficiency is predicted. From these data, we extract the ionization width of $\Delta_{\text{eff}} = 0.26\,\mu$m with unity probability for ionization. The value of Δ_{eff} is consistent with a previous estimate of the reduction of the ionization width via selective field ionization, which showed an improvement of one to two orders of magnitude compared with nonselective field ionization, with $\Delta_{\text{eff}} \approx 1\,\mu$m [12].

VII. CONCLUSION

Mapping of the Stark states below the ionization threshold allowed for the observation of selective field-ionization states, but insufficient resolution in the data around the localized growth of the ionization rate limited our ability to determine the states' suitability for the creation of a monochromatic electron beam. Further work is required to determine whether localized growth of the ionization rate below the ionization threshold is sufficient to allow for simultaneously efficient and localized ionization. It is possible that the low-ionization rates typical of states below the threshold will limit their usefulness in creation of monochromatic electron beams. Above the threshold, where ionization rates are much larger, we predict values of $\Delta_{\text{eff}} < 260$ nm are readily achievable. An ionization width on the order of hundreds of nanometers represents an improvement by a factor of at least ten compared with direct photoionization. Using high-numerical-aperture in-vacuum lenses permits laser spot sizes of the order a few microns, but getting below this limit represents a major challenge. By using field-assisted ionization of Rydberg atoms, any reduction in the ionization width linearly improves the beam monochromaticity, commensurate with a reduction of the value of d_{50}. If such a super-resolution ionization scheme were realized, it would result in an electron beam with a relative energy spread better than 1 part in 10^5, removing the need for a monochromator for many experiments. By implementing a high-efficiency photoexcitation scheme, for example, one similar to that already implemented in a cold atom source [44], this would allow for the creation of a high-current highly monochromatic electron beam. Additionally, the application of the same system to focused ion-beam science would be extremely powerful. For example, in a 30 kV cold atom beam ion source operating in low-current mode (0.1 pA), the expected value of d_{50} is 200 pm [19] when using photoionization. This value could potentially be reduced to $d_{50} = 50$ pm by using Rydberg ionization. Likewise, a field-ionization source operating in high-current mode (1 nA) could reach $d_{50} = 4$ nm, a factor ten below current state-of-the-art liquid-metal ion sources.

ACKNOWLEDGMENTS

The authors would like to thank Guyve Khalili for contributions to the two-level model and Francis Robicheaux for useful discussions. B.M.S. acknowledges the support of a University of Melbourne McKenzie Fellowship. This work was supported by the Australian Research Council Discovery

Project DP140102102 and by the EU through the FET-Open Xtrack Project HAIRS.

APPENDIX: MODELLING AVOIDED CROSSINGS

We seek to estimate the form of the ionization rate for a given state as a function of the electric field. We consider the two-state system of $|\phi_1\rangle$ and $|\phi_2\rangle$ with an energy separation $\hbar\delta = \mathscr{E}_1 - \mathscr{E}_2$, which experiences an anticrossing at a field of F_χ due to a coupling of strength V_c. Because we are interested in states that display selective field-ionization behavior, we consider the crossing of a stable blue state with an unstable red state. The Hamiltonian is then given by

$$\hat{H} = \begin{pmatrix} -\delta/2 & V_c \\ V_c & \delta/2 - i\Gamma/2 \end{pmatrix}, \tag{A1}$$

where Γ is the ionization rate of the dominant loss channel. At the anticrossing, the eigenstates will have the form $|\phi_1 \pm \phi_2\rangle$ where $|\phi_1\rangle$ and $|\phi_2\rangle$ are the eigenstates away from the crossing. The eigenvalues for the system can be extracted from the matrix $\hat{H}$, yielding the state energies $\bar{\delta}_\pm$ and ionization rates $\bar{\Gamma}_\pm$ for the upper and lower states of the mixed system:

$$\bar{\Gamma}_\pm = \tfrac{1}{4}\big(-\Gamma \pm \mathrm{Im}\big\{\sqrt{16V_c^2 - (\Gamma + 2i\delta)^2}\big\}\big),$$
$$\bar{\delta}_\pm = \pm\tfrac{1}{4}\mathrm{Re}\big\{\sqrt{16V_c^2 - (\Gamma + 2i\delta)^2}\big\}. \tag{A2}$$

The energy of the states $\mathscr{E}_1$ and $\mathscr{E}_2$ is calculated from the hydrogen Stark system, which we take to the fourth-order expansion [32]. The ionization rate Γ for the hydrogen Stark system can then be expressed as [45]

$$\Gamma = \frac{4R^{2n_2+m+1}}{n_1^3 n_2!(n_2+m)!}\exp\left\{-\frac{2R}{3} - \frac{n_1^3 F}{4}\left[34\big(n_2^2 + n_2 m\big) + 46n_2 + 7m^2 + 23m + \frac{53}{3}\right]\right\}, \tag{A3}$$

where $R = (-2\mathscr{E})^{3/2}/F$ and n_1, n_2, and m are the usual parabolic quantum numbers. By calculating $\mathscr{E}$, one can calculate a value of δ and, in conjunction with Eq. (A3), the ionization rates of the mixed system $\bar{\Gamma}_\pm$ can be calculated near the anticrossing.

By using quantum-defect theory one can estimate the expected core coupling [41] but, as a general trend, if the coupling is too weak, no strong state mixing is observed and narrowing either does not occur or only weakly occurs, resulting in no growth in the ionization rate. For stronger couplings, the effect begins to become delocalized and a growth in the ionization rate is seen over a range of field values. In the context of achieving highly localized ionization, the latter is highly undesirable. The maximum coupling rate occurs for any value of $V_c > \Gamma/4$, with the minimum ionization width and the maximum ionization rate simultaneously occurring for $V_c = \Gamma/4$. Physically, the actual value of coupling cannot be tuned as a simple parameter, but rather will be determined by the states in question. Some degree of tunability is present by changing the value of n_1 for the red state, moving to a neighboring crossing. If no states with desirable properties and appropriate coupling can be found, then the crossing of a different blue state should be considered. In practice a model, such as the one presented here, would be used to find potentially appropriate states and then a high-resolution scan performed experimentally to identify the optimum states.

[1] O. L. Krivanek, J. P. Ursin, N. J. Bacon, G. J. Corbin, N. Dellby, P. Hrncirik, M. F. Murfitt, and Z. S. Szilagyi, Philos. Trans. R. Soc., A **367**, 3683 (2009).

[2] B. Schaffer, K. Riegler, G. Kothleitner, W. Grogger, and F. Hofer, Micron **40**, 269 (2009).

[3] Q. M. Ramasse, C. R. Seabourne, D.-M. Kepaptsoglou, R. Zan, U. Bangert, and A. J. Scott, Nano Lett. **13**, 4989 (2013).

[4] S. Morishita, M. Mukai, K. Suenaga, and H. Sawada, Phys. Rev. Lett. **117**, 153004 (2016).

[5] A. Lafosse, M. Bertin, and R. Azria, Prog. Surf. Sci. **84**, 177 (2009).

[6] K. L. Moore, M. Schröder, Z. Wu, B. G. Martin, C. R. Hawes, S. P. McGrath, M. J. Hawkesford, J. F. Ma, F.-J. Zhao, and C. R. Grovenor, Plant Physiol. **156**, 913 (2011).

[7] P. E. Batson, *Transmission Electron Energy Loss Spectrometry in Materials Science and the EELS Atlas*, 2nd ed. (Wiley-VCH Verlag GmbH & Co KgaA, Weinheim, 2005), p. 353.

[8] B. J. Claessens, S. B. van der Geer, E. J. D. Vredenbregt, and O. J. Luiten, Phys. Rev. Lett. **95**, 164801 (2005).

[9] A. McCulloch, D. Sheludko, S. Saliba, S. Bell, M. Junker, K. Nugent, and R. Scholten, Nat. Phys. **7**, 785 (2011).

[10] R. W. Speirs, C. T. Putkunz, A. J. McCulloch, K. A. Nugent, B. M. Sparkes, and R. E. Scholten, J. Phys. B: At., Mol. Opt. Phys. **48**, 214002 (2015).

[11] A. J. McCulloch, B. M. Sparkes, and R. E. Scholten, J. Phys. B: At., Mol. Opt. Phys. **49**, 164004 (2016).

[12] L. Kime, A. Fioretti, Y. Bruneau, N. Porfido, F. Fuso, M. Viteau, G. Khalili, N. Šantić, A. Gloter, B. Rasser *et al.*, Phys. Rev. A **88**, 033424 (2013).

[13] P. C. Tiemeijer, M. Bischoff, B. Freitag, and C. Kisielowski, in *EMC 2008 14th European Microscopy Congress 1–5 September 2008, Aachen, Germany*, edited by M. Luysberg, K. Tillmann, and T. Weirich (Springer-Verlag, Berlin, Heidelberg, 2008), pp. 53–54.

[14] J. Barth and P. Kruit, Optik **101**, 101 (1996).

[15] P. W. Hawkes and E. Kasper, *Principles of Electron Optics* (Academic Press, London, 1996), Vol. 3.

[16] P. Hawkes and E. Kasper, *Principles of Electron Optics: Applied Geometrical Optics* (Academic Press, London, 1989).

[17] A. McCulloch, D. Sheludko, M. Junker, and R. Scholten, Nat. Commun. **4**, 1692 (2013).

[18] W. Engelen, M. van der Heijden, D. Bakker, E. Vredenbregt, and O. Luiten, Nat. Commun. **4**, 1693 (2013).

[19] J. J. McClelland, A. V. Steele, B. Knuffman, K. A. Twedt, A. Schwarzkopf, and T. M. Wilson, Appl. Phys. Rev. **3**, 011302 (2016).
[20] W. van de Water, D. R. Mariani, and P. M. Koch, Phys. Rev. A **30**, 2399 (1984).
[21] M. Førre and J. P. Hansen, Phys. Rev. A **67**, 053402 (2003).
[22] T. W. Ducas, M. G. Littman, R. R. Freeman, and D. Kleppner, Phys. Rev. Lett. **35**, 366 (1975).
[23] T. Gallagher, L. Humphrey, R. Hill, and S. Edelstein, Phys. Rev. Lett. **37**, 1465 (1976).
[24] M. G. Littman, M. L. Zimmerman, and D. Kleppner, Phys. Rev. Lett. **37**, 486 (1976).
[25] R. Damburg and V. Kolosov, Phys. Lett. A **61**, 233 (1977).
[26] T. F. Gallagher, L. M. Humphrey, W. E. Cooke, R. M. Hill, and S. A. Edelstein, Phys. Rev. A **16**, 1098 (1977).
[27] J.-L. Vialle and H. Duong, J. Phys. B: At. Mol. Phys. **12**, 1407 (1979).
[28] S. Liberman and J. Pinard, Phys. Rev. A **20**, 507 (1979).
[29] J.-Y. Liu, P. McNicholl, D. A. Harmin, J. Ivri, T. Bergeman, and H. J. Metcalf, Phys. Rev. Lett. **55**, 189 (1985).
[30] D.-H. Yang, D. Lieberman, P. van der Straten, T. Bergeman, and H. Metcalf, Phys. Rev. A **40**, 5026 (1989).
[31] J. Grimmel, M. Mack, F. Karlewski, F. Jessen, M. Reinschmidt, N. Sándor, and J. Fortágh, New J. Phys. **17**, 053005 (2015).
[32] M. L. Zimmerman, M. G. Littman, M. M. Kash, and D. Kleppner, Phys. Rev. A **20**, 2251 (1979).
[33] S. Feneuille, S. Liberman, J. Pinard, and A. Taleb, Phys. Rev. Lett. **42**, 1404 (1979).
[34] S. Feneuille, S. Liberman, E. Luc-Koenig, J. Pinard, and A. Taleb, J. Phys. B: At. Mol. Phys. **15**, 1205 (1982).
[35] C. Chardonnet, D. Delande, and J. C. Gay, Opt. Commun. **51**, 249 (1984).
[36] C. Chardonnet, D. Delande, and J. C. Gay, Phys. Rev. A **39**, 1066 (1989).
[37] SIMION, http://www.simion.com, Scientific Instrument Services, Inc., 1027 Old York Rd, Ringoes, NJ 08551, United States (2011).
[38] R. Damburg and V. Kolosov, J. Phys. B: At. Mol. Phys. **12**, 2637 (1979).
[39] D. A. Harmin, Phys. Rev. A **30**, 2413 (1984).
[40] T. Gallagher, *Rydberg Atoms* (Cambridge University Press, Cambridge, 2005), Vol. 3.
[41] I. Komarov, T. Grozdanov, and R. Janev, J. Phys. B: At. Mol. Phys. **13**, L573 (1980).
[42] G. Khalili, Ph.D. thesis, Université Paris Sud - Paris XI, 2015, https://tel.archives-ouvertes.fr/tel-01233284/.
[43] W. Li, I. Mourachko, M. W. Noel, and T. F. Gallagher, Phys. Rev. A **67**, 052502 (2003).
[44] B. M. Sparkes, D. Murphy, R. J. Taylor, R. W. Speirs, A. J. McCulloch, and R. E. Scholten, Phys. Rev. A **94**, 023404 (2016).
[45] R. Feynman, J. Hollingsworth, M. Vennettilli, T. Budner, R. Zmiewski, D. P. Fahey, T. J. Carroll, and M. W. Noel, Phys. Rev. A **92**, 043412 (2015).

PHYSICAL REVIEW A **96**, 013427 (2017)

Ionization spectra of highly Stark-shifted rubidium Rydberg states

Jens Grimmel,* Markus Stecker,† Manuel Kaiser, Florian Karlewski, Lara Torralbo-Campo, Andreas Günther, and József Fortágh‡

Center for Quantum Science, Physikalisches Institut, Eberhard-Karls-Universität Tübingen, Auf der Morgenstelle 14, D-72076 Tübingen, Germany

(Received 21 March 2017; published 26 July 2017)

We report on the observation and numerical calculation of ionization spectra of highly Stark-shifted Rydberg states of rubidium beyond the classical ionization threshold. In the numerical calculations, a complex absorbing potential (CAP) allows us to predict the energy levels and ionization rates of Rydberg states in this regime. Our approach of adjusting the CAP to the external electric field reduces the number of free parameters from one per resonance to a single one. Furthermore, we have measured the ionization spectra of magneto-optically trapped rubidium atoms which are excited to principal quantum numbers of 43 and 70 at various electric fields. The emerging ions are detected using an ion optics. We find good agreement between the numerically and experimentally obtained spectra.

DOI: 10.1103/PhysRevA.96.013427

I. INTRODUCTION

Stark spectra of alkali-metal Rydberg states above the classical ionization threshold exhibit an intricate energy-level structure with strongly varying ionization behavior, including rapidly ionizing states as well as the extreme of narrow resonances where ionization is almost suppressed [1]. The latter feature is clearly distinct from hydrogen, where the ionization rate of a given state grows exponentially with the applied external electric field [2]. The study of these ionization spectra of nonhydrogenic atoms is therefore of particular interest not only from a fundamental point of view, but also for the prospect of improved control over the ionization process in Rydberg gases.

The method of complex rotation (CR) is well known for the theoretical treatment of ionization rates of highly Stark-shifted states of hydrogen and alkali atoms [3–5]. It is applied by substituting the location and momentum operators in the Hamiltonian by the complex terms $\hat{r} \rightarrow \hat{r} \cdot \exp(i\theta)$ and $\hat{p} \rightarrow \hat{p} \cdot \exp(-i\theta)$, respectively, which results in a non-Hermitian Hamiltonian. This leads to complex eigenvalues of the Hamiltonian which can be used to obtain the energy levels and linewidths, i.e., the ionization rates in the present case. As an alternative to this method, a complex absorbing potential (CAP) can be employed to create a non-Hermitian Hamiltonian [6–9]. The CAP is added to the original Hamiltonian in the form $-i\eta W(\vec{r})$. Both of these methods, CR and CAP, work with free parameters θ and η, respectively, which are determined for every single resonance of the system by a variational method.

In a previous work [10] we have calculated Stark-shifted energy levels including the corresponding dipole matrix elements by diagonalization of a matrix representation of the Hamiltonian [11]. While this methods yields very precise results for spectra at electric fields below the classical ionization threshold, the broadening of the states by ionization at higher fields can no longer be neglected. Hence, in this work, we combine the matrix diagonalization method with an adaptive CAP method by choosing a potential that is adjusted to the external electric field. This removes the need to determine the free parameter η for each resonance separately and thereby greatly reduces the computational effort for the numerical calculation. We calculate ionization spectra near the unperturbed $43S_{1/2}$ and $70S_{1/2}$ ^{87}Rb Rydberg states for electric fields far beyond the classical ionization threshold. Furthermore, we present an experiment in which rubidium atoms in a magneto-optical trap (MOT) are excited to Rydberg states in the presence of an external electric field. When the atoms ionize from these Stark-shifted Rydberg states, the ions are guided to a detector by an ion-optical system [12]. We have measured ionization spectra by ramping up the external electric field and scanning the excitation laser frequency near the aforementioned states.

The methods we present here can be used to search for resonances from the ionization spectra, such as highly Stark-shifted states which have a desirable ionization rate or sensitivity to the external electric field across a certain range. Furthermore, this opens up the possibility to tune a coupling between ionizing and nonionizing states by the external electric field. This way of tailoring the ionization process is highly useful for the design of sources of cold ions and electrons for microscopy purposes [13–16]. Moreover, a precise knowledge of these ionization spectra opens new perspectives for experiments incorporating Rydberg atoms near surfaces, where static electric fields arise due to adsorbates [17–20].

II. APPLICATION OF A COMPLEX ABSORBING POTENTIAL

The Hamiltonian $\hat{H}$ for an atom in an external electric field F_E along the z axis is given by

$$\hat{H} = \hat{H}_0 + F_E \hat{z}, \tag{1}$$

where $\hat{H}_0$ denotes the unperturbed Hamiltonian, i.e., the unperturbed atomic energy levels, which are calculated from quantum defect theory [21–24]. Note that all formulas in this

*jens.grimmel@uni-tuebingen.de
†markus.stecker@uni-tuebingen.de
‡fortagh@uni-tuebingen.de

section are given in atomic units. The Stark-shifted energy levels corresponding to this Hamiltonian are routinely calculated by choosing a subset of the basis given by $\hat{H}_0$, representing $\hat{H}$ as a matrix in this basis and computing the eigenvalues of this matrix [11]. For the high-field region considered in this work, it is crucial to include all total angular momentum quantum numbers j in the subset of the basis. However, as we use a two-photon excitation scheme in the experiment, we can limit our calculations to $|m_j| \in \{1/2,3/2,5/2\}$. The subset of the basis is then chosen symmetrically in energy above and below the desired energy region. The convergence of this method can be assured by increasing the subset of the basis until changes of the resulting eigenvalues are well below the experimental resolution. In our previous work, we have extended the calculations of [11] and determined a measure D for the transition strength in the three-level ladder scheme by calculating the dipole matrix elements between the states [10]. Here, we further extend these calculations by introducing a complex absorbing potential (CAP) to the model, which allows for an estimate of the ionization rates of Stark-shifted states in the regime of high electric fields beyond the classical ionization threshold.

The CAP is added to the Hamiltonian $\hat{H}$, resulting in a new non-Hermitian Hamiltonian,

$$\hat{H}_{\mathrm{CAP}} = \hat{H} - i\eta W(\hat{r}, F_{\mathrm{E}}). \tag{2}$$

In general, the free parameter $\eta \in \mathbb{R}^+$ should be adjusted for each resonance that is studied at each value of the electric field. However, in the approach we present in this work, we also adjust the function $W(\hat{r}, F_{\mathrm{E}})$ depending on the electric field, which in effect allows us to choose the parameter η only once for a whole region of the spectrum.

We have chosen a CAP combining $\hat{r}^6$ as in Ref. [8] with the Heaviside function Θ as in Ref. [7], similar to the rectangular-box CAP in Ref. [25]:

$$W(\hat{r}, F_{\mathrm{E}}) = \Theta[\hat{r} - r_{\mathrm{c}}(F_{\mathrm{E}})][\hat{r} - r_{\mathrm{c}}(F_{\mathrm{E}})]^6. \tag{3}$$

This results in a spherical potential scaling as $\hat{r}^6$, but radially shifted to a radius r_{c}. The matrix representation of this CAP is calculated using the same radial wave functions as for the $\hat{z}$ operator, which are obtained by integrating a parametric model potential [26]. It is worth noting that due to its spherical symmetry, this choice for the CAP does not introduce any coupling between different states and therefore results in a purely diagonal matrix representation. Furthermore, the Hamiltonian can still be treated separately for different values of $|m_j|$ and the basis for the matrix representation is chosen as in previous works by including enough states nearby in energy for the results to converge [10,11].

The potential $W(\hat{r}, F_{\mathrm{E}})$ is changed along with the external electric field F_{E} via the radius r_{c}. To determine r_{c}, we use a Coulomb potential to approximate the atomic potential with an external electric field,

$$V_{\mathrm{C,E}} = -\frac{1}{r} - F_{\mathrm{E}} z. \tag{4}$$

This potential is also used for the definition of the classical ionization threshold, which is given by

$$E_{\mathrm{ion}} = -2\sqrt{F_{\mathrm{E}}}, \tag{5}$$

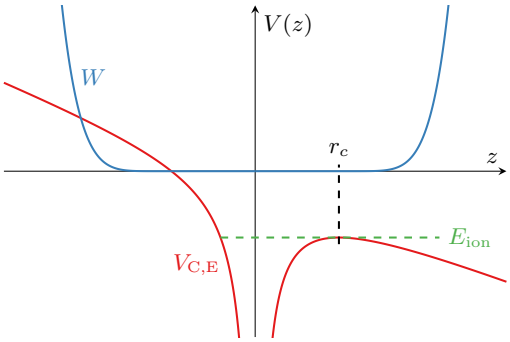

FIG. 1. Illustration of the complex absorbing potential (CAP). The parameter r_{c} is determined according to Eq. (6) which places it at the radius of the saddle point of the potential $V_{\mathrm{C,E}}$ [see Eq. (4)]. Note that in this 1D graph along the z axis, the saddle point appears as a local maximum. This choice of r_{c} creates a potential W that resembles the shape of r^6 but is spherically shifted by r_{c}.

and marks the saddle point where the potential opens towards the continuum. The location of the saddle point, which is a local maximum along the z axis, is then given by

$$r_{\mathrm{c}}(F_{\mathrm{E}}) = \frac{1}{\sqrt{F_{\mathrm{E}}}}, \tag{6}$$

and we use this radius to place the onset of r^6 in the potential $W(\hat{r}, F_{\mathrm{E}})$, as illustrated in Fig. 1. Graphically speaking, this allows us to distinguish between an inside and an outside region of the atom and to ensure that the CAP only absorbs the parts of the wave functions that protrude to the outside region.

The Hamiltonian $\hat{H}_{\mathrm{CAP}}$ may yield complex eigenvalues which can be written as

$$E_{\mathrm{c}} = E_r - i\frac{\Gamma}{2}, \tag{7}$$

where the real part determines the energy level E_r of the resonance and the imaginary part determines its ionization rate Γ. In the calculations, the free parameter η from Eq. (2) is varied for exemplary values of the electric field. The first of these exemplary points is conveniently chosen near the classical ionization threshold to determine a first estimate for η because, assuming no other previous knowledge about the spectrum, this region generally features a large number of resonances with different ionization rates. Subsequently, further points are chosen at higher electric fields to continue the variation of η following the initial estimate. The parameter η is then fixed to a value in the center of a region which leaves the resulting eigenvalues E_c mostly unchanged. For all spectra investigated here, this region spans multiple orders of magnitude of η, which is a direct consequence of our field-dependent choice for the CAP. It is also worth noting that within this region, changes of η affect the broadest resonances, i.e., broader than the frequency range in the experiment, more than narrow resonances. Therefore, the resulting changes do not visibly alter the spectrum.

In order to create a diagram of the spectrum from the calculated eigenvalues in terms of intensity I with respect to the transition energy E, we sum up Lorentzian peaks for

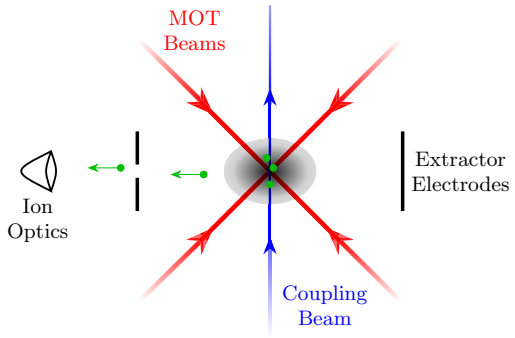

FIG. 2. Schematic diagram of the experimental setup. Rubidium atoms are trapped at the intersection of the MOT beams (red). Atoms from the MOT are continuously excited to Rydberg states by the coupling laser (blue) at various electric fields, which are applied via the extractor electrodes. The field is also used to guide the ions (green) to the ion optics.

each resonance at a given electric field,

$$I(E) = \frac{D}{\pi} \frac{\Gamma}{\Gamma^2 + (E - E_r)^2}. \quad (8)$$

For the resulting resonances which would have linewidths smaller than 25 MHz, we set the linewidth to 25 MHz, which is approximately the linewidth of resonances in the region that is not dominated by ionization and also the resolution of our experimental data. Please note that ionization is the only decay channel that we consider in these calculations. All other decay channels as well as redistribution by blackbody radiation are negligible for strongly ionizing states.

III. EXPERIMENTAL SETUP

We excite Rydberg atoms in a cloud of ^{87}Rb atoms confined to a standard six-beam magneto-optical trap (MOT). The cooling light is provided by a diode laser running at ≈780 nm, which is frequency stabilized to the cooling transition $5S_{1/2}(F = 2) \rightarrow 5P_{3/2}(F = 3)$ with a red detuning of 10 MHz. The MOT is positioned in between two electrodes which are used both to generate the desired electric field at the position of the MOT and to extract ions out of the MOT (see Fig. 2). An ion optics consisting of a set of electrostatic lenses guides the ions to a microchannel plate detector (MCP) where they can be detected with single-particle sensitivity [12].

The excitation of rubidium atoms from the ground state to a Rydberg level is done in a two-step process. The lower transition $5S_{1/2} \rightarrow 5P_{3/2}$ is driven by the MOT beams themselves. The upper transition from the intermediate state $5P_{3/2}$ to a Rydberg level is done by a frequency-doubled, grating stabilized diode laser (Toptica DL-SHG pro) with a tuneable wavelength around 480 nm (hereafter referred to as "coupling laser"). The frequency of the coupling laser is stabilized by a HighFinesse WSU-30 Wavemeter. The ionization rate of the excited Rydberg atoms is determined by counting the emerging ions with the MCP detector.

In order to measure the ionization spectra of highly Stark-shifted Rydberg states, we fix the coupling laser to a certain frequency and ramp the voltage at the extractor electrodes to probe the desired field region and simultaneously detect the generated ions. This ramp is repeated for different coupling laser frequencies. The MOT beams and the coupling beam remain switched on during the whole measurement and the MOT is continuously loaded from rubidium dispensers. With this scheme, we were able to scan a large field region in a reasonably small measurement time, while still getting a good signal-to-noise ratio.

We measured Stark spectra near the unperturbed $43S_{1/2}$ and $70S_{1/2}$ state in a wide electric-field range, mostly around and above the classical ionization limit. In these measurements, we used voltage ramps with a ramping speed of 1 V/s and 25 MHz steps for the frequency of the coupling laser.

IV. MEASUREMENTS AND COMPARISON TO CAP-THEORY RESULTS

We present experimental results in comparison to results from our numerical calculations near the unperturbed state $43S_{1/2}$ in Fig. 3. The experimental resolution of the voltage was 100 mV, equivalent to 30.6 mV/cm, and the step size of the electric field in the numerical calculations was 40 mV/cm. The classical ionization threshold for this state is at ≈127 V/cm, so it is located just within the lower limit of the electric-field range of this figure. The variation of the free parameter η described in Sec. II led to a value of $\eta = 1\times10^6$ in the depicted region and we used ≈4000 states for the matrix representation of $\hat{H}_{\mathrm{CAP}}$. The results from the experiment and numerical calculations are in very good agreement. Both data sets clearly show a general broadening of the lines with increasing electric field as one would naively expect above the classical ionization threshold. However, we also find some resonances which are still narrow even at high electric fields as well as overlapping narrow and broad resonances, for example at ≈143 V/cm in Figs. 3(a) and 3(b).

The results near the unperturbed state $70S_{1/2}$ are depicted in Figs. 4–7. The experimental results were recorded with a resolution of 50 mV, equivalent to 15.4 mV/cm, and the numerical calculation was performed using steps of 10 mV/cm. The ionization threshold near this state is within the range of Fig. 4 at ≈16.1 V/cm. In this region, the variation of the free parameter η resulted in a value of $\eta = 2\times10^5$ and the matrix for $\hat{H}_{\mathrm{CAP}}$ is represented using ≈10 000 states. Again, we find a general broadening of the resonances beyond the classical ionization threshold. This broadening increases as the electric field gets stronger, but even in the high-field range of Fig. 6 we still find some narrow resonances with linewidths on the order of magnitude of our experimental resolution of 25 MHz.

In the highest-field range (see Figs. 6 and 7), the larger ionization rates result in overlapping resonances with different linewidths. In some parts of these spectra, the results from the numerical calculations deviate from the experimental results showing antiresonancelike features instead of resonances, e.g., in Fig. 7(a), where such a feature starts at 30.5 V/cm near −1 GHz and crosses the whole frequency range of the recorded spectrum up to 31 V/cm and 2 GHz. These parts of the spectra, where we find deviations from Lorentzian line shapes, may be interpreted as Fano resonances [27]. A Fano-type resonance arises due to interference between different excitation paths to an ionized continuum state. Such Fano resonances have

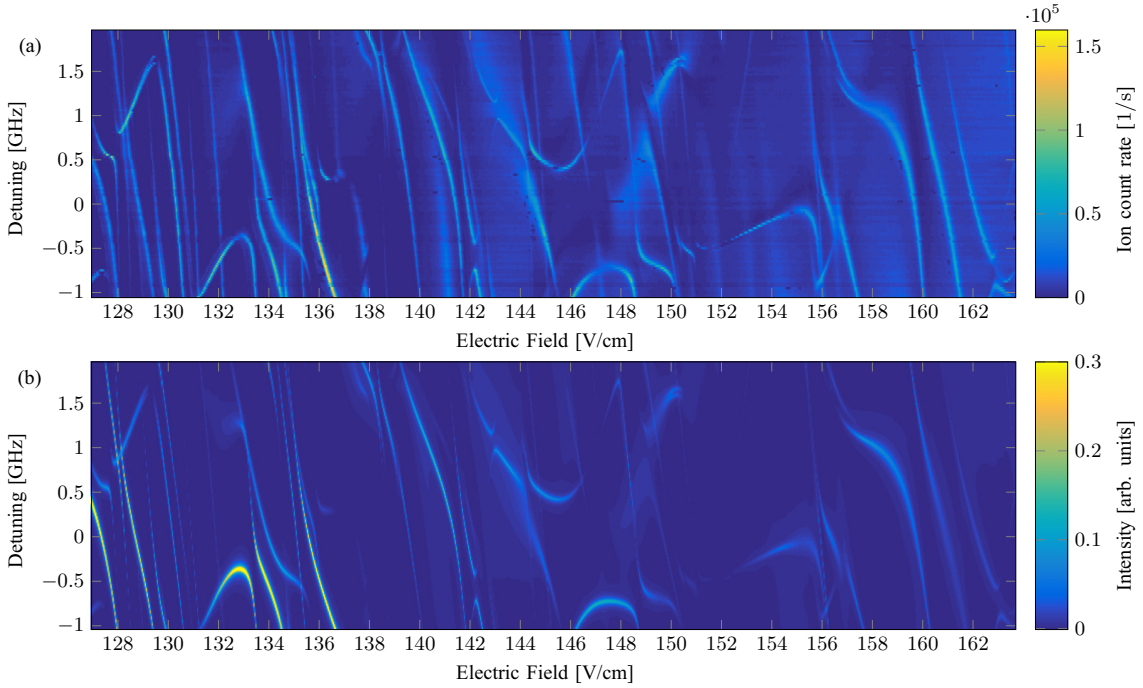

FIG. 3. Ionization Stark spectrum near $43S_{1/2}$. (a) Detected ion signal from the experiment. (b) Results from the numerical calculations for $\eta = 1\times10^6$. The detuning is given relative to the unperturbed state. We have applied a linear scaling to match the electric field from the experiment to the theoretical results. The classical ionization threshold is located at $\approx$127 V/cm.

been observed previously in similar systems [28–30]. In the present case, besides the discrete Rydberg state that decays to a continuum state by autoionization, there is also the possibility of direct photoionization. Furthermore, several overlapping Rydberg resonances with possibly different ionization rates may lead to more complicated interference effects and thereby

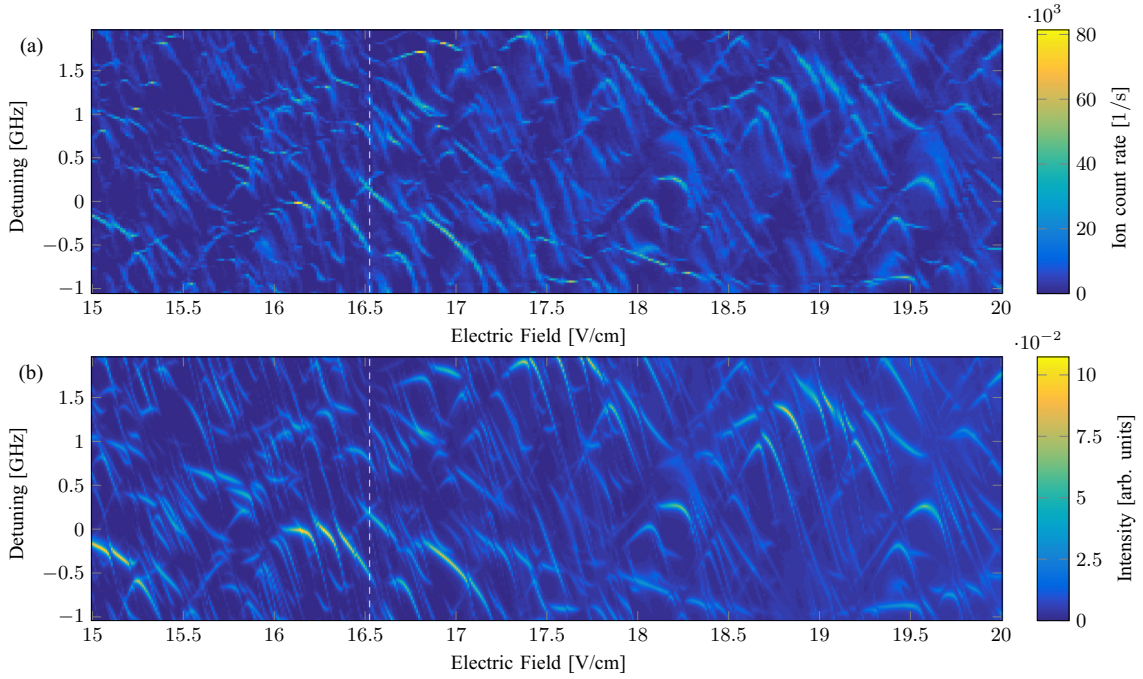

FIG. 4. Ionization Stark spectrum near $70S_{1/2}$. (a) Detected ion signal from the experiment. (b) Results from the numerical calculations for $\eta = 2\times10^5$. The detuning is given relative to the unperturbed state. We have applied a linear scaling to match the electric field from the experiment to the theoretical results. The classical ionization threshold is located at $\approx$16.1 V/cm. The white dashed lines mark the cut that is shown in more detail in Fig. 8(a).

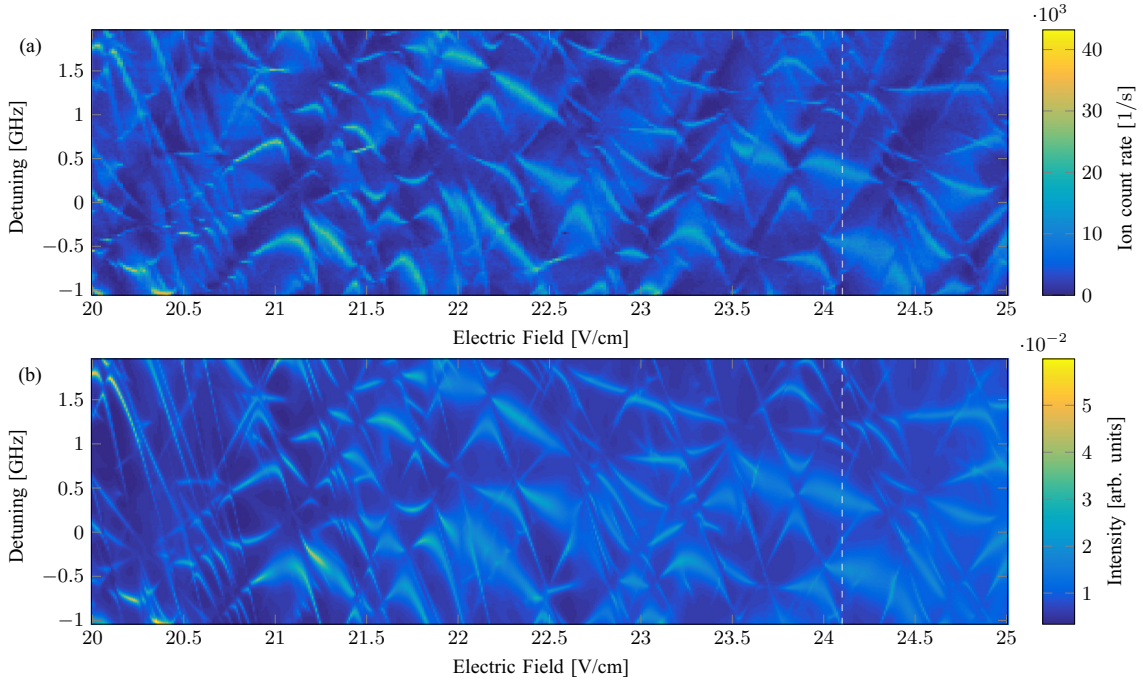

FIG. 5. Ionization Stark spectrum near $70S_{1/2}$. Continuation from Fig. 4. The white dashed lines mark the cut that is shown in more detail in Fig. 8(b).

more convoluted spectral features. A complete study of these possible Fano resonances may yield a more accurate prediction of the spectrum, but is beyond the scope of this work.

The numbers of states that were used for the matrix representations of the Hamiltonians were determined in order to calculate a dataset which is bigger than what is shown in this work. We estimate that ≈3000 and ≈6000 states should be enough to reproduce our results near $43S_{1/2}$ and $70S_{1/2}$, respectively. Therefore, all results from the numerical calculations are well converged in the regions depicted in Figs. 3–7. Some discrepancies between the results may arise from slow drifts of the voltage source that was used in the experiment. Since the measurement was performed for one

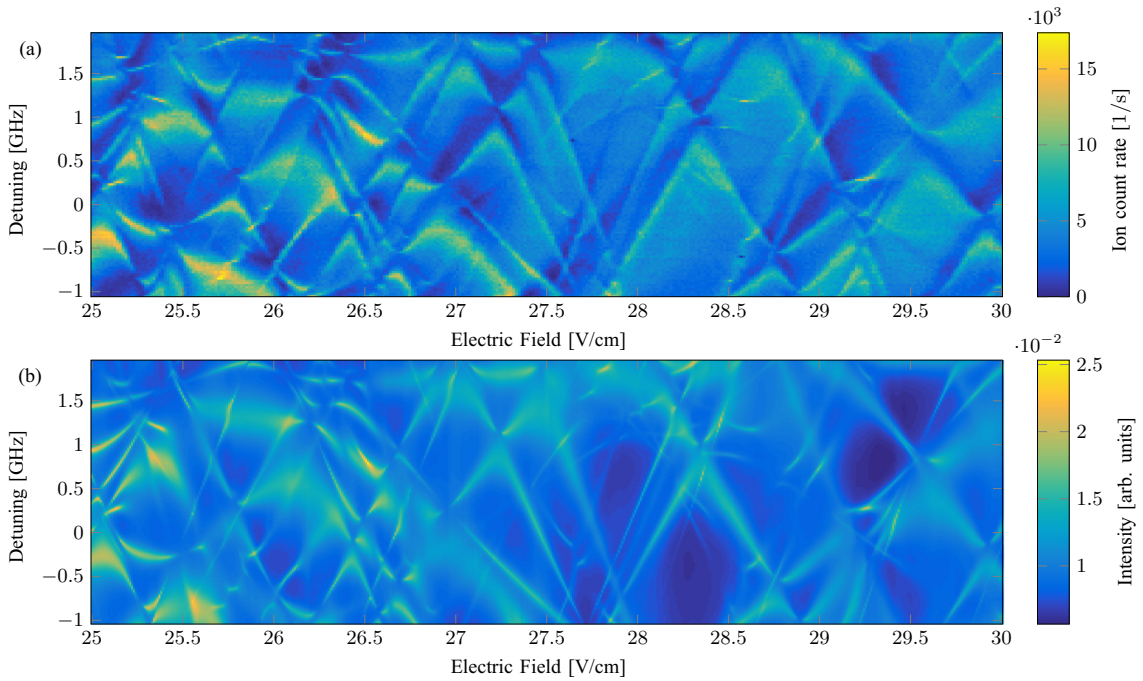

FIG. 6. Ionization Stark spectrum near $70S_{1/2}$. Continuation from Fig. 5.

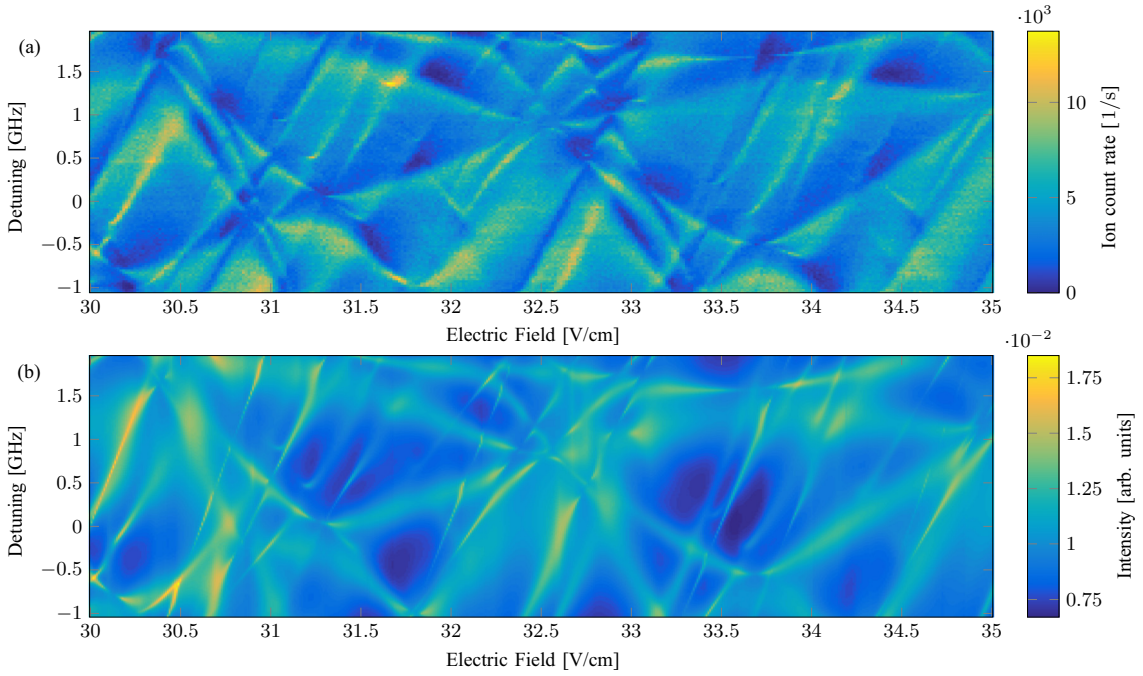

FIG. 7. Ionization Stark spectrum near $70S_{1/2}$. Continuation from Fig. 6.

horizontal line in the data after the other, this results in a horizontal mismatch of the experimental data of up to ± 0.05 V/cm in comparison to the numerically calculated results. Another minor source of deviations between the results may arise since the detection efficiency in the experiment changes as the extractor voltage is increased. Therefore, the ion counts we obtain from the experiment do not scale directly to the results for the intensity from the numerical simulations on the whole range simultaneously. However, this effect is small for the figures presented here since the color maps have been rescaled for each electric-field range separately.

For a more detailed analysis of the results from the experiment and the numerical calculations, we present cuts of the spectra at two different values of the electric field from Figs. 4 and 5 in Fig. 8. The data shown in Fig. 8(a) corresponds to an external electric field of 16.53 V/cm, i.e., just above the classical ionization threshold. In this region, the peak positions and widths of the experimentally detected and numerically calculated ionization spectra agree within our experimental frequency resolution of 25 MHz. For the higher electric field of 24.10 V/cm shown in Fig. 8(b), we find that the shapes of the two resonances with the highest intensities deviate slightly, namely, by an asymmetry of the experimentally obtained signals. We see these asymmetries as another possible manifestation of Fano resonances in this system. Further deviations in the region between 1.3 and 2 GHz can be mapped to an electric-field region of ± 0.05 V/cm and are caused by drifts of the voltage source, as discussed before, in combination with the high sensitivity of these particular resonances to the external electric field (see Fig. 5).

V. CONCLUSION

In this work, we have implemented an extension of the CAP method, in which we alter the shape of the complex

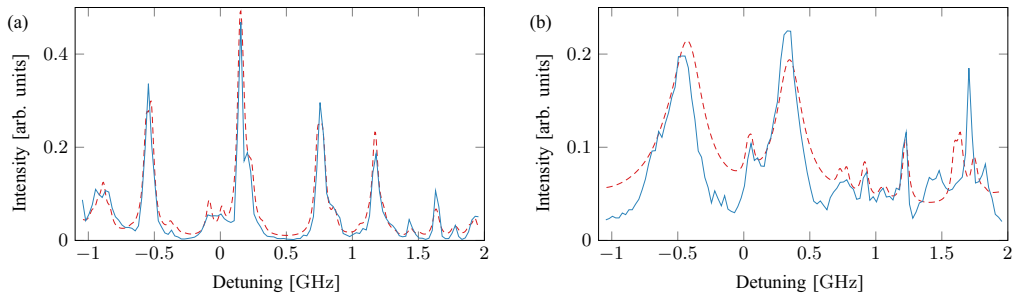

FIG. 8. Ionization Stark spectra from the experiment (blue solid lines) and the numerical calculations (red dashed lines) near $70S_{1/2}$ at (a) 16.53 V/cm (see Fig. 4) and (b) 24.10 V/cm (see Fig. 5). While we find agreement within our experimental resolution of 25 MHz in (a), some small deviations can be seen in (b). The two highest peaks from the experimental data in (b) have a slightly asymmetric line shape, which may indicate possible Fano resonances. Furthermore, we find discrepancies around 1.3–2 GHz, which we attribute to drifts of the voltage source that was used in the experiment and the high sensitivity of these resonances to the electric field.

absorbing potential according to the change of the external electric field. Furthermore, we have presented experimental results from a setup in which rubidium atoms are continuously ionized through Rydberg states in the presence of an external electric field. Our experimental data show the existence of rich ionization spectra with sharp resonances even far beyond the classical ionization threshold. The presented numerical calculations are capable of predicting the measured spectra of highly Stark-shifted Rydberg states, including the sharp resonances. Thus it is suitable for improving control over the excitation to such states and the subsequent ionization process. An in-depth theoretical study of the possible Fano resonances that we have observed in the experimental data may improve this control even further.

ACKNOWLEDGMENTS

This work was financially supported by the EU FET-Open Xtrack Project HAIRS and by Deutsche Forschungsgemeinschaft through SFB TRR21 and SPP 1929 (GiRyd). M.S. acknowledges financial support from Landesgraduiertenförderung Baden-Württemberg. We thank P. Schmelcher for advice on complex rotation methods. We thank N. Schopohl and N. Sándor for helpful discussions.

[1] T. F. Gallagher, *Rydberg Atoms*, 1st ed. (Cambridge University Press, Cambridge, 1994).
[2] R. J. Damburg and V. V. Kolosov, J. Phys. B **12**, 2637 (1979).
[3] W. P. Reinhardt, Int. J. Quantum Chem. **10**, 359 (1976).
[4] W. P. Reinhardt, Annu. Rev. Phys. Chem. **33**, 223 (1982).
[5] G. D. Stevens, C.-H. Iu, T. Bergeman, H. J. Metcalf, I. Seipp, K. T. Taylor, and D. Delande, Phys. Rev. A **53**, 1349 (1996).
[6] R. Kosloff and D. Kosloff, J. Comput. Phys. **63**, 363 (1986).
[7] U. V. Riss and H. D. Meyer, J. Phys. B **26**, 4503 (1993).
[8] S. Sahoo and Y. K. Ho, J. Phys. B **33**, 2195 (2000).
[9] Y. K. Ho, Few-Body Syst. **54**, 31 (2013).
[10] J. Grimmel, M. Mack, F. Karlewski, F. Jessen, M. Reinschmidt, N. Sándor, and J. Fortágh, New J. Phys. **17**, 053005 (2015).
[11] M. L. Zimmerman, M. G. Littman, M. M. Kash, and D. Kleppner, Phys. Rev. A **20**, 2251 (1979).
[12] M. Stecker, H. Schefzyk, J. Fortágh, and A. Günther, New J. Phys. **19**, 043020 (2017).
[13] L. Kime, A. Fioretti, Y. Bruneau, N. Porfido, F. Fuso, M. Viteau, G. Khalili, N. Šantić, A. Gloter, B. Rasser, P. Sudraud, P. Pillet, and D. Comparat, Phys. Rev. A **88**, 033424 (2013).
[14] D. Murphy, R. E. Scholten, and B. M. Sparkes, Phys. Rev. Lett. **115**, 214802 (2015).
[15] D. J. Thompson, D. Murphy, R. W. Speirs, R. M. W. van Bijnen, A. J. McCulloch, R. E. Scholten, and B. M. Sparkes, Phys. Rev. Lett. **117**, 193202 (2016).
[16] E. Moufarej, M. Vielle-Grosjean, G. Khalili, A. J. McCulloch, F. Robicheaux, Y. J. Picard, and D. Comparat, Phys. Rev. A **95**, 043409 (2017).
[17] A. Tauschinsky, R. M. T. Thijssen, S. Whitlock, H. B. van L. van den Heuvell, and R. J. C. Spreeuw, Phys. Rev. A **81**, 063411 (2010).
[18] R. P. Abel, C. Carr, U. Krohn, and C. S. Adams, Phys. Rev. A **84**, 023408 (2011).
[19] H. Hattermann, M. Mack, F. Karlewski, F. Jessen, D. Cano, and J. Fortágh, Phys. Rev. A **86**, 022511 (2012).
[20] K. S. Chan, M. Siercke, C. Hufnagel, and R. Dumke, Phys. Rev. Lett. **112**, 026101 (2014).
[21] W. Li, I. Mourachko, M. W. Noel, and T. F. Gallagher, Phys. Rev. A **67**, 052502 (2003).
[22] M. Mack, F. Karlewski, H. Hattermann, S. Höckh, F. Jessen, D. Cano, and J. Fortágh, Phys. Rev. A **83**, 052515 (2011).
[23] J. Han, Y. Jamil, D. V. L. Norum, P. J. Tanner, and T. F. Gallagher, Phys. Rev. A **74**, 054502 (2006).
[24] K. Afrousheh, P. Bohlouli-Zanjani, J. A. Petrus, and J. D. D. Martin, Phys. Rev. A **74**, 062712 (2006).
[25] R. Santra and L. S. Cederbaum, J. Chem. Phys. **115**, 6853 (2001).
[26] M. Marinescu, H. R. Sadeghpour, and A. Dalgarno, Phys. Rev. A **49**, 982 (1994).
[27] U. Fano, Phys. Rev. **124**, 1866 (1961).
[28] S. Feneuille, S. Liberman, J. Pinard, and A. Taleb, Phys. Rev. Lett. **42**, 1404 (1979).
[29] T. S. Luk, L. DiMauro, T. Bergeman, and H. Metcalf, Phys. Rev. Lett. **47**, 83 (1981).
[30] D. A. Harmin, Phys. Rev. A **26**, 2656 (1982).

PHYSICAL REVIEW A **96**, 043401 (2017)

Observation of the motional Stark shift in low magnetic fields

Manuel Kaiser,[1,*] Jens Grimmel,[1] Lara Torralbo-Campo,[1] Markus Mack,[1] Florian Karlewski,[1] Florian Jessen,[1] Nils Schopohl,[2,†] and József Fortágh[1,‡]

[1]*Center for Quantum Science, Physikalisches Institut, Eberhard-Karls-Universität Tübingen, Auf der Morgenstelle 14, D-72076 Tübingen, Germany*

[2]*Center for Quantum Science, Institut für Theoretische Physik, Eberhard-Karls-Universität Tübingen, Auf der Morgenstelle 14, D-72076 Tübingen, Germany*

(Received 16 May 2017; revised manuscript received 5 July 2017; published 2 October 2017)

We report on the observation of the motional Stark effect of highly excited ^{87}Rb Rydberg atoms moving in the presence of a weak homogeneous magnetic field in a vapor cell. Employing electromagnetically induced transparency for spectroscopy of an atomic vapor, we observe the velocity-, quantum state-, and magnetic-field-dependent transition frequencies between the ground and Rydberg excited states. For atoms moving at velocities around 400 m/s, the principal quantum number $n = 100$ of the valence electron, and a magnetic field of $B = 100$ G, we measure a motional Stark shift of $\sim$10 MHz. Our experimental results are supported by numerical calculations based on a diagonalization of the effective Hamiltonian governing the valence electron of ^{87}Rb in the presence of crossed electric and magnetic fields.

DOI: 10.1103/PhysRevA.96.043401

The motional Stark effect (MSE) introduces a coupling between the electronic structure of electronically bound particles and their center-of-mass motion in an external field. This correlation pointed out in the seminal work of Lamb [1] plays an important role in fusion plasma diagnostics [2,3] for measuring the magnetic fields, in astrophysics for the evaluation of hydrogen spectra in the vicinity of neutron stars [4,5], as well as in solids for the magneto-Stark effect of excitons [6]. Although the atomic motion in magnetic fields is always accompanied by the MSE [7–11] and the center-of-mass motion of atoms becomes entangled with the internal dynamics [12–14], the MSE has received little attention so far. With advanced spectroscopic techniques [15,16] and the quest for the development of quantum devices based on hot atomic vapors [17–22], the MSE of atoms becomes a measurable quantity and adds features of key importance: atoms are no longer described by a single wave function but a two-body core-electron wave function that is coupled through a pseudomomentum. At the same time, atoms are highly controllable quantum systems and enable the development of general models and experimental test opportunities for the coupled two-body problem of charged particles in external fields with direct impact on research on plasmas, electron-hole pairs [23,24], and particle-antiparticle symmetries [25].

In our paper we extend the investigation of the MSE to low magnetic fields and quantify it on an element other than hydrogen. For ^{87}Rb Rydberg atoms we measured spectral shifts up to 10 MHz with a spectroscopic resolution of 2 MHz for the principal quantum number $n = 100$ and a field of 100 G, using the phenomenon of electromagnetically induced transparency (EIT) on atoms in a thermal vapor cell. We complement the experimental data with numerical calculations of an atom in crossed magnetic and electric fields and thereby show that our theory based on an effective two-body system describes the complex rubidium Rydberg atom well.

The elementary attributes of atoms that govern all interaction processes with the electromagnetic field are charge and spin. Pieced together from orbital angular momentum and spin, the magnetic moments of atoms interact with the field of magnetic induction $\mathbf{B}$ and give rise to various splittings and changes of the internal atomic energy structure. As a consequence, the spectrum of atoms moving in the presence of a $\mathbf{B}$ field may, besides the Doppler shift, be altered because a charge moving at velocity $\mathbf{v}$ in the presence of a magnetic induction field experiences in its (instantaneous) rest frame a Lorentz electric field,

$$\mathbf{E}_L = \mathbf{v} \times \mathbf{B}. \tag{1}$$

This causes the positively charged nucleus and the electrons of an atom to sense a Lorentz force acting in opposite directions, when moving in a magnetic field (see Fig. 1). Consequently excited atoms in motion will emit a spectrum featuring not only the usual Doppler shift but also a Stark effect whose magnitude is primarily dependent on the atom's velocity and flight direction.

In distinction from the hydrogen atom (and its isotopes) the theoretical description of the electronic structure of heavier atoms poses a formidable many-body problem that cannot be solved exactly. Therefore, one has to rely on an approximate description in terms of an effective hydrogenlike problem, in which the bound-state spectrum of the excited valence electron of an alkali-metal atom with mass M can be well described by the spherically symmetric effective potential $V_{\text{eff}}(r)$ of Marinescu *et al.* [26]. Here the variable $r = |\mathbf{r}^{(e)} - \mathbf{r}^{(c)}|$ denotes the distance between the valence electron at position $\mathbf{r}^{(e)}$ and a collective coordinate $\mathbf{r}^{(c)}$ that determines the position of the center of mass of the ionic core with charge $Z|e| - (Z-1)|e| = |e|$ and mass $m^{(c)} = M - m^{(e)}$.

We therefore propose to describe the spectrum of an alkali-metal Rydberg atom moving in the presence of external electromagnetic fields with the effective two-body

*manuel.kaiser@student.uni-tuebingen.de
†nils.schopohl@uni-tuebingen.de
‡fortagh@uni-tuebingen.de

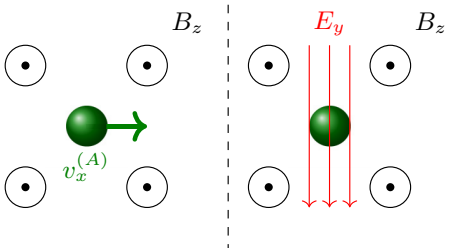

FIG. 1. Atoms moving in the laboratory frame at velocity $\mathbf{v}^{(A)}$ in the presence of a magnetic induction field $\mathbf{B}$ are in their reference frame subject to a Lorentz electric field [Eq. (1)].

Hamiltonian:

$$H^{(2)} = \frac{[\mathbf{p}^{(c)} - |e|\mathbf{A}(\mathbf{r}^{(c)})]^2}{2m^{(c)}} + \frac{[\mathbf{p}^{(e)} + |e|\mathbf{A}(\mathbf{r}^{(e)})]^2}{2m^{(e)}} + V_{\text{eff}}(|\mathbf{r}^{(e)} - \mathbf{r}^{(c)}|) + \frac{\mu_B}{\hbar} g_S \mathbf{S}\cdot\mathbf{B} + |e|\boldsymbol{\mathcal{E}}\cdot(\mathbf{r}^{(e)} - \mathbf{r}^{(c)}). \quad (2)$$

Here $\boldsymbol{\mathcal{E}}$ is a homogeneous static external electric field, and $\mathbf{B} = \text{rot}\mathbf{A}$ is a homogeneous external magnetic induction field, in the symmetric gauge $\mathbf{A}(\mathbf{x}) = \frac{1}{2}\mathbf{B}\times\mathbf{x}$. It is convenient to rewrite $H^{(2)}$ in the center-of-mass frame with new variables, $\mathbf{R} = \frac{m^{(e)}\mathbf{r}^{(e)} + m^{(c)}\mathbf{r}^{(c)}}{M}$ and $\mathbf{r} = \mathbf{r}^{(e)} - \mathbf{r}^{(c)}$ with the conjugate momenta $\mathbf{P} = \mathbf{p}^{(c)} + \mathbf{p}^{(e)} = \frac{\hbar}{i}\nabla_R$ and $\mathbf{p} = \frac{m^{(c)}}{M}\mathbf{p}^{(e)} - \frac{m^{(e)}}{M}\mathbf{p}^{(c)} = \frac{\hbar}{i}\nabla_r$. However, the associated Schrödinger eigenvalue problem for this Hamiltonian is not separable, because for $\mathbf{B} \neq \mathbf{0}$ the total momentum $\mathbf{P}$ is not conserved. Instead the Cartesian components $\mathcal{P}_a$ of the pseudomomentum

$$\boldsymbol{\mathcal{P}} = \mathbf{p}^{(c)} + |e|\mathbf{A}(\mathbf{r}^{(c)}) + \mathbf{p}^{(e)} - |e|\mathbf{A}(\mathbf{r}^{(e)}) = \mathbf{P} - \frac{|e|}{2}\mathbf{B}\times\mathbf{r} \quad (3)$$

are conserved [27]:

$$[\mathcal{P}_a, H^{(2)}] = 0, \quad [\mathcal{P}_a, \mathcal{P}_{a'}] = 0. \quad (4)$$

These commutator relations engender the existence of a complete system of orthonormal two-body eigenfunctions $\Psi_{\mathbf{k},\nu}(\mathbf{r}^{(e)},\mathbf{r}^{(c)}) \equiv \widetilde{\Psi}_{\mathbf{k},\nu}(\mathbf{R},\mathbf{r})$ that are eigenfunctions of both operators, $\mathcal{P}_a$ and $H^{(2)}$, simultaneously:

$$H^{(2)}\widetilde{\Psi}_{\mathbf{k},\nu} = E_{\mathbf{k},\nu}\widetilde{\Psi}_{\mathbf{k},\nu}, \quad \mathcal{P}_a\widetilde{\Psi}_{\mathbf{k},\nu} = \hbar k_a \widetilde{\Psi}_{\mathbf{k},\nu}. \quad (5)$$

Here ν is a multi-index labeling intrinsic quantum states of the valence electron. It follows, assuming box normalization with regard to the center-of-mass variable $\mathbf{R}$, that the sought eigenfunctions of $H^{(2)}$ and $\mathcal{P}_a$ are [23]

$$\widetilde{\Psi}_{\mathbf{k},\nu}(\mathbf{R},\mathbf{r}) = \frac{\exp\left[i\left(\mathbf{k} + \frac{|e|}{2\hbar}\mathbf{B}\times\mathbf{r}\right)\cdot\mathbf{R}\right]}{\sqrt{L^3}}\psi_{\mathbf{k},\nu}(\mathbf{r}), \quad (6)$$

where $\psi_{\mathbf{k},\nu}(\mathbf{r})$ is an eigenfunction associated with a single-particle Hamiltonian $H_{\mathbf{k}}^{(1)}$ depending parametrically on the eigenvalue $\hbar\mathbf{k}$ of the pseudomomentum $\boldsymbol{\mathcal{P}}$ [12]:

$$H_{\mathbf{k}}^{(1)}\psi_{\mathbf{k},\nu}(\mathbf{r}) = E_{\mathbf{k},\nu}\psi_{\mathbf{k},\nu}(\mathbf{r}). \quad (7)$$

We then find that Eq. (7) has, besides the terms dependent on $\hbar\mathbf{k}$, the guise of the standard Hamiltonian of the valence electron of an alkali-metal atom [28], including paramagnetic, diamagnetic, and electric-field interactions:

$$H_{\mathbf{k}}^{(1)} = \frac{\hbar^2\mathbf{k}^2}{2M} + \frac{\mathbf{p}^2}{2\mu} + V_{\text{eff}}(r) + \frac{\mu_B}{\hbar}(g_L\mathbf{L} + g_S\mathbf{S})\cdot\mathbf{B} + |e|\left(\boldsymbol{\mathcal{E}} + \frac{\hbar\mathbf{k}}{M}\times\mathbf{B}\right)\cdot\mathbf{r} + \frac{|e|^2}{8\mu}(\mathbf{B}\times\mathbf{r})^2, \quad (8)$$

with effective mass $\frac{1}{\mu} = \frac{1}{m^{(e)}} + \frac{1}{m^{(c)}}$, g factor $g_L = 1 - \frac{m^{(e)}}{m^{(c)}}$, and orbital angular momentum operator $\mathbf{L} = \mathbf{r}\times\mathbf{p}$. For the atom velocity in the Heisenberg picture one obtains $\mathbf{v}^{(A)} = \frac{d}{dt}\mathbf{R} = \frac{1}{i\hbar}[\mathbf{R}, H^{(2)}] = \frac{1}{M}(\mathbf{P} + \frac{|e|}{2}\mathbf{B}\times\mathbf{r})$. We can now eliminate the center-of-mass momentum $\mathbf{P}$ instead of the pseudomomentum $\boldsymbol{\mathcal{P}}$, see Eq. (3), and obtain

$$\mathbf{v}^{(A)} = \frac{1}{M}(\boldsymbol{\mathcal{P}} + |e|\mathbf{B}\times\mathbf{r}). \quad (9)$$

For strong magnetic fields the term $|e|\mathbf{B}\times\mathbf{r}$ can have a high impact on the atomic motion [29]. However, in weak magnetic fields such as considered here and at thermal atom speeds $\mathbf{v}^{(A)}$ the term can be neglected on the level of accuracy of our measurements up to Rydberg levels $n < 110$. This permits replacing $\mathbf{v}^{(A)} \leftarrow \frac{\hbar\mathbf{k}}{M}$ and interpreting the term $\frac{\hbar\mathbf{k}}{M}\times\mathbf{B}$ in the effective single-particle Hamiltonian Eq. (8) as a Lorentz electric field; see Eq. (1). For Rydberg levels as high as $n = 150$ the correction to $\mathbf{v}^{(A)}$ due to the dipole term in Eq. (9) amounts to $\sim$100 m/s. The difference between $\mathbf{v}^{(A)}$ and $\frac{\hbar\mathbf{k}}{M}$ may be seen better in other experiments, for example by monitoring the dipole mode of an ultracold alkali-metal atom cloud moving in a magnetic trap, by separating an atomic beam in a Stern-Gerlach-like experiment by laser excitation and thereby changing the internal energy structure or by measuring the structure factors (quantum correlations) of a classical gas during excitation to Rydberg states.

Even though the MSE is similar to the regular Stark effect at first sight, there is an important difference, as a $\mathbf{B}$ field cannot do work on a moving atom and therefore cannot ionize it. Hence, using Eq. (1), we can still analyze the MSE numerically on the basis of Eq. (8) as if it was a system in crossed fields configuration. The position operator $\mathbf{r}$ can be expressed in spherical coordinates where the angular parts can be evaluated with matrix elements from [30]. For the calculation of the radial wave functions we use the parametric model potential $V_{\text{eff}}(r)$ from [26], adapted to the experimental situation with the theory of [31]. We then calculate the energy levels of the crossed fields system using an energy matrix diagonalization similar to [32]. The energy levels in zero field are calculated using quantum defects from [33]. For each energy eigenvalue $E_{\mathbf{k},\nu}$ we represent the corresponding eigenvector of $H_{\mathbf{k}}^{(1)}$ as a linear combination of zero-field eigenstates, to calculate the dipole transition strength taking into account the laser polarizations as in [34]. These eigenvectors for states in external fields are also used to estimate the dipole moment $\mathbf{d}_{\mathbf{k},\nu} = -|e|\langle\Psi_{\mathbf{k},\nu}\,|\,\mathbf{r}\,|\,\Psi_{\mathbf{k},\nu}\rangle$ from Eq. (9), resulting in a calculated difference of velocity $\mathbf{v}^{(A)}$ and the pseudomomentum on the order of 0.1 m/s for the conditions of our experiment.

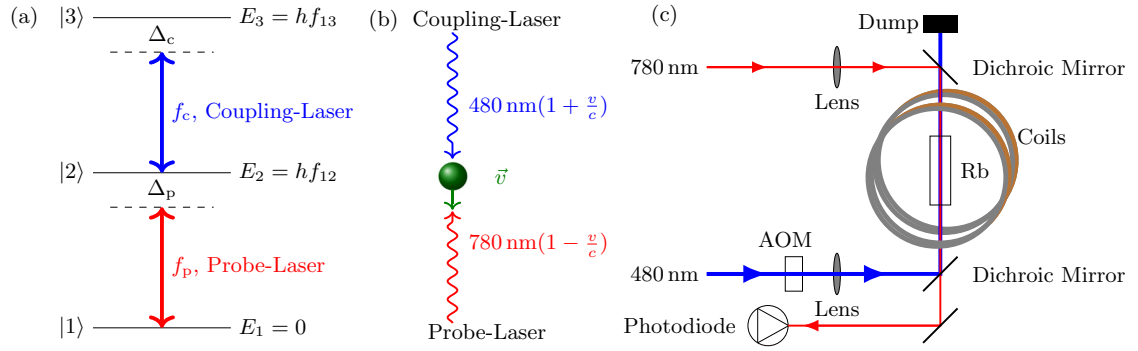

FIG. 2. (a) Energy-level diagram for EIT spectroscopy in ladder configuration. A strong-coupling beam at ∼480 nm induces a narrow transparency window for a weak probe beam at ∼780 nm. (b) Detunings from the resonance frequencies can be compensated by Doppler shifts of moving atoms. By detuning both lasers reversely only a selected velocity class contributes to the EIT signal. (c) Optical setup for the EIT spectroscopy. The coupling laser is intensity modulated with an acousto-optic modulator (AOM) and focused inside a vapor cell. It is overlapped in the cell with the counterpropagating probe laser, whose transmission is detected on a photodiode. The cell at ∼50 °C is placed in between two magnetic coils in Helmholtz configuration.

On the experimental side, we analyze the motional Stark shifts by using a two-photon spectroscopy method based on EIT in a ladder scheme similar to [15]. A strong laser which couples the intermediate state $5P_{3/2}$ and a Rydberg state leads to a narrow transparency window for a laser probing the lower $5S_{1/2} \rightarrow 5P_{3/2}$ transition, in case both lasers are in resonance with an atomic transition [see Fig. 2(a)]. The difference in frequency of the two transitions allows us to select a velocity class $v^{(A)}$ by detuning the laser frequencies f_p and f_c according to the Doppler shifted two-photon resonance condition

$$\Delta_p + \Delta_c = v^{(A)}\left(\frac{f_p - f_c}{c}\right), \tag{10}$$

with the detunings Δ_p and Δ_c of the probe and coupling laser, respectively, and the speed of light c [see Fig. 2(b)]. We can select atoms at rest (100 m/s) from a vapor with Maxwell-Boltzmann distributed atom velocities by fixing the probe laser frequency to the atomic transition, i.e., $\Delta_p = 0\,\text{MHz}\,(\Delta_p = f_p\frac{v^{(A)}}{c} \approx 128\ \text{MHz})$. If we scan the coupling laser over the atomic resonance, the maximum transparency in zero field then appears for a coupling laser detuning of $\Delta_c = 0$ MHz $(\Delta_c \approx -209\ \text{MHz})$.

For our measurement we use a standard rubidium vapor cell with a length of 75 mm at ∼50 °C enabling us to obtain spectra from a large range of velocity classes up to ∼600 m/s. The cell is placed in between a pair of coils in Helmholtz configuration which provides fields up to 100 G [see Fig. 2(c)]. The magnetic field is calibrated using a Hall sensor with an error smaller than 0.1 G leaving only a small offset magnetic field. Stray electric fields are effectively canceled by charges inside the cell [15].

The linearly polarized coupling laser (TA-SHG pro, Toptica) at 480 nm with a power of ∼80 mW is focused inside the cell (∼150 μm $\frac{1}{e^2}$ width). An also linearly polarized but counterpropagating probe beam (DL pro, Toptica) at 780 nm is overlapped with the coupling laser in the cell and is detected with a photodiode (APD110A, Thorlabs). For a better signal-to-noise ratio we use a lock-in amplifier (HF2LI, Zurich Instruments) which modulates the intensity of the coupling laser with an AOM and demodulates the probe laser signal from the photodiode. Each of the lasers is locked to a Fabry-Perot interferometer (FPI 100, Toptica). The FPI of the probe laser is locked to a frequency comb (FC 1500, Menlo Systems). The coupling laser FPI is controlled by a wavelength meter (WS Ultimate 2, HighFinesse) which is calibrated to the beat of the coupling laser frequency at 960 nm with the frequency comb. Within the measurement times the frequency accuracy of our laser system is better than 2 MHz.

We investigate the MSE by comparing the shifts at different velocity classes in a magnetic field. The probe beam is always on resonance with the corresponding Doppler shifted transition frequency. The coupling laser is scanned and at each step the photodiode signal is recorded for 10 s. The **B** field is set to a fixed value for each cycle. We estimate the errors of the peak-center frequencies by fitting Lorentzian peaks to the obtained EIT spectrum, averaging over multiple measurement cycles and adding the uncertainties of 2 MHz of the lasers. The measured spectra are fitted to the numerical calculations with a fixed offset magnetic field for all velocity classes as the only free parameter.

The motional electric field for atoms moving with ∼390 m/s in a field of 98 G is ∼0.038 V/cm. This results in a shift of ∼10 MHz for the measured spectrum of the $100D_{5/2}$ state [see Fig. 3(a)]. A single resonance is shown in detail [see Fig. 3(b)] where the theory values (arrows) are calculated as described before with a matrix dimension of 20 000, where a variation in the dimension only accounts for a submegahertz variation in frequency. Within the limits of our experimental accuracy we find good agreement between the experiment and the theory for an offset magnetic-field parameter smaller than 1 G. Moreover, they match well for measurements of other states (not shown here), which entails the demonstration of the strong dependence of the MSE on the quantum state.

Furthermore atoms resting and moving parallel to the **B** field do not show a motional Stark shift [inset of Fig. 3(b)]. For this measurement we changed the direction of the magnetic field and recorded EIT spectra of the $100D_{5/2}$ state in a field of 98 G. Due to geometrical restrictions a shorter cell was used for this part of the experiment. Even though no shift is observed, the transmission peak shows an asymmetry. Simulations of the line shape of the EIT signal taking into account the MSE for

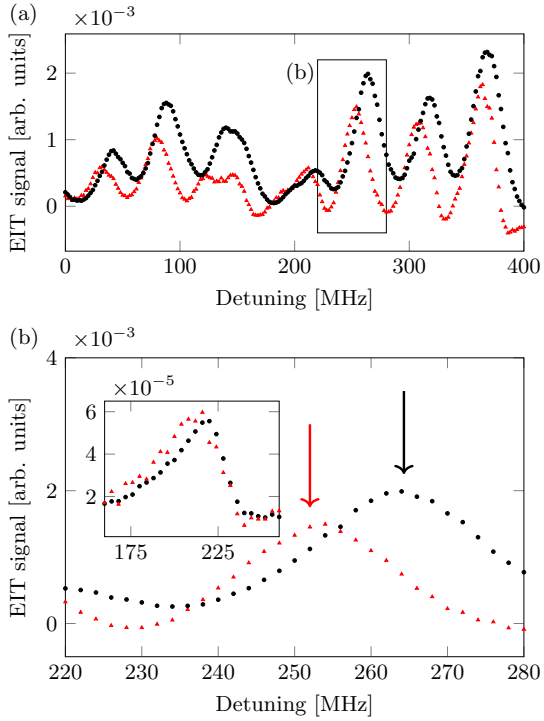

FIG. 3. (a) The EIT signal for the $100D_{5/2}$ state is shown in dependence on the coupling laser detuning Δ_c relative to the selected velocity class. The motional Stark shifts are on the order of 10 MHz in a field of 98 G for atoms at rest (black dots) compared to atoms moving at $v^{(A)} = 390$ m/s (red triangles). (b) EIT signal in dependence of Δ_c for the $100D_{5/2}$ in detail for two velocity classes $v^{(A)} = 0$ m/s (black dots) and $v^{(A)} = 390$ m/s (red triangles) with the corresponding calculated resonances (arrows). The MSE vanishes for atoms moving parallel to the **B** field (inset).

velocity components perpendicular to the optical axis indicated a much smaller asymmetry. We attribute this discrepancy to an additional inhomogeneity of the magnetic field.

Beyond the dependence on the quantum state and the direction of **B** and $\mathbf{v}^{(A)}$, the absolute value of the velocity

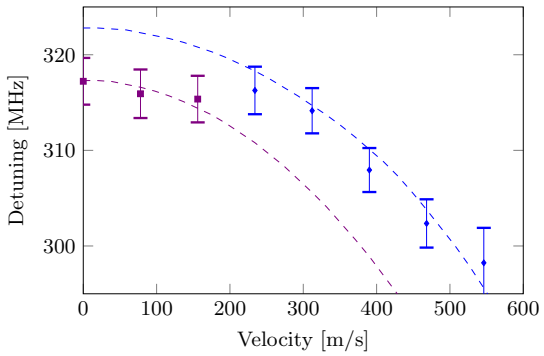

FIG. 4. Velocity dependence of the MSE for the $100D_{5/2}$ state. The squares and diamonds with error bars are the measured transmission peaks for coupling laser detunings Δ_c representing the resonance frequencies in a field of 98 G. The two dashed lines are calculated energy levels. Mixing effects exchange oscillator strengths between the states and the measured transmission peak can be assigned to either of them.

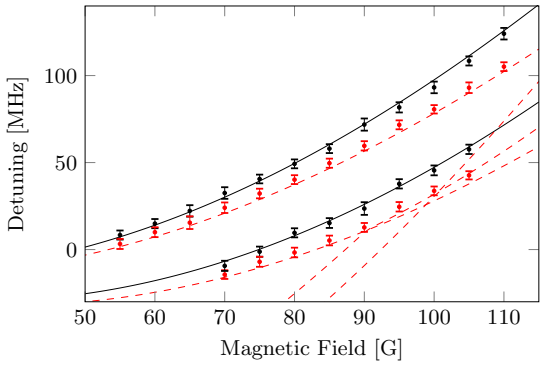

FIG. 5. The EIT resonances of the two velocity classes $v^{(A)} = 0$ m/s (black lines) and $v^{(A)} = 390$ m/s (dashed red lines) for the $100D_{5/2}$ state are shifted by the MSE dependent on the magnetic field. The detunings Δ_c relative to the selected velocity classes for the maximal probe laser transmission (dots with error bars) match the theory lines well. The oscillator strength for different states (red lines in the lower part) are altered through the MSE and the evaluated peak does not follow one theory line.

component perpendicular to the field plays an important role. This velocity dependence of the shift is shown in Fig. 4. The velocities correspond to probe laser detunings between 0 and 700 MHz. From our numerical calculation we can assign the measured peak to two different substates whose intensities are transferred from one state to another through the MSE at around 250 m/s.

Furthermore the $\mathbf{v}^{(A)} \times \mathbf{B}$ term relates the MSE to the magnetic field which is shown in Fig. 5. For magnetic fields lower than 50 G the shift is smaller than the uncertainties from the laser system and therefore not shown here. For zero field the energy levels of the states coincide. The lower resonance lines indicate a transfer of oscillator strengths between different states through the appearance of anticrossings of m states due to the motional electric field.

In conclusion, our work expands the experimental investigations of the MSE to low static magnetic fields. We observed the motional Stark effect on ^{87}Rb Rydberg atoms in a vapor cell using EIT spectroscopy with an accuracy better than 2 MHz. At 100 G the shifts are on the order of 10 MHz for the $100D_{5/2}$ state, which is in good agreement with the results of our numerical calculation based on an energy matrix diagonalization of the atom in crossed fields. We introduced a two-body model system for alkali-metal Rydberg atoms along with experimental data and conclude that it opens opportunities in describing many-body systems. The theoretical description of the MSE by a two-body Hamiltonian also confirms that the influence of the coupling of internal dynamics to the collective motion of the atom is small, but we estimate it to become crucial for states of $n \geqslant 150$ for a magnetic field of 100 G. Finally, calculations of atomic multielectron spectra in crossed fields configurations can be tested experimentally using the MSE as the condition $\boldsymbol{\mathcal{E}} \perp \mathbf{B}$ is exactly fulfilled with $\boldsymbol{\mathcal{E}} = \mathbf{E}_L$ which otherwise is hardly achievable in experiments with two external fields.

This work was financially supported by Deutsche Forschungsgemeinschaft through SPP 1929 (GiRyd).

[1] W. E. Lamb, Phys. Rev. **85**, 259 (1952).
[2] F. M. Levinton, R. J. Fonck, G. M. Gammel, R. Kaita, H. W. Kugel, E. T. Powell, and D. W. Roberts, Phys. Rev. Lett. **63**, 2060 (1989).
[3] F. Levinton, Rev. Sci. Instrum. **70**, 810 (1999).
[4] G. G. Pavlov and P. Mészáros, Astrophys. J. **416**, 752 (1993).
[5] K. Mori and C. J. Hailey, Astrophys. J. **564**, 914 (2002).
[6] D. G. Thomas and J. J. Hopfield, Phys. Rev. **124**, 657 (1961).
[7] M. Rosenbluth, T. A. Miller, D. M. Larsen, and B. Lax, Phys. Rev. Lett. **39**, 874 (1977).
[8] G. C. Neumann, B. R. Zegarski, T. A. Miller, M. Rosenbluh, R. Panock, and B. Lax, Phys. Rev. A **18**, 1464 (1978).
[9] H. Crosswhite, U. Fano, K. T. Lu, and A. R. P. Rau, Phys. Rev. Lett. **42**, 963 (1979).
[10] C. W. Clark, K. Lu, and A. F. Starace, *Progress in Atomic Spectroscopy Part C* (Plenum, New York, 1984), pp. 247–320.
[11] R. J. Elliott, G. Droungas, and J. P. Connerade, J. Phys. B **28**, L537 (1995).
[12] J. Avron, I. Herbst, and B. Simon, Ann. Phys. **114**, 431 (1978).
[13] H. Herold, H. Ruder, and G. Wunner, J. Phys. B. **14**, 751 (1981).
[14] P. Schmelcher and L. S. Cederbaum, *Atoms and Molecules in Intense Fields* (Springer, Berlin, Heidelberg, 1997), pp. 27–62.
[15] A. K. Mohapatra, T. R. Jackson, and C. S. Adams, Phys. Rev. Lett. **98**, 113003 (2007).
[16] O. Arnoult, F. Nez, L. Julien, and F. Biraben, Eur. Phys. J. D **60**, 243 (2010).
[17] B. Julsgaard, J. Sherson, J. I. Cirac, J. Fiurášek, and E. S. Polzik, Nature (London) **432**, 482 (2004).
[18] J. Appel, E. Figueroa, D. Korystov, M. Lobino, and A. I. Lvovsky, Phys. Rev. Lett. **100**, 093602 (2008).
[19] R. Löw and T. Pfau, Nat. Photon. **3**, 197 (2009).
[20] Y.-W. Cho and Y.-H. Kim, Opt. Express **18**, 25786 (2010).
[21] H. Kübler, J. Shaffer, T. Baluktsian, R. Löw, and T. Pfau, Nat. Photon. **4**, 112 (2010).
[22] Y. Fang, Z. Qin, H. Wang, L. Cao, J. Xin, J. Feng, W. Zhang, and J. Jing, Sci. China: Phys., Mech. Astron. **58**, 1 (2015).
[23] L. Gor'kov and I. Dzyaloshinskii, Sov. Phys. JETP **26**, 449 (1968).
[24] M. Kurz, P. Grünwald, and S. Scheel, Phys. Rev. B **95**, 245205 (2017).
[25] J. Alford and M. Strickland, Phys. Rev. D **88**, 105017 (2013).
[26] M. Marinescu, H. R. Sadeghpour, and A. Dalgarno, Phys. Rev. A **49**, 982 (1994).
[27] B. R. Johnson, J. O. Hirschfelder, and K.-H. Yang, Rev. Mod. Phys. **55**, 109 (1983).
[28] T. F. Gallagher, *Rydberg Atoms*, 1st ed. (Cambridge University Press, Cambridge, England, 1994).
[29] T. Pohl, H. R. Sadeghpour, and P. Schmelcher, Phys. Rep. **484**, 181 (2009).
[30] H. A. Bethe and E. E. Salpeter, *Quantum Mechanics of One and Two Electron Atoms* (Springer, Berlin, 1957).
[31] A. Sanayei, N. Schopohl, J. Grimmel, M. Mack, F. Karlewski, and J. Fortágh, Phys. Rev. A **91**, 032509 (2015).
[32] M. L. Zimmerman, M. G. Littman, M. M. Kash, and D. Kleppner, Phys. Rev. A **20**, 2251 (1979).
[33] M. Mack, F. Karlewski, H. Hattermann, S. Höckh, F. Jessen, D. Cano, and J. Fortágh, Phys. Rev. A **83**, 052515 (2011).
[34] J. Grimmel, M. Mack, F. Karlewski, F. Jessen, M. Reinschmidt, N. Sándor, and J. Fortágh, New J. Phys. **17**, 053005 (2015).

Controlling the dipole blockade of highly Stark-shifted rubidium Rydberg states

Markus Stecker,[1,*] Jens Grimmel,[1] Raphael Nold,[1] József Fortágh,[1] and Andreas Günther[1,†]

[1] *Center for Quantum Science, Physikalisches Institut, Eberhard Karls Universität Tübingen, Auf der Morgenstelle 14, D-72076 Tübingen, Germany*

(Dated: November 6, 2017)

We report on the observation of excitation blockade for strongly Stark-shifted Rydberg states. We make use of the fact that even for electric fields above the classical ionization limit, there are Rydberg states with small ionization rates. We have developed a detection scheme for controlled ionization and magnified imaging of those states with high spatial and temporal resolution by adiabatic transfer to a state with a suitable ionization rate. We show that the strength of the blockade effect can be altered by choosing states with varying electric dipole moment.

Rydberg systems exhibit strong correlations due to the electrostatic interaction between the highly excited atoms. This property makes them a promising candidate for quantum information processing [1, 2]. The interaction can be of van der Waals or dipole-dipole type [3] and manifests itself in the so called Rydberg blockade, where, in the presence of a first excitation, a second excitation is suppressed. The efficiency of the blockade and with it the fidelity of a blockade-based quantum gate depends on the strength of the Rydberg-Rydberg interaction [4, 5]. Consequently, since the first measurement of the Rydberg blockade [6, 7], efforts have been undergone to enhance and tune the interaction for example by tuning a state with a small electric field to a Förster resonance [8–10], using a state with a near resonant dipole-dipole interaction at zero field [11], the AC Stark shift [12], Rotary echo [13] or a small DC electric field [14–16]. Coherent collective Rydberg excitation in the strong blockade regime has been achieved [17] as well as blockade between two individiual atoms [18, 19]. A two-qubit CNOT gate and entanglement between pairs of atoms via the blockade interaction has been demonstrated [20–22] and a quantum Ising model out of single Rydberg atoms has been realized [23]. Spatially resolved measurement of the Rydberg blockade has been studied with separate excitation areas [24, 25], quantum gas microscopes [26, 27], interaction enhanced imaging [28, 29] and direct spatially resolved imaging by field ionization [30–33].

In this work, we investigate Rydberg-Rydberg interactions in an electric field region close to the classical ionization limit, which is typically not considered adequate for this kind of experiment. We identify states at high electric fields with high transition dipole moments and low ionization rates suitable for observing blockade effects in this regime. We show that we can tune the interaction strength by a small change in the external electric field and observe Rydberg blockade of different effectiveness. Furthermore, we implement a detection scheme in which the excited Rydberg atoms are ionized by adiabatic transfer to a state with a defined ionization rate. Spatially resolved detection is achieved by imaging the ions with a high resolution ion microscope for cold atoms [34].

The energy landscape of highly Stark-shifted Rydberg atoms exhibits an intricate form [35] and is governed by strongly varying line broadening due to ionization. Nevertheless, as predicted by numerical calculations [36], we find states, which are mostly unaffected by ionization and have a varying dipole-dipole interaction strength. In order to choose a suitable state for spatially resolved detection of Rydberg atoms, we aim for states which undergo a rapid change in their ionization rate, changing from a few kilohertz to about 1 MHz within around 1 V/cm. This way, we can transfer the excited state with a small change of the electric field to an ionizing state with a defined ionization rate. Conventionally, Rydberg atoms are ionized by simply switching the electric field to a much higher value. In contrast, our approach realizes a very controlled way of ionization. We can choose a state with an ionization rate that is on the one hand high enough that the atoms do not move or decay significantly before they get ionized, but on the other hand low enough that saturation of the ion detector is avoided. Besides this technical advantage, our ionization method also allows for a reversal of this transfer, bringing the ionizing state back to the original state. This is virtually impossible when switching to a much higher field, because during the time evolution through the Stark map, the state gets redistributed over many Stark-shifted states [37].

Our experimental setup consists of a vacuum setup with a standard magneto-optical trap (MOT) for ^{87}Rb with 10^7 atoms at a temperature of 150 µK. The spatially resolved detection of ions out of the MOT is done with an ion microscope composed of four consecutive electrostatic lenses and an MCP in conjunction with a delay line detector for electronic readout of the individual ion positions and time stamps. The MOT is positioned between two extractor electrodes which can be used to generate the desired electric field at the position of the atoms. For details about the experimental setup see [34]. Typically, the magnification of the ion microscope is around 1000, resulting in an imaging area of 40 µm diameter. Rydberg atoms are excited via a two-photon transition from the $5S_{1/2}$ state via the intermediate $5P_{3/2}$ state to a Rydberg

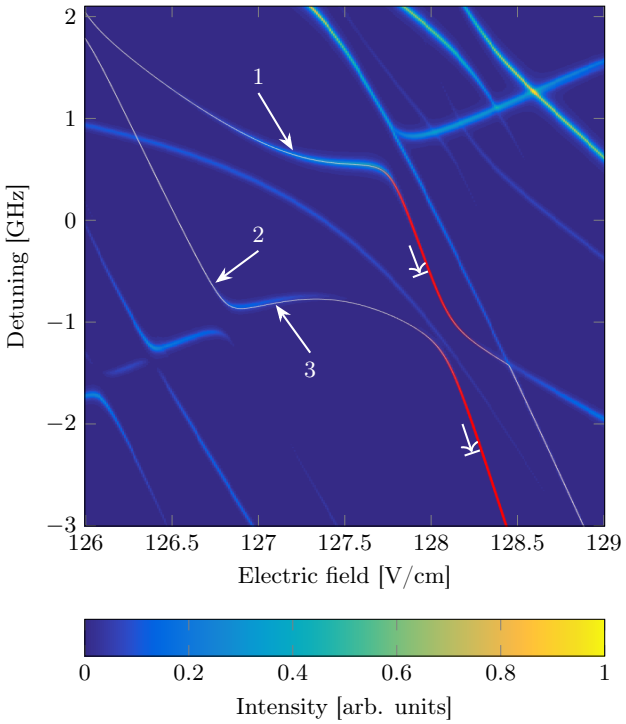

FIG. 1. Numerically calculated Stark spectrum of ^{87}Rb [36]. The detuning is given relative to the unperturbed $43S_{1/2}$ state (classical ionization limit of 127.2 V/cm). The colorplot shows transition strength and linewidth of the resonances. The solid lines depict the ionization rates of the two states that were used in the experiment from nonionizing (white) to strongly ionizing (red). The arrowheads with delimiters mark the ionizing state that the Rydberg state is transferred to for detection.

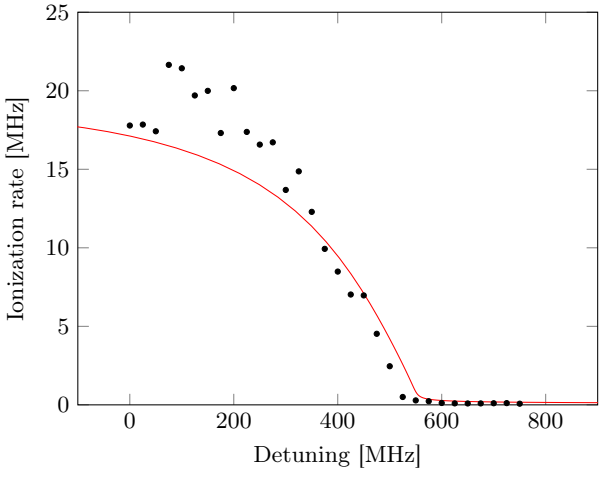

FIG. 2. Measured (black dots) and calculated (solid red line) ionization rates following the line containing resonance 1 (see Fig. 1). Deviations between theory and experiment arise from the fact that the free parameter of the CAP potential was optimized for a broad spectral range and not for a single resonance.

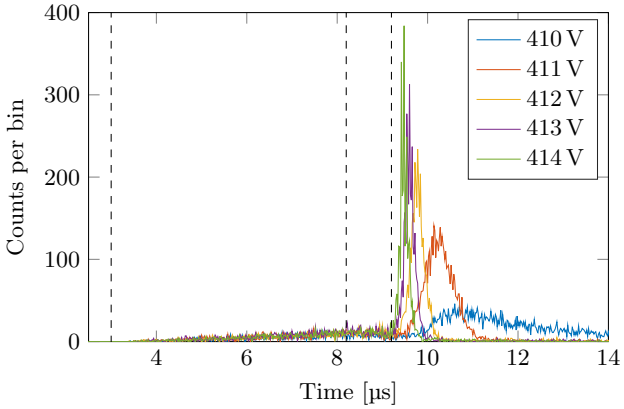

FIG. 3. Histogram of ion arrival times for different final values of the extractor voltage (bin size of 20 ns, sum over 500 excitation pulses for each curve). The first two dashed vertical lines depict the Rydberg excitation pulse (duration of 5 µs), the third line shows the start of the electric-field ramp (transition time ≈ 1 µs). With increasing voltage, the ionization occurs earlier and faster.

state. The lower transition at ≈ 780 nm is provided by the cooling lasers of the MOT. The beam for the upper transition at ≈ 480 nm is directed perpendicular to the optical axis of the ion imaging. The laser is frequency stabilized by a HighFinesse Wavelength Meter WS-U2. The blue beam going into the vacuum chamber is focused to a light sheet with beam waists of 9 µm and 80 µm, respectively, in order to limit the excitation depth in the direction of the ion-optical axis while still having high light intensity in the imaging area.

In order to demonstrate the applicability of our excitation and detection scheme, we first validate the predictions of our numerical calculation [36] experimentally. The calculations make use of a complex absorbing potential [38–40] to predict ionization spectra of highly Stark-shifted Rydberg states. The results for a small energy region corresponding to the unperturbed $43S_{1/2}$ state and an electric field of 126-129 V/cm can be seen in Fig. 1 (the corresponding classical ionization limit is 127.2 V/cm). We picked this region because there are two resonance lines present that undergo a strong change in ionization rate from non-ionizing to strongly ionizing. To measure the ionization rates, we excite Rydberg atoms at different points along the resonance line with a blue laser pulse of 1 - 5 µs duration (depending on the transition strength) and simultaneously detect the arrival time of the ions reaching the detector. The lower transition is provided by the MOT-lasers which are continuously on during the experiment. With one excitation pulse typically yielding 1-30 ions depending on the transition strength of the resonance, the excitation pulse is repeated several thousand times. A histogram of the arrival times is derived and the ionization rate of the state

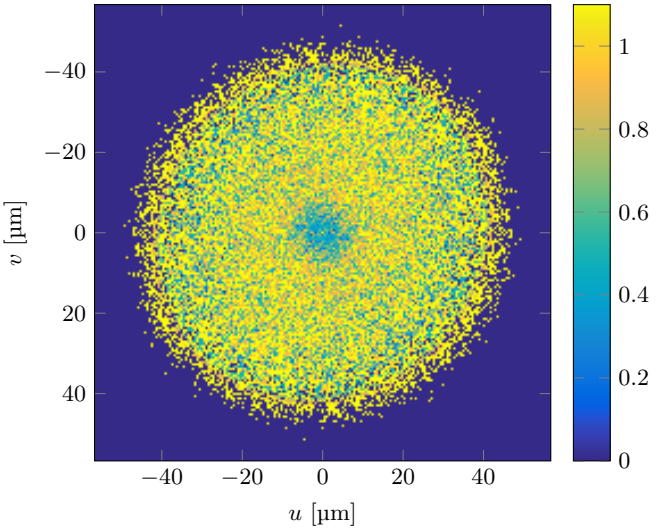

FIG. 4. Spatial correlation function $g^{(2)}(u, v)$ when exciting resonance 1 of Fig. 1. The Rydberg blockade effect manifests itself by a decrease of $g^{(2)}$ to values smaller than 1 for interatomic separations smaller than the blockade radius.

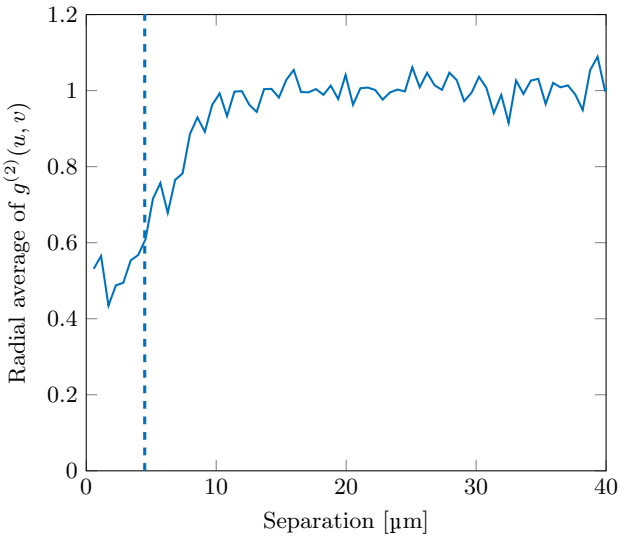

FIG. 5. Radial average of $g^{(2)}(u, v)$ for excitation of resonance 1. The dashed line depicts the blockade radius calculated following Eq. 3.

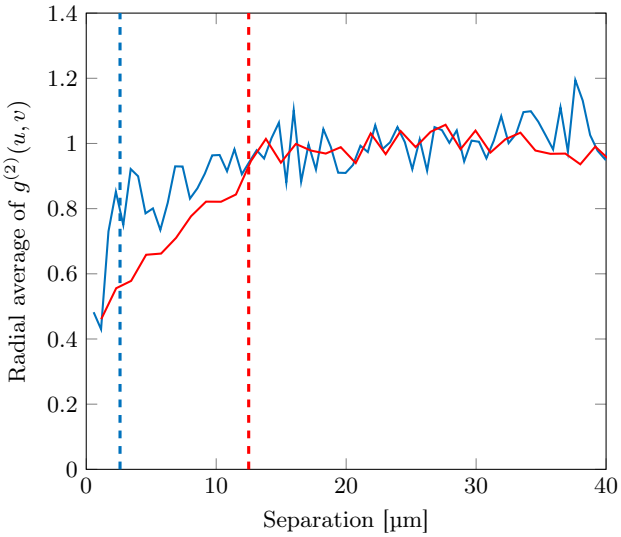

FIG. 6. Radial average of $g^{(2)}(u, v)$ for excitation of resonances 2 (red, large blockade radius) and 3 (blue, small blockade radius). The dashed lines depict the blockade radii calculated following Eq. 3.

can be determined by the decay of the ion signal after the end of the excitation pulse assuming other decay and ionization channels to be negligible. Radiative decay to lower states and redistribution to higher and lower states by black body radiation can alter the ionization rate to both higher and lower values. Since the lifetimes of Rydberg atoms are in general tens of microseconds [41] and the redistribution by black body radiation is in the kHz regime [42], we do not expect a major influence of these mechanisms on our measurements. However, it has to be pointed out that in the strongly Stark-shifted regime, the redistribution could differ from the zero-field case. Nevertheless, the experimental data shows good agreement with the results from the numerical calculation (see Fig. 2).

For the spatially resolved detection of Rydberg atoms we now set electric field and laser frequency to a slowly ionizing state and pulse the blue laser. After the excitation, the voltage at the extractor electrodes is ramped up by around 1 V/cm in order to transfer the Rydberg atoms to an ionizing state. A high voltage switch is used to change the electric field with a transition time of $\approx 1\,\mu s$. Time of flight and position of the ions hitting the detector are recorded. The excitation-detection-cycle is repeated up to several thousand times. Each pulse typically yields 2-8 ions. In Fig. 3, the effect of different end values for the extractor voltages is shown (the transition times remain unchanged). The ionization takes place faster for atoms transferred to a state with higher ionization rate. Furthermore, the onset of ionization shifts to earlier values since the atoms start ionizing before the end value is reached. We excite the three resonances depicted with arrows and numbers in Fig. 1 and choose the end value of the extractor voltage such that the Rydberg population gets ionized within 1 µs. For resonance 1, the excitation is done at an electric field of 127.2 V/cm and a laser detuning of 686 MHz (with respect to the unperturbed 43S state). For ionization, the field is then switched to ≈ 128 V/cm. For exciting resonance 2, the electric field is set to 126.7 V/cm and the laser detuning to −614 MHz. For resonance 3, the electric field is 127.1 V/cm and the detuning −794 MHz. The ionization of these two states

is done by switching the field to $\approx 128.3\,\mathrm{V/cm}$. The magnification of the ion-optical system was set to 1129.

For each pulse, the two-dimensional spatial second order correlation function

$$g^{(2)}(u,v) = \frac{\langle\langle f(x+u,y+v)f(x,y)\rangle\rangle_{x,y}}{\langle\langle f(x+u,y+v)\rangle\rangle_{x,y}\langle\langle f(x,y)\rangle\rangle_{x,y}}, \quad (1)$$

with the detector function $f(x,y)$ and displacements u,v is calculated. The detector function can be written as

$$f(x,y) = \sum_{i=1}^{N} \delta(x-x_i)\delta(y-y_i), \quad (2)$$

with the coordinates x_i, y_i of the N incoming ions on the detector after one excitation pulse. The correlation results for the individual pulses are summed up. In order to account for the spatially inhomogeneous excitation efficiency (due to inhomogeneous laser power) and the influence of the finite detector size, the result is normalized to the correlation function calculated from all events of the different pulses at once. In the resulting signal (Figs. 4, 5 and 6), an excitation blockade manifests itself in a decreased (< 1) correlation function in a certain region around the origin. In order to characterize the blockade by a blockade radius, the radial mean of $g^{(2)}$ is calculated by radial binning and averaging of the results from $g^{(2)}(u,v)$.

For resonance 1, the blockade effect starts at an interatomic distance of 9 µm, for resonance 2 at 12 µm and for resonance 3 at 2 µm. For $r \to 0$, the value of $g^{(2)}$ does not reach zero because our excitation area is not perfectly two dimensional. The strong blockade effect of resonances 1 and 2 show that even in this high electric-field regime, which is normally governed by ionization, we can observe Rydberg-Rydberg interaction. When we compare the results for resonances 2 and 3 which are both part of the same resonance line, we see that we can drastically alter the interaction strength by a small change of the electric field.

As a theoretical value for the blockade radius, we define the distance r_b at which the energy shift ΔW due to the interatomic interaction equals the excitation laser linewidth $\delta\nu_L$:

$$\hbar 2\pi\delta\nu_L = \Delta W(r_b). \quad (3)$$

We estimate $\delta\nu_L \approx 5\,\mathrm{MHz}$ for our experiment. The energy shift due to dipole-dipole interactions is

$$\Delta W = \frac{1}{4\pi\epsilon_0}\frac{p_z^2}{R^3}\left(1-3\cos^2\Theta\right), \quad (4)$$

with the permanent electric dipole moment p_z (electric field in z-direction), the interatomic distance R and the angle between R and z-axis Θ. The light sheet is oriented perpendicular to the optical axis of the ion imaging system and the electric field of the extractor electrodes points along the optical axis, so we assume $\Theta = \pi/2$. The dipole moment p_z of a Stark-shifted state in an electric field F with energy $E(F)$ can be determined by evaluating the slope of the resonance line $-dE(F)/dF$.

We find $r_b = 4.5$ µm for resonance 1, 12.5 µm for resonance 2 and 2.6 µm for resonance 3, as depicted in Figs. 5 and 6 via the dashed vertical lines. We see that the radial average of the $g^{(2)}$ correlation function of resonances 2 and 3 in Fig. 6 fit nicely to the calculated blockade radii resulting from dipole-dipole interaction. The slope at resonance 2 in the Stark map is big (see Fig. 1), the resulting dipole moment is $1.90 \cdot 10^{-26}\,\mathrm{Cm}$. This high value leads to a strong dipole-dipole interaction resulting in a large blockade radius. In contrast to that, we have a small slope at resonance 3 with a small dipole moment of $1.76 \cdot 10^{-27}\,\mathrm{Cm}$ leading to a weak excitation blockade. For resonance 1, the calculated blockade radius of 3.5 µm ($p_z = 4.19 \cdot 10^{-27}\,\mathrm{Cm}$) does not match the measured value. The decrease of the radial average of the correlation function in Fig. 5 starts at ≈ 9 µm. Besides the dipole-dipole interaction there is also a second-order van der Waals interaction which could lead to the observed blockade. Furthermore, the interaction could be enhanced by resonant energy transfer [3].

In summary, we have shown that the Rydberg blockade can be observed at highly Stark-shifted states and is tunable by small changes in the electric field. In many experiments, residual electric fields are present, especially when atoms are brought close (< 100 µm) to surfaces where adsorbates play a crucial role [43–46]. These small distances are often necessary, for example to reach the strong coupling regime of atoms coupled to a coplanar superconducting resonator [47, 48]. Conventionally, the fields have to be compensated by a set of electrodes to account for all directions which can be challenging and cumbersome. Instead of trying to reach a zero field condition, we have shown in our work that the complicated "spaghetti region" of the Stark spectrum with its diversity of states can be seen as an advantage instead of an annoyance and represents the opportunity for tailoring excitation, interaction and ionization of Rydberg states.

This work was financially supported by Deutsche Forschungsgemeinschaft through SPP 1929 (GiRyd). M.S. acknowledges financial support from Landesgraduiertenförderung Baden-Württemberg.

* markus.stecker@uni-tuebingen.de
† a.guenther@uni-tuebingen.de

[1] D. Jaksch, J. I. Cirac, P. Zoller, S. L. Rolston, R. Côté, and M. D. Lukin, Phys. Rev. Lett. **85**, 2208 (2000).
[2] M. D. Lukin, M. Fleischhauer, R. Cote, L. M. Duan, D. Jaksch, J. I. Cirac, and P. Zoller, Phys. Rev. Lett. **87**, 037901 (2001).
[3] A. Reinhard, T. C. Liebisch, B. Knuffman, and

G. Raithel, Phys. Rev. A **75**, 032712 (2007).
[4] M. Saffman and T. G. Walker, Phys. Rev. A **72**, 022347 (2005).
[5] X. L. Zhang, A. T. Gill, L. Isenhower, T. G. Walker, and M. Saffman, Phys. Rev. A **85**, 042310 (2012).
[6] D. Tong, S. M. Farooqi, J. Stanojevic, S. Krishnan, Y. P. Zhang, R. Côté, E. E. Eyler, and P. L. Gould, Phys. Rev. Lett. **93**, 063001 (2004).
[7] K. Singer, M. Reetz-Lamour, T. Amthor, L. G. Marcassa, and M. Weidemüller, Phys. Rev. Lett. **93**, 163001 (2004).
[8] T. Vogt, M. Viteau, J. Zhao, A. Chotia, D. Comparat, and P. Pillet, Phys. Rev. Lett. **97**, 083003 (2006).
[9] A. Reinhard, K. C. Younge, T. C. Liebisch, B. Knuffman, P. R. Berman, and G. Raithel, Phys. Rev. Lett. **100**, 233201 (2008).
[10] S. Ravets, H. Labuhn, D. Barredo, L. Béguin, T. Lahaye, and A. Browaeys, Nat. Phys. **10**, 914 (2014).
[11] A. Reinhard, K. C. Younge, and G. Raithel, Phys. Rev. A **78**, 060702 (2008).
[12] P. Bohlouli-Zanjani, J. A. Petrus, and J. D. D. Martin, Phys. Rev. Lett. **98**, 203005 (2007).
[13] N. Thaicharoen, A. Schwarzkopf, and G. Raithel, Phys. Rev. Lett. **118**, 133401 (2017).
[14] T. Vogt, M. Viteau, A. Chotia, J. Zhao, D. Comparat, and P. Pillet, Phys. Rev. Lett. **99**, 073002 (2007).
[15] N. Thaicharoen, L. F. Gonçalves, and G. Raithel, Phys. Rev. Lett. **116**, 213002 (2016).
[16] L. F. Gonçalves and L. G. Marcassa, Phys. Rev. A **94**, 043424 (2016).
[17] R. Heidemann, U. Raitzsch, V. Bendkowsky, B. Butscher, R. Löw, L. Santos, and T. Pfau, Phys. Rev. Lett. **99**, 163601 (2007).
[18] E. Urban, T. A. Johnson, T. Henage, L. Isenhower, D. D. Yavuz, T. G. Walker, and M. Saffman, Nat. Phys. **5**, 110 (2009).
[19] A. Gaëtan, Y. Miroshnychenko, T. Wilk, A. Chotia, M. Viteau, D. Comparat, P. Pillet, A. Browaeys, and P. Grangier, Nat. Phys. **5**, 115 (2008).
[20] L. Isenhower, E. Urban, X. L. Zhang, A. T. Gill, T. Henage, T. A. Johnson, T. G. Walker, and M. Saffman, Phys. Rev. Lett. **104**, 010503 (2010).
[21] T. Wilk, A. Gaëtan, C. Evellin, J. Wolters, Y. Miroshnychenko, P. Grangier, and A. Browaeys, Phys. Rev. Lett. **104**, 010502 (2010).
[22] K. M. Maller, M. T. Lichtman, T. Xia, Y. Sun, M. J. Piotrowicz, A. W. Carr, L. Isenhower, and M. Saffman, Phys. Rev. A **92**, 022336 (2015).
[23] H. Labuhn, D. Barredo, S. Ravets, S. de Léséleuc, T. Macrì, T. Lahaye, and A. Browaeys, Nature **534**, 667 (2016).
[24] C. S. E. van Ditzhuijzen, A. F. Koenderink, J. V. Hernández, F. Robicheaux, L. D. Noordam, and H. B. van Linden van den Heuvell, Phys. Rev. Lett. **100**, 243201 (2008).
[25] T. J. Carroll, K. Claringbould, A. Goodsell, M. J. Lim, and M. W. Noel, Phys. Rev. Lett. **93**, 153001 (2004).
[26] P. Schauß, M. Cheneau, M. Endres, T. Fukuhara, S. Hild, A. Omran, T. Pohl, C. Gross, S. Kuhr, and I. Bloch, Nature **491**, 87 (2012).
[27] P. Schauss, J. Zeiher, T. Fukuhara, S. Hild, M. Cheneau, T. Macri, T. Pohl, I. Bloch, and C. Gross, Science **347**, 1455 (2015).
[28] G. Günter, M. Robert-de-Saint-Vincent, H. Schempp, C. S. Hofmann, S. Whitlock, and M. Weidemüller, Phys. Rev. Lett. **108**, 013002 (2012).
[29] G. Gunter, H. Schempp, M. Robert-de Saint-Vincent, V. Gavryusev, S. Helmrich, C. S. Hofmann, S. Whitlock, and M. Weidemuller, Science **342**, 954 (2013).
[30] A. Schwarzkopf, R. E. Sapiro, and G. Raithel, Phys. Rev. Lett. **107**, 103001 (2011).
[31] A. Schwarzkopf, D. A. Anderson, N. Thaicharoen, and G. Raithel, Phys. Rev. A **88**, 061406 (2013).
[32] N. Thaicharoen, A. Schwarzkopf, and G. Raithel, Phys. Rev. A **92**, 040701 (2015).
[33] D. P. Fahey, T. J. Carroll, and M. W. Noel, Phys. Rev. A **91**, 062702 (2015).
[34] M. Stecker, H. Schefzyk, J. Fortágh, and A. Günther, New J. Phys. **19**, 043020 (2017).
[35] J. Grimmel, M. Mack, F. Karlewski, F. Jessen, M. Reinschmidt, N. Sandor, and J. Fortagh, New J. Phys. **17**, 53005 (2015).
[36] J. Grimmel, M. Stecker, M. Kaiser, F. Karlewski, L. Torralbo-Campo, A. Günther, and J. Fortágh, Phys. Rev. A **96**, 013427 (2017).
[37] R. Feynman, J. Hollingsworth, M. Vennettilli, T. Budner, R. Zmiewski, D. P. Fahey, T. J. Carroll, and M. W. Noel, Phys. Rev. A **92**, 043412 (2015).
[38] R. Kosloff and D. Kosloff, J. Comput. Phys. **63**, 363 (1986).
[39] U. V. Riss and H. D. Meyer, J. Phys. B **26**, 4503 (1993).
[40] S. Sahoo and Y. K. Ho, J. Phys. B **33**, 2195 (2000).
[41] T. F. Gallagher, *Rydberg atoms* (Cambridge University Press, 1994).
[42] I. I. Beterov, I. I. Ryabtsev, D. B. Tretyakov, and V. M. Entin, Phys. Rev. A **79**, 052504 (2009).
[43] J. M. McGuirk, D. M. Harber, J. M. Obrecht, and E. A. Cornell, Phys. Rev. A **69**, 062905 (2004).
[44] J. M. Obrecht, R. J. Wild, and E. A. Cornell, Phys. Rev. A **75**, 062903 (2007).
[45] A. Tauschinsky, R. M. T. Thijssen, S. Whitlock, H. B. van Linden van den Heuvell, and R. J. C. Spreeuw, Phys. Rev. A **81**, 063411 (2010).
[46] H. Hattermann, M. Mack, F. Karlewski, F. Jessen, D. Cano, and J. Fortágh, Phys. Rev. A **86**, 022511 (2012).
[47] S. Bernon, H. Hattermann, D. Bothner, M. Knufinke, P. Weiss, F. Jessen, D. Cano, M. Kemmler, R. Kleiner, D. Koelle, and J. Fortágh, Nat. Commun. **4**, 2380 (2013).
[48] H. Hattermann, D. Bothner, L. Y. Ley, B. Ferdinand, D. Wiedmaier, L. Sárkány, R. Kleiner, D. Koelle, and J. Fortágh, arXiv:1707.02730 (2017).